IMPROVING OZONE MEASUREMENTS FROM GROUND- AND SPACE-BASED INSTRUMENTS

OMID MOEINI NAJAFABADI

A DISSERTATION SUBMITTED TO
THE FACULTY OF GRADUATE STUDIES
IN PARTIAL FULFILLMENT OF THE REQUIREMENTS
FOR THE DEGREE OF

DOCTOR OF PHILOSOPHY

GRADUATE PROGRAM IN EARTH AND SPACE SCIENCE
YORK UNIVERSITY
TORONTO, ONTARIO
November 2017

© OMID MOEINI NAJAFABADI, 2017

Abstract

Three topics that are outstanding issues in ozone research were discussed in this study.

First, physical models of two primary standard instruments for total ozone measurements (the Dobson and Brewer ozone spectrophotometers) were developed to help better understand the effect of stray light on ozone measurements. The models showed that the error caused by stray light for a typical single Brewer at large ozone slant paths can be up to 5%, and up to 25% for a typical Dobson instrument. For the first time, new ozone absorption coefficients were calculated for the Brewer and Dobson instruments taking into account the effect of stray light.

MAESTRO is a moderate-resolution spectrometer onboard SCISAT satellite since 2003. The O_2 absorption bands are used by the MAESTRO retrieval to retrieve pressure and temperature profiles. In this study the MAESTRO p-T retrieval software was updated using the improved O_2 spectroscopic parameters from HITRAN (**hi**gh-resolution **tran**smission molecular absorption database) 2012 database. The MAESTRO preliminary p-T retrievals were reprocessed using the updated software and compared with the ACE-FTS (Atmospheric Chemistry Experiment – Fourier Transform Spectrometer) profiles and the processed results with HITRAN 2004. The analyses showed promising improvements to the p-T profiles below 50 km from the use of HITRAN 2012 parameters. New p-T profiles are capable to be used for the MAESTRO tangent height determination which makes the MAESTRO products independent from ACE-FTS pointing information and also leads to an improvement of the retrievals of other atmospheric constituents from the MAESTRO instrument.

Finally, a unique objective method (The Differential Back Trajectory (DBT) method) was developed using the data collected at a network of ozonesonde sites to evaluate the contribution of fire ozone to the tropospheric ozone budget. Fire ozone accounted over 18 sites, located across Canada and the U.S, using the DBT method and more than 1000 ozonesonde profiles collected during summer time of 2006, 2008, 2010 and 2011. The analysis showed that ozone amounts at sites nearer to the large fires were less influenced by the fires.

Dedication

Dedicated to

my love, my wife and my best friend, ***Zahra Anjomani****.*

Acknowledgements

First of all, I would like to extend my sincerest thanks to my supervisors, David Tarasick and Tom McElroy. This couldn't have happened without your guidance, support, and feedback. I am deeply grateful to be given an opportunity to be involved in so many exciting and interesting projects.

I would like to thank my committee members, Rob McLaren and Jim Whiteway for all of their help and encouragements that kept me on track. Thank you to my examiners and exam chair, Donald Hastie, Jinjun Shan and Peter Taylor for their time and valuable suggestions for revising this thesis. Thank you especially to my external examiner, Doug Degenstein, who came all the way from Saskatoon to make sure I had the right stuff.

Special thanks to Caroline Nowlan for providing me the MAESTRO pressure-temperature retrieval codes and so many other functions that helped me through processing and analyzing the MAESTRO retrievals. Thanks to Jason Zou for his help to access the MAESTRO and ACE-FTS data. I would like to thank Volodya Savastiouk for helping me better understand the Brewer retrieval. Thank you to Irina Petropavlovskikh and Bob Evans for their invaluable comments that helped me better understand the Dobson data. Thank you to Jane Liu for her great help working with HYSPLIT model and analyzing the output data. Thank you to David Barton for his help in the lab (PSE 403) through all of these years.

I thankfully acknowledge the Environment and climate change Canada and York University for their financial support.

To my office mates and friends at York University and Environment and Climate Change Canada: Zahra Vaziri, William Feng, Gurpreet Singh, and Mohammad Osman, thank you for all the good times we had together.

Finally, to my wife, **Zahra**, thank you for your patience, support and faith in me. This could not have been completed without your assistance and encouragements.

Table of Contents

List of Tables

List of Figures

1.Introduction

Ozone plays a significant role in atmospheric chemistry, climate and air quality. The existence of ozone and its presence in the atmosphere were discovered by the German chemist C.F. Schoenbein in 1839 [*Schoenbein*, 1850]. Soon after, *Hartley* [1881] identified its UV spectrum and its role as a UV filter in the atmosphere. While in the stratosphere (the "ozone layer") ozone absorbs most of the harmful solar ultraviolet (UV) radiation and protects life at the Earth's surface [*Crutzen*, 1970]; in the upper troposphere, ozone acts as an important greenhouse gas [*Forster et al.*, 2007] and at the surface it is an air pollutant with adverse impacts on human health [*Anenberg et al.*, 2010; *Bell et al.*, 2004; *Lippmann*, 1991; *McConnell et al.*, 2002] and plant physiology [*Darrall*, 1989; *Kangasjärvi et al.*, 1994].

The first instrument for routine atmospheric total column ozone measurements was developed by Gordon M.B. Dobson in 1930s [*Dobson*, 1931]. In 1957 a global network of total ozone monitoring stations was established as a part of International Geophysical Year. Since the 1970s, it has been recognized that stratospheric ozone was depleted by the release of a number of manmade chemicals [*Crutzen*, 1974; *Lovelock*, 1974; *Rowland* and *Molina*, 1975; *Stolarski* and *Cicerone*, 1974]. Ozone depleting substances (ODSs) which are responsible for the observed ozone depletion (e.g. in Polar regions; the "Ozone Hole" above

Antarctica) [*McElroy et al.*, 1986; *Tung et al.*, 1986] are produced in the troposphere and, because their atmospheric lifetimes are long compared with the time needed to reach the stratosphere, are able to be transported into the stratosphere [*Lovelock*, 1974]. In 1987, the Montreal Protocol was adopted to control the substances that deplete the ozone in the stratosphere. According to the Montreal protocol and its subsequent amendments and adjustments, many nations of the world agreed to reduce their use of ODSs ["Montreal protocol on substances that deplete the ozone layer," 1987]. Several studies have suggested that the ozone decline has stopped near mid-1990s [*Liu et al.*, 2013; *Newman et al.*, 2004; *Weatherhead* and *Andersen*, 2006; *Yang et al.*, 2005]. Now, nearly 20 years after the peak of ozone depleting substances in the stratosphere, identifying the ozone recovery, trends and their impacts on climate are important.

Ground based measurements have had key role in the recognition of ozone depletion and understanding the effects of ODSs on the global ozone layer, starting before the satellite era and continuing to the present day. Ground-based instruments with excellent long-term stability and accuracy are still essential to track the calibration of space-based, ozone-measuring instrument. Understanding the uncertainties of the measurements using ground- and space-based instruments is a matter of utmost importance for ozone studies. Two primary ground based instruments (the Brewer and Dobson spectrophotometers [*Brewer*, 1973; *Dobson*, 1931]) for total ozone measurements are modeled in this research to better understand their behaviors especially at large ozone slant column amounts as in the Arctic and Antarctic.

In addition, improvements to the retrieval algorithm of a space-based instrument, Measurement of Aerosol Extinction in the Stratosphere and Troposphere Retrieved by

Occultation (MAESTRO) [*McElroy et al.*, 2007], on board the Canadian SCISAT satellite have been developed.

One of the major sources of tropospheric ozone information is balloon-borne ozonesondes. A clear understanding of ozone production in the troposphere is increasingly important due to concern about air quality [*Baylon et al.*, 2015; *Cooper*, 2010; *Huang et al.*, 2013; *Jaffe* and *Wigder*, 2012; *Mckendry et al.*, 2011; *Monks et al.*, 2009; *Parrington et al.*, 2012; *Teakles et al.*, 2016]. While wildfires generate substantial amounts of ozone precursors, O_3 production from wildfires have been poorly understood as yet [*Jacob et al.*, 2010; *Jaffe* and *Wigder*, 2012; *Palmer et al.*, 2013; *Parrington et al.*, 2012; *Pfister et al.*, 2008]. With climate change, the frequency and intensity of boreal forest fires is likely to increase [*Gillett et al.*, 2004; *Westerling et al.*, 2006]. In the research presented here the impact of boreal forest fires on tropospheric ozone has been studied using high-vertical-resolution ozonesonde profiles.

1.1. Ozone, climate and air quality

Atmospheric ozone and Climate change are closely coupled. In the stratosphere, ozone decline due to emissions of anthropogenic ozone-depleting substances (ODS) and recovery from the depleted state as ODSs decline results in temperature and circulation changes [*Gillett* and *Thompson*, 2003; *WMO*, 2010]. The effect of ODSs on stratospheric ozone can clearly be seen in the annual appearance of the Antarctic ozone hole. Severe depletion of Antarctic ozone has occurred since 1980, without exception, in every year during the austral springtime (Figure 1.1).

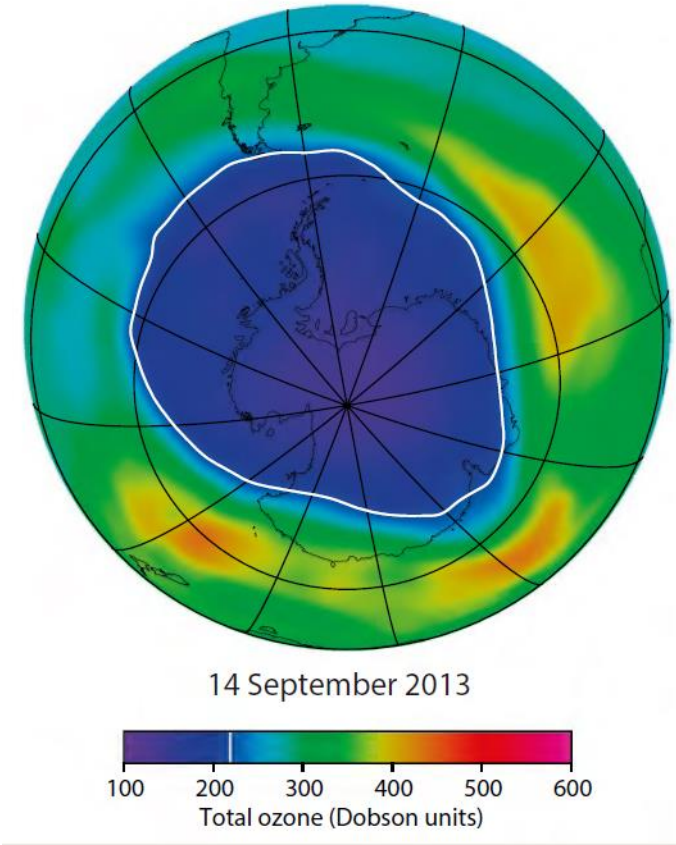

Figure 1.1: Antarctic total column ozone values on September 14, 2013 as measured by satellite. Severe ozone depletion (ozone hole) occurs every spring (white line). Minimum values inside the ozone hole are about 100 Dobson Unit (DU) compared with normal Antarctic springtime values of about 350 DU. The white line outlines the ozone hole area defined as the geographical area within the 220-DU contour on total ozone maps [*WMO*, 2014].

The average total ozone column in October has been about 40% below the values of 1980 resulting in 55-85% larger average erythemal UV measured at the South Pole. The annually averaged total ozone has decreased about 7% since 1979 as result of ODS emissions [*WMO*, 2006].

Cooling in the lower and upper stratosphere has been linked to ozone changes. Between 1980 and 1995 the global average temperature of the lower and upper stratosphere decreased by 1-2 K and 4 to 6 K respectively and since then it has remained constant mainly

due to declining ozone depletion and increasing CO_2 emissions [*IPCC*, 2013; *WMO*, 2010]. Stratospheric temperature changes resulted from ozone loss in the Antarctic are caused by the observed changes in Southern Hemisphere tropospheric circulation with associated impacts on surface climate and ocean. Furthermore, it is expected that ozone recovery over the next 50 years will influence the Southern Hemisphere climate and oceans [*McLandress et al.*, 2011; *Polvani et al.*, 2011; *WMO*, 2014].

Ozone in the troposphere is also an important short-lived climate pollutant. Ozone absorbs infrared radiation emitted from the Earth's surface in both the stratosphere and troposphere and is the fourth most important greenhouse gas after water vapor (H_2O), carbon dioxide (CO_2) and methane (CH_4). These gases have a large influence on the Earth's energy budget [*IPCC*, 2013; *WMO*, 2014]. Therefore, ozone changes and variations in both the stratosphere and troposphere influence climate.

Many of the ODSs and their substitutes are potent greenhouse gases [*IPCC*, 2013; *WMO*, 2014]. As a result, changes to these gases – increasing in the past decades and decreasing in response to compliance with the Montreal Protocol in future – influence global warming. The contribution of halocarbons (ODSs are the halocarbons controlled under Montreal Protocol) to climate forcing is the fifth largest forcing after carbon dioxide, methane, tropospheric ozone and water vapor [*WMO*, 2014].

Climate change also influences ozone changes in both stratosphere and troposphere. The mid to upper stratosphere cooling has been related to increases in Carbon dioxide (CO_2) via radiation to space [*Shine et al.*, 2003; *Thompson et al.*, 2012]. Stratospheric cooling slows down the gas-phase destruction of ozone resulting in an ozone increase in middle and upper

stratosphere which will slightly reduce the cooling in return [*Brasseur* and *Hitchman*, 1988; *WMO*, 2014].

Tropospheric changes also affect stratospheric ozone levels. More methane (CH_4) production in the troposphere leads to more methane (CH_4) transportation to the stratosphere, where the active chlorine that destroys ozone is converted to inactive hydrogen chloride (HCl) as a result of the reaction with methane [*Revell et al.*, 2012]. With a similar mechanism, nitrous oxide (N_2O) variations can influence ozone destruction [*Portmann et al.*, 2012] [Details in Chapter 2].

Climate models suggest that increasing greenhouse gases will likely lead to redistribution of ozone within stratosphere - decreases in column ozone in the tropics and increases elsewhere - via acceleration of the stratospheric Brewer-Dobson circulation [*Diallo et al.*, 2012]. The projected acceleration of Brewer-Dobson circulation along with ozone recovery will lead to increased transport of ozone from the stratosphere into the troposphere [*Randel* and *Thompson*, 2011; *Sioris et al.*, 2014].

Ozone in the troposphere is a principal factor in air quality, due to its effects on human respiratory health [*Bell et al.*, 2007; *Jerrett et al.*, 2009; *Lippmann*, 1991; *McConnell et al.*, 2002]. It is also responsible for significant damage to forests and crops [*Avnery et al.*, 2011; *Mauzerall* and *Wang*, 2001]. Climate change influences tropospheric ozone as well. Redistribution of the stratospheric ozone due to the acceleration of Brewer-Dobson circulation will affect tropospheric ozone via changing the UV flux at the Earth's surface and thus the photolysis rates [*Tang et al.*, 2011]. Changes in the UV radiations also will have impacts on air quality via influencing the chemically active tropospheric species [*Tang et al.*,

2011; *WMO*, 2014]. Further it will affect the lifetimes of chemically active greenhouse gases such as methane [*Voulgarakis et al.*, 2013; *WMO*, 2014].

The frequency and intensity of forest fires is likely to increase as a result of climate change. It has been shown that the frequency of fires over the area burned for Canadian and US forests is related to an increase in temperature and reduction of moisture at the area of interest [*Kasischke* and *Turetsky*, 2006; *Westerling et al.*, 2006]. Climate change is the key factor in explaining changes in fire frequency and intensity over recent decades [*Gillett et al.*, 2004; *Westerling et al.*, 2006]. Forest fires generate large amount of ozone precursors such as carbon monoxide, volatile organic compounds and nitrogen oxides. It is very likely that fires contribute to exceedances of the ozone air quality threshold concentrations via production and long-range transport of O_3 and its photochemical precursors [*Jaffe et al.*, 2004; *Jaffe* and *Wigder*, 2012; *Mckendry et al.*, 2011; *Teakles et al.*, 2016].

1.2. Objectives

Dobson and Brewer spectrophotometers are the primary standard instruments for ground-based ozone measurements under the World Meteorological Organization's (WMO) Global Atmosphere Watch program. It has been known that the Brewer and Dobson ozone measurements suffer from non-linearity due to the presence of stray light caused by scattering from optical elements within the instruments [*Basher*, 1982b; *Fioletov et al.*, 2000]. The target accuracy for ground-based ozone measurements is 1% while the error at large ozone slant paths can be up to 8% for the single Brewer and up to 20% for Dobson AD pair measurements [*Basher*, 1982b]. This error restricts measurements at high latitudes, like

Arctic stations, particularly in the late winter and early spring when the ozone column and SZA are large. One of the objectives of this research is to understand, analyze and document the error caused by the stray light in Brewer and Dobson ozone measurements.

MAESTRO (Measurement of Aerosol Extinction in the Stratosphere and Troposphere Retrieved by Occultation) is a UV-Visible-NIR, low-resolution spectrometer on-board the Canadian satellite SCISAT as part of the Atmospheric Chemistry Experiment (ACE) mission flying along with a Fourier Transform Spectrometer (the ACE-FTS) since 2003 [*McElroy et al.*, 2007]. The MAESTRO retrieval is able to determine pressure and temperature profiles by using the measurement of O_2 *A*- and *B*- bands as the mixing ratio of the oxygen molecule is known and constant in the troposphere and stratosphere [*Nowlan et al.*, 2007]. An analysis using simulated data demonstrated the capability of MAESTRO measurements to retrieve p-T profiles [*Nowlan et al.*, 2013]. The HITRAN-2004 (high-resolution transmission molecular absorption database) was used as a source for spectroscopic parameters for the retrieval forward model. O_2 band spectral features have been significantly improved in recent update of HITRAN (2012) [*Rothman et al.*, 2013]. Analyzing the impact of different HITRAN datasets on MAESTRO p-T profiles retrieved using data acquired by the satellite instrument on-orbit is another objective of this research. Currently, the MAESTRO retrievals rely on the pointing information provided by the ACE-FTS p-T profiles. As a result any ACE-FTS poor retrieval directly impacts the MAESTRO profile. Ideally MAESTRO must be completely independent from the ACE-FTS. Accurate pressure profiles calculated from O_2 bands can be used to determine the pointing information for the MAESTRO which will eventually lead to the improvements of MAESTRO ozone profiles and other constituents.

Tropospheric ozone (O_3) is an important air pollutant, in addition to its well-known effects on crop production and human respiratory health [*Avnery et al.*, 2011; *Jerrett et al.*, 2009; *Lippmann*, 1991]. Wildfires generate large amounts of O_3 precursors [*Andreae* and *Merlet*, 2001; *Crutzen et al.*, 1979] and a number of studies suggest that the fires can contribute to exceedance of the O_3 air quality threshold concentrations via production and long-range transport of O_3 and its precursors [*Jaffe* and *Wigder*, 2012; *Mckendry et al.*, 2011; *Teakles et al.*, 2016]. On the other hand, the frequency and intensity of forest fires is likely to increase over Canada and US as a result of climate change [*Gillett et al.*, 2004; *Spracklen et al.*, 2009; *Westerling et al.*, 2006]. Different approaches and datasets used to study the ozone production from boreal fires appear to give conflicting results [*Jaffe* and *Wigder*, 2012]. While dozens of studies suggest some degree of ozone production by wildfires [*Pfister et al.*, 2006; *Real et al.*, 2007; *Singh et al.*, 2010], a number of observations, mainly in boreal regions, show that O_3 is minimally enhanced or even depleted downwind of some biomass burning plumes [*Alvarado et al.*, 2010; *Jacob et al.*, 2010]. Using several hundred ozone profiles collected at regular Canadian ozonesonde sites and through a number of campaigns during June to August 2006, 2008, 2010, and 2011, this research presents a new method to estimate the fire-generated ozone budget in the total tropospheric ozone column as the last objective of this thesis. This is a unique method for evaluating the contribution of fire ozone to the tropospheric ozone budget as it uses a network of observing sites at fixed locations.

1.3. Scientific contributions

To achieve the objectives, this research was designed in three parts:

1. Error analysis of Brewer and Dobson ozone spectrophotometers, the primary standard instruments for ground-based ozone measurements;
2. Improvements to the ACE-MAESTRO satellite measurements;
3. Estimating boreal fire-generated ozone over North America using ozonesonde measurements.

Physical models of the Dobson instrument and two types of Brewer spectrophotometer were developed by me to help better understand the effects of stray light on ozone measurements. The influence of other assumptions such as fixed ozone layer height in air mass calculations and its error contributions to the ozone retrieval also have been examined. The data collected by a Brewer MKIII and three Dobson collocated at South Pole station also compared to characterize the effect of stray light on the instrument measurements. A manuscript on this study is completed and will soon be submitted to "*Atmospheric Measurements and Techniques*".

I also spent some time to analyze the Brewer data collected by 22 instruments at X Inter-Comparison Campaign of the Regional Brewer Calibration Center-Europe, Huelva, Spain, 2015 and also the data collected at three Arctic sites (Resolute, Egbert, and Alert) since 2004 to characterize the effect of stray light. These studies were not included in this thesis and may lead to future publications.

MAESTRO preliminary pressure-Temperature retrieval had been developed by Caroline Nowlan [*Nowlan*, 2006]. The HITRAN 2012 database was implemented into the code by me. More than 80 p-T profiles were reprocessed using the HITRAN 2012 database

and HITRAN 2004 using most recent pointing information provided by ACE-FTS retrievals. Three subsets of profiles were compared with the coincident ACE-FTS profiles. The results of this research are in-progress to be published in "*Journal of Quantitative Spectroscopy and Radiative Transfer*".

A trajectory-based method which calculates the average ozone difference between fire-affected and fire-unaffected layers at each site is developed by myself and presented here. Suspected stratospheric (ST) intrusions are removed from the ozone profiles to avoid potential biases from ST ozone. The average difference between ozone concentrations associated with fire-affected and fire-unaffected parcels at each individual site is estimated using back-trajectory calculations (employing HYSPLIT, The Hybrid Single-Particle Lagrangian Integrated Trajectory model) and MODIS (MODerate Image Spectroradiometer) fire data. The possibility that potential regional biases in the origins of fire-affected and non-affected air-parcels influenced the results is addressed by several methods including a cluster analysis of the back-trajectories; such effects are shown to be small. A manuscript is in preparation from the results of this research and will be soon submitted to "*Atmospheric Chemistry and Physics*".

In addition, I contributed to generation of global ozone and carbon monoxide climatology datasets derived from trajectory mapping of ozonesonde and MOZAIC-IAGOS data [*Liu et al.*, 2013; *Liu et al.*, 2013; *Osman et al.*, 2016].

1.4. Thesis outline

This chapter presents an introduction to the climate change and ozone interactions that are the scientific motivation of this research. The principles of atmospheric chemistry and physics applicable to this work are provided in chapter 2. The description of the Brewer and Dobson instruments along with their retrieval algorithms are provided in Chapter 3. Stray light and stray light effects are also described on Chapter 3 and the physical models of the Brewer and Dobson instruments are presented. Comparison between the coincident total ozone measurements collected by three Dobson instruments and a double Brewer Mark III collocated at Amundsen-Scott (South Pole) site is provided in Chapter 3 as well. Chapter 4 describes the MAESTRO instrument along with a discussion about the retrieval theory used to perform pressure-temperature retrievals, including the retrieval methodology implemented. The improvements of oxygen parameters from HITRAN 2012 are discussed and compared with data from HITRAN 2004. The retrieved p-T profiles using HITRAN 2012 are compared with previously retrieved profiles using HITRAN 2004 and with coincident ACE-FTS profiles. Chapter 5 describes the ozonesonde instrument and discusses a new method developed to estimate fire generated ozone over Northern America. The empirically calculated ozone enhancements over 18 sites across US and Canada are also discussed in Chapter 5. The results of this thesis and outlines and recommendations for future work are summarized in Chapter 6.

2. Atmospheric Physics and Chemistry

2.1. Atmosphere vertical structure

The general vertical temperature profile of the atmosphere is depicted in Figure 2.1. The Earth's atmosphere could be divided into four separate layers based on temperature profile. In the lowest part of the atmosphere, called the troposphere, the temperature decreases, on average, from about 288 K at the surface to about 220 K at top of the layer, which is called the tropopause with approximate height ranging between 8 and 18 km depending on the latitude [*Liou*, 2002]. The typical lapse rate (the rate at which the temperature changes with height) in the troposphere is 6.5 K km^{-1}. The second layer, above the troposphere, is called the stratosphere and is characterized by a roughly isothermal layer from tropopause up to about 20 km then an increase in temperature up to 270 K at the stratopause. This is the layer in which ozone is predominantly produced resulting in radiation absorption and increasing the temperature. The stratosphere is mainly affected by absorption of solar ultraviolet radiation by ozone and infrared energy emitted by carbon dioxide.

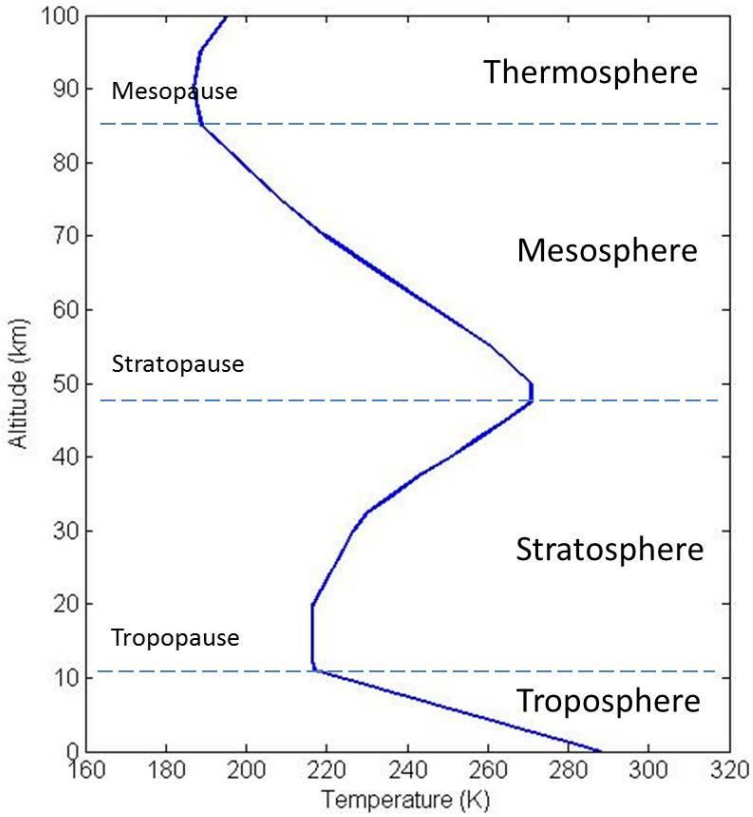

Figure 2.1: Vertical temperature profile for standard atmosphere as defined by Union of Geodesy and Geophysics (IUGG). Data from *US standard Atmosphere* [1976].

The temperature decreases with respect to height between about 50 and 85 km in mesosphere. Above this layer temperatures increase and range between 500 and 2000 K, depending on solar activity [*Liou*, 2002].

2.2. Atmospheric radiative transfer

2.2.1. Blackbody and Planck's Law

The concept of a blackbody is useful to better understand the interaction of radiation with the atmosphere. A blackbody is any object that absorbs all incoming radiation. The

emission from the wall of a blackbody depends on the rate of absorption and the temperature of the medium in which the emission and absorption reach an equilibrium condition. *Planck* [1901] explained the emission from the wall of a blackbody by assuming the atoms of the wall are small electromagnetic oscillators and each of which oscillates at a specific frequency. Thus, according to the Planck, the function describing the average energy emitted per oscillator in units of energy per unit area per unit time per frequency interval per unit solid angle is expressed as:

$$\boldsymbol{B_{\tilde{\nu}}(T) = \frac{2h\tilde{\nu}^3}{c^2\left(exp(\frac{h\tilde{\nu}}{kT}) - 1\right)}} \quad \textbf{(2.1)}$$

Where $\tilde{\nu}$ is the frequency of the oscillator (c/λ), h is Planck's constant, $\boldsymbol{k}$ is Boltzmann's constant, c is the speed of light, and T is the temperature. By integrating the Planck function over all frequencies the energy flux or the power emitted per unit area by a blackbody can be obtained:

$$\boldsymbol{F = \sigma T^4} \quad \textbf{(2.2)}$$

Where F is irradiance and σ is the Stefan-Boltzmann constant. The Planck Law which is illustrated as Eq. (2.1) indicates that the radiant intensity emitted from a blackbody in thermodynamic equilibrium condition depends on the frequency of the radiation and the temperature of the medium. The earth's atmosphere is in thermodynamic equilibrium up to about 60-70 km so that the Planck and Stefan-Boltzmann laws are valid for all molecules in the atmosphere up to that level [*Liou*, 2002].

The radiation emitted from the Sun covers a wide range of wavelengths from gamma rays to radio waves. Figure 2.2 shows the solar spectrum at the top of the atmosphere as a function of wavelength. The Planck function for a medium with a temperature of 5800 K is

also plotted. This temperature is close to the average temperature of the sun's surface. The Earth's surface absorbs a large portion of incoming solar radiation. The absorbed energy is re-emitted to space by the surface of the Earth to keep the energy state in balance. The Earth emits electromagnetic waves in a wide range of wavelengths peaking around a wavelength of 10 μm, as determined by the average surface temperature and the Planck function.

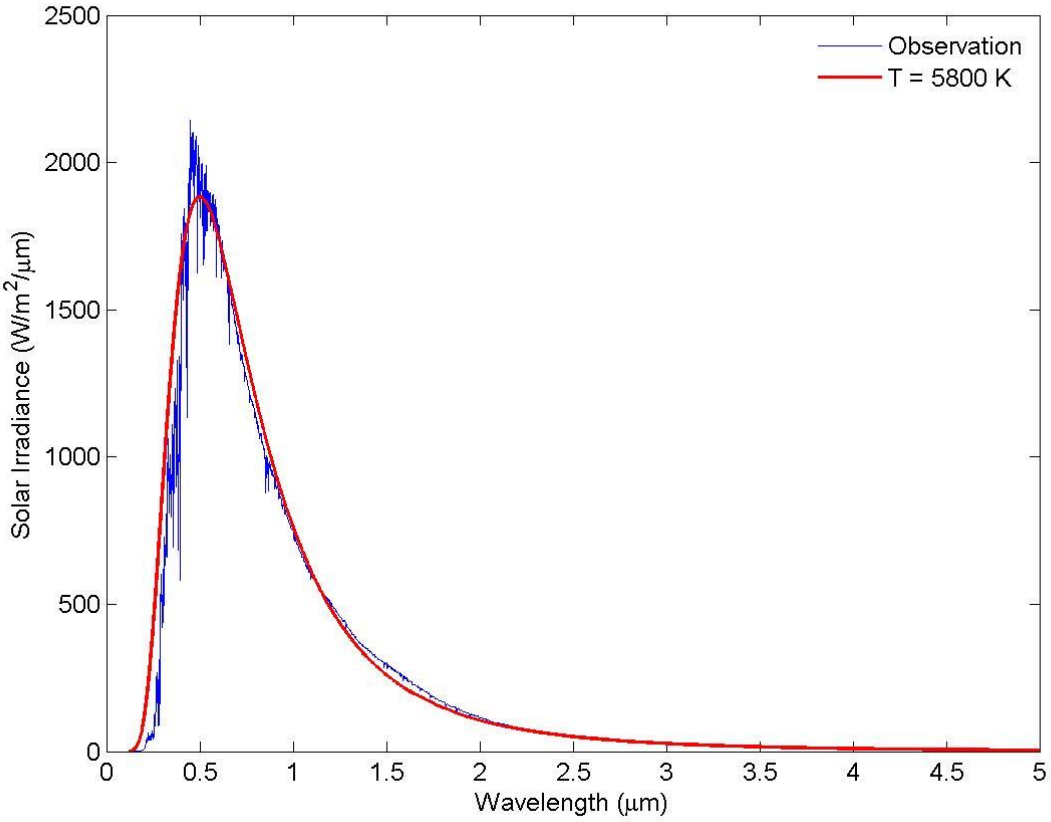

Figure 2.2: Solar spectrum at top of the atmosphere [*ASTM*, 2014]. The flux for a blackbody with a temperature of 5800 K is also shown.

The emission spectrum of the Earth is very close to the spectrum emitted from a blackbody with a temperature of about 290 K, which is close to the temperature of the Earth's surface [*Liou*, 2002]. Not all emitted radiation from the sun reaches the surface of the Earth.

Radiation can be absorbed, scattered, or re-emitted following interaction with the atmosphere. Figure 2.3 shows the attenuation of a ray after passing through a thin layer atmosphere.

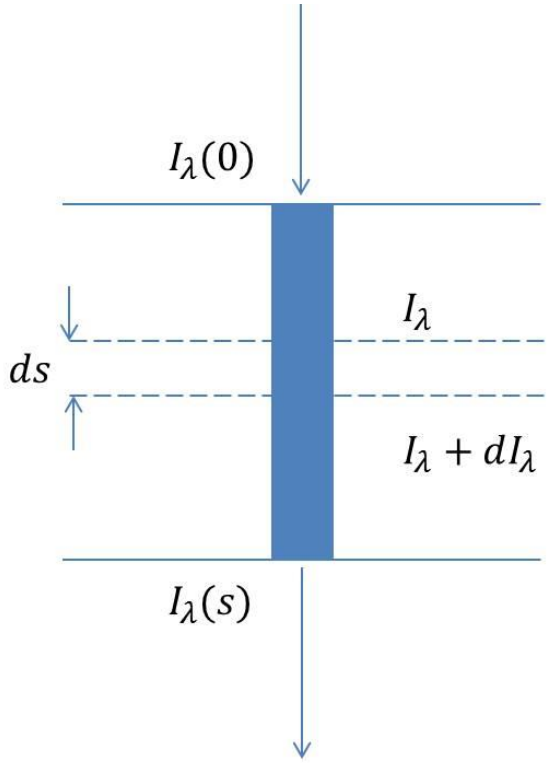

Figure 2.3: Change in intensity of traveling radiation through a path of length S.

2.2.2. Atmospheric absorption

The Beer-Bouguer-Lambert's law or Beer's law describes change in intensity of radiation due to an absorbing medium after propagating through a segment ds as:

$$\boldsymbol{dI_\lambda = -I_\lambda \sigma_\lambda N(s) ds} \qquad \textbf{(2.3)}$$

Where I_λ is the radiance, $N(s)$ is the number density (in unit of molecules per unit volume), and $\sigma_\lambda$is the absorption cross section (in units of effective absorption area per molecule) of the material. The absorption, emission and scattering features of a medium are characterized

by the wavelength dependence of its cross section function. Assuming the incident radiation, $I_\lambda(0)$, travels through a path of length S, the Beer's law is expressed as:

$$\boldsymbol{I_\lambda(S) = I_\lambda(0)\exp(-\tau(\lambda))} \quad \textbf{(2.4)}$$

where $\tau(\lambda)$ is the optical depth:

$$\boldsymbol{\tau(\lambda) = \int_0^s \sigma_\lambda N(s) ds} \quad \textbf{(2.5)}$$

2.2.3. Atmospheric scattering

Rayleigh scattering

Scattering of light by the atmospheric particles and molecules strongly depends on the ratio of the particle size to the wavelength of the incident radiation. The physical law of light scattering by the small particles ($2\pi a/\lambda \ll 1$, where a is the radius of particle) is first discovered by *Rayleigh* [1871]. The Rayleigh scattering is applicable to the scattering of sunlight by the air molecules [*Bates*, 1984; *Bodhaine et al.*, 1999; *Liou*, 2002; *Penndorf*, 1957]. The Rayleigh scattering cross section per molecule is defined as:

$$\boldsymbol{\sigma_R(\lambda) = \frac{24\pi^3(n^2-1)^2}{\lambda^4 N^2 (n^2+2)^2}\left(\frac{6+3\rho}{6-7\rho}\right)} \quad \textbf{(2.6)}$$

where $\boldsymbol{N}$ is the molecular number density and $\boldsymbol{n}$ is the refractive index of air; the term $\boldsymbol{(6+3\rho)/(6-7\rho)}$ is called the depolarization term or the King factor and represents the anisotropic property of molecules; $\boldsymbol{\rho}$ is the depolarization factor. Thus the scattering optical depth for entire molecular atmosphere can be calculated as:

$$\boldsymbol{\tau_{R0}(\lambda) = \int_0^{z_\infty} \sigma_R(\lambda) N(z) d(z)} \quad \textbf{(2.7)}$$

Therefore, the Rayleigh scattering optical depth depends on the total number of molecules per unit area in the column above the site, and this depends on the pressure. An approximation expression for Rayleigh optical depth at the standard pressure ($\boldsymbol{P_0}$ = 1013.25 hPa) usually is used for atmospheric research. The one that was suggested by *Hansen* and *Travis* [1974] is as:

$$\boldsymbol{\tau_{R0}(\lambda) = \beta(\lambda) = 0.008569\lambda^{-4}(1 + 0.0113\lambda^{-2} + 0.00013\lambda^{-4})} \quad \textbf{(2.8)}$$

The scattering optical depth above any pressure level, $\boldsymbol{P}$, can be found from:

$$\boldsymbol{\tau_R(\lambda) = \beta(\lambda)\frac{P}{P_0}} \quad \textbf{(2.9)}$$

Mie scattering

For the large particles whose sizes are comparable or larger than the wavelength ($2\pi\, a/\lambda \geq 1$) such as aerosols the scattering is governed by *Mie* theory. It is very difficult to calculate the exact optical properties of aerosols without a knowledge of the nature of aerosols and usually an approximate expression is used for aerosol scattering. One of the common expressions is the *Angstrom* approximation:

$$\boldsymbol{\tau_a(\lambda) = \delta(\lambda) = A\lambda^{-B}} \quad \textbf{(2.10)}$$

where $\boldsymbol{A}$ is Angstrom turbidity coefficient which represents the amount if aerosol in the atmosphere; $\boldsymbol{B}$ is the wavelength exponent with a typical value between 0.5-1.3.

2.3. Atmospheric chemistry and composition

2.3.1. Atmospheric composition of the Earth

The dry air is comprised of mostly nitrogen (78%), oxygen (21%), and argon (0.96%) with constant volume ratios up to an altitude of about 60 km [*Liou*, 2002]. The remaining 0.04% consists of several different trace gases including carbon dioxide (CO_2), ozone (O_3), nitrous oxide (N_2O), methane (CH_4), and water vapour (H_2O) (ranging between 0 to 4%), which despite their low concentrations, play an important role in the Earth's radiation budget. These gases absorb infrared radiation emitted at the Earth's surface and re-emit a significant amount of radiation causing the 'greenhouse effect'.

The concentrations of trace gases change in response to human activities. According to IPCC fifth assessment report, the concentrations of greenhouse gases have increased dramatically since Industrial revolution [*IPCC*, 2013]. Carbon dioxide is the most important greenhouse gas [*IPCC*, 2013]. Observations indicate that the concentration of CO_2 has been increasing as a result of fossil fuel combustion, moderated by photosynthesis, and absorption and release by oceans [*Forster et al.*, 2007]. Increasing CO_2 has also impact on stratospheric climate. Modeling studies suggest that carbon dioxide increasing leads to a cooling of the stratosphere resulting in a reduction of temperature dependent ozone loss processes and thus increasing the upper stratospheric ozone [*Brasseur* and *Hitchman*, 1988; *Pitari et al.*, 1992]. However, cooling in the Arctic stratosphere has the opposite effect by increasing the volume of air that reaches temperatures low enough to support the formation of polar stratospheric clouds and prime the system for rapid ozone loss in the late winter and early spring.

Methane is the second most important greenhouse gas [*IPCC*, 2013]. There is evidence that the concentration of methane today is more than 2 times greater than that of

preindustrial times (pre 1750) [*Hartmann et al.*, 2013]. CH_4 is a long-lived gas (with a lifetime of 9-12 years) emitted by natural sources such as wetlands, as well as human activates such as rice paddies, livestock, and during the production, processing, storage, transmission, and distribution of natural gas. In addition to influence on average global temperature, methane affects the stratospheric ozone by acting as a sink for reactive chlorine (producing HCl as a reservoir species; more details in section 2.3.2). Generally, increasing global CH_4 leads to an increase in the total column ozone [*Portmann et al.*, 2012; *Revell, Bodeker, Smale, et al.*, 2012].

Nitrous oxide is another greenhouse gas [*Myhre et al.*, 2013] that also is an important ozone depleting substances [*Ravishankara et al.*, 2009]. The long lifetime of N_2O (about 114 years) allows it to become the primary source of stratospheric NO_x ($NO+NO_2$). NO_x in the stratosphere destroy ozone through a catalytic process. Emissions of nitrous oxide are not controlled and it has anthropogenic sources in addition to natural ones. The ocean, biomass burning, livestock, chemical fertilizer, and soils are the main sources of N_2O [*Ravishankara et al.*, 2009].

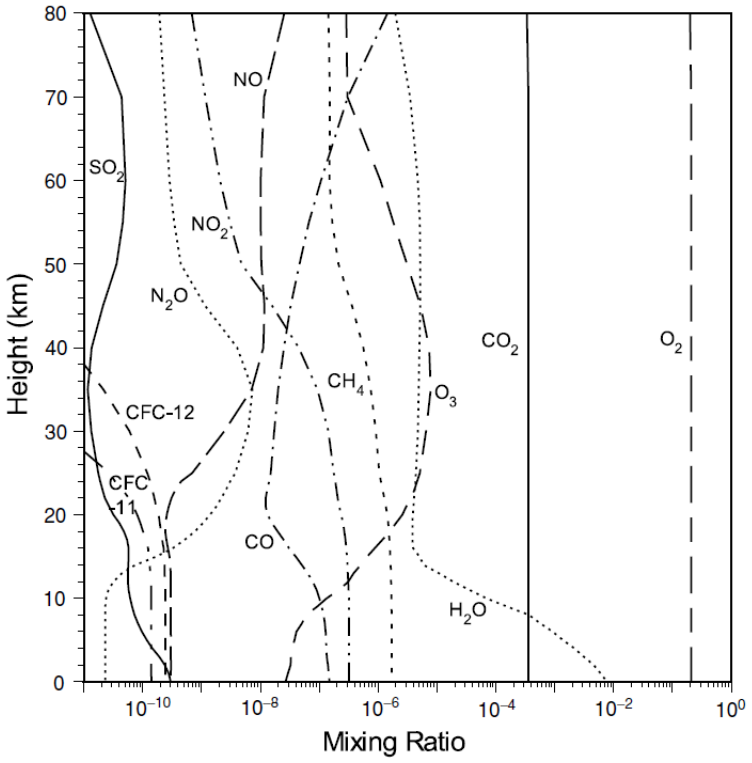

Figure 2.4: Mixing ratio of selected gases with respect to height for mean middle latitude conditions (from [*Liou*, 2002]).

In addition to the greenhouse effect in the upper troposphere, ozone also absorbs harmful ultraviolet radiation in the stratosphere and protects life on Earth. The annual average of total ozone has declined about 7% over the Arctic region since 1980 due to the release of chlorofluorocarbon (CFC) molecules [*Forster et al.*, 2007; *WMO*, 2006]. Many gases that are produced by human activities have long lifetimes (i.e. years, decades, or centuries). Once these gases are released into the atmosphere, they can have a long-term impact on the atmospheric chemistry and radiation balance, affecting the Earth's climate. For example, CFCs are man-made chemicals with very long lifetimes (in some cases more than 100 years). Figure 2.4 represents the typical vertical profile of selected gases for middle latitude conditions.

The temporal and spatial variation of trace gases depends on their production, destruction and transportation in the atmosphere. For example, local production of anthropogenic emissions including CFCs (ozone depleting substances) is very low in the polar regions due to the limited human population in these areas, but these gases can be transported to remote areas thanks to their very long lifetimes and atmospheric dynamics.

Aside from gases, atmospheric aerosols also play important roles in atmospheric chemistry and climate by participating in chemical reactions, scattering sunlight and providing condensation nuclei for cloud droplets. Anthropogenic aerosols are liquid and solid particles of various sizes, from nanometer to millimeter, commonly formed from sulphates, nitrates, organics and black carbon produced by fossil fuels, biomass burning and agricultural processes [*Bruhl et al.*, 2012]. Studies have shown that liquid aerosols in the stratosphere have a critical role in the first step in a series of chemical reactions leading to severe and fast ozone depletion over polar regions [*Solomon*, 2006]. Some of the chemical reactions in the stratosphere that are important to ozone chemistry only occur on the surfaces of particles of polar stratospheric clouds (PSCs) at very low temperatures.

2.3.2. Ozone chemistry in the stratosphere

The ozone mixing ratio in the atmosphere varies with time and location. Chemical reactions and dynamical processes are the two reasons for ozone variations. Ozone is produced and destroyed naturally in the stratosphere via a mechanism that was proposed first by *Chapman* [1930]. The Chapman mechanism is expressed as:

$$\boldsymbol{O_2 + h\nu \rightarrow O + O} \qquad \textbf{(2.11)}$$

$$\boldsymbol{O + O_2 + M \rightarrow O_3 + M} \qquad \textbf{(2.12)}$$

$$\boldsymbol{O_3 + h\upsilon \rightarrow O_2 + O} \quad \textbf{(2.13)}$$

$$\boldsymbol{O + O + M \rightarrow O_2 + M} \quad \textbf{(2.14)}$$

$$\boldsymbol{O + O_3 \rightarrow 2O_2} \quad \textbf{(2.15)}$$

Where $h\upsilon$ represents UV photon, M is any other molecule (e.g. O_2 and N_2) required for momentum and energy balance.

The Chapman cycle starts with the absorption of high-energy ultraviolet photons (wavelength shorter than 242 nm) by oxygen molecule that produces two oxygen atoms (2.11). The rate of this reaction depends on the number of high energy photons which quickly decrease as the solar light penetrates into the atmosphere. The atomic oxygen then can combine with molecular oxygen to form ozone (2.12). Ozone itself strongly absorbs UV radiation and can be dissociated to form atomic oxygen and an oxygen molecule (2.13). The newly formed oxygen atom then reacts again with an oxygen molecule to form ozone. These reactions participate in a rapid cycle in the stratosphere to interconvert ozone and atomic oxygen. The lifetime of ozone in the upper stratosphere and mesosphere (above 30 km) is quit short while in the lower altitudes it is much longer (i.e. months to years) allowing the relatively slow indirect circulation (the Brewer-Dobson Circulation [*Brewer*, 1949]) in the stratosphere to transport ozone from the tropical regions where it is originally formed to higher latitudes. These three reactions are responsible for ozone production and conversion of solar UV light to heat in the stratosphere. According to the Chapman process ozone reacts with atomic oxygen to form oxygen molecules (2.15). However, soon after the Chapman cycle was introduced measurements showed that this reaction set is much too slow to account for the observed ozone and oxygen concentrations in the lower stratosphere. Instead, it

became clear that catalytic cycles involving other molecules are important processes that destroy stratospheric ozone. In catalytic processes the active species which initiate the chemical reactions are regenerated so each catalyst molecule can participate in a catalytic cycle many times before becoming non-reactive via other reactions. Therefore, even relatively small amounts of these substances can produce significant ozone destruction. The most important catalytic cycles are of the form:

$$XO + O \rightarrow X + O_2 \quad \textbf{(2.16)}$$

$$X + O_3 \rightarrow XO + O_2 \quad \textbf{(2.17)}$$

where X can be OH, , H, NO, Cl or Br [*Bates* and *Nicolet*, 1950; *Crutzen*, 1970, 1971; *Stolarski* and *Cicerone*, 1974; *Wofsy et al.*, 1975]. The reaction (2.16) is more important in the upper stratosphere and mesosphere as it is limited by the availability of atomic oxygen. Illustrative of such reactions are:

$$O + OH \rightarrow O_2 + H \quad \textbf{(2.18)}$$

$$H + O_2 + M \rightarrow HO_2 + M \quad \textbf{(2.19)}$$

$$O + HO_2 \rightarrow O_2 + OH \quad \textbf{(2.20)}$$

$$\overline{\textbf{Net Cylce}: O + O + M \rightarrow O_2 + M} \quad \textbf{(2.21)}$$

Reaction (2.17) followed by:

$$OH + O_3 \rightarrow HO_2 + O_2 \quad \textbf{(2.22)}$$

$$HO_2 + O_3 \rightarrow OH + 2O_2 \quad \textbf{(2.23)}$$

$$\overline{\textbf{Net Cycle}: 2O_3 \rightarrow 3O_2} \quad \textbf{(2.24)}$$

is more important in the lower stratosphere as atomic oxygen is not involved. The following two cycles from the products of reaction (2.17) can destroy odd-oxygen (ozone plus atomic oxygen) more efficiently in the lower stratosphere without being limited by atomic oxygen. The first one involves Br and Cl [*McElroy et al.*, 1986; *Tung et al.*, 1986]:

$$Cl + O_3 \rightarrow ClO + O_2 \quad \textbf{(2.25)}$$

$$Br + O_3 \rightarrow BrO + O_2 \quad \textbf{(2.26)}$$

$$BrO + ClO \rightarrow Br + ClO_2 \quad \textbf{(2.27)}$$

$$ClO_2 + M \rightarrow Cl + O_2 + M \quad \textbf{(2.28)}$$

$$\overline{Net\ Cycle: 2O_3 \rightarrow 3O_2} \quad \textbf{(2.29)}$$

while the second cycle starts with the self-reaction of ClO [*Molina* and *Molina*, 1987; *Stolarski* and *Cicerone*, 1974]:

$$ClO + ClO + M \rightarrow Cl_2O_2 + M \quad \textbf{(2.30)}$$

$$Cl_2O_2 + h\nu \rightarrow Cl + ClO_2 \quad \textbf{(2.31)}$$

$$ClO_2 + M \rightarrow Cl + O_2 + M \quad \textbf{(2.32)}$$

$$2(Cl + O_3 \rightarrow ClO + O_2) \quad \textbf{(2.33)}$$

$$\overline{Net\ Cycle: 2O_3 \rightarrow 3O_2} \quad \textbf{(2.34)}$$

These cycles are particularly important in the production of severe ozone loss over polar regions. ClO abundances reach large values in the cold Antarctic polar night as a result of very low temperatures which cause the removal of reactive nitrogen compounds from the

system. The cycles initiated by self-reaction of ClO or reaction of ClO with BrO significantly destroy ozone resulting in the formation of the Antarctic ozone hole.

The concentrations of Cl and Br are relatively small in the natural atmosphere (from volcanic and oceanic emissions). But, as a result of anthropogenic emissions of CFCs, halons, and methyl bromide the concentrations of these species have now significantly increased. There are other important reactions that efficiently occur on the surface of particles:

$$\boldsymbol{HCl + ClONO_2 \rightarrow HNO_3 + Cl_2} \quad \textbf{(2.35)}$$

$$\boldsymbol{ClONO_2 + H_2O \rightarrow HNO_3 + HOCl} \quad \textbf{(2.36)}$$

$$\boldsymbol{HCl + HOCl \rightarrow H_2O + Cl_2} \quad \textbf{(2.37)}$$

$$\boldsymbol{BrONO_2 + H_2O \rightarrow HNO_3 + HOBr} \quad \textbf{(2.38)}$$

$$\boldsymbol{HCl + BrONO_2 \rightarrow HNO_3 + BrCl} \quad \textbf{(2.39)}$$

$$\boldsymbol{HCl + HOBr \rightarrow H_2O + BrCl} \quad \textbf{(2.40)}$$

During the polar night, when the temperature drops below -78^{o} C, Polar Stratospheric Clouds (PSCs) made up of nitric acid trihydrate (NAT) form [*Solomon*, 1999]. The reactions ((2.35)-(2.40)) are heterogeneous, and rapidly take place on the PSC ice particle surfaces. These reactions convert chlorine from inactive species to active forms (HOCl, Cl_2, ClO_x) which can be easily photolyzed by UV and visible solar radiation [*Jacob*, 2000; *Solomon*, 1999]. The above reactions also convert NO_x ($NO + NO_2$) to the non-reactive form (HNO_3). This limits the reaction between ClO and NO_2 that forms $ClONO_2$ which is non-reactive under normal conditions. During the polar night the concentration of active chlorine increases dramatically within the isolated airmass of the Antarctic polar vortex as a result of conversion

from non-reactive forms by heterogeneous reactions. When the sun rises in early spring ozone is depleted rapidly and severely. As heterogeneous reactions occur efficiently on the surface of PSCs the ozone hole lasts until the late spring when the warmer ozone-rich air from middle latitudes breaks up the polar vortex and the stratosphere is not cold enough anymore to form PSCs.

The catalytic cycles are interrupted by other reactions in which active species convert to inactive forms. The following are some of the important reservoir reactions [*Solomon et al.*, 1997; *Solomon et al.*, 1994]:

$$Cl + CH_4 \rightarrow HCl + CH_3 \quad \textbf{(2.41)}$$

$$ClO + NO_2 + M \rightarrow ClONO_2 + M \quad \textbf{(2.42)}$$

$$OH + NO_2 + M \rightarrow HNO_3 + M \quad \textbf{(2.43)}$$

A large portion of the chlorine in the stratosphere is converted to inactive forms by these reactions. The concentrations of bromine are much less than those of chlorine in the stratosphere but there are no such reservoir reactions to convert them to inactive forms. Therefore, despite much lower abundances, bromine is an important catalytic species [*Solomon*, 1999].

2.3.3. Tropospheric ozone chemistry

Ozone acts as a greenhouse gas in the upper troposphere. It absorbs some of the infrared radiation emitted from the Earth's surface [*Forster et al.*, 2007]. It also is an air pollutant with well recognized impacts on human health [*Bates*, 2005; *WMO*, 2006]. Ozone is transported from the stratosphere into the troposphere and is removed by deposition to the

surface [*Hauglustaine et al.*, 1998; *Wang et al.*, 1998]; however, tropospheric ozone is produced and consumed in the troposphere primarily via chemical reactions [*Jacob*, 2000].

Ozone in the troposphere is produced through a chain oxidation of CO and hydrocarbons in the presence of NO_x ($NO+NO_2$) [*Jacob*, 2000]. The chain is initiated by formation of hydroxyl (OH) radicals:

$$O_3 + h\nu \rightarrow O_2 + O(^1D) \quad (\lambda < 320\,nm) \tag{2.44}$$

$$O(^1D) + H_2O \rightarrow 2OH \tag{2.45}$$

then followed by:

$$OH + CO \rightarrow H + CO_2 \tag{2.46}$$

$$H + O_2 + M \rightarrow HO_2 + M \tag{2.47}$$

$$NO + HO_2 \rightarrow OH + NO_2 \tag{2.48}$$

$$NO_2 + h\nu \rightarrow NO + O \tag{2.49}$$

$$O + O_2 + M \rightarrow O_3 + M \tag{2.50}$$

$$\overline{Net\ Cycle: CO + 2O_2 \rightarrow CO_2 + O_3} \tag{2.51}$$

Hydrocarbons (RH) are also oxidized via similar reactions:

$$RH + OH(+O_2) \rightarrow RO_2 + H_2O \tag{2.52}$$

$$RO_2 + NO \rightarrow RO + NO_2 \tag{2.53}$$

$$RO + O_2 \rightarrow CARB + HO_2 \tag{2.54}$$

Followed by (2.48)-(2.49). Carbonyl compounds (CARB) can react with OH to produce additional ozone or photolyze to produce additional HO_x. HO_x is consumed in the troposphere by:

$$\boldsymbol{HO_2 + HO_2 \rightarrow H_2O_2 + O_2} \quad \textbf{(2.55)}$$

$$\boldsymbol{RO_2 + HO_2 \rightarrow ROOH + O_2} \quad \textbf{(2.56)}$$

$$\boldsymbol{OH + HO_2 \rightarrow H_2O + O_2} \quad \textbf{(2.57)}$$

$$\boldsymbol{NO_2 + OH + M \rightarrow HNO_3 + M} \quad \textbf{(2.58)}$$

The formation of HNO_3 is the dominant sink for NO_x. HNO_3 may photolyze to recycle HO_x or be removed by deposition [*Jacob*, 2000]. The lifetime of HNO_3 is about 2 weeks. Another sink for NO_x is formation of $CH_3C(O)OONO_2$ (peroxyacetylnitrate, PAN). It can be formed for example by oxidation of acetaldehyde:

$$\boldsymbol{CH_3CHO + OH + (O_2) \rightarrow CH_3C(O)OO + H_2O} \quad \textbf{(2.59)}$$

$$\boldsymbol{CH_3C(O)OO + NO_2 + M \rightarrow CH_3C(O)OONO_2 + M} \quad \textbf{(2.60)}$$

The main loss of PAN is by thermal decomposition, regenerating NO_x:

$$\boldsymbol{PAN + M \rightarrow CH_3C(O)OO + NO_2 + M} \quad \textbf{(2.61)}$$

The lifetime of PAN is about 1 h at 295 K and several months at 250 K [*Jacob*, 2000]. Generally, the formation of PAN is less important than HNO_3 as a sink for NO_x. However, in the middle and upper troposphere, the long lifetime of PAN at low temperature allows it to act as a reservoir for NO_x as it can be transported over long distances and decompose to release NO_x far from its source.

2.4. Brewer – Dobson circulation

The term “Brewer – Dobson circulation” refers to a global mass circulation proposed by *Dobson* [1929, 1956] and *Brewer* [1949] in which air is transported from the troposphere into the stratosphere in the tropics and then poleward and finally descent in the middle and polar latitudes. Dobson suggested this circulation as an explanation for the high ozone concentration at high latitudes in spring and low concentration in the tropics, considering the action of solar light in ozone formation. Brewer also used this model to explain observed phenomena in upper air water vapor measurements. The Brewer-Dobson circulation (BDC) is generally recognized as a basic description of meridional transport of trace gases from the tropics to the poles.

Rossby waves play a key role in the BDC [*Charney* and *Drazin*, 1961]. Topographical features and meridional temperature gradients together with the rotation of the earth (resulting in the Coriolis force), generate large-scale Rossby waves. Large-amplitude planetary-scale Rossby waves propagate upward from troposphere into the winter stratosphere [*McIntyre* and *Palmer*, 1983]. These easterly waves decelerate the westerly wintertime stratospheric jet stream and continuously break at the edge of the polar vortex [*Holton et al.*, 1995]. They can even displace the polar vortex allowing middle latitude warmer air intrusion into the polar region. The warm air cools and sinks, bringing higher ozone mixing ratios to lower altitudes, increasing ozone concentrations.

The BDC consists of two branches. The shallow branch comprises a two-cell structure in the lower stratosphere, with upwelling air in the tropics and descending air in middle and high latitudes, while the deep branch is a single cell from the tropics to the upper stratosphere and descending into the winter hemisphere at higher altitudes [*Plumb*, 2002] (Figure 2.5).

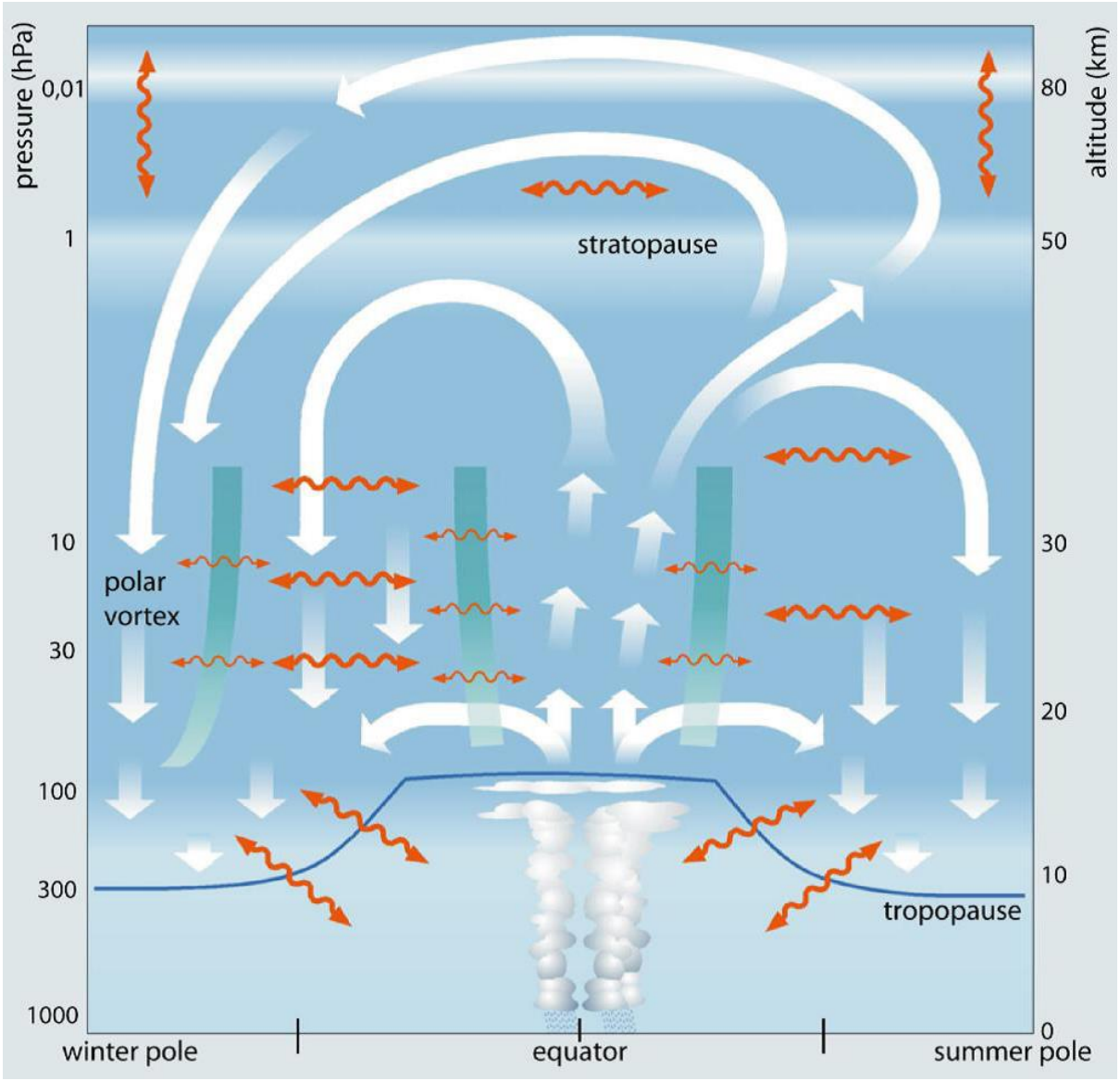

Figure 2.5: Schematic of the BDC as the combined effect of residual circulation and mixing in the stratosphere and mesosphere. The thick white arrows depict the Transformed Eulerian Mean (TEM) mass streamfunction as representation of the residual circulation whereas the wavy orange arrows indicate two-way mixing processes. Both circulation and mixing are mainly induced by wave activity on different scales (planetary to gravity waves). The thick green lines represent stratospheric transport and mixing barriers (Image retrieved from: http://www.goethe-university-frankfurt.de/47669287/Atmospheric_Transport).

The BDC transports trace gases from the tropical troposphere into the stratosphere and moves them poleward. Ozone also is redistributed from its production in the equatorial tropical stratosphere to high latitudes.

The downward branch of the BDC in the middle latitudes penetrates into the troposphere while over polar regions it only reaches the lower stratosphere. The BDC is weaker in the southern hemisphere due to lack of topographical features and less of the ocean-land temperature gradient required to generate large-scale Rossby waves. This results in a colder and more isolated polar vortex in the Antarctic in the absence of warm air intrusion from middle latitudes [*Plumb*, 2002]. The colder Antarctic polar vortex compared to the Arctic vortex results in more polar stratospheric cloud (PSC) formation over the Antarctic, leading to more ozone destruction near the South Pole in comparison to the North Pole.

Many different model simulations predict a future strengthening of the BDC due to greenhouse gas increases [*Butchart et al.*, 2006] with significant influence on tropospheric and stratospheric composition. A change in the strength of the BDC would impact the water vapor concentration [*Randel et al.*, 2006], and the temperature and the dynamics of the stratosphere [*Lin et al.*, 2009]. It also would change the transport of ozone and ozone depleting substances [*Butchart* and *Scaife*, 2001] with associated impacts on the tropospheric ozone budget [*Sudo et al.*, 2003] and surface UV index [*Hegglin* and *Shepherd*, 2009].

2.5. Ozone distribution and variability

2.5.1. Ozone variability: short-term, long-term, and vertical distribution

Total column ozone varies with time and location. The ozone distribution and variability in the atmosphere are governed by chemical and dynamical processes. More than 90% of the ozone column is found between 10 and 50 km in the atmosphere. Ozone concentration rapidly increases from 10 km and reaches a maximum between 20 and 25 km, depending on latitude (Figure 2.6 and Figure 2.7). Ozone is produced mainly in the tropical regions at an altitude of 35-40 km where its highest mixing ratios are found (Figure 2.7).

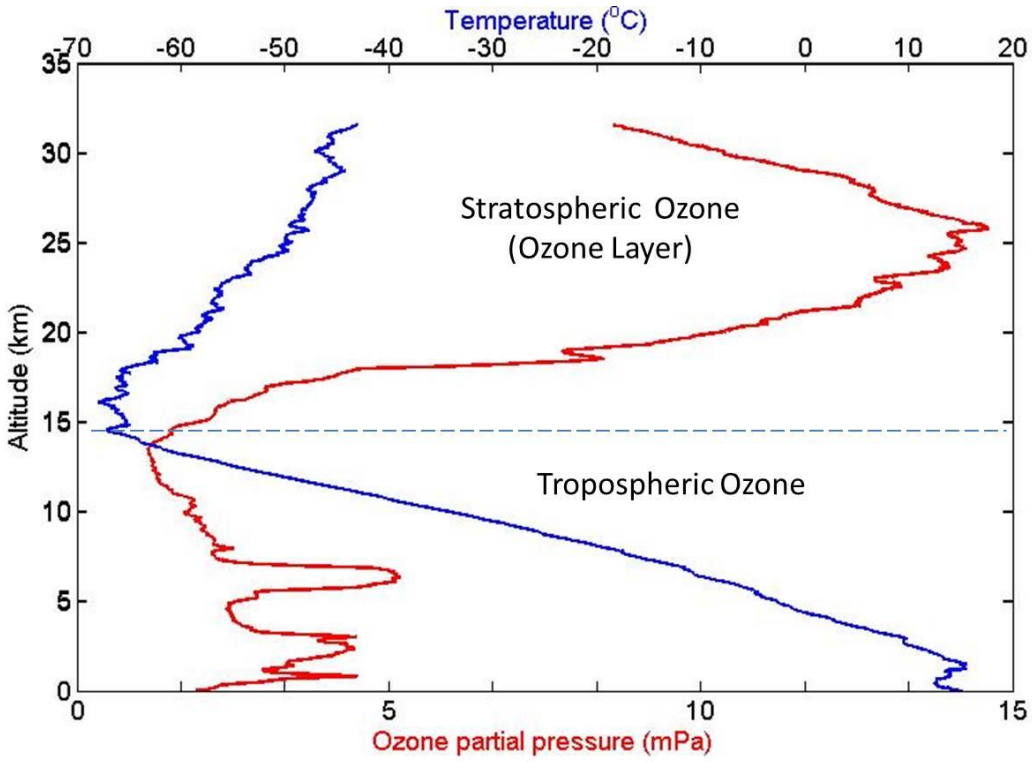

Figure 2.6: Ozone and Temperature vertical profile in the atmosphere. (Data collected from WOUDC datacenter for Egbert, Lat. 43.87 N, Long. 66.1 W, on September, 07, 2011)

The lifetime of ozone is short in the upper stratosphere altitude (above ~30 km) and the ozone amount is determined by photochemistry. The longer lifetime of ozone at lower altitudes allows the BDC to transport it from the tropics toward higher latitudes where it descends to the lower stratosphere.

On a daily basis ozone column changes are mainly due to dynamical processes rather than chemistry. Strong correlations between the ozone column and meteorological conditions were found in the early years of ozone measurement [*Reed*, 1950]. Ozone is correlated with meteorological parameters such as temperature [*Hansen* and *Trond*, 2005] and potential vorticity [*Allraat et al.*, 1993] in the lower stratosphere as a result of its long lifetime in those altitudes. Ozone also is correlated with the tropopause height [*Steinbrecht* and *Claude*, 1998] and tropopause pressure [*Weiss* and *Staehelin*, 2001].

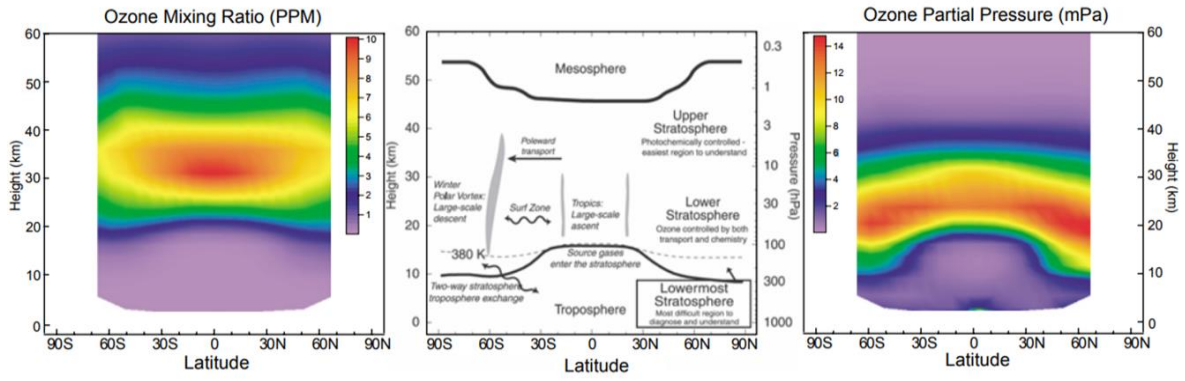

Figure 2.7: (left and right) Annual mean ozone mixing ratio in ppm and ozone partial pressure in mPa as a function of latitude and altitude based on satellite data (SAGE II version 6.20 for 1984–2004). (middle) Schematic illustrating the structure of, and transport within, the stratosphere (From [*Fioletov*, 2008] and [*WMO*, 2002]).

While extratropical ozone has a clear annual cycle, the total ozone over tropical regions remains almost constant throughout the year. The total ozone in extratropical regions is determined by a balance between transport and photochemical processes. Ozone reaches a

maximum value in early spring as a result of wintertime transport. During the summertime photochemical loss is dominant which results in a minimum amount in early fall [*Andrews et al.*, 1987]. The reason the springtime ozone amounts are greater in the northern hemisphere than the southern hemisphere is that the wintertime transport is stronger in the northern hemisphere due to the larger planetary-wave amplitudes [*Fioletov*, 2008]. During the fall the photochemical process is dominant which results in similar ozone amounts in both hemispheres.

Other processes such as the El Nino-Southern Oscillation (ENSO) and Quasi-Biennial Oscillation (QBO) can moderately affect ozone amounts through influencing the strength of the BDC. The impact of ENSO on the lower stratosphere and troposphere over the equatorial belt and the tropics has been reported by a number of studies (e.g. [*Randel* and *Cobb*, 1994; *Zerefos et al.*, 1992]). The QBO also influences equatorial and tropic column ozone with a period of 27-28 months [*Bowman*, 1989; *Chandra* and *Stolarski*, 1991].

The rate of ozone production and destruction in the upper stratosphere is also moderately influenced by solar flux variations. On a decadal time scale, the correlation of ozone variability and the 11-year solar cycle has been well established [*Bojkov* and *Fioletov*, 1996; *Chandra* and *Mcpeters*, 1994]. The 27-day rotation period of the sun also has a periodic effect on ozone generation in the upper stratosphere [*Chandra* and *Mcpeters*, 1994; *Hood* and *Zhou*, 1999].

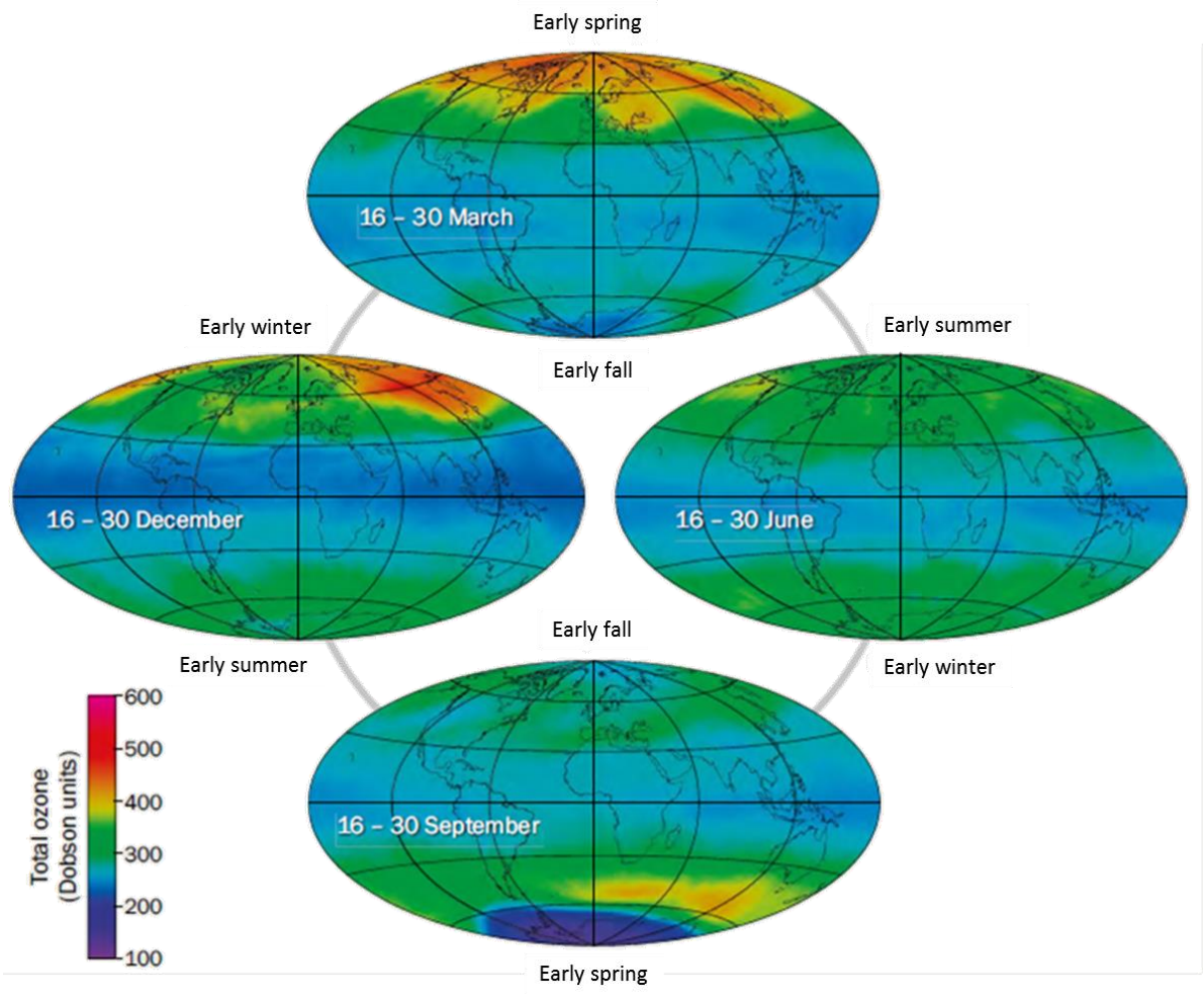

Figure 2.8: Two-week averages of total ozone as measured by a satellite instrument in 2009. Tropical ozone (20°N–20°S latitudes) remains almost constant throughout the year. Total ozone varies over mid and high latitudes on daily and seasonal basis as the Brewer-Dobson circulation transports ozone-rich air from tropics toward high latitudes. The low ozone values over the South Pole in September correspond to the "ozone hole" in 2009. The ozone hole occurs every year since the 1980s in late winter and early spring over Antarctica (From [*WMO*, 2014].

2.5.2. Ozone variability at high latitudes and the polar regions

Early measurements by the Dobson instrument in the tropics and high latitudes showed that there is a gradient in total column ozone with low ozone in the tropics and an increase toward the poles [*Fioletov*, 2008; *Solomon*, 1999]. However, in the southern

hemisphere, the maximum ozone occurs at 50-60^{o} S, not at the pole. Similar conditions occur in the Northern hemisphere in some years. A lower ozone concentration over polar regions is related to the polar vortex which isolates polar air from air at lower latitudes. The absorption of solar UV radiation by ozone is the major source of heating in the stratosphere. The absence of solar radiation during the wintertime leads to cooling of the polar stratosphere and hence a large temperature gradient develops between mid-latitudes and the poles. This thermal gradient establishes a strong westerly flow, 'jet', which isolates the air within the vortex from the surrounding mid-latitude regions, resulting in lower ozone inside the vortex. The condition inside the polar vortex is favorable for the formation of Polar Stratospheric Clouds (PSCs) which have key role in severe ozone depletion through heterogeneous reactions (see sections 2.3.2). In early spring when solar radiation increases, the vortices weaken and eventually break down, allowing mixing of warm ozone-rich air from lower latitudes with the air inside the vortex. The polar vortex is weaker and has a shorter lifespan in the northern hemisphere than in the southern hemisphere, mainly due to stronger atmospheric waves (as noted above) and circulation patterns that are related to the surface topography (the distribution of continents and mountains) [*Solomon,* 1999; *Solomon et al.*, 1986] in the north. The Arctic vortex is more interrupted by atmospheric waves generated by upcoming flow over more variable surface topography. The wintertime Arctic ozone abundances and the lower stratosphere temperatures increase in response to such perturbations. These perturbations cause more mixing and downward motion which brings down more ozone-rich air from the upper stratosphere and warms the lower stratosphere. The Antarctic vortices are colder and less variable compared to the Arctic vortices, leading to stronger ozone depletions.

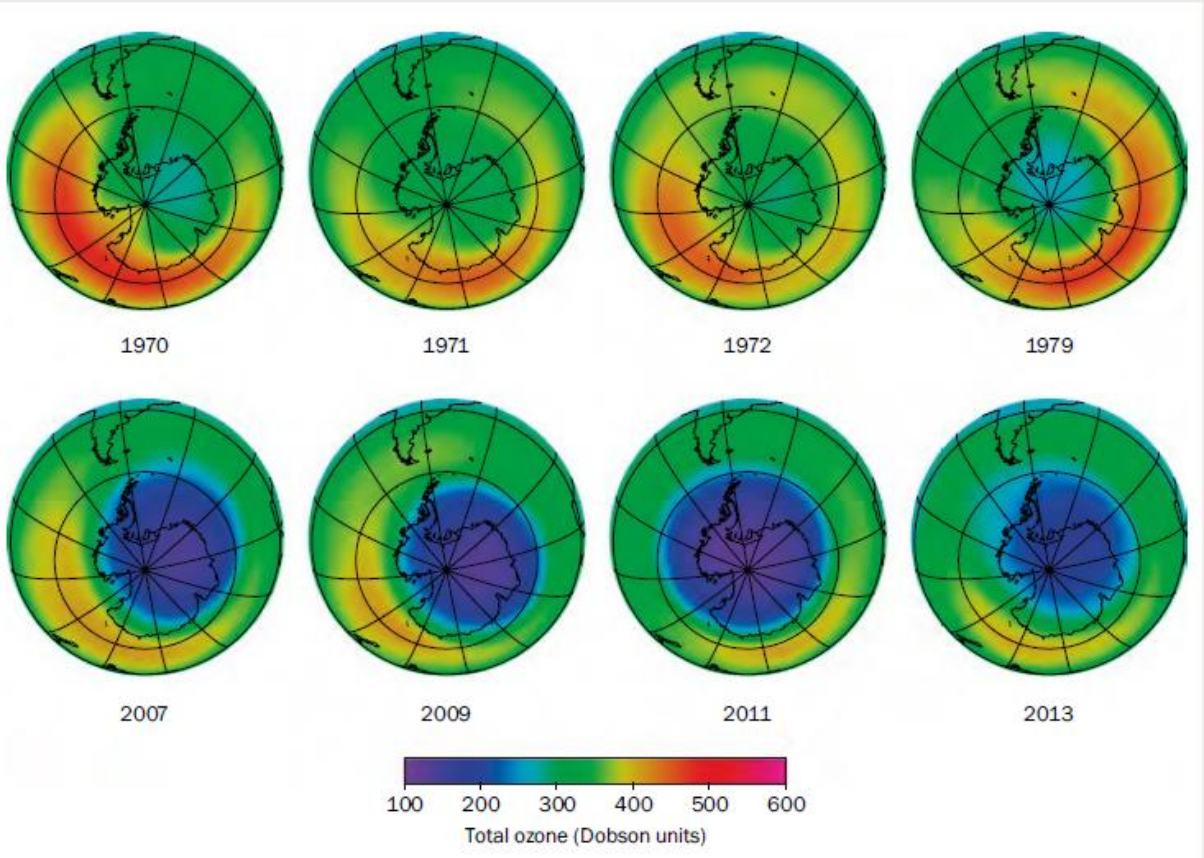

Figure 2.9: Antarctic average total ozone during October as measured by satellite instruments for different years. There is no evidence of an ozone hole before the 1980s. The ozone hole has occured every year since the 1980 in the Antarctic (From [*WMO*, 2014]).

2.5.3. Global and mid-latitude ozone changes and trends

Severe ozone depletion was first observed at the British Antarctic Survey station at Halley Bay [*Farman et al.*, 1985]. It was shown that springtime total ozone over south polar latitudes had declined by about 30% compared to the 1970s [*Farman et al.*, 1985]. Detailed studies revealed that natural factors cannot explain the ozone changes, but rather that the reactions described in section 2.3.2 are responsible [*Solomon*, 1999]. Since then, ozone decline has taken place every spring over the South Pole area every spring (Figure 2.9) [*WMO*, 2014]. Soon after, observations showed a statistically significant decline in total

ozone over middle and high latitudes of both hemispheres in all seasons [*Solomon*, 1999]. According the WMO's last ozone assessment report [*WMO*, 2014], present-day average global ozone (60°S–60°N) is lower by about 2% compared to the pre-1980s. For middle latitudes (35°–60°) it is 3.5 % for the NH and 6% for the SH [*WMO*, 2014].

Following implementation of the Montreal Protocol, which was adopted in 1987 to control ozone-depleting substances, tracking the expected recovery of stratospheric ozone has attracted considerable attention [*Eyring et al.*, 2010; *Shepherd* and *Jonsson*, 2008; *Waugh et al.*, 2009; *Weatherhead* and *Andersen*, 2006]. The complexity of ozone natural variability as well as the complex impacts of greenhouse gas induced climate change and declining ODSs due to the Montreal Protocol keep ozone recovery a challenging scientific issue. Figure 2.10 shows long-term ozone changes over Canada using Brewer and Dobson data from four Canadian sites with long records (Toronto (44°N, 79°W), Goose Bay (53°N, 60°W), Edmonton (54°N, 114°W), and Churchill (59°N, 94°W)).

The area-weighted average over northern mid-latitudes (35^{o}-60^{o}N) from merged satellite data are also depicted in Figure 2.10. Both data sets indicate the same long-term ozone changes showing that even a limited number of ground-based stations can provide valuable information about long-term changes in the ozone layer. There are long records of total column ozone measurements from the Brewer and Dobson instruments that can be used for long term trend analysis. The Dobson was developed in the 1930s for total ozone measurements [*Dobson*, 1931] and in 1957 a global ozone monitoring network was established. The Brewer ozone spectrophotometer was designed and developed in the 1980s [*Kerr et al.*, 1981]. Now, more than 100 Dobson and 200 Brewer instruments are in operation around the world. The Dobson and Brewer are both capable of meeting the GAW (Global

Atmosphere Watch) requirement of a precision better than 1% [WMO, 2014] which is a challenging task for satellite measurements [*Stolarski et al.*, 2006].

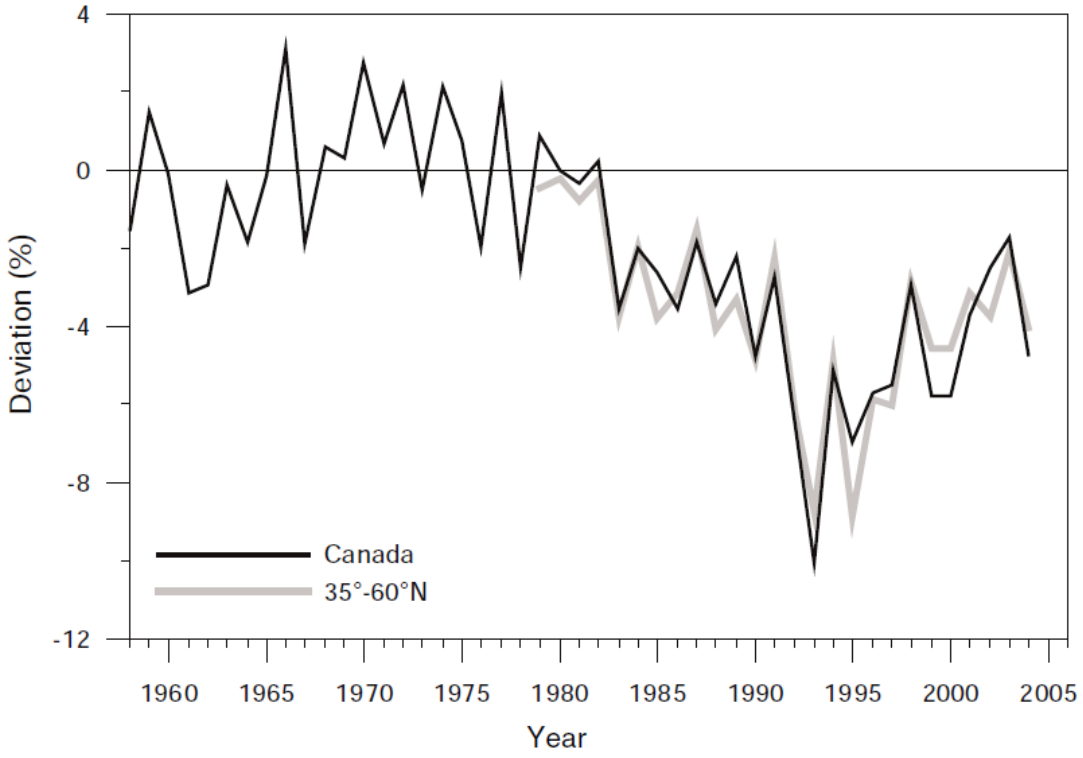

Figure 2.10: Annual mean deviations from the 1958–80 total ozone averages estimated from four Canadian stations and from merged satellite data (area-weighted average for 35°–60°N) (From [*Fioletov*, 2008]).

2.5.4. Tropospheric ozone distribution

Ozone plays a key role in the chemistry of the troposphere. Serving as a primary precursor of the hydroxyl (OH) radical, tropospheric ozone controls the lifetime of trace gases influenced by oxidation [*Monks*, 2005]. Tropospheric ozone is an important greenhouse gas [*IPCC*, 2013; *Stevenson et al.*, 2013] and is therefore also referred to as a short-lived climate pollutant [*Shindell et al.*, 2012].

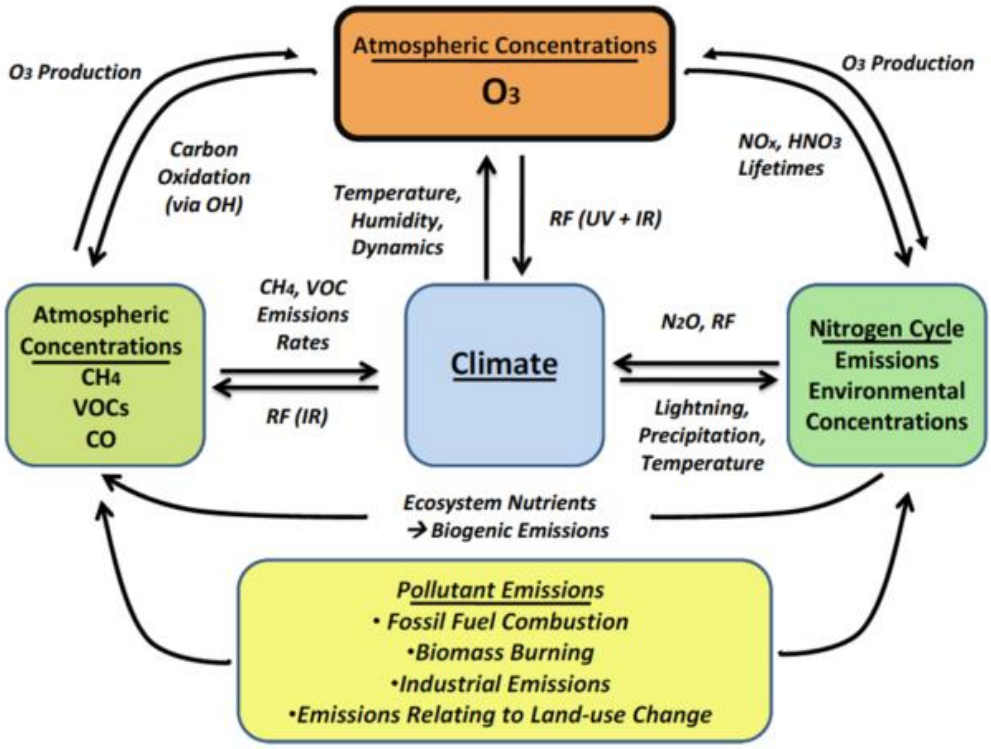

Figure 2.11: Schematic of ozone interactions in the Earth system (From [*EPA*, 2009])

At the surface ozone is recognized as an air pollutant with adverse impacts on human health, natural vegetation and crop yield and quality [*Avnery et al.*, 2011; *Bell et al.*, 2004; *Chossière et al.*, 2013; *Jerrett et al.*, 2009; *Lippmann*, 1991; *Mauzerall* and *Wang*, 2001; *McConnell et al.*, 2002].

Ozone has a relatively short lifetime (hours) in polluted urban areas. However, its globally averaged lifetime in the troposphere is about 23 days [*Stevenson et al.*, 2006; *Young et al.*, 2013] which is long enough for it to be transported over intercontinental distances [*Akimoto*, 2003]. Therefore, it can impact air quality at distances far from its sources. Due to its importance, the tropospheric ozone distribution and trends are assessed by the IPCC every 5-6 years.

The distribution of tropospheric ozone is highly variable by season, location, and altitude due to the heterogeneity of its sources, sinks, and lifetime. The tropospheric ozone budget is determined by photochemical processes, including chemical production and destruction, and physical processes, such as transport from upwind sources and surface deposition.

For a long time the stratosphere was thought to be the primary source of tropospheric ozone [*Chatfield* and *Harrison*, 1976; *Danielsen*, 1968; *Fabian* and *Pruchniewicz*, 1977; *Junge*, 1962]. Studies in the 1950s showed that ozone is also generated in the troposphere [*Haagen-Smit et al.*, 1952] and until the 1970s it was thought that high ozone in the troposphere was associated with air pollution. Further research in the 1970s and the 1980s suggested that ozone is produced in the troposphere by photochemical reactions involving ozone precursors (e.g. nitrogen oxides (NOx), non-methane VOC, methane, or carbon monoxide) and sunlight. Since then, the understanding of natural and anthropogenic sources of ozone precursors has significantly improved. Ozone precursors have natural and anthropogenic sources such as wildfires, lightning NOx, biogenic NOx emitted from soil, biogenic hydrocarbon emissions, and also fossil fuel and biofuel combustion, or crop burning [*Chameides* and *Walker*, 1973; *Crutzen*, 1974; *Levy et al.*, 1972; *Lin et al.*, 1988]. Recent chemistry-climate models suggest that chemical production is the dominant source

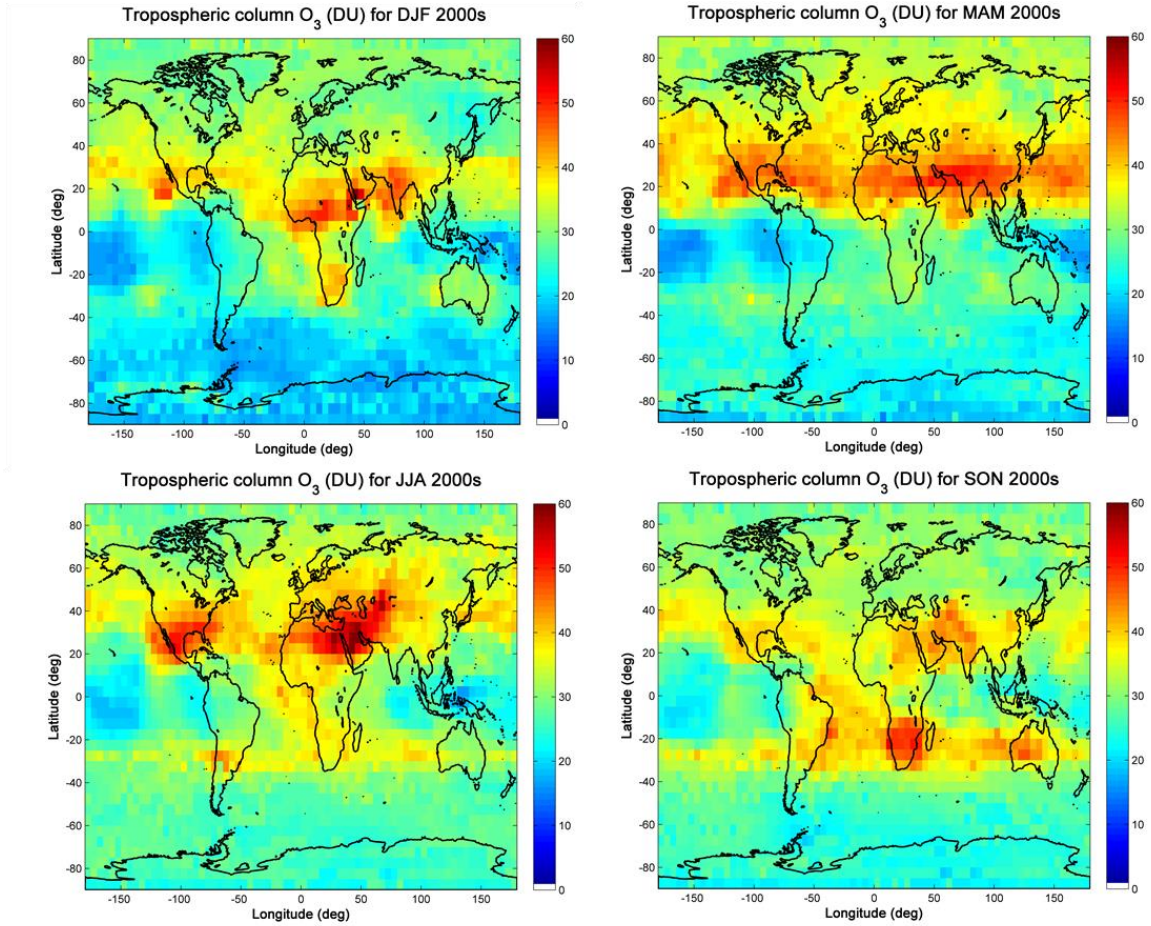

Figure 2.12: Tropospheric ozone column by season as derived from trajectory-mapped ozone sounding [*Liu et al.*, 2013].

with 7-15 times more contribution to the global tropospheric ozone than the stratosphere [*Mclinden et al.*, 2000; *Olson et al.*, 2001; *Stevenson et al.*, 2006; *Young et al.*, 2013]. Some of the main interactions that lead to ozone productions in the troposphere are depicted in Figure 2.11.

The anthropogenic ozone precursor emissions around the world generally are produced in regions with higher population. Approximately 90% of fossil fuel NOx emissions are generated in the northern hemisphere (NH), while emissions from biomass burning mainly caused by human activity are similar in the hemispheres [*Cooper et al.*,

2014]. Production of ozone precursor emissions are declining in Europe and North America and shifting from NH high latitudes to low latitudes [*Parrish et al.*, 2013; *Zhang et al.*, 2016]. In contrast, East Asia is experiencing an increase of these emissions [*Granier et al.*, 2011].

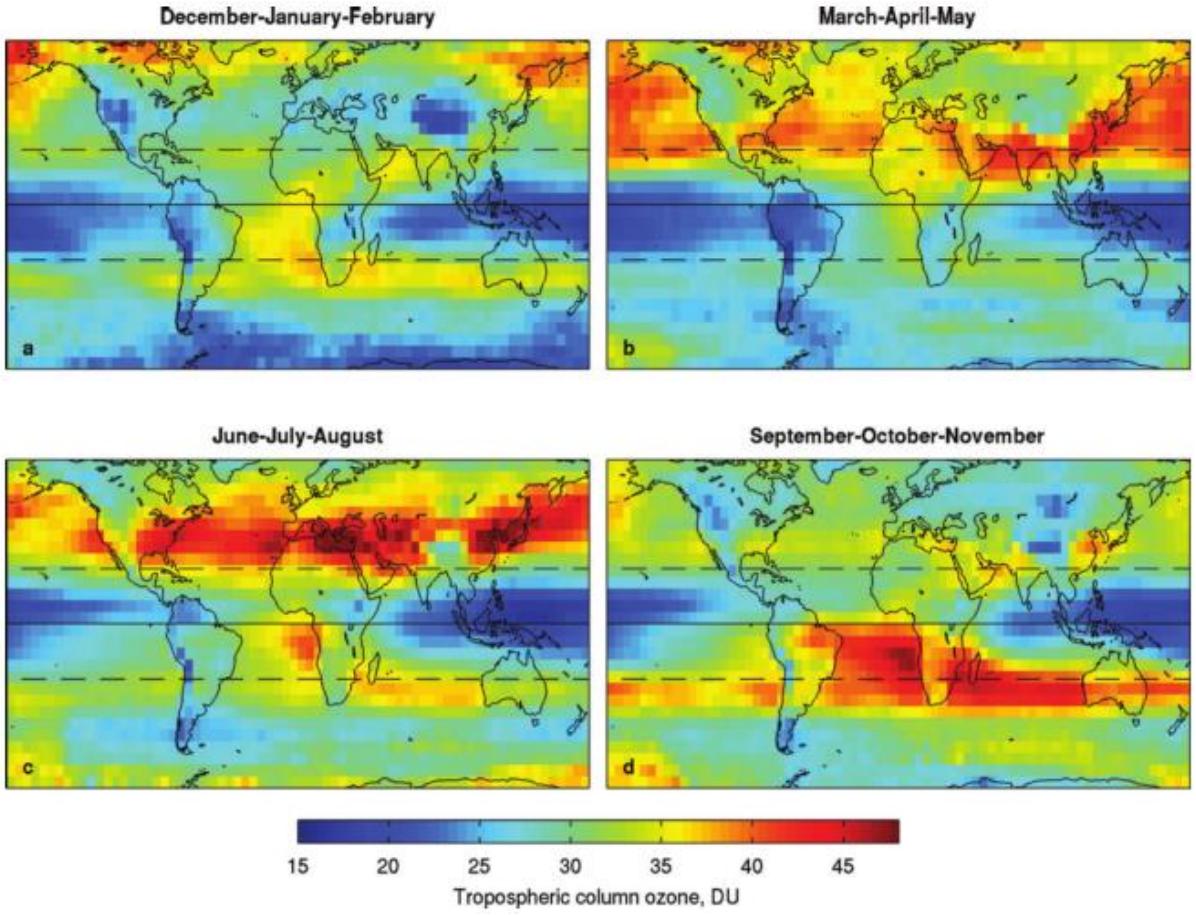

Figure 2.13: Tropospheric ozone column by season as derived from OMI/MLS observations during October 2004 to December 2010. The data are derived from combination of OMI (Ozone Monitoring Instrument) total column ozone measurements and MLS (Microwave Limb Sounder) observations of stratospheric ozone [*Ziemke et al.*, 2006]. Adopted from *Cooper et al.* [2014].

Net ozone production in the troposphere from chemical reactions occurs over the continental boundary layer in response to high ozone precursor emissions (e.g. methane) [*Bloss et al.*, 2005], and in the upper troposphere where ozone destruction is low [*Kuhlmann*

et al., 2003; *Wild* and *Palmer*, 2008]. Net chemical destruction occurs in the mid-troposphere and marine boundary layer, where precursor emissions are low, and in localized urban and polar areas as a result of reaction with NO and halogen-catalyzed destruction during springtime, respectively [*Monks et al.*, 2015].

Available observations show that lowest ozone amounts occur over remote oceans in tropical areas with no vertical gradient (Figure 2.12 and Figure 2.13). Greater chemical production and more stratosphere intrusions in mid-latitude result in higher ozone concentrations and an increase with height. Ozone generally is greater in the NH marine boundary layer than the SH, and increases over land.

Tropospheric column ozone climatologies derived from OMI/MLS observations and also from trajectory-mapped ozone sounding show that the seasonal maximum occurs in spring and summer time at mid-latitudes in the northern hemisphere which is likely due to a combination of dynamical/transport processes and photochemistry [*Monks*, 2000]. In the southern hemisphere ozone peaks in spring in the tropics and subtropics between South America and Africa and over a band between southern Africa and Australia (Figure 2.13).

2.5.5. Tropospheric ozone trends

The existence of ozone and its presence in the atmosphere was discovered first by the German chemist *Schoenbein* [1850] in 1839. Soon after, *Hartley* [1881] identified its UV spectrum and its role as a UV filter in the atmosphere. There were a limited number of sites during the late 1800s and early 1900s that measured surface ozone. Those data coupled with modeling studies suggest changes in tropospheric ozone during the industrial era due to increases of ozone precursor emissions [*Cooper et al.*, 2014; *Monks et al.*, 2015], although the validity of this conclusion is debated.

Recent changes in tropospheric ozone are mixed [*Oltmans et al.*, 2013]. A tropospheric ozone trend analysis by *Cooper et al.* [2014] finds that ozone has increased by a factor of 2 between the 1950s and 2000s over Europe in response to a global increase in fossil fuel combustion [*IPCC*, 2013; *Staehelin et al.*, 1994]. Data available from 13 sites in the NH indicate more than a 100% ozone increase since the 1950s and 9-55% since the 1970s. A more limited number of sites (6 monitoring stations) in the Southern Hemisphere (SH) also show significant positive trends over the SH. Free troposphere ozone has also apparently increased since 1971 over Europe, Japan, and coastal Antarctica [*Cooper et al.*, 2014], although this apparent growth has leveled off [*Oltmans et al.*, 2013] and may be in part due to instrument artifact. Aircraft measurements have shown significant upper tropospheric trends in one or more seasons above the north-eastern USA, the North Atlantic Ocean, Europe, the Middle East, northern India, southern China and Japan. Surface ozone trends have varied by region between 1990 and 2010 [*Cooper et al.*, 2014; *IPCC*, 2013]. Ozone has shown an increase in Western Europe in the 1990s followed by a leveling off or decrease since 2000 [*Cooper et al.*, 2014]. In the western USA, a few rural sites show decreasing ozone while half of all the sites indicate a significant increase in spring. The available data indicate that rural surface ozone has decreased strongly in summer, is largely unchanged in spring, and has increased in winter. The decrease in ozone in Europe and the eastern USA is attributed to the decrease in ozone precursor emissions in those areas. At the same time, surface ozone generally has been increasing in East Asia where ozone precursor emissions are growing. However the analysis of tropospheric ozone trends and interpretation of such trends is hampered by sampling issues [*Lin et al.*, 2015] and by issues of representativeness due to generally in adequate sampling of this highly reactive trace gas.

2.6. Methods used for ozone measurement

Generally, there are two approaches to measure ozone concentrations in the atmosphere, *remote sounding* and *in-situ* measurements. Ozone concentrations can be determined directly by taking a sample of air and analyzing it for ozone using chemical or optical techniques. Such measurements are called in-situ as they provide information of the ozone concentrations in the atmosphere at the place of the measurements. Electro-chemical cell ozonesondes (See section 5.2.1 for details) and some gas-analyzers are from the in-situ instruments.

Remote sounding methods exploit the ability of ozone to absorb and emit the electromagnetic radiation. The natural source of radiation such as sun and moon light and also the thermal emission of the atmosphere itself can be used to probe the atmosphere. These measurements are called passive remote sounding. Artificial light sources such as lasers are used for active remote sounding. Instruments for ozone measurements are also categorized to ground- and space-based depending of the location of measurements. Some of the instruments are designed to measure the ozone concentrations from the surface of the Earth; and some are on board the satellites.

2.6.1. Ground-based remote sounding

Ground-based instruments utilize the direct beam solar radiation transmitted through the atmosphere to measure ozone and Aerosol. From the geometry given in Figure 2.14 and using the Beer's law presented in section 2.2.2, the solar radiation measured at the ground can be expressed as:

$$I(\lambda) = I_0(\lambda)\exp[-\tau(\lambda)m(\theta_0)] \quad \textbf{(2.62)}$$

where I_0 is the solar intensity at the top of the atmosphere; $m(\theta_0) = 1/\cos(\theta_0)$ is the air mass factor, where θ_0 is the solar zenith angle; and the total optical depth is the sum of the optical depths of all constituents including all atmospheric gases, aerosols, and molecular (Rayleigh) scattering as follows:

$$\tau(\lambda) = \tau_{Aerosols}(\lambda) + \tau_{Rayleigh}(\lambda) + \tau_{Ozone}(\lambda) + \tau_{gas2}(\lambda) + \cdots + \tau_{gasN}(\lambda) \quad \textbf{(2.63)}$$

The optical depths of Rayleigh scattering and other molecules for a given wavelength are assumed to be known in the calculation of ozone concentrations.

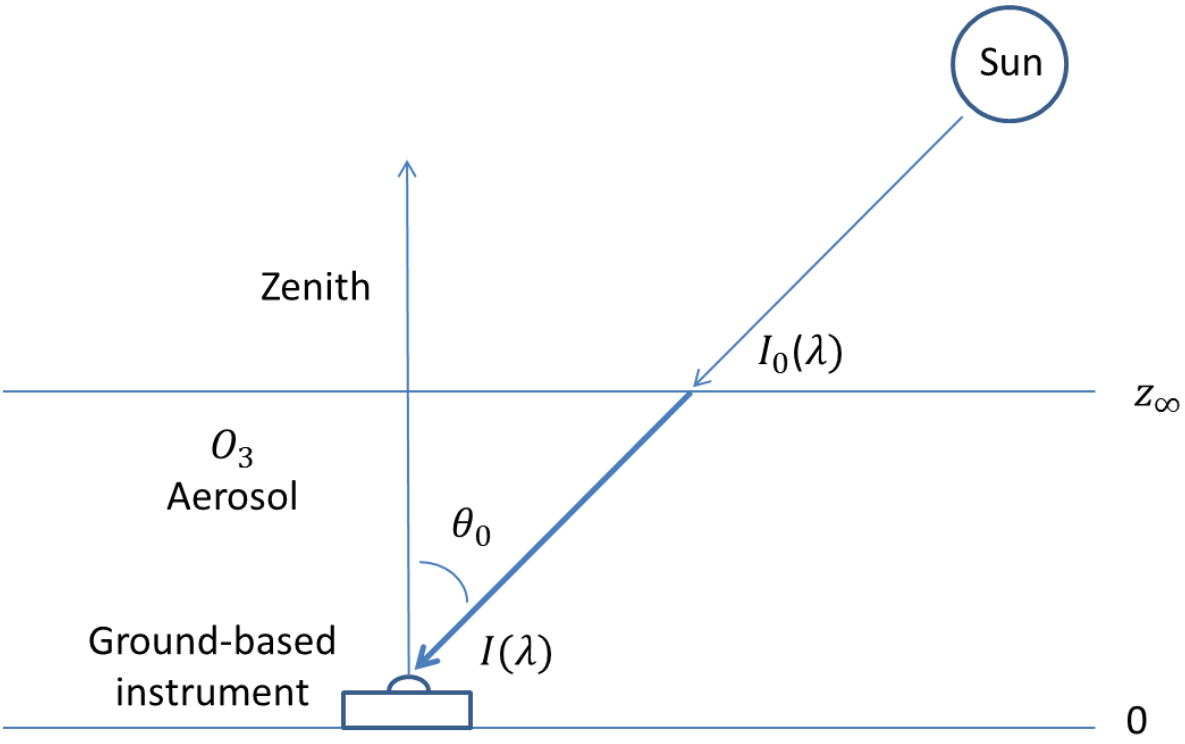

Figure 2.14: Geometry of a Ground-based instrument to measure a direct solar beam.

As the aerosol scattering is linear over a narrow wavelength range, a region of spectrum where ozone absorption is weak, but the scattering of aerosols are similar to the selected

region for ozone measurements (UV-B) is also monitored. By ratioing the two values the effect of aerosols is minimize and the total column in the atmosphere can be obtained.

The Brewer and Dobson ozone spectrophotometers are the most widely used ground-based instruments for total ozone measurements. These instruments use a selected wavelengths for ozone in which the absorption of other molecules is negligible. A linear combination of four wavelengths is used by Brewer and Dobson to suppress the effect of aerosols (Details in section 3.2.2).

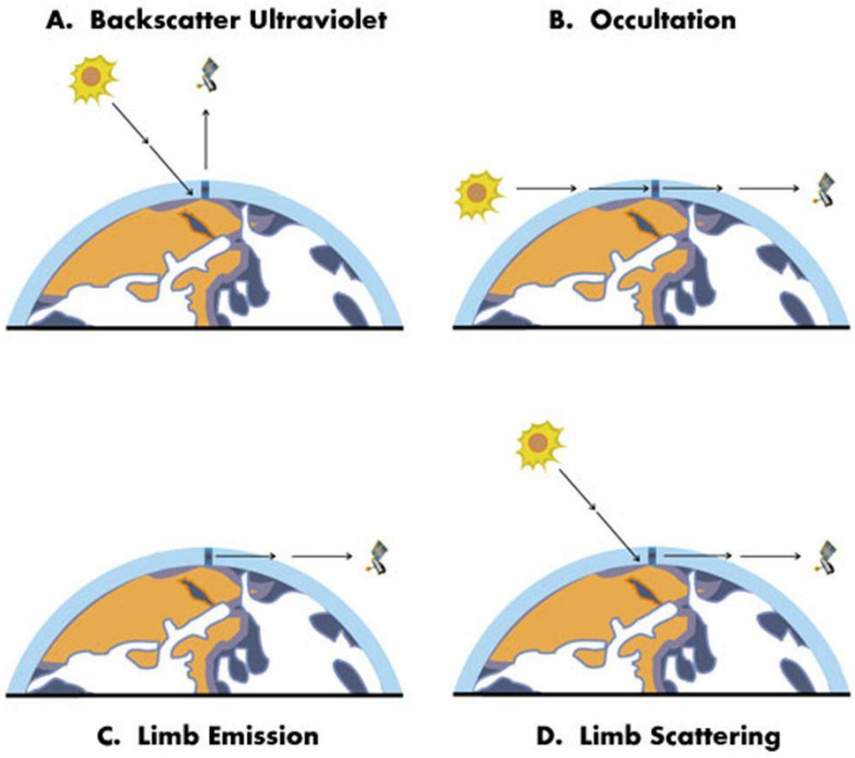

Figure 2.15: Techniques used for ozone measurements from satellites (Adopted From [*Wallace* and *Hobbs*, 2006]).

2.6.2. Space-based remote sounding

The instruments onboard the satellites can measure the ozone concentrations using four main techniques: backscatter UV (BUV), occultation, limb scattering and limb emission (Figure 2.15). Two pairs of measurements are required for total ozone determination using BUV technique; the incoming and backscatter UV radiance at a wavelength that ozone absorbs strongly and a similar pair of measurements at a wavelength that is absorbed by ozone weakly (Figure 2.15a). The total column ozone can be calculated from the difference between these two pairs of measurements. In the occultation technique the radiation from sun, moon or a star during rising or setting is measured by the instrument through the limb of the atmosphere (Figure 2.15b). By measuring the radiation at various wavelengths absorbed by the atmosphere, vertical profiles of various species can be determined. The infrared and microwave radiation emitted by the atmosphere along the line of sight of the instrument is used in the limb emission technique to derive the ozone concentrations (Figure 2.15c). In the limb scattering technique, the instrument measures the scattered light from the sun or moon instead of the direct light (Figure 2.15d). Using this technique continues measurements can be provided as long as the sun is visible.

.

3. Brewer and Dobson Error Analysis

The Dobson and Brewer spectrophotometers are the primary, standard instruments for ground-based total column ozone measurements under the World Meteorological Organization's (WMO) Global Atmosphere Watch program. The accuracy of the data retrieval for both instruments depends on a knowledge of the ozone absorption coefficients and some assumptions underlying the data analysis. Instrumental stray light causes non-linearity in the response of both the single-monochromator Brewer and the Dobson to ozone at large ozone slant paths. In addition, it affects the effective ozone absorption coefficients and extraterrestrial constants that are both instrument dependent. This effect has not been taken into account in the calculation of ozone absorption coefficients that are currently recommended by WMO for the Dobson network. The ozone absorption coefficients are calculated for each Brewer instrument individually, but in the current procedure the effect of stray light is not being considered. This study documents the error caused by the effect of stray light in the Brewer and Dobson total ozone measurements using a mathematical model for each instrument. It shows that the differences detected between the total ozone amounts

deduced from Dobson AD and CD wavelengths are related to the level of stray light within the instrument. The error introduced by the assumption of a fixed height for the ozone layer for Brewer ozone measurements at high latitude sites is also evaluated. The Dobson measurements at the South Pole site are compared with ozone data from a collocated double monochromator Brewer spectrophotometer (Mark III).

A manuscript on this study is completed and will be soon submitted to Journal of "*Atmospheric Measurements and Techniques*".

3.1. Introduction

Routine atmospheric total column ozone measurements started in the mid-1920s with a Féry photographic spectrometer [*Dobson,* 1931]. Following the International Geophysical Year (1958) a worldwide network was developed with a number of Dobson spectrophotometer that were installed around the world to monitor total ozone variations. In the early 1980s the automated Brewer became commercially available [*Kerr et al.,* 1981] with more advanced technology. A similar network was introduced for the Brewer as observing organizations started to use these instruments alongside the Dobson for long-term measurements.

Although the principle of the measurements for the Brewer and Dobson instruments is generally the same, seasonal and systematic differences in respective TOZ (Total Ozone) products became evident after long-term, co-incident measurements were accumulated [*Staehelin et al.,* 1998; *Vanicek,* 2006]. The adoption of the *Bass* and *Paur* [1985] ozone cross-sections (BP) for the Dobson instrument in 1992 put both instruments on the same

reference scales (Brewer uses BP) and reduced the difference to 4% [*Kerr et al.*, 1988] but it did not resolve the seasonal and offset differences [*Vanicek,* 2006].

Temperature corrections to the ozone absorption cross-sections may reduce the systematic errors of Dobson ozone data by up to 4% [*Bernhard et al.*, 2005]. The seasonal differences between the measurements by the two instrument types is related to the ozone effective temperature, which affects differently the ozone absorption measured by the Brewer and Dobson instruments [*Bernhard et al.*, 2005; *Kerr et al.*, 1988; *Scarnato et al.*, 2009; *Van Roozendael et al.*, 1998; *Vanicek,* 2006].

The impact of different laboratory-determined ozone cross-sections has also been investigated and showed up to 3% changes for Brewer and 1% for Dobson data [*Redondas et al.*, 2014].

To facilitate the replacement of Dobson instruments with Brewers, statistical methods have been developed to derive transfer functions for converting Dobson measurements to the Brewer scale. These methods have been partly successful, but they cannot entirely explain the differences between the measurements of the two instruments [*Scarnato et al.*, 2010].

Analysis of the data obtained by the Dobson at the South Pole showed that the assumption of the ozone layer being at a fixed height leads to an error in the air mass calculation. The errors caused by this assumption may exceed 4% in ozone measurements when the ozone distribution is distorted by the "ozone hole" [*Bernhard et al.*, 2005].

While stray light has been demonstrated to affect measurements by both instrument types [*Bais et al.*, 1996], the effect of the stray light on measurements at large solar zenith angles (SZA), have not been analyzed properly yet. The errors caused by stray light are particularly significant at high latitudes when measurements are made at large SZA and large

TOZ. The main goal of this study is to investigate and document the sources of errors in total ozone as measured by the Dobson and Brewer instruments at high latitudes.

3.2. Method

3.2.1. Instrument description

The Brewer instrument

The Brewer spectrophotometer is designed to measure total ozone, SO_2 and spectral UV irradiance. Figure 3.1 shows the optical components of a Brewer Mark IV which consist of the fore-optics, the spectrometer and the photomultiplier. There are several different optical elements in fore-optics to direct incoming light onto the entrance slit of the spectrometer.

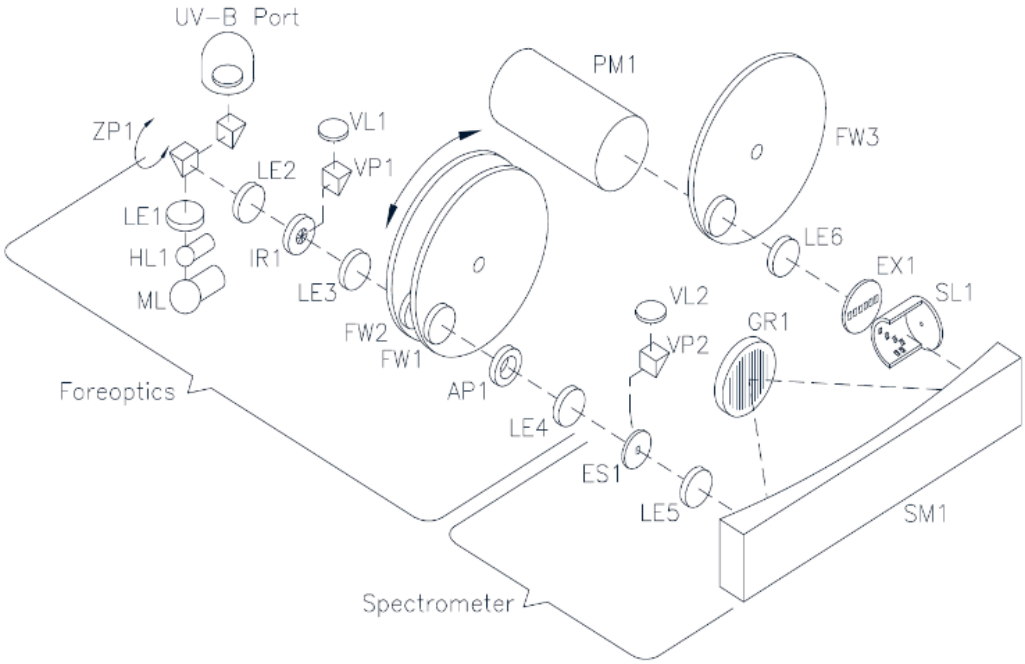

Figure 3.1: Brewer MkIV optical layout ["Brewer MKIV Spectrophotometer Operator's Manual," 1999].

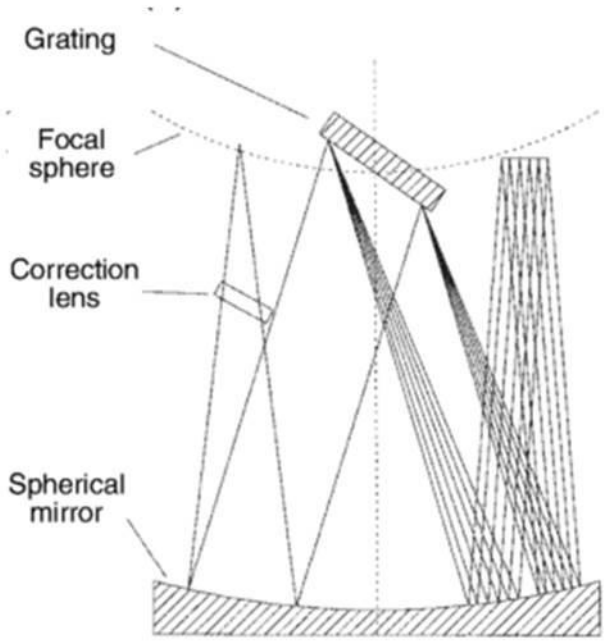

Figure 3.2: A schematic diagram of Brewer spectrometer (From [*Kerr* and *McElroy*, 2000]).

The spectrometer disperses the incident light into a high-quality spectrum along the exit slits focal plane. A schematic diagram of the spectrometer is shown in Figure 3.2. Six exit slits are approximately evenly spaced across the focal plane at ozone and SO_2 operating wavelengths. The shortest wavelength, 302.1 nm is used for wavelength calibration using a mercury lamp. The wavelengths of 310.1 nm, 313.5 nm, 316.8 nm and 320.1 nm with ~0.55 nm resolution are used for ozone and SO_2 measurements. The wavelength setting is adjusted by rotating the grating using a stepper motor. A cylindrical mask that covers the exit slits exposes only one wavelength slit at a time. The mask is rotated rapidly by a stepper motor resulting in near-simultaneous measurements of all five wavelengths and a dark position ["Brewer MKIV Spectrophotometer Operator's Manual," 1999].

In the Mark II and Mark IV versions of the Brewer, the light passing through the exit slits is collected by a Fabry lens and falls on a low-noise photomultiplier. For the Mark III version of the instrument a 45^o mirror reflects the radiation into a second spectrometer

(recombining spectrometer) that mirrors the dispersing spectrometer (Figure 3.3) [“Brewer MKIII Spectrophotometer Operators Manual,” 2005]. The light then goes through the second spectrometer or reaches the photomultiplier. This reduces stray light as off-axis light will not pass through the second spectrometer.

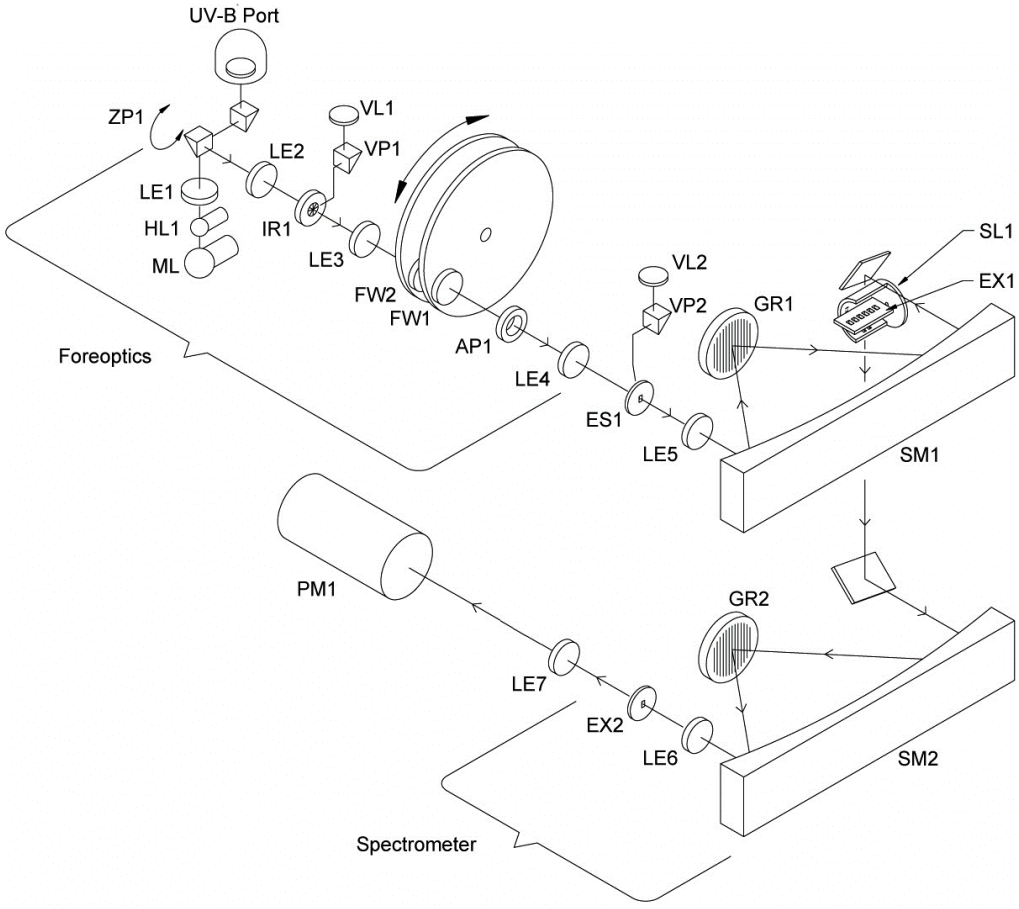

Figure 3.3: The Brewer MkIII optical layout [“Brewer MKIII Spectrophotometer Operators Manual,” 2005].

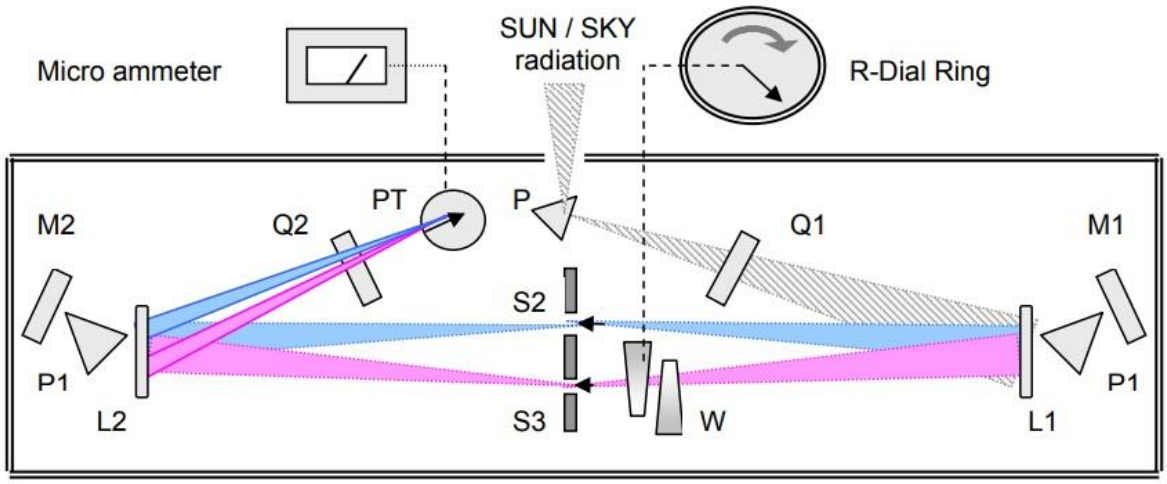

Figure 3.4: A schematic of optical system of the Dobson instrument (From [*Vanicek et al.*, 2003])

The Dobson instrument

The Dobson spectrophotometer is designed to measure the relative intensities of a selected pair of wavelengths in the UV part of the solar spectrum. A detailed descriptions of the instrument function can be found in several fundamental publications (e.g. [*Evans* and *Komhyr*, 2008; *Komhyr*, 1980; *Komhyr et al.*, 1989]). Figure 3.4 shows the optical system of the Dobson instrument. The entering solar light is directed by prism P to the first half of the spectrometer where the light is dispersed by a double pass through prism P1, reflected by mirror M1, and then is focused as spectrum by lens L1 onto the focal plane at slits S2 and S3. The selected wavelengths can be controlled by rotating the quartz plate Q1 and therefore changing the angle of the light incident on P1 and allowing different wavelengths to be selected and focused at slits S2 and S3. The selected wavelengths then pass through the second half of the spectrometer where various optical elements (i.e. L1, M2, P2, and Q2) reassemble the light so both wavelengths fall on the final exit slit. The photons are then collected by the photomultiplier PM. The S2 and S3 slits allow only predefined wavelengths

pairs with strong (SHORT wavelength) and weak (LONG wavelength) ozone absorption to pass through the second half of the spectrometer and reach to the photomultiplier. Two logarithmic attenuators, called optical wedges in front of the LONG wavelength are used to balance the intensity of the radiation flux passing through S3 with that of the S2. The position of the wedges is controlled by a manually operated external circular dial (the R-dial).

3.2.2. Brewer and Dobson retrieval algorithm

According to the Beer-Lambert law, the spectral irradiance $I(\lambda)$ from a direct solar spectrum at the Earth's surface is expressed as:

$$\boldsymbol{I(\lambda) = I_0(\lambda) exp(-\tau(\lambda))} \quad \textbf{(3.1)}$$

where $\tau(\lambda)$ is the optical thickness of the incident path

$$\boldsymbol{\tau(\lambda) = \alpha(\lambda) X \mu + \beta(\lambda) \frac{P_s}{P_0} m_R + \delta(\lambda) m_a} \quad \textbf{(3.2)}$$

And

$I_0(\lambda)$ - Extraterrestrial irradiance at wavelength λ

$\alpha(\lambda)$ - Monochromatic ozone absorption coefficient at wavelength λ

X - Total column ozone (TOZ)

μ - Relative optical air mass appropriate for ozone absorption

$\beta(\lambda)$ - Rayleigh optical depth for a one-atmosphere path

P_s - Station pressure

P_0 - Mean sea level pressure (1013.25 hPa)

m_R - Relative optical air mass for Rayleigh scattering (extinction)

$\delta(\lambda)$ - Aerosol optical depth

m_a - Relative optical air mass for aerosol scattering (extinction)

The Dobson spectrophotometer does not measure the intensity of sunlight at a single wavelength but instead determines the ratio between the irradiance at two wavelengths, one strongly absorbed and the other more weakly affected by ozone. Several wavelength pairs are used by the Dobson algorithm for calculating total column ozone. In order to minimize the effect of aerosol and other absorbers, two wavelengths pairs are used such as AD, AC or CD where the A pair is (305.5 / 325.4 nm), C is (311.5 / 332.4 nm) and D is (317.6 / 339.8 nm) [*Basher*, 1982a; *Evans* and *Komhyr*, 2008]. For example, the total ozone using AD wavelength pair observations is retrieved using the following expression:

$$\boldsymbol{X = (N_A - N_D - K - \Delta\beta_{AD}\frac{P_s}{P_0}m_R - \Delta\delta_{AD}m_a)/(\mu\Delta\alpha_{AD})} \quad \textbf{(3.3)}$$

$$\boldsymbol{N_A = log[I_0(305.5)/I_0(325.4)] - log[I(305.5)/I(325.4)]} \quad \textbf{(3.4)}$$

$$\boldsymbol{N_D = log[I_0(317.6)/I_0(339.8)] - log[I(317.6)/I(339.8)]} \quad \textbf{(3.5)}$$

$$\boldsymbol{\Delta\beta_{AD} = [\beta(305.5) - \beta(325.4)] - [\beta(317.6) - \beta(339.8)]} \quad \textbf{(3.6)}$$

$$\boldsymbol{\Delta\delta_{AD} = [\delta(305.5) - \delta(325.4)] - [\delta(317.6) - \delta(339.8)]} \quad \textbf{(3.7)}$$

$$\boldsymbol{\Delta\alpha_{AD} = [\alpha(305.5) - \alpha(325.4)] - [\alpha(317.6) - \alpha(339.8)]} \quad \textbf{(3.8)}$$

where $\Delta\alpha$ is the differential ozone absorption coefficient at -46.3 degree Celsius and $\boldsymbol{K}$ is the instrument constant. Other double wavelength pairs such as CD can be used for the ozone calculation by modifying Eq. (3.3) [*Komhyr et al.*, 1993] to replace N_A with N_C .

The basic measurement principle for the Brewer instrument is the same as the Dobson. However, the Brewer measures the intensity of four operational wavelengths quasi-simultaneously. The total ozone is calculated using the following equation:

$$\boldsymbol{X = (MS9 + \Delta\beta \frac{P_s}{P_0} m_R - B)/(\Delta\alpha\mu)} \quad \textbf{(3.9)}$$

where $\Delta\alpha$ and B are the differential ozone absorption coefficient at -45 degree Celsius and the Extra-terrestrial Constant (ETC) respectively. Both are obtained from a linear weighted combination of their individual values at the four wavelengths used for the total ozone retrieval [*Kerr*, 2002]. $MS9$ is calculated from a linear combination of the logarithms of the intensities (F_i) measured at the four wavelengths $\lambda_i = (310.0, 313.5, 316.8, 320.0)$, multiplied by the weighting coefficients w_i.

$$\begin{aligned} \boldsymbol{MS9} &= \sum_{i=1}^{4} \boldsymbol{w_i . log F_i} \\ &= \boldsymbol{log[I(310.0)] - 0.5\, log[I(313.5)]} \\ &\quad \boldsymbol{- 2.2\, log[I(316.8)] + 1.7\, log[I(320.0)]} \end{aligned} \quad \textbf{(3.10)}$$

$$\Delta\boldsymbol{\alpha} = \sum_{i=1}^{4} \boldsymbol{w_i . \alpha_i} \quad \textbf{(3.11)}$$

$$\Delta\boldsymbol{\beta} = \sum_{i=1}^{4} \boldsymbol{w_i . \beta_i} \quad \textbf{(3.12)}$$

The weighting coefficients, w_i = (1.0, -0.5, -2.2 and 1.7), have been selected to minimize the absorption of SO_2 and suppress any variations that change linearly with wavelength. Hence, the aerosol scattering effect, which is approximately linear with wavelength over a narrow wavelength range, is suppressed in the calculation. The ETC of

primary standard instruments located in Toronto are determined at Mauna Loa observatory using the zero air mass factor extrapolation (Langley plot method). It can be transferred to other instruments by comparisons with a traveling standard instrument [*Fioletov et al.*, 2005].

3.2.3. Effective ozone absorption coefficients

To calculate the effective ozone absorption coefficients, the laboratory-determined ozone cross-sections at an effective atmospheric ozone layer temperature must be convolved with the instrument slit function, weighted by the solar flux. The BP ozone cross-sections were recommended by the International Ozone Commission (IO_3C) in 1992 (http://www.esrl.noaa.gov/gmd/ozwv/dobson/papers/coeffs.html) for the Brewer and Dobson networks. The calculation of the absorption coefficients, which are currently recommended by WMO for Dobson instruments, is described by *Komhyr et al.* [1993] (K93 hereinafter) and the re-evaluation is described by *Bernhard et al.* [2005] (B05 hereinafter). Recently IO_3C has recommended the ozone cross-sections measured by *Serdyuchnko et al.* [2014], as they reduce the Dobson temperature sensitivity. In this study for consistency with previous works the BP cross-sections are used. A correction factor

$$\boldsymbol{f_c = 1.0112 - 0.6903/[87.3 - (T - T_0)]} \qquad \textbf{(3.13)}$$

based on the results of *Barnes and Mauersberger* [1987] as suggested by K93 is used to adjust the cross-sections. This correction has also been implemented in the Dobson and Brewer networks. For wavelengths longer than 340 nm, where BP data are not available, the *Brion et al.* [1993], *Daumont et al.* [1992] and *Malicet et al.* [1995] (BDM) data are used. These data sets are available at individual temperatures and also with the associated quadratic coefficients of temperature dependence on the IGACO (Integrated Global Atmospheric

Chemistry Observations) web page. The temperature dependence of the cross-sections is expressed as:

$$\boldsymbol{\sigma(\lambda,T) = C_0(\lambda) + C_1(\lambda)T + C_2(\lambda)T^2} \quad \textbf{(3.14)}$$

where C_0, C_1 and C_2 are the quadratic coefficients at wavelength λ. The quadratic coefficients used throughout this study are consistent with the K93 and B05 calculations. The absorption coefficients are calculated from the ozone cross-sections $\sigma(\lambda, T)$ and the ozone number density $N(z)$:

$$\boldsymbol{\alpha(\lambda) = \frac{1}{X}\int_{z_0}^{\infty} \sigma\big(\lambda, T(z)\big) N(z) dz} \quad \textbf{(3.15)}$$

where z_0 is the altitude of the station and T is the temperature in Kelvin. The total ozone column, X, (in Dobson unit equal to 2.69×10^{16} ozone molecules per square centimeter) is defined as:

$$\boldsymbol{X = \frac{kT_0}{P_0}\int_{z_0}^{\infty} N(z) dz} \quad \textbf{(3.16)}$$

where T_0 is 273.15 K and $\boldsymbol{k}$ is the Boltzman constant (It should be noted that X is used in the equations whereas TOZ is used in the text). In order to account for the finite bandwidth of the Brewer and Dobson slit functions, the effective ozone absorption coefficient $\bar{\alpha}_i$ is used instead of $\alpha(\lambda)$ in Eq. (3.2) and (3.3) [*Basher*, 1982a; *Vanier* and *Wardle*, 1969]:

$$\boldsymbol{\bar{\alpha}_i = \frac{-1}{X\mu} log\left(\frac{\int I_0(\lambda) S(\lambda,\lambda_i) exp(-\alpha(\lambda) X\mu - \beta(\lambda)\frac{P_s}{P_0} m_R) d\lambda}{\int I_0(\lambda) S(\lambda,\lambda_i) exp(-\beta(\lambda)\frac{P_s}{P_0} m_R) d\lambda}\right)} \quad \textbf{(3.17)}$$

where $S(\lambda, \lambda_i)$ is the slit function for a wavelength λ_i.

The Brewer operative method employs a simpler approximation, which is identical to the approximation method of B05 and the simplest approach of K93, and also used by *Redondas et al.* [2014], *Van Roozendael et al.* [1998], *Scarnato et al.* [2009] and *Fragkos et al.* [2013]:

$$\bar{\alpha}_i^{approx} = \frac{\int \alpha(\lambda) S(\lambda, \lambda_i)\, d\lambda}{\int S(\lambda, \lambda_i)\, d\lambda} \quad \textbf{(3.18)}$$

3.2.4. Ozone air mass calculations

Both Brewer and Dobson retrievals assume a fixed height for a thin layer of ozone to calculate the ozone air mass. The following expression is used by both instruments to calculate relative optical air mass at a solar zenith angle of θ_0:

$$\mu(\theta_0) = (Re + h)/[(Re + h)^2 - (Re + r)^2 sin^2\theta_0]^{0.5} \quad \textbf{(3.19)}$$

where *Re* is the radius of the Earth, *r* is the altitude of the station and *h* is the height of the ozone layer. Using the mean Earth radius for *Re* instead of the actual Earth radius at the station does not introduce a significant error in μ. However, it is important that the correct value of the station altitude and the height of the ozone layer be used in Eq. (3.19). The Dobson community has adopted an ozone layer height that changes with latitude, which to some extent is in agreement with ozone climatology, while a fixed height of 22 km is used in the Brewer network.

3.2.5. Slit function and stray light effect

Stray light is unwanted radiation from other wavelengths that arrives at the detector during measurements at a selected wavelength. Scattering by instrument optical elements and inefficient out-of-band (OOB) rejection of the light by dispersive elements, e.g. the grating,

are the main sources of stray light in the spectrometers. Particulate scattering within the instruments may also contribute to the stray light. Generally, holographic gratings with higher line densities generate lower stray light. The Mark II and IV versions of the Brewer demonstrate higher levels of stray light compared to the Mark III as the Mark III instruments utilize a double monochromator with higher line density gratings that leads to significantly better rejection of the OOB light. The stray light within the Dobson instrument is comparable to that of within the Brewer Mark IV and II.

Since the gradient of ozone absorption is large in the ultraviolet spectral region, the stray light contribution from longer wavelengths can make up a significant fraction of the signal measured at shorter wavelengths where it is reduced by ozone absorption. As the ozone slant path increases, the impact of stray light on the measurements also increases. Stray light results in an underestimated ozone column at larger ozone slant column amounts.

To properly characterize the stray light in an instrument it is necessary to measure the instrument slit function. A He-Cd laser (single line at 325.029 nm) has been used to measure the slit functions of the Brewer. Figure 3.5 shows the measured slit functions of a Brewer Mark IV #009 (single monochromator) and Mark III #119 (double monochromator) located at Mauna Loa Observatory (MLO). Several Brewer Mark IV, Mark II, and Mark III slit functions have been measured throughout various inter-comparison campaigns (e.g. The Fourth North American Interagency Inter-comparisons of Ultraviolet Monitoring near Boulder, Colorado, in 1997 and published by *Lantz et al.*, [2002] and Inter-Comparison Campaigns of the Regional Brewer Calibration Center-Europe (RBCC-E)). The slit function contains the core (band-pass), the shoulders, and the extended wings (Figure 3.5). The stray light measured from nearby wavelengths (the wings of the slit function) is typically below

10^{-6} times that of the primary wavelength in the Mark III double Brewers as compared to 10^{-4} in the Mark II and Mark IV single Brewers. To reduce the effect of stray light, the Brewer Mark II uses a cutoff filter which strongly attenuates wavelengths longer than 345 nm. A solar blind filter (SBF) made of nickel sulphate hexahydrate ($NiSO_4.6H_2O$) crystal sandwiched between two UV colored glass filters (similar to Schott UG5 or UG11) is also used in the Mark IV. Figure 3.6 shows the transmission of typical UG-11-$NiSO_4$ filter measured by a Cary 5E spectrophotometer. The stray light level depends on the optical and mechanical configuration which is unique for each instrument, and thus two apparently identically configured instruments can have somewhat different OOB light rejection.

For this study, a symmetrical trapezoid is fitted to the measured slit functions of Brewer #009 (Single – Mark IV) and Brewer #119 (Double – Mark III). The model slit function fit to the data (red line) includes three parts: a trapezoid with 0.55 nm FWHM at the core band-pass, the shoulders which are modeled by fitting a Lorentzian function (details in Table 3.1) to the measured data and two horizontal straight lines for the outer parts (wings). To investigate the effect of stray light, an ideal slit function which is trapezoidal with a flat top at 0.87 of the full height and two straight lines to zeros with 0.55 nm FWHM has been used (Figure 3.5, top left).

The slit functions of the world standard Dobson #83 were experimentally measured by Komhyr using a tunable light source [*Komhyr et al.*, 1993]. However, the published slit functions are restricted to the core band-passes. It has been assumed that the Dobson instrument restricts OOB light from entering the slit. The extended wings have not been measured for the Dobson instrument. *Basher* [1982] attempted to estimate the level of stray light within the Dobson instrument by fitting a mathematical model to the AD pair direct sun

measurements and analyzing the total column ozone changes with Solar Zenith angle. His analysis suggested that for most Dobson instruments the level of stray light is 10^{-4} based on the non-linearity of the AD direct sun measurements beyond an air mass factor of 3.

Another approach has been used by *Evans et al.* [2009] to measure the stray light entering the Dobson instrument. They used a filter that is opaque to the C-pair nominal short wavelength band-pass, and transparent outside of this range (Fig. 6 in *Evans et al.,* [2009]). The idea is the filter would remove the desired band-pass from the signal and any current remaining is from OOB light. This method was used to estimate the contribution of stray light in zenith sky measurements of Dobson #65 in Boulder, CO. They also used a model approach for the stray light contribution in zenith sky measurements and concluded that the level of stray light in Dobson #65 is likely 2×10^{-5}. However, the shortest wavelengths that pass through the test, band-limiting filter do not include at wavelengths near by the slit nominal wavelength. Close-by wavelengths may important in contributing to stray light, based on the Brewer measurements.

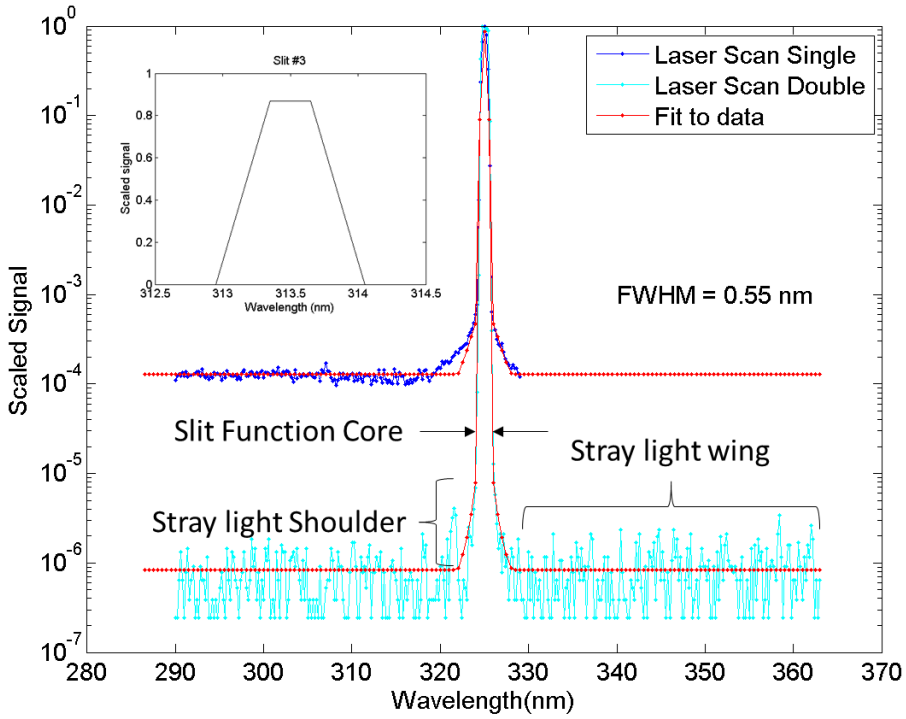

Figure 3.5: Slit functions measured with a He-Cd laser for single #009 and double #119 Brewers at Mauna Loa as well as fitted models; The ideal slit function is also shown inside the main graph.

Table 3.1: Optical characteristics of the Dobson and Brewer

	Dobson	Brewer
Nominal Wavelengths (nm)	305.5/325.0, 311.5/332.40, 317.5/339.9	310.0, 313.5, 316.8, 320.0
Slit Function	Short Channels: trapezoid 1.66, 1.84, 2.02 nm at the base and 0.16, 0.16, 0.16 nm at the top Long Channels: trapezoid 4.60, 5.40, 5.75 nm at the base and 2.35, 2.50, 2.50 nm at the top	Single: trapezoid at centre 0.55 nm FWHM, Lorantzian fitted to the measured slit of #009 for shoulders Double: trapezoid at centre 0.55 nm FWHM, Lorantzian fitted to the measured slit of #119 for shoulders
Other Filters	Cobalt filter (cuts off light above ~360 nm)	Single: UG-11 and NiSO4 filters – zero below 280 and above ~345 nm Double: Grating, PMT set zero below 250nm and above 800 nm
Stray light	1×10^{-5} and 1×10^{-4}	Single: ~ 1×10^{-4} Double: ~ 1×10^{-6}

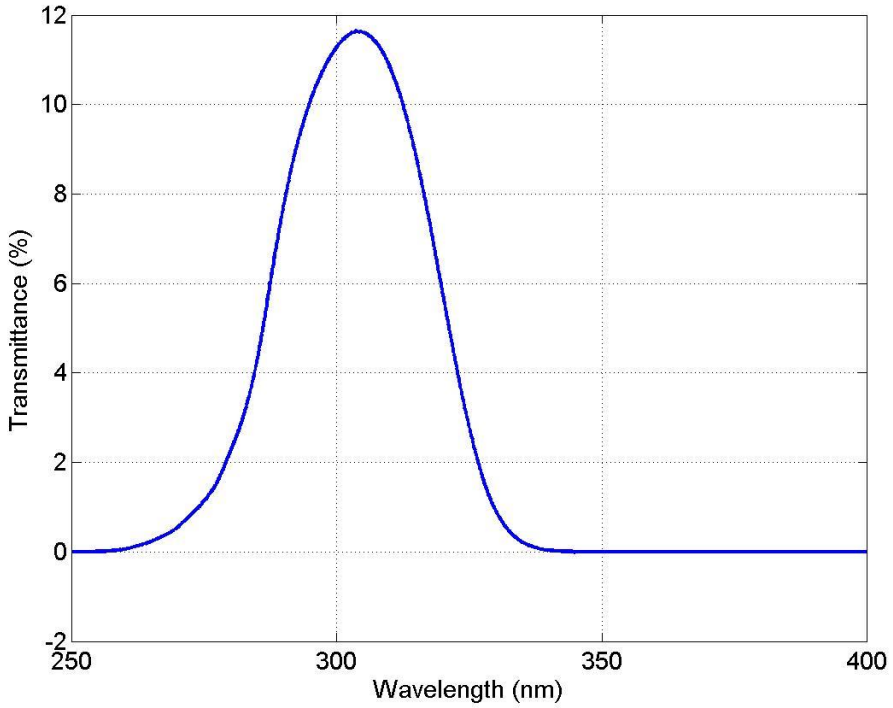

Figure 3.6: The response of typical combined UG-11-$NiSO_4$ filter utilized by Brewer Mark IV to reduce the stray light measured with a Cary 5E spectrophotometer for Brewer #154 filters.

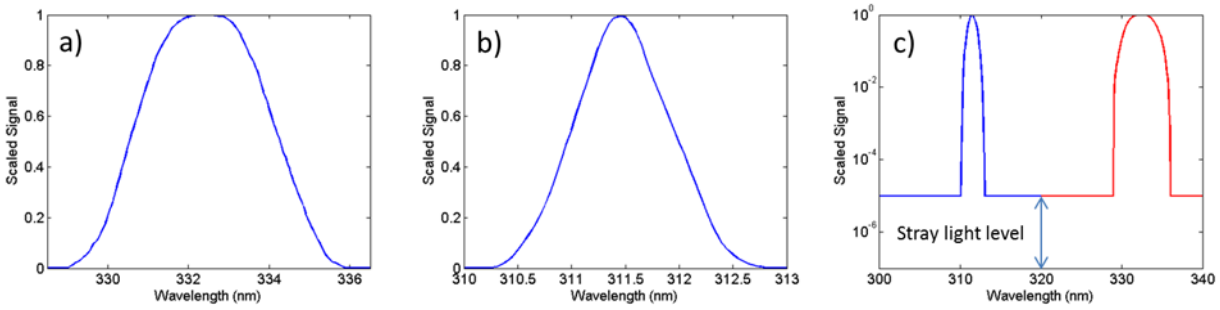

Figure 3.7: a, b) Dobson C-pair ideal slit functions. c) Dobson Modeled slit function. Two straight lines have been added to the core slit functions in order to account for stray light.

The Dobson slit functions for short and long wavelengths are approximately a triangle with FWHM of 1.06 nm and a trapezoid with FWHM of 3.71 nm respectively (Figure 3.7). For this study, symmetrical trapezoids centered at the nominal Dobson wavelengths were fitted to the experimentally determined slit functions of Dobson #83 and used as ideal slit

functions. The characteristics of these trapezoids are given in Table 3.1. In order to account for stray light, two straight lines were added to the outer parts of the ideal slit functions.

3.3. Discussion

3.3.1. The effect of stray light on ozone absorption coefficients

To calculate the ozone absorption coefficients, the standard values defined in Table 3.1 and Table 3.2 are employed. In Table 3.3 the coefficients calculated for the Brewer single and double versions are shown. The values of $\bar{\alpha}_i^{approx}$ calculated with the ideal (trapezoidal) slit functions are the same as the operational values which are currently being used for Brewer numbers #009 and #119. These values were calculated to test the retrieval that is used in this study. Comparing $\bar{\alpha}_i$ calculated using modeled slit functions with $\bar{\alpha}_i^{approx}$ calculated using ideal slit functions shows 0.7% difference for the single and less than 0.01% for the double (highlighted in Bold at Table 3.3). Overestimating the coefficients according to Eq. (3.9) leads to an underestimation of the total ozone amount.

The values of $\bar{\alpha}_i$ and $\bar{\alpha}_i^{approx}$ calculated for the Dobson instrument using the modeled slit functions are provided in Table 3.4. $\bar{\alpha}_i^{adjusted}$ is the adjusted set of coefficients which are recommended by WMO to be used for the Dobson network. After applying the K93 data set to the observations made by World Standard Dobson Instrument #083 at Mauna Loa observatory, 0.8% for AD pair and 2.2 % for CD pair differences in the calculated total ozone values were detected. K93 realized that increasing $\bar{\alpha}_D$ by 2% would decrease the discrepancies to below 0.5%. Thus, the adjusted values were recommended by WMO to be used for the Dobson instruments.

The $\bar{\alpha}_i^{approx}$, and $\bar{\alpha}_i$ calculated in this study using ideal (trapezoid slit functions without stray light) slit functions and the slit functions with 10^{-5} level of stray light show less than 0.1% differences. However, the same comparison between the ideal slit values and the results using the slits with 10^{-4} level of stray light shows 4.0% and 6.9% difference between $\bar{\alpha}_i$ values for AD and CD pair respectively.

The values of $\bar{\alpha}_i^{approx}$ calculated using ideal slit functions and the slit functions with 10^{-5} level of stray light agree with the corresponding values of K93 to within ±2.0%. In the case of $\bar{\alpha}_i$, the comparison indicates agreement to within ±3.4% except for $\bar{\alpha}_{339.9}$ where the difference is about 67%. Approximately the same difference was reported by B05 for the same wavelength compared to K93. B05 have investigated this discrepancy by using Molina and Molina [1986] cross-sections to extend the BP datasets for Dobson calculations and concluded that the K93 value for $\bar{\alpha}_{339.9}$ is unreasonably high. As in B05, the calculated value, $\bar{\alpha}_D$, agrees better with the empirically adjusted value, $\bar{\alpha}_D^{adjusted}$. The comparison shows agreement to within ±1.6% between the values calculated for this work and the K93 adjusted values.

Generally, the differences between values presented here and those from K93 are slightly higher than the difference between B05 and K93. However, it should be noted that the slit functions and the parameters used in the calculations presented here are slightly different from those used by K93 and B05 (Table 3.1 and Table 3.2). The AD coefficient calculated for a Dobson instrument with 10^{-4} level of stray light shows a 3.6% deviation compared to the adjusted values and for the CD pair the difference is about 7.2%.

Clearly, the stray light level within each instrument has an effect on the ozone absorption coefficient calculations. This effect is negligible for the instruments with a stray

light level on the order of 10^{-5}. But the difference could be up to 4.0% and 6.9% for AD and CD pair coefficients respectively for the instruments with levels of stray light on the order of 10^{-4} when compared with the values calculated using ideal slits. These differences translate to an underestimation of ozone values through Eq. (3.3). However, by applying the Dobson calibration procedure the difference between the AD measurements of the Standard instrument and a calibrated one is reduced to less than 0.7% [*Evans* and *Komhyr*, 2008]. Using the quasi-simultaneous measurements of AD and CD pairs a scaling factor can be calculated to reduce the CD measurements to the AD level. Therefore Dobson measurements should be accurate to within ±1%.

Table 3.2: Parameters for calculations of ozone absorption coefficients for standard conditions

Parameter	This Work	*Komhyr* [1993]
Effective temperature	-46.3°C	-46.3°C
Ozone profile	*Bhartia et al.* [1985] for 45 N and 325 DU	*Bhartia et al.* [1985] for 45 N and 325 DU
Air mass	2	2
Ozone absorption cross-sections	*Bass and Paur* [1985], adjusted with *Barnes and Mauersberger* [1987]*	*Bass and Paur* [1985], adjusted with *Barnes and Mauersberger* [1987]*
Slit function	Dosbon: Parameterized from Figure 1 of *Komhyr et al.* [1993] Brewer: Parameterized from laser scan of #009 and #119 (Details in Table 3.1)	A, B, C and D pair slit functions from Figure 1 of *Komhyr et al.* [1993]
Extraterrestrial spectrum	*Chance and Kurucz* [2010]	*Furukawa et al.* [1967]
Rayleigh optical depth	*Bates* [1984]	*Bates* [1984]

* For the work presented here the BDM Ozone cross-sections data set was used to extend the BP cross section to wavelengths beyond 340 nm; K93 used unpublished data by Bass and Paur.

An attempt is underway to measure the slit functions and the level of stray light of the world standard Dobson #083 accurately (Personal communication with Irina Petropavlovskikh, 2017). It is advisable that the new measured slit functions are used to

recalculate the absorption coefficients. The new values should be recommended by WMO to be applied in the Dobson retrieval algorithm.

Table 3.3: Brewer Ozone Absorption Coefficients

		Effective Ozone Absorption Coefficient (atm cm)$^{-1}$			
		Operational	Slit Function		Ratio *
			Ideal	Model	
Single	$\bar{\alpha}_i^{approx}$	0.3390	0.3388	0.3409	0.994
	$\bar{\alpha}_i$		0.3398	0.3363	1.011
	$\bar{\alpha}_i^{approx}/\bar{\alpha}_i$		0.997	1.014	**1.007**
Double	$\bar{\alpha}_i^{approx}$	0.3395	0.3394	0.3394	1.000
	$\bar{\alpha}_i$		0.3398	0.3397	1.000
	$\bar{\alpha}_i^{approx}/\bar{\alpha}_i$		0.999	0.999	**0.999**

* Ideal/Model

Table 3.4: Dobson wavelengths and Ozone Absorption coefficients

	Effective Ozone Absorption Coefficient (atm cm)$^{-1}$								
	Komhyr et al. [1993]			This Work					
				Model (Ideal)		Model (10^{-5})*		Model (10^{-4})	
Wavelength, nm or pair	$\bar{\alpha}_i^{approx}$	$\bar{\alpha}_i$	$\bar{\alpha}_i^{adjusted}$	$\bar{\alpha}_i^{approx}$	$\bar{\alpha}_i$	$\bar{\alpha}_i^{approx}$	$\bar{\alpha}_i$	$\bar{\alpha}_i^{approx}$	$\bar{\alpha}_i$
305.5	1.917	1.915		1.912	1.930	1.913	1.929	1.867	1.870
325	0.115	0.109		0.114	0.111	0.114	0.111	0.119	0.111
A	1.802	1.806	1.806	1.799	1.819	1.799	1.818	1.748	1.759
311.5	0.87	0.873		0.867	0.879	0.868	0.879	0.848	0.846
332.4	0.039	0.04		0.041	0.042	0.041	0.042	0.042	0.042
C	0.831	0.833	0.833	0.826	0.838	0.827	0.838	0.806	0.804
317.5	0.379	0.384		0.383	0.390	0.384	0.390	0.393	0.387
339.9	0.01	0.017		0.010	0.010	0.010	0.010	0.010	0.011
D	0.369	0.367	0.374	0.373	0.380	0.374	0.380	0.382	0.376
AD	1.433	1.439	1.432	1.426	1.439	1.425	1.438	1.366	1.383
CD	0.462	0.466	0.459	0.453	0.458	0.452	0.458	0.424	0.428

* The numbers inside the braces are showing the levels of stray light.

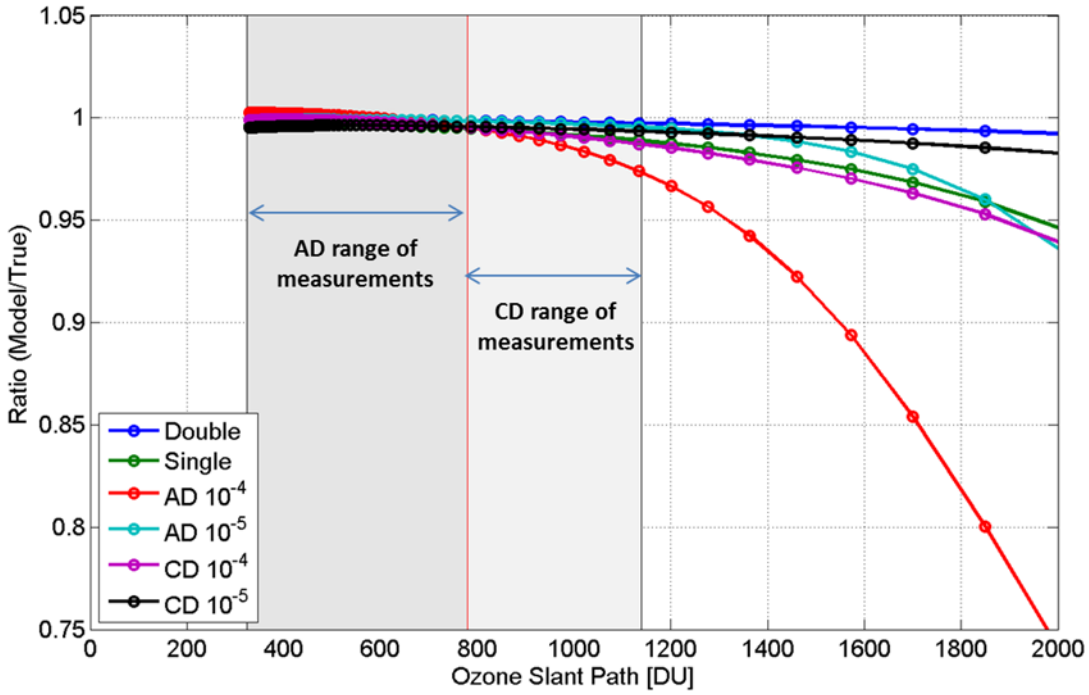

Figure 3.8: Ratio of the values retrieved from modeled single and double Brewers as well as a Dobson instrument with different levels of stray light (the numbers in front of the pairs are showing the levels of stray light) for an assumed 325 DU of ozone in the atmosphere (See text for details). The calculations reported here for the absorption coefficients have been used to retrieve total ozone. It should be noted that the air mass factor range recommended for AD measurements is 1.015 to 2.5 or less than 800 DU OSP and for CD measurements is 2.4 to 3.5 or less than 1200 DU OSP [*Evans* and *Komhyr*, 2008].

3.3.2. Stray light influence on low-sun measurements

To illustrate the effect of stray light on low-sun measurements, the percentage difference between ozone derived using Brewer and Dobson retrievals with assumed constant ozone in the atmosphere are depicted as a function of ozone slant path (OSP, total ozone times air mass) in Figure 3.8. Equation **(3.1)** along with parameters indicated in Table 3.2 is used to model the atmosphere and calculate the solar spectrum at the surface. To retrieve the ozone values, the absorption coefficients calculated in the previous sections are used. The

ETC values are calculated using the Langley method considering the data corresponds to air mass factors less than 2 and 3 for Brewer and Dobson respectively. For Dobson models the same ETC values as the one calculated using Ideal slits are used for the other models (i.e. with 10^{-4} and 10^{-5} levels of stray light). Two versions of the Brewer are compared with the Dobson instrument measurements with two levels of stray light. AD measurements with 10^{-4} order of stray light show approximately 25% discrepancy at 2000 DU OSP (air mass 6.2 in this case). The difference is about 5% for a typical single Brewer at the same OSP. The underestimation of total ozone as measured by the AD pair of a Dobson instrument with 10^{-5} level of stray light could be up to 6% at 2000 DU OSP. It has to be noted here that AD pair measurements are done for air mass factors less than 2.5 and thus during the ozone hole period (total column ozone is less than 300 DU) Dobson data will be reported for OSPs less than 750 DU [*Evans* and *Komhyr*, 2008].

Evidently, the CD pair is less influenced by scattered light than the AD pair because of the smaller ozone cross-sections at the CD wavelengths and the consequent smaller gradient with respect to wavelength in the spectrum measured. For a Dobson instrument with a minimum level of stray light (10^{-5}) the difference for the CD pair could be up to 1.8% at 2000 DU OSP while it is less than 0.8% for a typical double Brewer at the same OSP. It has to be noted that Dobson CD total ozone is reported for air mass values between 2.4 and 3.5, and thus OSP is less than 1100 DU for total ozone (TOZ) less than 300 DU [*Evans* and *Komhyr*, 2008].

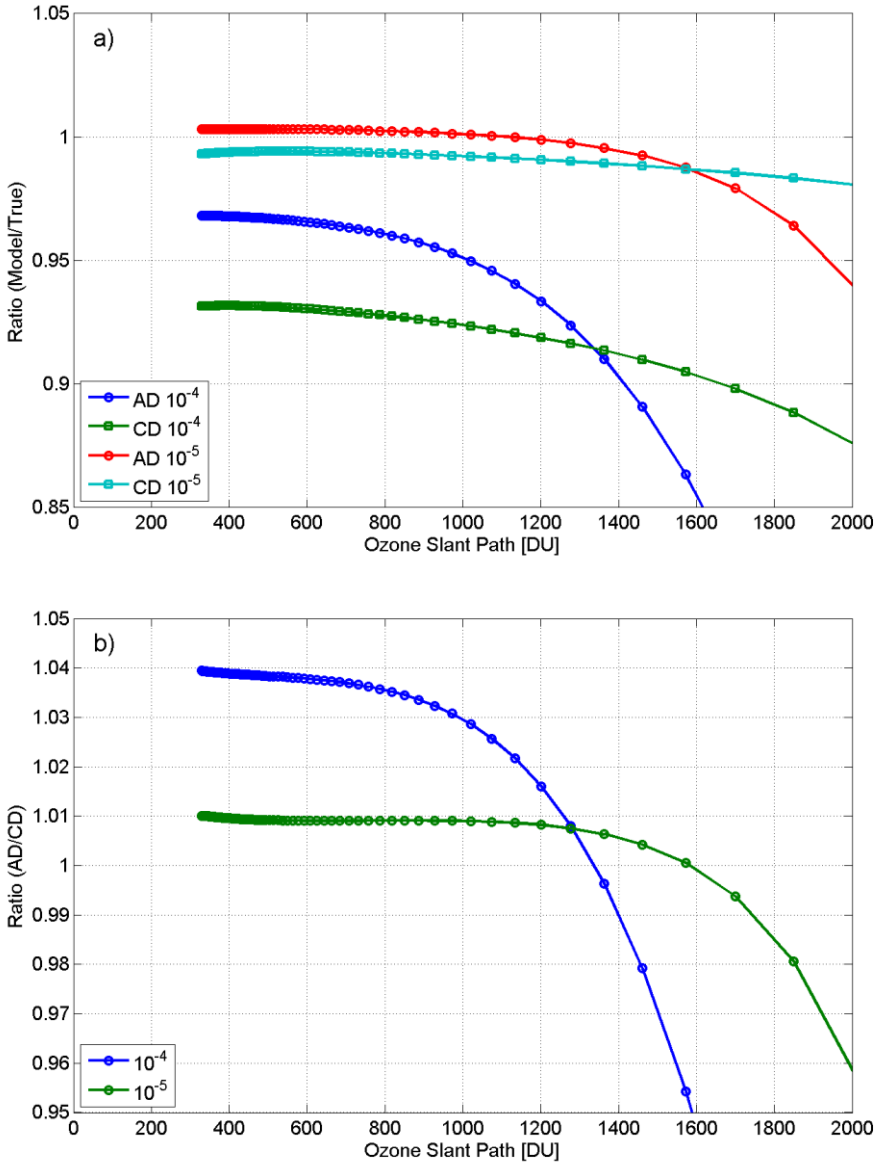

Figure 3.9: a) The ratio of total ozone retrieved from modeled Dobson AD and CD pairs with different levels of stray light to true ozone as a function of OSP. b) The ratio of AD to CD values. The adjusted coefficients recommended by WMO are used to derive the total ozone amounts for these models. The ETC values that were calculated using the Langley method for an ideal instrument are used here as well.

3.3.3. Total ozone values retrieved from Dobson AD and CD pairs

For decades the Dobson community has faced a discrepancy between the ozone values deduced from quasi-simultaneous AD and CD pair measurements. As indicated by the Dobson operational handbook, AD observations are the standard for the Dobson instrument and all other observations must, therefore, be reduced to the AD level by determining a multiplying factor. For example, the ozone values deduced from measurements on CD wavelengths should be multiplied by the factor of X_{AD}/X_{CD} (where X_{AD} and X_{CD} are the average ozone measurements retrieved from AD and CD pairs) derived from a large number of quasi-simultaneous observations covering a broad range of μ values greater than 2.0 to be reduced to those deduced from AD measurements.

Figure 3.9 illustrates the percentage discrepancy in total ozone reduced from AD and CD pairs for two modeled Dobson instruments with different levels of stray light as a function of OSP. The ratio of the AD to the CD pair is also shown. The adjusted coefficients calculated by K93 and recommended by WMO are used to derive the total ozone amounts for this model. The ETC values that were calculated using the Langley method for an ideal instrument are used here as well. It can be seen that, as the level of stray light increases, the difference between the AD and CD values increases, indicating the role of stray light in the observed discrepancy between AD and CD values. Clearly, such a difference varies for different Dobson instruments as it depends on the level of stray light which is unique for each individual instrument. It should be noted that, as discussed in 3.3.1, these discrepancies are generally reduced during calibration using simultaneous measurements with a well-maintained, standard instrument.

3.3.4. Error caused by air mass calculation

To retrieve the total ozone from direct sun measurements, it is required that the ozone air mass value be calculated. For measurements at the South Pole, the following values are used by the Dobson community in Eq. (3.19): Re = 6356.912, r = 2.81 km, and h = 17 km. Figure 3.10 shows the ratio of calculated air mass values using these numbers and those calculated using four different sets of assumptions. It is obvious that the fixed ozone layer height of 22 km, as used by Brewer retrieval, can cause up to a 2.2% difference at an air mass of 5.4. In addition, the altitude of the site can introduce a significant difference at high solar zenith angles.

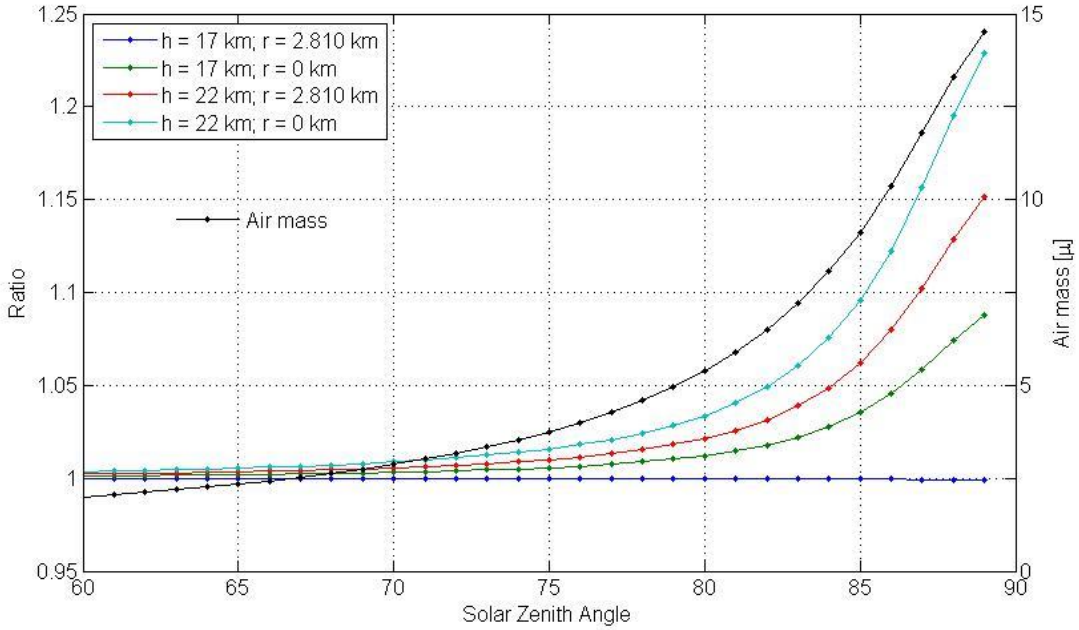

Figure 3.10: The left-hand axis shows the ratio of air mass calculated for the South Pole employing Re = 6356.912 km, r = 2.81 km, and h = 17 km as a reference to those calculated using a mean value for Re = 6370 km as used in the Brewer retrieval and different values for the altitude of site (r) and the height of ozone layer (h). The blue line indicates the discrepancy resulting from different values assumed for the radius of the Earth.

3.4. Brewer and Dobson measurements at the South Pole

Total ozone measurements collected by three Dobson instruments (#82, #42, and #80) and one double Brewer Mark III, #085, collocated and operated simultaneously at the Amundsen-Scott site (24.80W, 89.99S, altitude 2810m) were used for this comparison. Double Brewer #085 was installed at the South Pole station in 2008 and since then it was in routine operation until it was replaced in 2016. The Dobson instruments have been repeatedly changed out and calibrated against reference Dobson instrument #83.

Quasi-simultaneous direct sun measurements performed within 5 minutes during the period February 2008 and December 2014 were used in the present analysis. The air masses calculated by the Brewer retrieval were corrected using Eq. (3.19) by applying the values used by Dobson instruments (Re = 6356.912, r = 2.81 km, and h = 17 km) to be consistent with the Dobson air masses.

The data presented here comprise the entire data set collected by the instruments for research and maintenance purposes. The ozone absorption coefficients calculated by [*Komhyr et al.*, 1993] and recommended by WMO have been used to retrieve ozone values for AD and CD pairs. It is necessary to mention that only the data collected with an air mass factor less than 2.5 or OSP less than 800 DU would be reported for AD pair measurements to the World Ozone and Ultraviolet Data Centre (WOUDC) or other institutes for regular research purposes. The range of air mass factor for CD measurements is 2.4 to 3.5 and that means, in the case of the South Pole station, the maximum OSP would be 1100 DU.

Figure 3.11 presents a comparison of the Brewer total ozone measurements with Dobson ozone observations reduced from the direct sun AD pair as a function of OSP. The ratio between the uncorrected Brewer data and Dobson measurements are also shown in the

same plot. The ratios between the Brewer-corrected data and the Dobson values shows some dependence on OSP: the Dobson #82, #42, and #80 are on average 1%, 0.46% and 1.6% higher respectively for OSPs below 800 DU. When the OSP is above 800 DU, Dobson measurements gradually become lower by up to 4% for OSPs up to 1400 DU for Dobson #42 and #80 and up to 5% for OSPs up to 1200 DU for Dobson number #82 (Figure 3.12 and Figure 3.13). Figure 3.12 and Figure 3.13 shows a box plot of the difference between double Brewer ozone measurements and Dobson values retrieved from AD and CD pairs. The data are binned in 100 DU intervals from 400 to 2000 DU. On each box, the central red line is the median, the edges of the box are the 25th and 75th percentiles, the whiskers extend to the most extreme data points not considered outliers, and outliers are plotted individually.

The ratio between Dobson CD pair measurements and the Brewer data also shows a dependence on OSP (Figure 3.11). However, CD pair ozone values are on average 3.4%, 4.5%, and 2.5% higher for almost the entire measurement set for Dobson #82, #42, and #80, respectively. It should be noted that the CD pair values are scaled to the AD pair for each individual Dobson instrument. The scaling factors used for Dobson #82, #42, and #80 were 1.043, 1.025, and 1.03 respectively. The calibration procedures and the method for calculating the scaling factor are described and published by WMO in GAW report No. 183 [*Evans* and *Komhyr*, 2008].

It can be seen from this analysis that Dobson #42 TOZ values show less dependence on OSP. Based on the physical model developed in this work, it could be concluded that this instrument has a significantly lower level of stray light than the other Dobson instruments (#80 and #82).

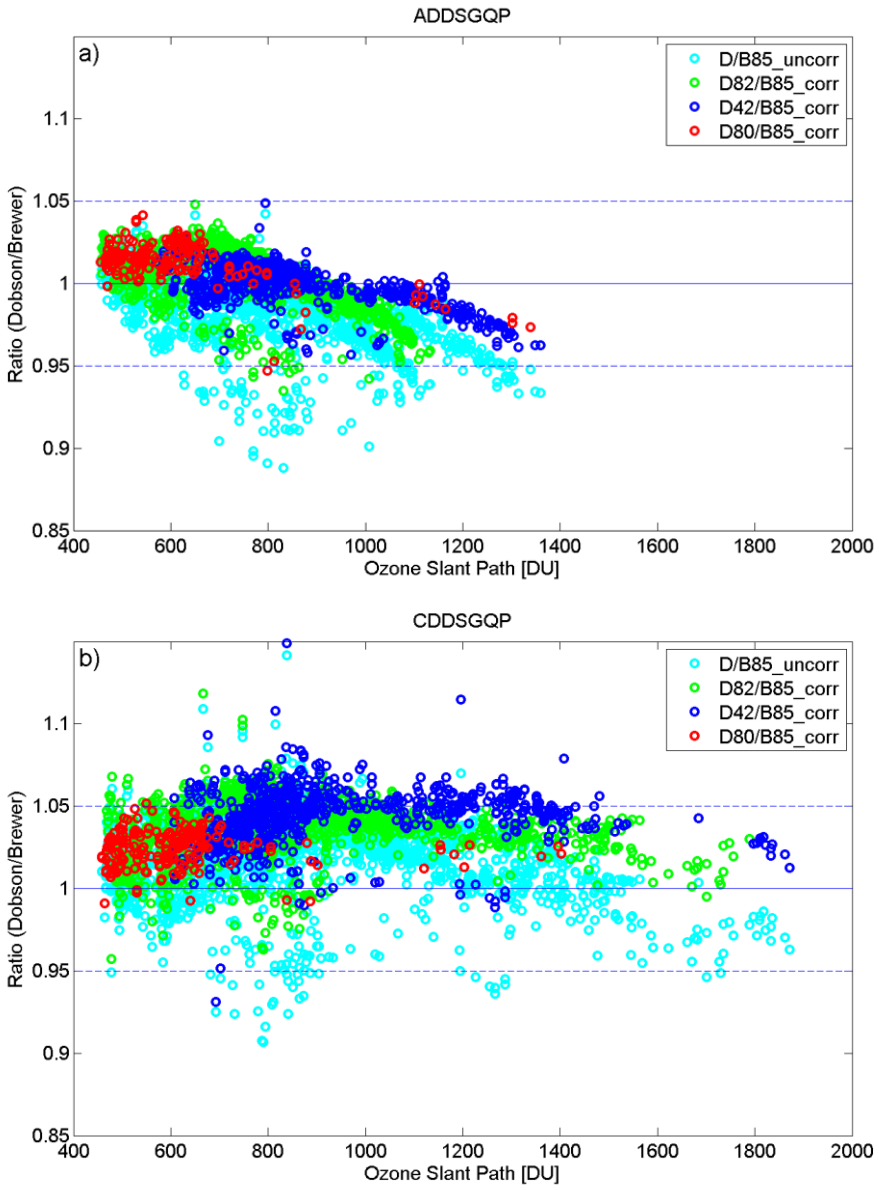

Figure 3.11: a) The ratio of quasi-simultaneous observations (within 5 min) using Dobson AD wavelengths to double Brewer #085 data at the South Pole. b) Same as (a) using Dobson CD pairs. Brewer air masses have been corrected using the values used for the Dobson measurements for the radius of the Earth, ozone layer height and the altitude of the site. D/B85 is the ratio of all data from three Dobson instruments and Brewer data before corrections for ozone layer height and station altitude. ADDSGQP: AD direct sun measurement using a ground quartz plate, and CDDSGQP: CD direct sun measurement using ground quartz plate.

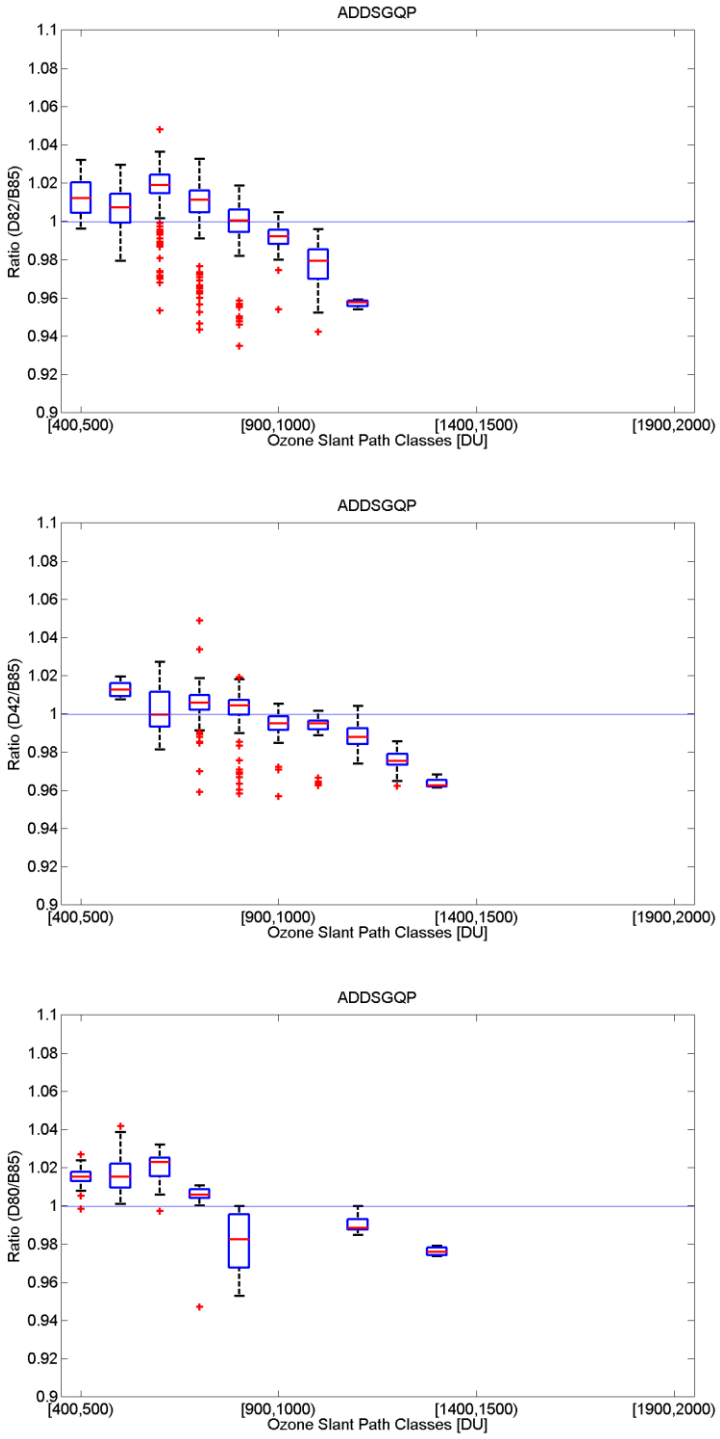

Figure 3.12: The ratio of quasi-simultaneous direct sun observations (within 5 min) by Dobson #82, #42, and #80, AD wavelengths to data from double Brewer #085 at the South Pole.

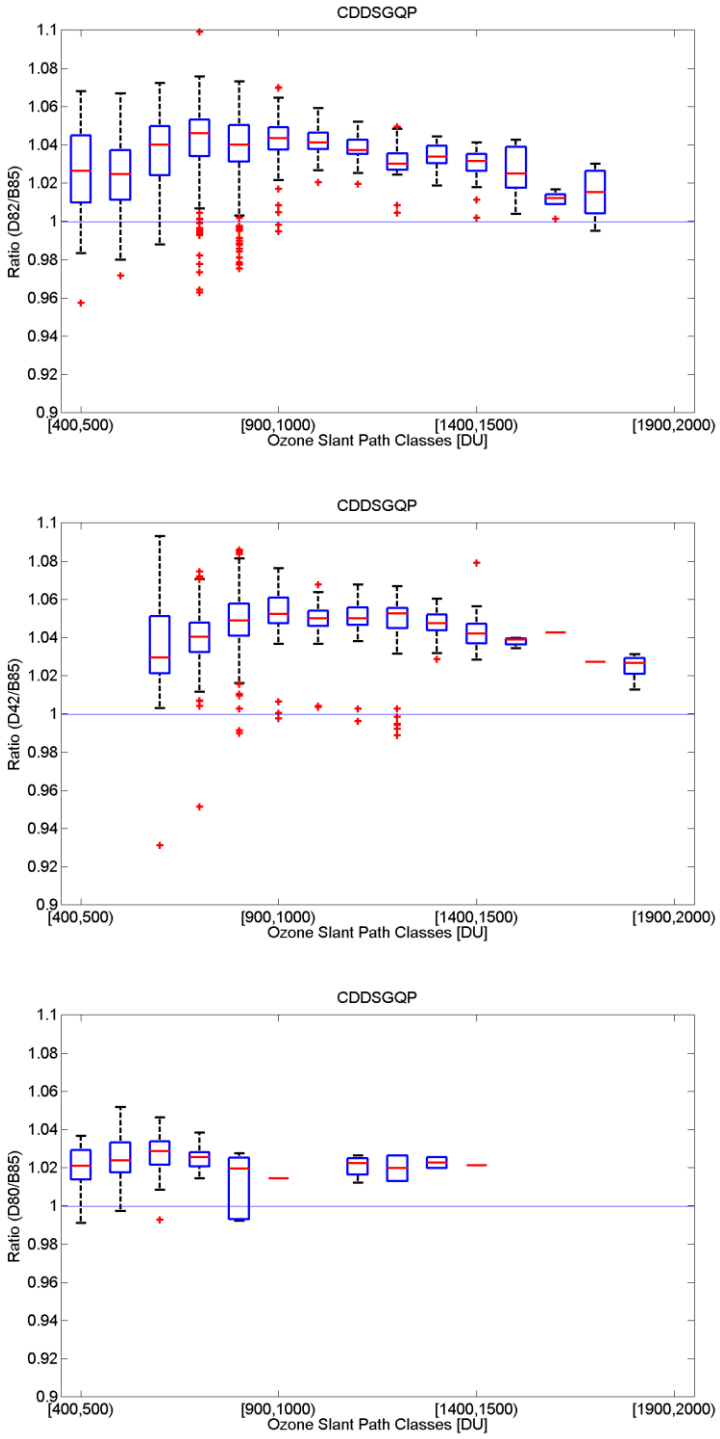

Figure 3.13: Same as Figure 3.12 for CD pair. On each box, the central red line is the median, the edges of the box are the 25th and 75th percentiles, the whiskers extend to the most extreme data points not considered outliers, and outliers are plotted individually.

3.5. Summary and conclusions

Physical models of the Dobson instrument and two types of Brewer spectrophotometer were developed to help better understand the effects of stray light on ozone measurements. The influence of assuming a fixed ozone layer height on air mass calculations and its error contribution to the ozone retrieval were also examined. The target accuracy for ground-based ozone measurements is 1%, while mathematical models show that the stray light effect can cause a discrepancy for a typical single Brewer and Dobson AD pair at large ozone slant paths of up to 5% and 25%, respectively. At 2000 DU OSP the difference for a double Brewer and a Dobson CD-pair with minimum level of stray light (10^{-5}) is up to 0.8% and 1.8%, respectively. This effect restricts measurements at high latitudes, like polar stations, particularly in the late winter and early spring when the ozone slant column is particularly large.

Stray light also can affect the calculation of ozone absorption coefficients. Currently, an approximation method is used to calculate the absorption coefficients for Brewer instruments. The analysis shows that using a measured slit function (instead of an idealized trapezoidal one) and taking into account the solar spectrum, leads to a 0.7% difference in calculated coefficients for a typical single Brewer.

Absorption coefficients for the Dobson spectrophotometers, taking into account the effect of stray light, have been calculated and compared with the results of similar calculations by K93, which are the coefficients recommended by WMO. The slit functions of Dobson #83 have been measured using a tunable light source (K93). It is assumed that the slit functions of other Dobson spectrophotometers are similar to the standard one. The slit functions were modeled to examine the effect of stray light on the calculation of ozone

absorption coefficients. The results show that 10^{-5} level of stray light has negligible effect on absorption coefficient calculations while the difference could be up 4.0% and 6.9% for AD and CD coefficients for an instrument with 10^{-4} level of stray light.

Coefficients for a Dobson with a minimum level of stray light (10^{-5}) agree to within $\pm$0.01% and $\pm$1.7% for $\bar{\alpha}_{AD}$ and $\bar{\alpha}_{CD}$ with K93 respectively, noting that the slit functions and parameters used by K93 and in this work (Table 3.1 Table 3.2) are slightly different. The calculation for $\bar{\alpha}_{339.9}$ shows a 67% difference with K93's result leading to differences of 3.4%, and -1.7% in $\bar{\alpha}_D$, and $\bar{\alpha}_{CD}$. B05 also have found approximately the same difference for this value ($\bar{\alpha}_{339.9}$) with K93's calculation. They concluded that K93's value for this wavelength is unreasonably large and likely caused by an error in K93's calculation. The adjusted value for $\bar{\alpha}_D$ recommended by WMO is K93's $\bar{\alpha}_D$ value, but increased by 2%. The differences between the calculations in this work (using Ideal slit function and slit function with 10^{-5} level of stray light) and the WMO values are 1.6%, 0.5%, and -2.6% for $\bar{\alpha}_D$, $\bar{\alpha}_{AD}$, and $\bar{\alpha}_{CD}$, respectively.

Using modeled slit functions with 10^{-4} level of stray light up to -3.5%, and -7.2% differences between calculated coefficients and WMO values for $\bar{\alpha}_{AD}$, and $\bar{\alpha}_{CD}$ are found. Overestimating the $\bar{\alpha}$ values translates to an underestimation of total ozone. However, through the calibration procedure, the difference between Dobson AD values of the standard instrument and a calibrated one were reduced to less than 0.7%.

When quasi-simultaneous measurements are made using Dobson AD and CD wavelengths, the results may not agree. For decades the Dobson community has faced such differences. The AD pair is the standard for Dobson measurements and the observations using other pairs' data should be scaled to the AD pair before release. Our analysis indicates

that the difference between quasi-simultaneous measurements using AD and CD pairs is related to the level of stray light inside each Dobson instrument. Higher levels of stray light lead to larger differences between the values deduced from AD and CD wavelengths.

Both Brewer and Dobson retrievals assume a fixed height for the ozone layer to calculate the ozone air mass. A fixed height of 22 km is used by the Brewer network for all sites while a variable ozone layer height changing with latitude is employed by the Dobson community. The assumption of a 22 km height for the ozone layer at the South Pole, compared to the 17 km height used in the Dobson analysis, leads to a 2.2% difference in ozone column at an air mass of 5.4.

Comparisons with total ozone data from a double Mark III Brewer spectrophotometer located at the South Pole indicate some dependence on OSP for the Dobson measurements. For the OSPs below 800 DU the AD vales are generally 1% high. However, for OSPs larger than 800 DU the Dobson AD measurements are low by up to 4% at 1400 DU OPS.

The observations made at the CD wavelengths also show some dependence on OSP. Compared to Brewer data, the CD values are, on average, 4% higher for almost the entire range of measurements. However, as is the case for the AD pair, the CD pair values also decrease at larger OSPs. It should be noted that the Dobson AD and CD pair measurements are not reported for air mass factors above 2.5 and 3.5 respectively due to the effect of stray light.

4. Improvements to the ACE-MAESTRO Measurements

The MAESTRO (Measurement of Aerosol Extinction in the Stratosphere and Troposphere Retrieved by Occultation) instrument is a UV-Visible-NIR moderate-resolution spectrometer on-board the Canadian satellite SCISAT as part of the Atmospheric Chemistry Experiment (ACE) mission flying along with a Fourier Transform Spectrometer (the ACE-FTS) since August 2003. It collects solar occultation spectra in the visible and near infrared regions of the solar spectrum from 400-1010 nm with resolution of approximately 2 nm. MAESTRO is able to measure the strong absorption features of the oxygen molecule in the *A*- and *B*-bands at 762 nm and 690 nm, respectively, which are used to derive atmospheric temperature and pressure profiles. The retrieval algorithm is based on a global fit that simultaneously fits all spectra from a single occultation to determine a density profile, which is then used to determine pressure and temperature. The forward model uses a fast line-by-line calculation and correlated-k technique to accurately model atmospheric absorption and the nonlinear saturation effects in the occultation geometry. The O_2 spectroscopic parameters

formerly used in forward model were from HITRAN 2004 (high-resolution transmission molecular absorption database; 2004 release). Line data for the O_2 *A*- and *B*-band spectral features have been significantly improved in the most recent update of HITRAN (2012). This research discusses the improvement of the retrievals with the new oxygen parameters. Temperature-pressure profiles derived using these new parameters are compared with previous profiles and the profiles retrieved from ACE-FTS (Fourier Transform Spectrometer) data. The new p-T retrievals could be used to derive accurate pointing information for MAESTRO which has the potential improvement for MAESTRO profiles of ozone and other constituents.

A manuscript on this study is completed and will be soon submitted to Journal of "*Atmospheric Measurements and Techniques*".

4.1. Introduction

MAESTRO is part of the Atmospheric Chemistry Experiment (ACE) mission. It was launched on the Canadian satellite, SCISAT, on August 12, 2003. MAESTRO measures a wide range of solar spectra in Occultation mode from 400 nm in UV region up to 1000 nm in the visible with a spectral resolution between 1.5 and 2.5 nm. Three bands of molecular oxygen appear in the MAESTRO visible and near-infrared spectra: the strong *A*-band centred at 762 nm, the weaker *B*-band at 690 nm, and the much weaker γ-band at 630 nm. The MAESTRO retrieval is able to determine the pressure and temperature profiles by using the measurement of the O_2 *A*- and *B*- bands as the mixing ratio of the oxygen molecule is known and constant in the troposphere and stratosphere.

The primary goal of MAESTRO instrument in the ACE mission is the measurement of ozone, NO_2 and aerosol extinction. However, the simultaneous measurement of pressure and temperature, along with trace constituents, is highly desirable because it guarantees accurate altitude assignment for measurements through the entire measurement altitude range with a consistent instrument field of view (FOV). Pressure and temperature profiles are also essential for use in the retrieval of trace gases with temperature-dependent cross sections, accurately calculating Rayleigh scattering and ray tracing, which are both dependent on the atmospheric density profile. Air density data are also used in determining mixing ratios from retrieved number density profiles of constituents. Moreover, MAESTRO's high-vertical-resolution temperature profiles could be used as an independent data product for stratospheric temperature trend analysis, or in polar stratospheric cloud studies.

The molecular oxygen constant vertical mixing ratio in combination with the O_2 *A*-band feature has been used by various space-based missions for remote sounding of the atmosphere. The O_2 *A*-band mostly is used for deriving a column air mass for determining cloud top heights, pressure and surface pressure or to provide a reference air mass [*Crisp et al.*, 2008; *Wang et al.*, 2008]. The Orbiting Carbon Observatory (OCO) mission also uses the *A*-band to determine O_2 columns for improving the accuracy of CO_2 mixing ratio retrievals [*Crisp et al.*, 2008]. Using the *A*-band for p-T retrievals has been attempted by the Improved Limb Atmospheric Sounder (ILAS) [*Sugita et al.*, 2001], ILAS-II [*Sugita et al.*, 2004] and the Stratospheric Aerosol and Gas Experiment (SAGE) III [*Pitts* and *Thomason*, 2003] but none of their sensors cover the *B*-band.

Daniel et al. [2003] showed that adding the *B*-band and the O_2-O_2 feature near 477 nm to the calculation of cloud parameters from *A*-band measurements could improve the

retrieval uncertainties by as much as 50%. It also could be used for measuring chlorophyll emission [*Gordon et al.*, 2011], which can contribute to biases in O_2 *A*-band measurements over growing vegetation [*Frankenberg et al.*, 2011]. *Kuze* and *Chance* [1994] and *Yang et al.* [2013] also showed the potential of *B*-band measurements for deriving cloud-top pressure. The SCanning Imaging Absorption spectrometer for atMospheric CHartographY (SCIAMACHY) has used the *B*-band for tangent height corrections [*Meyer et al.*, 2005].

MAESTRO, appears to be the only occultation sensor that measures both the O_2 *A*- and *B*-bands (with the exception of occasional occultation observation by SCIAMACHY). An analysis using the simulated data demonstrated the capability of MAESTRO measurements to retrieve p-T profiles [*Nowlan et al.*, 2007]. It showed that pressures should be able to be retrieved to within 1% and temperatures to within 2 K over most altitudes. Spectroscopic parameters used in the forward model were one of the sources of uncertainty. HITRAN-2004 database formerly was used as a source for spectroscopic parameters for the retrieval forward model. The *B*-band parameters contained in HITRAN-2004 were not well-quantified. Also, there was limited information provided for uncertainty estimates. Even the *A*-band parameters provided in HITRAN-2004 were not characterized sufficiently [*Tran et al.*, 2006; *Yang et al.*, 2005]. Improvements of the spectroscopic parameters can result in an improvement of the MAESTRO p-T retrievals.

MAESTRO trace gas retrievals currently rely on the pointing information derived by ACE-FTS software from p-T profiles as pointing information provided by the SCISAT satellite is not reliable. A poor FTS tangent altitude retrieval results in a poor MAESTRO retrieval. An accurate MAESTRO p-T retrieval can also be used to derive more accurate pointing information for MAESTRO provided the profiles are temporally linked to the

MAESTRO trace gas observations. This may make the MAESTRO retrievals completely independent of those of FTS.

The eventual goal is that the retrieval algorithm developed for p-T profiles will be used operationally to retrieve a p-T profile and provide tangent altitude information for the retrieval of profiles of other constituents during each occultation. Reliable tangent height profile derived from an accurate p-T profile would improve the retrieval of ozone, NO_2, aerosol and other constituent profiles which have absorption features within the MAESTRO spectral range.

O_2 band spectral features have been significantly improved in the recent update of HITRAN (2012) [*Gordon et al.*, 2011; *Havey et al.*, 2009; *Long et al.*, 2010; *Robichaud et al.*, 2008]. In this study the impact of different HITRAN database on MAESTRO p-T profiles retrieved using data acquired by the satellite instrument on-orbit are discussed. Comparisons of profiles with the ACE-FTS satellite data are also presented.

4.2. Occultation measurements

Solar occultation is the primary mode of the ACE-MAESTRO measurement. In the solar occultation technique the transmission of sunlight after passing tangentially through the Earth's atmosphere is measured by the instrument. Figure 4.1 shows a schematic of a sunrise solar occultation measurement. The spectra collected during an occultation contain the spectral features of atmospheric constituents along the solar ray's path. The measurements are carried out at a series of tangent heights (closest distance between the ray and the Earth's surface), increasing in altitude during a sunrise and decreasing in altitude during a sunset.

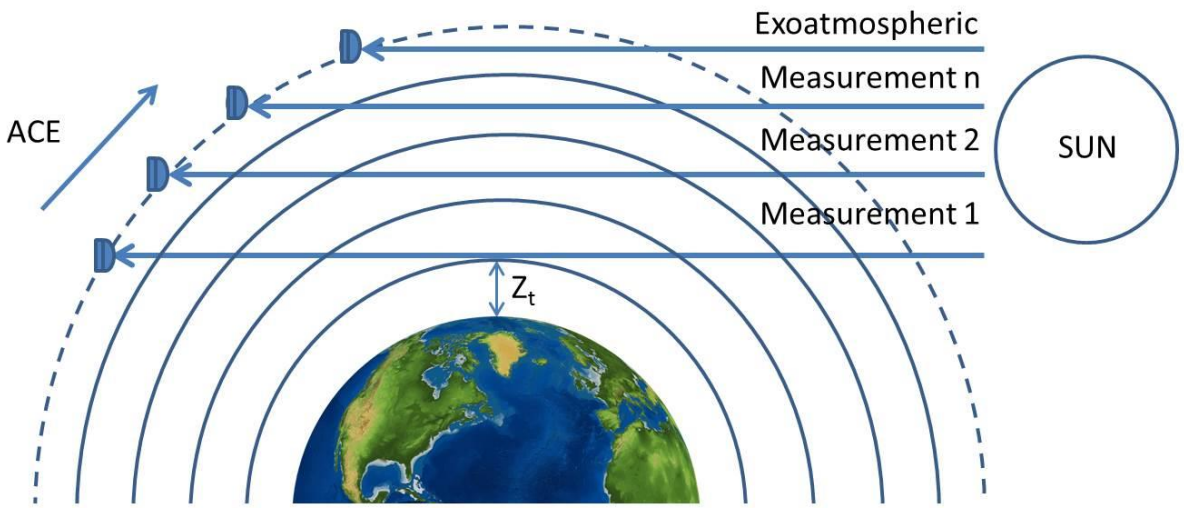

Figure 4.1: Schematic of a sunrise solar occultation measurement

The MAESTRO instrument collects approximately 60 spectra at different tangent heights ranging between 0 and 100 km during each measurement sequence. The exoatmospheric measurements (recorded where no atmospheric features are present) are also included in each occultation sequence. These measurements are used to create a solar reference spectrum which allows the occultation instrument to be self-calibrating. In occultation measurements, the instrument sensitivity changes and solar cycle variations over time are canceled out as the spectra collected at different tangent heights are ratioed to the solar reference measurements to determine optical depth spectra. Atmospheric profiles can be retrieved with high vertical resolution thanks to the occultation geometry as spectra are heavily weighted to the tangent layer. Poor horizontal resolution and lack of global coverage across latitude are the main disadvantages of occultation measurements. Fifteen sunrises and fifteen sunsets per day occur for SCISAT with its 650-km altitude and 74^{o}-inclination circular orbit. The latitudinal coverage for SCISAT occultations during one year is shown in Figure 4.2.

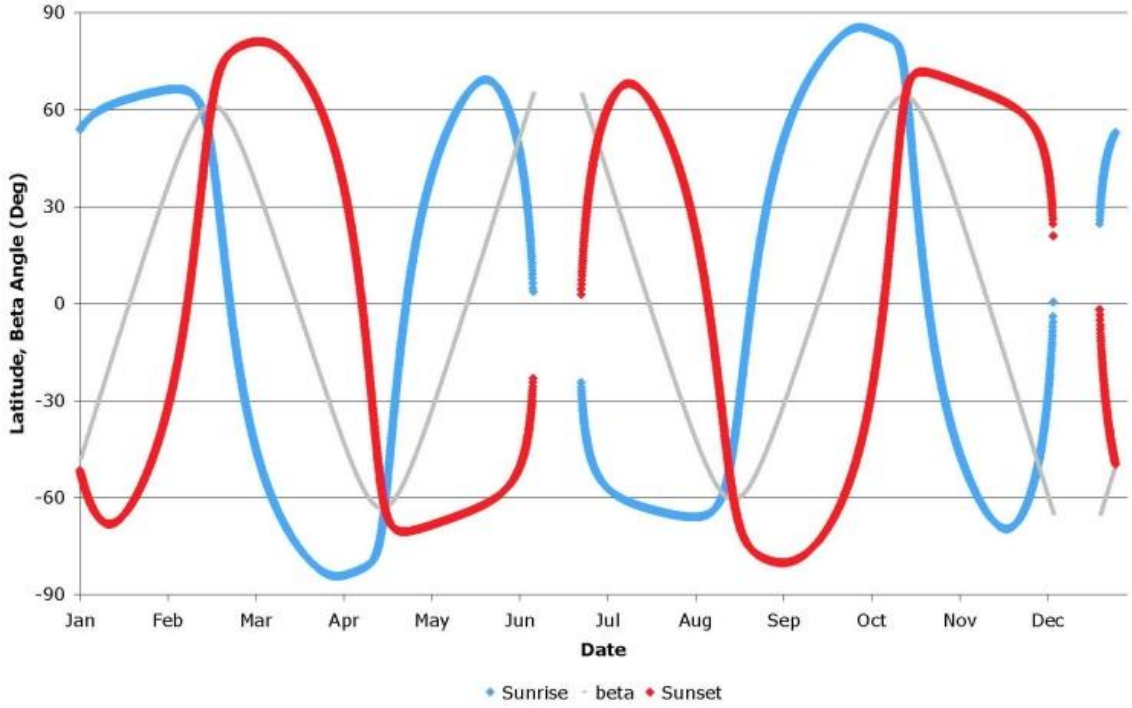

Figure 4.2: SCISAT latitude coverage during a year. (From ACE mission website http://www.ace.uwaterloo.ca/mission_orbit.php)

The Earth-Sun satellite geometry at the time of the measurements determines the location of a sunset or sunrise. The orbital parameters have been optimized to ensure that SCISAT's measurements occur in the respective spring seasons of both the Arctic and Antarctic when maximum ozone destruction takes place.

4.3. MAESTRO instrument description

The MAESTRO instrument comprises two independent spectrometers measuring (1) UV and Visible spectra from 280 to 525 nm (UV) with a resolution of approximately 1 nm

and (2) Visible and Near-Infrared spectra from 525 to 1010 nm (Vis) with spectral resolution of about 2 nm. Figure 4.3 shows a schematic of the MAESTRO optical design.

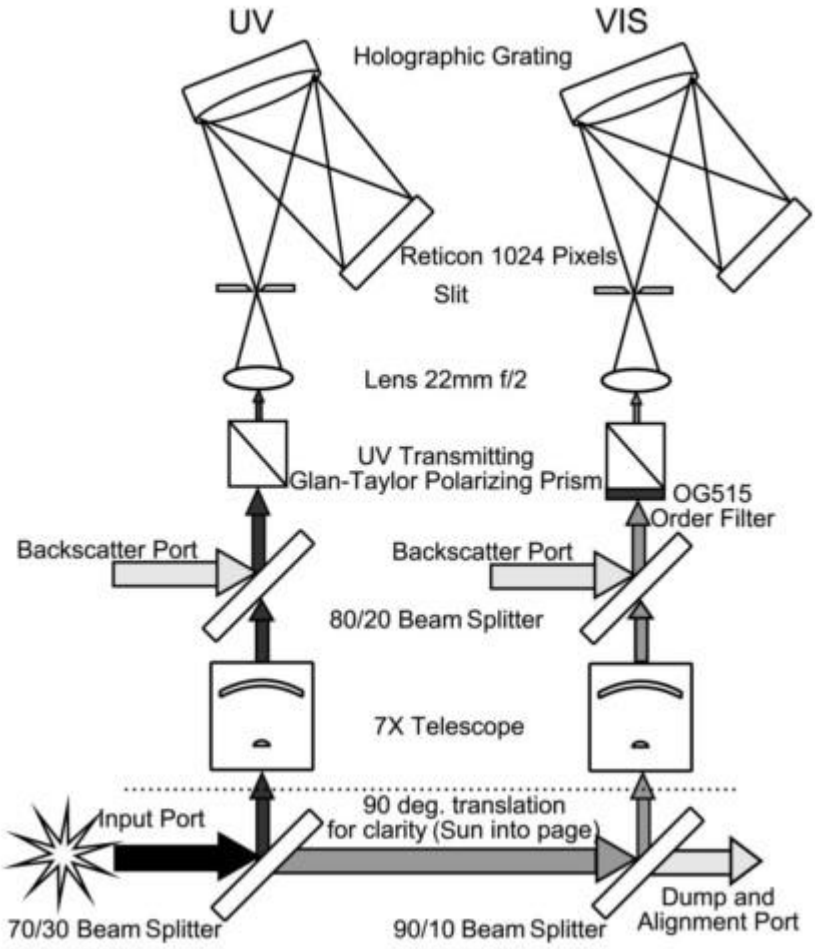

Figure 4.3: Schematic of the MAESTRO optical design (From *McElroy et al.* [2007]).

Each spectrometer consists of a lens, slit, concave holographic diffraction grating, and 1024 pixel Reticon photodiode array detector. During measurements, the MAESTRO instrument receives the solar light through the input port. Then the light passes the input fore-optics until it reaches to the two independent spectrometers contained within the full instrument. Light is then focused onto a slit using each lens. The holographic grating then diffracts and focuses the light onto the photodiode array where the intensity of solar radiation

is detected by the array of 1024 individual detector pixels at various wavelengths [*McElroy et al.*, 2007]. The main characteristics of MAESTRO are summarized in Table 4.1.

Table 4.1: Main characteristics of the MAESTRO (From *McElroy et al.* [2007])

	Spectrometer	
	UV	VIS
Nominal wavelength range	285–565 nm	515–1015 nm
Calibrated wavelength range in occultation	400–545 nm (pixels 463–954)	520–1010 nm (pixels 21–1010)
Spectral resolution	~1.5 nm	~2 nm
Pixel spacing	~0.3 nm	~0.5 nm
Main sources of extinction	O_3, NO_2, aerosol and molecular scattering	O_3, O_2, O_2–O_2, H_2O, aerosol and molecular scattering
Secondary sources of extinction	SO_2, OClO, BrO	NO_2
SCISAT orbit	circular, 650 km altitude, 74° inclination	
Instrument FOV	~1.2 km (elevation) × 25 km (azimuth) (at 22 km tangent)	
Observation modes	Solar occultation	
	Nadir backscatter	
Detectors	1024 pixel, Reticon photodiode array	
Gratings	Concave holographic, 94 mm focal length	
Signal to noise	~1000–3000 (high Sun)	

The spectral range of MAESTRO's spectrometers covers the absorption features of a number of atmospheric constituents. Table 4.2 presents the species that can be measured by MAESTRO and their expected accuracies.

Table 4.2: Data products of MAESTRO [*McElroy et al.*, 2007].

Product	Altitude (km)	Accuracy
O_3	50 - 80	10%
	20 - 50	3%
	10 - 20	10%
	8 - 10	15%
NO_2	40 - 50	15%
	20 - 40	10%
	10 - 20	15%
	8 - 10	25%
Aerosol Extinction	10 - 50	10−3 O.D.
	8 - 10	0.01 O.D.
Aerosol Wavelength Dependence	15 - 30	0.005 O.D. per 100 nm
Water Vapour	8 - 20	100 ppm

4.4. MAESTRO O_2 measurements

Three strong bands of oxygen appear in the Vis spectrometer observations made by MAESTRO. Figure 4.4 shows the optical depth spectra for several sample tangent heights derived from a sunset MAESTRO occultation measurement. The position of O_2 absorption features are also demonstrated in the MAESTRO spectra. The strong *A*-band of oxygen centered at 762 nm and lies in a region where other species absorb and scatter weakly. The slightly weaker *B*-band is centered at 690 nm and is more affected by ozone - the Chappius-band - and also more influenced by Rayleigh and Aerosol scattering than the *A*-band. The much weaker γ-band is centered at 630 nm and lies in a region with strong scattering and absorption by ozone. Preliminary assessment of MAESTRO spectra shows that it is difficult to distinguish this band from instrument noise especially when much of the signal is removed by Rayleigh scattering at low tangent heights. Therefore, it is not being used in the pressure-Temperature retrieval.

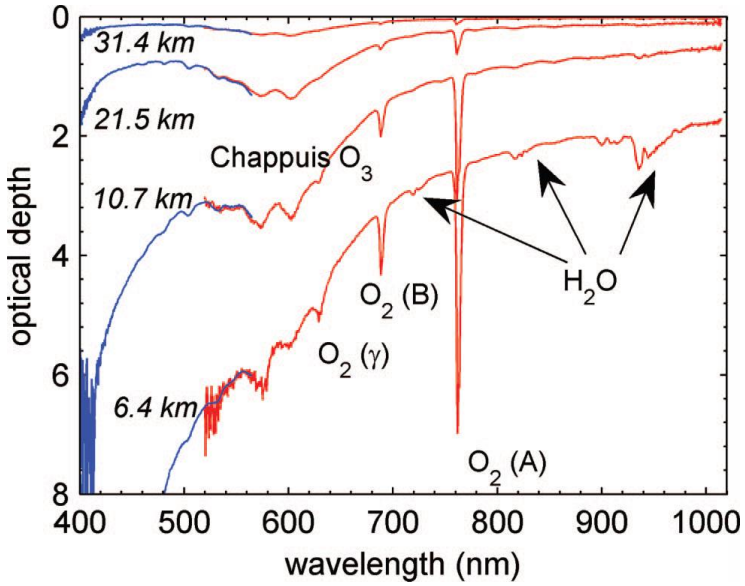

Figure 4.4: MAESTRO Optical depth spectra for several sample tangent heights from occultation ss4043 [***McElroy et al.*, 2007**].

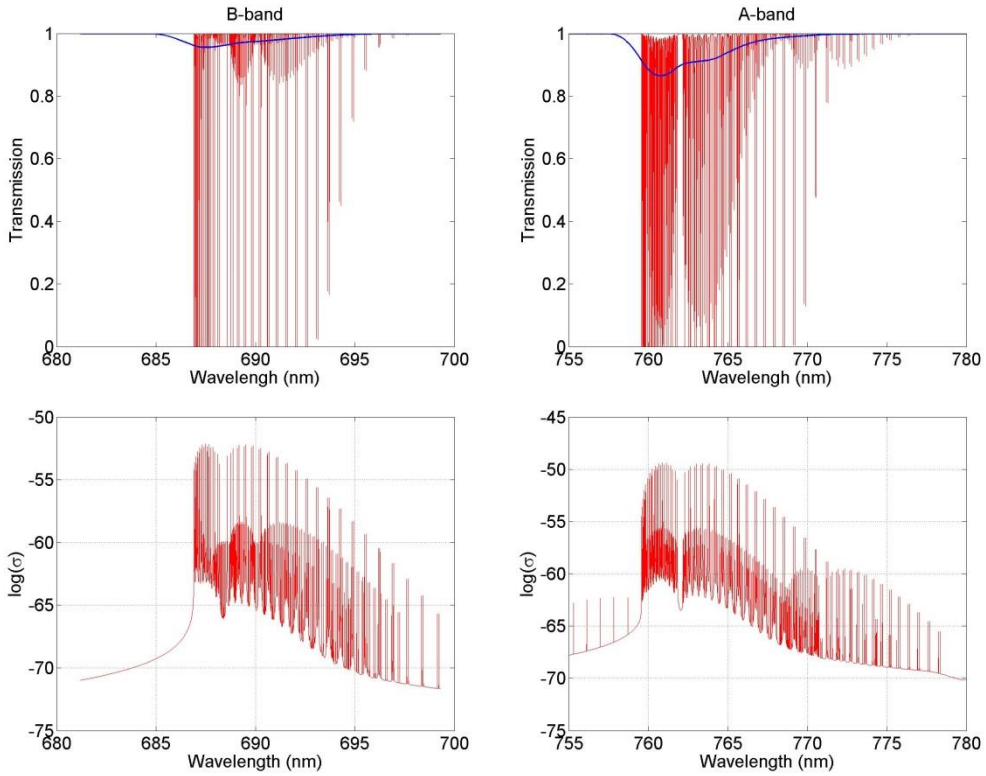

Figure 4.5: (top) transmission calculated for O_2-only through the atmosphere for the A- and B-bands, at tangent height of 30 km; high spectral resolution (red) and 2-nm MAESTRO spectral resolution (blue). (bottom) High-resolution cross-sections of O_2 A- and B-band for a typical pressure (12 hPa) and temperature (226 K) at an altitude of 30km.

Figure 4.5 shows high-resolution O_2 A- and B-band cross-sections for a typical temperature and pressure at 30 km altitude as well as simulated O_2 measurements for a tangent height of 30 km for a high-spectral-resolution calculation and for the MAESTRO 2-nm resolution. Even at this altitude many absorption lines of the most abundant O_2 isotope have saturated, and thus the contributions of relatively weak branches of the less abundant O_2 isotopes become important. Although each O_2 band has hundreds of lines at high spectral resolution, MAESTRO's low-resolution VIS spectrometer detects only one broad feature for each band.

4.5. Pressure and temperature retrieval method

The p-T retrieval, developed by *Caroline Nowlan* [2006] for MAESTRO, closely follows the method of [*Rodgers*, 2000]. Here only a brief description of the method is presented following the notation of *Rodgers* [2000] and *Nowlan* [2006].

The remote sounding of atmosphere pressure and temperature vertical profiles involves the measurement of a well-mixed gas with a known mixing ratio as a function of altitude. CO_2 is commonly used for this purpose by Infrared sounders but the oxygen molecule is the only well-mixed gas that has absorption features that appear in MAESTRO spectra. The O_2 mixing ratio is 0.20974 and constant through the atmosphere up to about 85 km. It is possible to derive the profile of the O_2 number density in the atmosphere using the two strong absorption bands of oxygen (*A*- and *B*-bands) which appear in the MAESTRO spectra.

The MAESTRO p-T retrieval uses an inverse method to estimate the profile of the O_2 number density for each occultation from remote measurements of the radiation transmitted through the atmosphere as a function of wavelength in the spectral regions of the oxygen bands. The inversion algorithm fits the measured optical depths, derived from the measurements of the differential absorption between an exoatmospheric solar reference and occultation spectra at different tangent altitudes, to modeled optical depths, generated by a forward model that includes the atmosphere radiative transfer and instrument effects on the signal, to retrieve the oxygen number density profile. Then, using the known O_2 mixing ratio, the total air density ρ is derived as a function of altitude, z, from the retrieved profile of the oxygen density. The pressure can be calculated from the hydrostatic equation:

$$\boldsymbol{dp = -g(z)\rho(z)dz} \quad \textbf{(4.1)}$$

where g is the acceleration of gravity. And using the ideal gas law a temperature, T , for a gas can be derived from the known pressure and density as:

$$\boldsymbol{T(z) = \frac{M_r p(z)}{R\rho(z)}} \quad \textbf{(4.2)}$$

where M_r is the molecular weight and R is the gas constant per mole.

4.5.1. Retrieval algorithm

In atmospheric research the Optimal Estimation Method as developed by *Rodgers* [2000] is commonly used for retrievals to derive the atmospheric state from measured absorption spectra. Consider the atmospheric state or the quantities to be retrieved as a sate vector $\boldsymbol{x}$ with n elements, $x_1, x_2, \ldots, x_n$. The atmospheric measurements can be stored in a vector $\boldsymbol{y}$ consists of m elements with measurement errors $\varepsilon_1, \varepsilon_2, \ldots, \varepsilon_m$. Following expression relates the measurement vector $\boldsymbol{y}$ to the state vector $\boldsymbol{x}$:

$$\boldsymbol{y = F(x, b) + \varepsilon} \quad \textbf{(4.3)}$$

where the forward model $F(x,b)$ encapsulates our understanding of the physics of the measurements and the b vector contains the model parameters which are those parameters that impact the retrieval but are not included in the state vector (e.g. the radiative transfer parameters and instrument characteristics).

The desired value here is the state vector. Assuming the forward model is invertible, the best estimate of the state vector, $\boldsymbol{x}$, would be the retrieved vector, $\hat{\boldsymbol{x}}$, as:

$$\boldsymbol{\hat{x} = R(y, \hat{b}, x_a, c)} \quad \textbf{(4.4)}$$

R is the transfer function which maps the values from measurement to state. $\hat{b}$ contains the best estimate of the forward model parameters, x_a is a vector containing *a priori* estimate of the atmospheric state, and $\boldsymbol{c}$ includes retrieval method parameters which are any parameters that may influence the retrieval but are not included in the forward model, such as convergence criteria.

This is an inverse problem and the MAESTRO retrieval uses an iterative linearized χ^2 minimization to minimize a cost function that represents the squared difference between the observation $\boldsymbol{y}$ weighted by covariance matrix S_ϵ (derived from error vector ϵ) and the forward model *F(x)*, as expressed by:

$$\boldsymbol{\chi_m^2 = [y - F(x)]^T S_\epsilon^{-1} [y - F(x)]} \quad \textbf{(4.5)}$$

To simplify the problem, at each iteration *i* the forward model is linearized using Taylor series expansion about current guess x_i as:

$$\boldsymbol{y - F(x_i) = \frac{\partial F(x)}{\partial x}(x - x_i) + \epsilon = K(x - x_i) + \epsilon} \quad \textbf{(4.6)}$$

where *K* is weighting function (Jacobian Matrix) and its elements are $\boldsymbol{K_{ij} = \frac{\partial F_i(x)}{\partial x_j}}$.

In addition, the retrieval constrains the solution vector to *a priori* knowledge of the state (e.g. a forecast or external measurements) by minimizing the expression

$$\boldsymbol{\chi_a^2 = [x - x_a]^T S_a^{-1} [x - x_a]} \quad \textbf{(4.7)}$$

simultaneously with other constraints where x_a and S_a contains the best estimate of the state vector and its uncertainties respectively before the measurements are conducted.

In order to suppress any unphysical oscillation resulting from the noise during the measurements the retrieval employs a second order *Tikhonov* [1966] smoothing constraint

which minimizes the displacement of a retrieved value x_z relative to its two neighbors $(x_{z-1} - 2x_z + x_{z+1})$ by the expression

$$\boldsymbol{\chi_s^2 = \Sigma(Lx)^2} \tag{4.8}$$

where L is the second-derivative operator

$$\boldsymbol{L} = \begin{pmatrix} \mathbf{1} & \mathbf{-2} & \mathbf{1} & \mathbf{0} & \dots & \dots & \mathbf{0} \\ \mathbf{0} & \mathbf{1} & \mathbf{-2} & \mathbf{1} & \dots & \dots & \mathbf{0} \\ \mathbf{0} & & \dots & \dots & & & \mathbf{0} \\ \mathbf{0} & & \dots & \dots & & & \mathbf{0} \\ \mathbf{0} & & \dots & \dots & & & \mathbf{0} \\ \mathbf{0} & \dots & \dots & \mathbf{0} & \mathbf{1} & \mathbf{-2} & \mathbf{1} \end{pmatrix} \tag{4.9}$$

if x is defined on an evenly spaced grid. Thus, the cost function including the difference between measurements and the forward model, the *a priori* knowledge, and the smoothing constraint is expressed as:

$$\begin{aligned} \boldsymbol{J_{i+1}} &= \boldsymbol{\chi_m^2 + \chi_a^2 + \gamma_{i+1}\chi_s^2} \\ &= [y - F(x)]^T S_\epsilon^{-1}[y - F(x)] + [x - x_a]^T S_a^{-1}[x - x_a] + \gamma\, \Sigma(Lx_x)^2 \end{aligned} \tag{4.10}$$

To minimize the cost function, the derivative of J with respect to the retrieved parameter vector x should be set to zero ($\frac{\partial J}{\partial x} = 0$) after linearizing about the current guess x_i using equation (4.6). The retrieval attempts to minimize the cost function. At each iteration, *i+1* , the new state is defined as:

$$\boldsymbol{x_{i+1}} = \boldsymbol{x_i} + (\boldsymbol{K_i^T S_\epsilon^{-1} K_i + S_a^{-1} + \gamma H})^{-1}[\boldsymbol{K_i^T S_\epsilon^{-1}}\big(\boldsymbol{y - F(x_i)}\big) - \boldsymbol{S_a^{-1}}(\boldsymbol{x_i - x_a}) - \boldsymbol{\gamma H x_i}] \tag{4.11}$$

where $H = L^T L$ (the partial differentiation of smoothing term) and γ represents the strength of smoothing term and is optimally determined by the L-curve [*Hansen*, 1992] technique. The

iteration continues until a specified convergence criterion, as defined by Rodgers for minimization of the state's cost function is reached.

Furthermore, the gain matrix which represents the sensitivity of the retrieved state to a change in the measurements is expressed as:

$$\boldsymbol{G_y = \frac{\partial \hat{x}}{\partial y} = (K^T S_\epsilon^{-1} K + S_a^{-1} + \gamma H)^{-1} K^T S_\epsilon^{-1}} \quad \textbf{(4.12)}$$

and the sensitivity of the retrieved state to the true state at each layer (Averaging kernel matrix) is defined as:

$$\boldsymbol{A = G_y K = \frac{\partial \hat{x}}{\partial x}} \quad \textbf{(4.13)}$$

The trace of the averaging kernel represents the degrees of freedom of the retrieval:

$$\boldsymbol{d_r = tr(A)} \quad \textbf{(4.14)}$$

The MAESTRO retrieval simultaneously fits all spectra from one occultation to determine the state parameters. The measured optical depths are stored in the *y* vector and *F(x)* represents the modeled optical depths. The optical depth measurement noise errors are used to construct the error covariance matrix S_ϵ. It is assumed that the measurement error is uncorrelated between the MAESTRO detector pixels. Thus, the error covariance matrix contains the optical depth measurement errors on its diagonal and zeros elsewhere. The retrievals are performed for 55 pixels between 753 and 781 nm for the O_2 *A*-band and for 34 pixels between 682 and 699 nm for *B*-band [*Nowlan*, 2006]. The background ozone is pre-retrieved using the Chappuis band between 530 nm and 680 nm with cross-sections from *Bogumil et al.* [2003]. The retrieved air density is used to remodel the Rayleigh scattering for each iteration. The magnitude of the background aerosol extinction is estimated by retrieving

the offset and linear terms simultaneously with the O_2 number densities. A wavelength shift is retrieved for each spectrum in order to optimize the pixel-wavelength assignment at every iteration.

The compiled profiles from meteorological analyses at the ACE Science Operations Centre [*Boone et al.*, 2005] are used as O_2 first-guess and *a priori* profiles. The Global Environmental Multiscale (GEM) model of the Canadian Meteorological Centre (CMC) is used to produce the data from the surface to 10 hPa (about 30 km) on 28 vertical levels. These analyses then are interpolated to the ACE 30 km sub-tangent location in time and space. A data assimilation scheme is used to produce these *a priori* profiles 12 to 18 hours after the reference time using the data from a model, the radiosonde network, and operational nadir temperature sounders. The US Naval Research Laboratory, Mass Spectrometer Incoherent Scatter Radar Extended Model (NRL-MSISE-00) [*Picone et al.*, 2002] provides the data from below the stratopause to the top of the atmosphere. For the middle stratosphere, which is not covered by the models, the temperature is derived by linear interpolation of the temperature as function of natural logarithm of pressure (*ln p*).

The uncertainties in the ACE *a priori* profiles are not quantified above 30 km. As a result, the elements of the a priori covariance matrix, S_a, which represent uncertainties in retrieval layers are set to very small values for the levels below the lowest tangent height and very large values for the levels above. In this way, the retrieved profile is independent of the *a priori* at higher altitudes while below the lowest tangent height it is strongly constrained by the *a priori*.

4.5.2. Forward model

To determine the solar ray refraction and absorption a spherical-shell atmosphere with a 100-m-spaced grid is used by the MAESTRO forward model. Assuming the intensity of the incoming solar light as $I(\lambda, \theta)$ the modeled signal is expressed as:

$$\boldsymbol{S(\lambda_p, \theta_t) = R(\lambda_p) A \int_{\theta} \int_{\lambda} I(\lambda, \theta) G(\theta - \theta_t) F(\lambda - \lambda_p) d\lambda d\theta} \quad \textbf{(4.15)}$$

where λ_p is the wavelength at pixel *p* of the detector and $R(\lambda_p)$ is the responsivity of the detector. The slit area is described with A and $F(\lambda - \lambda_p)$ represents the instrument slit function at pixel *p*. Any incoming ray is weighted by the instrument FOV (Field Of View) before reaching to the detector. In the case of MAESTRO the azimuthal angle could be ignored as the MAESTRO slit views the entire solar disk in the azimuthal direction. Thus the instrument FOV weighting about elevation angle $\theta_t$can be expressed as $G(\theta - \theta_t)$.

Using the Beer-Lambert law and ignoring the source terms because of occultation geometry and smallness of the MAESTRO's FOV, the intensity of radiation incident on the instrument can be expressed as:

$$\boldsymbol{I(\lambda, \theta) = I_0(\lambda, \theta) \exp(-\tau(\lambda, \theta))} \quad \textbf{(4.16)}$$

where $I_0(\lambda, \theta)$ is the exoatmospheric spectrum and $\tau(\lambda, \theta)$represents the total optical depth of one ray. Following expression is used to calculate the total optical depth:

$$\boldsymbol{\tau(\lambda, \theta) = \sum_{c=1}^{N_c} \sum_{h=1}^{N_h} \sigma_{ch}(\lambda) N_{ch} L_h(\theta)} \quad \textbf{(4.17)}$$

This equation represents the sum of the optical depths of N_c absorbers and scatters along N_h shells. $\sigma_{ch}(\lambda)$ and N_{ch}**,** are the cross-sections and number density of a constituent *c* and $L_h(\theta)$ is a path length determined by the ray path.

An accurate forward model *F(x)* is required to perform the MAESTRO retrieval and calculate the O_2 number density profiles. O_2 bands are not broad absorbers in spectral space and have well-fined structures. Many of the absorption lines saturate during a typical occultation measurement in the O_2 bands which causes a nonlinear problem. As the MAESTRO instrument has low spectral resolution it is important to model the band at high resolution over its entirety in order to account for the saturation. It can be done best using a Line-by-Line (LBL) calculation. For this study the GENSPECT Matlab toolbox developed at University of Toronto [*Quine* and *Drummond*, 2002] is used for LBL calculations.

O_2 spectroscopic parameters

HITRAN (High Resolution TRANsmission molecular absorption database) is the standard reference for atmospheric molecular line parameters. It contains the spectral parameters including the line strength, and position, air- and self-broadened half-width, and temperature dependence for over one million spectral lines of atmospheric constituents. The parameters in the HITRAN database are calculated using theory and laboratory measurements. The O_2 spectroscopic parameters formerly used by the MAESTRO forward model were from HITRAN 2004. The *B*-band parameters contained in HITRAN 2004 were collected over forty years ago with limited information on uncertainty estimates [*Rothman et al.*, 2005]. Even the *A*-band parameters were not sufficiently characterized in HITRAN 2004 [*Tran et al.*, 2006; *Yang et al.*, 2005]. The O_2 parameters have been upgraded in the recent update of the HITRAN database: 2012 [*Rothman et al.*, 2013]. Recent studies have made significant progress in characterizing the O_2 band parameters [*Gordon et al.*, 2011; *Havey et al.*, 2009; *Long et al.*, 2011; *Robichaud et al.*, 2008] and all the results have been used for

improvements to HITRAN. The details of the recent changes, compared to previous versions of HITRAN, have been discussed in *Rothman et al.* [2013]. Figure 4.6 shows the transition calculated for O_2 only through the atmosphere for the *A*- and *B*-bands at tangent height of 30 km using HITRAN 2004 and 2012 databases. Significant differences in some lines can be seen for both bands for this sample tangent height. For this study the HITRAN 2004 has been replaced by HITRAN 2012 and the influence of this replacement on pressure and temperature profiles is discussed.

Fast Line-by-Line and correlated-k technique

The spectral absorption features of each molecule result from transitions between the molecules' quantized energy levels. The absorption bands of oxygen molecule in the red and infrared spectral regions result from a transition between vibrational levels of the ground electronic state and the second excited state. The transition between the very closely-spaced rotational levels results in the fine internal structure of each band. The absorption structures of oxygen bands are also highly dependent on the temperature and pressure.

The spacing between the energy levels defines the wavelengths of the absorption lines. However, these lines are broadened as a result of different processes such as natural broadening (upper and lower state finite lifetimes), pressure broadening (caused by collisions between molecules), and Doppler broadening (resulting from the distribution of velocities of the molecules) [*Liou*, 2002].

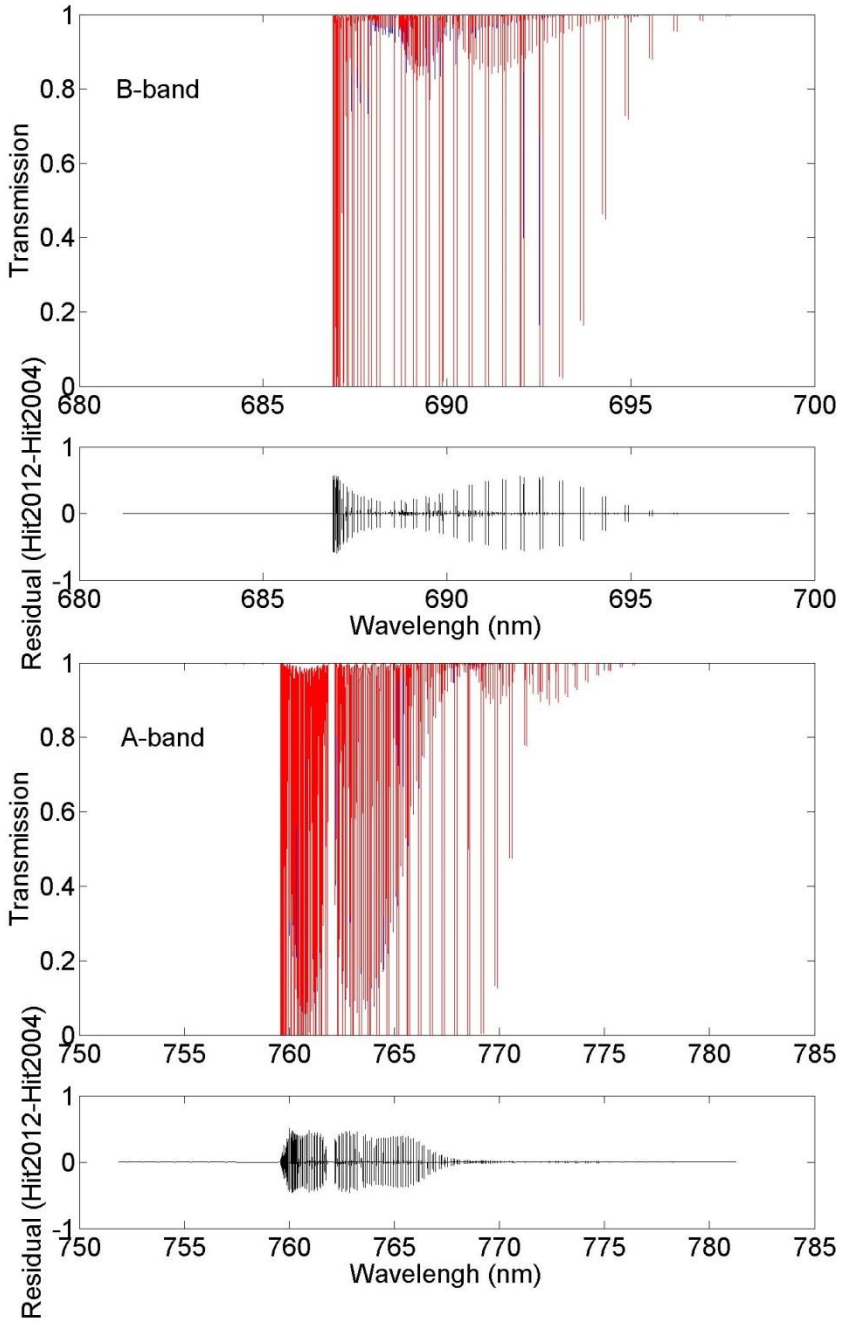

Figure 4.6: The transition calculated for O_2-only through the atmosphere for the A- and B-bands, at tangent height of 30 km using HITRAN 2012 (red) and HITRAN 2004 (blue) databases.

During a LBL calculation the high-resolution cross-sections are computed for particular pressures and temperatures using spectral parameters provided by the HITRAN database. A LBL calculation can be very time-consuming if a pure LBL model is used at every iteration of the retrieval, since a new set of cross-sections must be computed for the current guess of pressure and temperature, which then must be convolved with the 2-nm instrument line shape. Even if the convolution is performed in Fourier space, recalculation for 60 spectra for each column of the matrix *K* can be significant.

In order to improve the speed of computation, the MAESTRO retrieval uses a fast-line-by-line method described by *Turner* [1995]. In this method a table of cross-sections for a range of pressure and temperature on a pre-defined wavenumber grid is computed using a LBL model. In the case of the MAESTRO retrieval, the GENSPECT Matlab toolbox [*Quine* and *Drummond,* 2002] developed at the University of Toronto is used to calculate the high-resolution cross-sections. The logarithm of the cross-sections ($log(\sigma)$) are stored in the table as a function of $log(p/p_0)$ and T/T_0 for each wavenumber. At every iteration of the retrieval, the new $log(\sigma)$ is calculated from a two-dimensional interpolation. Ten equally spaced temperatures between 180 and 320 K and 20 pressures between 0.001 and 1060 hPa are used to construct the MAESTRO FLBL table. For the research presented here, two tables were computed using HITRAN 2004 and 2012 O_2 spectroscopic parameters. The wavenumbers are set with 0.005 cm^{-1} resolution in order to resolve *A*- and *B*-band lines. The typical Doppler HWHM (half widths at half-maximum) for the O_2 band lines is 0.011 cm^{-1} at 180 K and 0.015 cm^{-1} for 320 K. Details on optimizing the resolution for the wavenumbers and the number of pressures and temperatures for the tables can be found in *Nowlan* [2006].

The other technique that is used by the MAESTO retrieval is the correlated-*k* approximation method. The absorption coefficient, *k*, is used in original method [*Goody et al.*, 1989; *Lacis* and *Oinas*, 1991]. But, for MAESTRO the absorption cross-section σ (units of cm^2 /molecule) is used instead of the absorption coefficient, following the convention of UV-Vis remote sounding. This method involves the grouping by the strength of absorption cross-sections within a wavelength interval which results in a "σ-distribution" of absorption cross-sections. Using this method the transmission over a spectral interval can be expressed as:

$$\boldsymbol{T_{\bar{\lambda}} = \frac{1}{\lambda_{max} - \lambda_{min}} \int_{\lambda_{min}}^{\lambda_{max}} \exp(-\sigma_{\lambda} u)\, d\lambda = \int_{0}^{1} \exp(-\sigma(g) u) dg} \qquad \textbf{(4.18)}$$

Where g represents the cumulative distribution function, and $u = \int N(z)dz$ is a slant column density integrated along a path of number density *N*. To calculate g, the σ values corresponding to equally-spaced λs are sorted in increasing order and assigned to a g grid between 0 and 1. The function $\sigma(g)$ is relatively smooth and can be integrated using far fewer points, *M*, than is required for line-by-line computation over high-resolution wavelength space:

$$\boldsymbol{T_{\bar{\lambda}}(u) \cong \sum_{j=1}^{M} \exp(-\sigma(g_j) u) \Delta g_j} \qquad \textbf{(4.19)}$$

This method increases the speed of computation by reducing the number of required radiative transfer calculations. Figure 4.7 shows the O_2 *B*-band cross-sections for the 2-nm wavelength interval between 690 and 692 nm altitudes of 0, 30, and 50 km using typical pressures and temperatures at these altitudes. The digitized cumulative distribution function, g, corresponds to these cross-sections is also shown in Figure 4.7.

The transmission through N_h inhomogeneous atmospheric shells can be calculated using this method as:

$$\boldsymbol{\sigma(g_j)u = \sum_{h=1}^{N_h} \sigma_h(g_j)u_h} \tag{4.20}$$

This is true under one assumption: that the cross-sections strength is correlated in wavelength space.

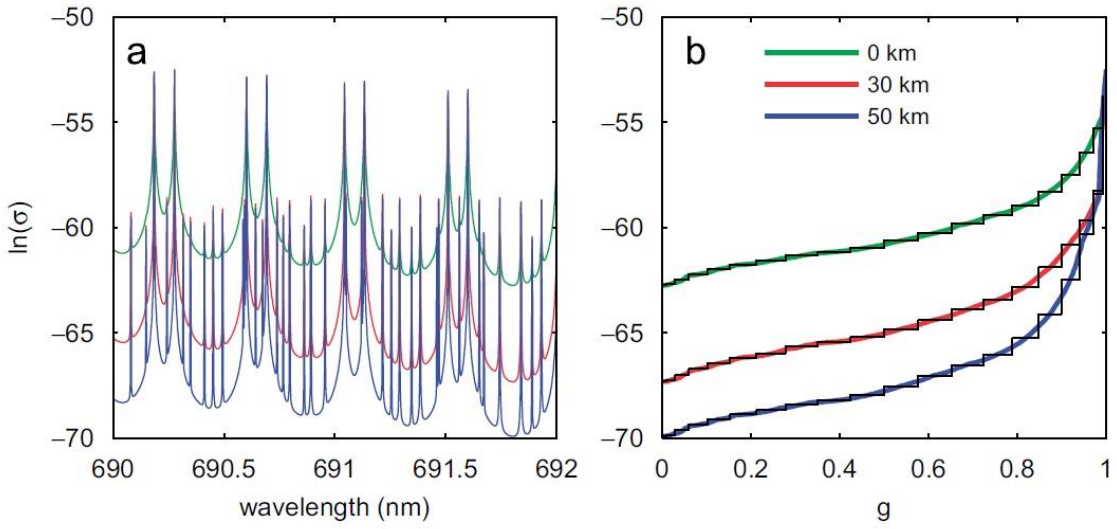

Figure 4.7: (a) O_2 B-band cross-sections between 690 and 692 nm for p = 1023 hPa, T = 288 K (0 km), p = 12 hPa, T = 226 K (30 km), and p = 0.8 hPa, T = 271 K (50 km). (b) The digitized g values over M = 20 points of their cumulative distribution functions (From *Nowlan et al.*, [2007]).

This means that the monotonic ordering by strength of absorption cross-sections remains the same at different altitudes in the atmosphere. *Goody et al.* [1989] and *Lacis* and *Oinas* [1991] have examined the validity of this assumption for weak and strong lines. A complete description of implementation of this method in the MAESTRO retrieval can be found in *Nowlan* [2006] and *Nowlan et al.* [2007].

4.6. Improvements to the retrieval performance

The MAESTRO p-T retrievals using the measurements of O_2 *A*- and *B*-bands were originally developed by *Caroline Nowlan* in Matlab and the details on the retrieval performance and error estimates can be found in *Nowlan* [2006]. The same code is used for this study to investigate the influence of the change to HITRAN 2012 O_2 spectroscopic parameters on the MAESTRO p-T profiles. In this section, sample MAESTRO p-T profiles retrieved using HITRAN 2004 and 2012 are compared with profiles from the ACE-FTS instrument.

4.6.1. MAESTRO data

The spectra used for this analysis are from Version 41.0 of the software SCALE, developed by C.T. McElroy at the Meteorological Service of Canada for correcting raw data from the MAESTRO spectrometers. As the MAESTRO O_2 p-T retrieval was developed in Matlab and it takes about 20 minutes to retrieve one profile, a subset of occultations is analyzed for this research due to time limitations. The surface latitude and longitude point of a 30 km tangent height measurement are used to reference the ACE occultations. Table 4.3 describes the occultations presented here in latitudinal and seasonal groups.

Table 4.3: Description of the Occultations used in this study

Region	Season	Start Date	End Date	Latitude Range	No. Occs.
Arctic	winter	Jan-05	Mar-05	65^o to 90^o N	42
Arctic	summer	Jul-04	Jul-04	65^o to 90^o N	12
Tropics	all	Jan-04	Dec-04	10^o S to 10^o N	18

The main focus of the ACE mission is the northern latitudes so the Arctic latitudes were chosen for the comparisons. A subset of data for tropical occultations between 10^o S and 10^o N was also analyzed to illustrate the contrast.

4.6.2. ACE-FTS data

Due to the problems with pointing information provided by the SCISAT satellite sensors, the current FTS CO_2 p-T retrievals are used to determine the satellite pointing as a function of time. As the ACE-FTS and MAESTRO share a common input beam the pointing information retrieved from FTS p-T retrievals are also used for MAESTRO apparent solar zenith angle determination for each spectrum. For the retrievals presented in this study the tangent heights derived with Version 3.5 of the FTS processing software are used.

The details of the FTS p-T retrievals and tangent altitude determination can be found in [*Boone et al.,* 2005, 2013]. In summary, to determine the temperature profile the FTS retrieval uses the high-resolution (approximately 0.02 cm^{-1}) CO_2 absorption lines in small microwindows of the spectra. The absolute strength of the lines within an absorption band provides significant information about the amount of CO_2 in the path, while the relative strengths of the rotational lines within the band provide most of the temperature information. As the FTS is a high-spectral-resolution spectrometer, its measurements can be used to extract the absolute and relative strengths of the absorption lines.

The FTS v3.5 temperature profiles have not been extensively validated yet, although the FTS v2.2 temperatures have been thoroughly validated by *Sica et al.* [2008]. The FTS v2.2 and v3.0 temperature profiles also have been compared with several remote sounding instrument profiles (e.g. MIPAS, HIRDLS, SABER, MLS, HALOE, OSIRIS and SOFIE) [*Garcia-Comas et al.*, 2014; *Gille et al.*, 2008; *Mamun et al.*, 2013; *Marshall et al.*, 2011;

Schwartz et al., 2008; *Sheese et al.*, 2012; *Stevens et al.*, 2012; *Stiller et al.*, 2012]. Generally, the ACE-FTS temperatures agree with other instruments within 2–5 K. However, the version 2.2 shows a warm bias of 3-6 K in the mesosphere which reduces to only 2 K in version 3.0.

The pointing information provided by the SCISAT satellite is not reliable. Thus, different approaches are used for different altitude ranges by the FTS software to retrieve p-T profiles and determine the tangent heights. For altitudes between 5 and 15 km (12 km in version 2.2) the p-T is not retrieved and the tangent heights are entirely determined from an *a priori* p-T profile using the hydrostatic equation. Between 15 km and 43 km the tangent heights are calculated from the retrieved temperature and pressure. The retrieval results are then shifted in altitude until the best possible agreement between the retrieved pressure and *a priori* pressure is achieved in the altitude range of 15 to 25 km. Above 43 km, the information available from simple geometry using knowledge of the satellite and sun position are used to determine the tangent heights; the temperature is retrieved and the pressure is forced to obey hydrostatic equilibrium. Above 70 km where the CO_2 mixing ratio cannot assume to be constant the temperature and CO_2 mixing ratio are both retrieved.

Although the FTS and MAESTRO both make measurements on unevenly-spaced tangent heights, the output profiles are on 1-km altitude grids. The FTS vertical resolution is about 3 km and the MAESTRO vertical resolution is approximately 1.2 km. The FTS software first retrieves the p-T values for each tangent height then, using interpolation generates the values on 1-km resolution. The MAESTRO retrieval output profile is on 1-km grids so the p-T values between MAESTRO tangent heights are calculated during the retrieval process which causes them to be strongly affected by the smoothing constraint at higher altitudes.

4.6.3. Discussion

Figure 4.8 to Figure 4.10 show comparisons between MAESTRO p-T retrievals derived from O_2 bands and the profiles determined from ACE-FTS measurements of CO_2 [*Boone et al.*, 2005] for three single occultations during high-latitude winter and summer and in the tropics. Retrievals derived using HITRAN 2004 and 2012 database are compared with ACE-FTS profiles. The temperature differences are derived using:

$$\boldsymbol{T_{diff} = T_{MAESTRO} - T_{FTS}} \tag{4.21}$$

while the pressure percent differences are calculated as:

$$\boldsymbol{P_{diff} = \frac{P_{MAESTRO} - P_{FTS}}{\frac{1}{2}(P_{MAESTRO} + P_{FTS})} \times 100\%} \tag{4.22}$$

Temperature and natural logarithm of the pressure profiles are also plotted for MAESTRO and ACE-FTS.

The biases near the altitude range of 25 to 35 km relative to the FTS indicate a consistent feature of the MAESTRO retrievals. These are produced as a result of O_2 forward model underestimation of signal near 30 km and a larger overestimation of the signal near 20 to 25 km. As the density profile adjusts itself accordingly, the retrievals near these altitudes usually become poor. The source of this error has not been entirely discovered yet but clearly the HITRAN 2012 database reduces the biases in this range indicating that uncertainties in the O_2 spectroscopic parameters are part of the problem. The spectroscopic parameters contained in HITRAN 2004 for the *B*-band were not well-quantified and no information about uncertainties of the parameters was provided. Even the *A*-band parameters had not been characterized sufficiently in that version [*Tran et al.*, 2006; *Yang et al.*, 2005]. Recent studies

have had significant improvements in determining the *A*- and *B*-bands parameters that have been included in HITRAN 2012 version [*Gordon et al.*, 2011; *Rothman et al.*, 2013].

The other possibility for the MAESTRO retrieval irregularities near 15 to 20 km is the satellite pointing knowledge. As it was mentioned before the pointing information derived by the FTS is used for MAESTRO p-T retrievals as well. Thus, usually a poor FTS p-T retrieval translates into an unreliable MAESTRO retrieval. The FTS pointing retrieval cross-over point is 15 km where the p-T profiles below that point is fixed to the *a priori* and the retrieved tangent heights are shifted (15 to 20 km) to match those retrieved using the *a priori* p-T profiles. Apparently, the irregularities may cause poor MAESTRO results as the MAESTRO retrieval forces the pressure and density profiles to be hydrostatically-consistent with the temperature versus the FTS altitude profiles.

Figure 4.11 to Figure 4.13 show comparisons between the MAESTRO and the ACE-FTS measurements for three subset profiles from high latitude summer and winter as well as tropic. A comparison using the combination of all profiles is also shown in Figure 4.14. The mean differences and root-mean-square (RMS) differences between the MAESTRO and ACE-FTS profiles are represented by the dashed and solid lines respectively in all figures. The mean and RMS differences are only presented above the tangent height at which at least there are three profile measurements. Generally, the mean differences shown by dashed lines represent the biases in the results. The RMS differences indicate the general accuracy of the retrieval. Overall, the differences between measured MAESTRO and FTS pressures are usually within 2 – 5% and for temperature less than 5 K below 50 km. At higher altitudes where the O_2 signals are weak the MAESTRO measurements are dominated by the smoothing term in the retrieval. MAESTRO pressures and temperatures agree with FTS in

terms of RMS differences to within 2 to 10% and 5 to 10 K below 50 km. When improved parameters contained in HITRAN 2012 are used as input for forward model the biases in pressure and temperatures are reduced up to 2% and 2 K respectively. This is promising since the O_2 bands spectroscopic parameters are still being improved as these bands are being increasingly considered for future satellite missions. In terms of the RMS differences, 1% improvement in pressure and 1 K in temperature differences are expected below 50 km from the using of new spectroscopic parameters (HITRAN 2012).

The *Nowlan* [2006] analysis showed that using the *A*-band at low tangent heights consistently results in poor retrievals likely due to the impact of uncertainties in stray light correction and slit function shape in the *A*-band which is saturated at lower altitudes. Therefore the *A*-band is not used for retrievals below 30 km while above this altitude a combined *A*-*B* band retrieval is used to derive p-T profiles.

The theoretical error analysis conducted by *Nowlan* [2006] showed approximately 1 to 1.5% error for pressure and 2 to 3 K in temperature over most altitudes from known sources including measurement noise, pointing, slit function width, forward model, and spectroscopy. However, in practice, the total error estimates are 2% for pressure and 2 to 5 K for temperature most likely due to additional significant uncertainties contributed from the slit function shape and stray light [*Nowlan et al.*, 2007]. The retrievals provide tangent altitudes for the retrieval of trace gas profiles with an estimated accuracy of better than 200 m.

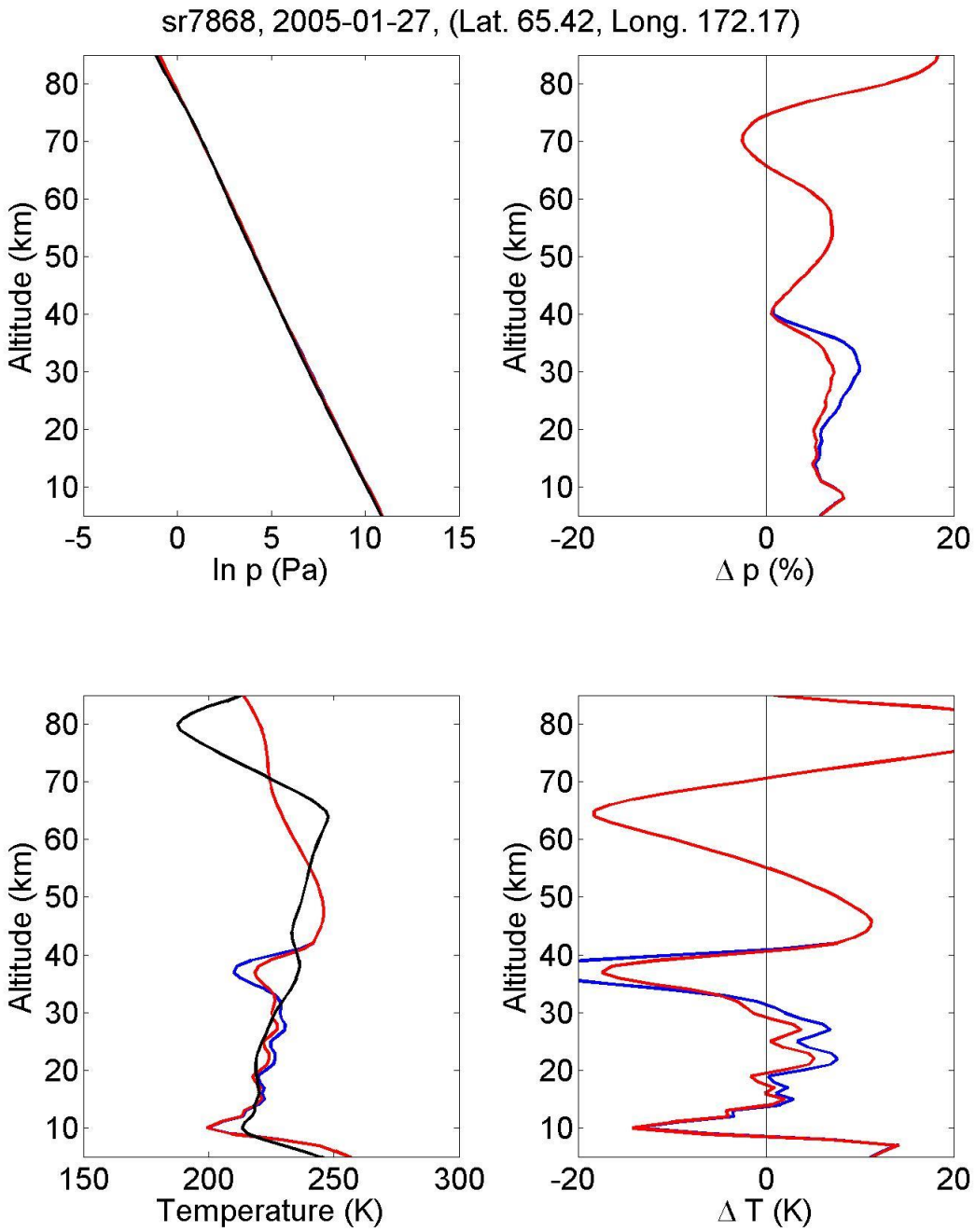

Figure 4.8: Pressure and temperature profiles from ACE-FTS (Black), and MAESTRO (blue: HITRAN 2004 / red: HITRAN 2012) for Occultation sr7868 (Arctic Winter). The difference in temperature and the percentage difference in pressure between MAESTRO and ACE-FTS also are depicted.

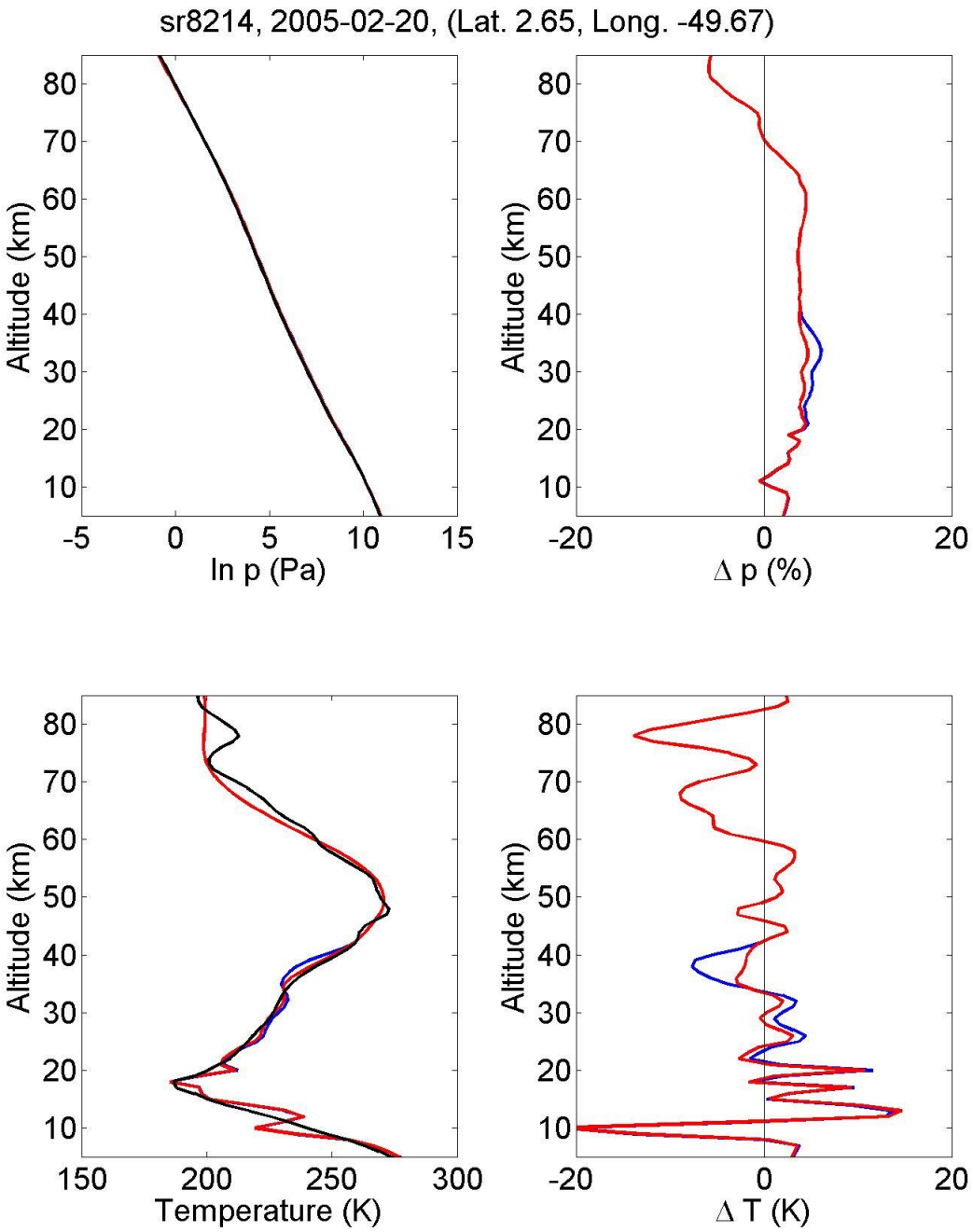

Figure 4.9: Same as Figure 4.8 for Occultation sr8214 (Tropics).

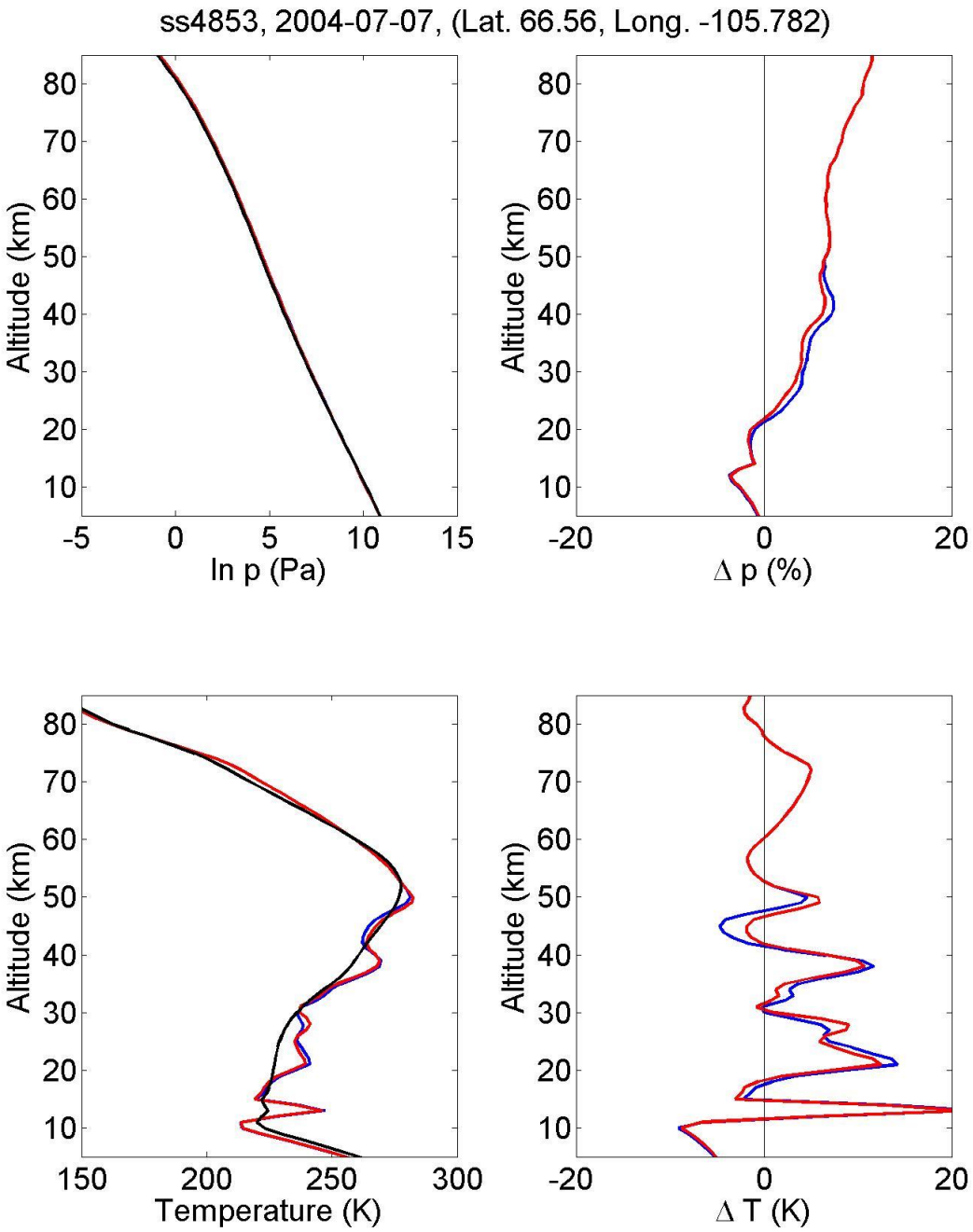

Figure 4.10: Same as Figure 4.8 for Occultation ss4853 (Arctic Summer).

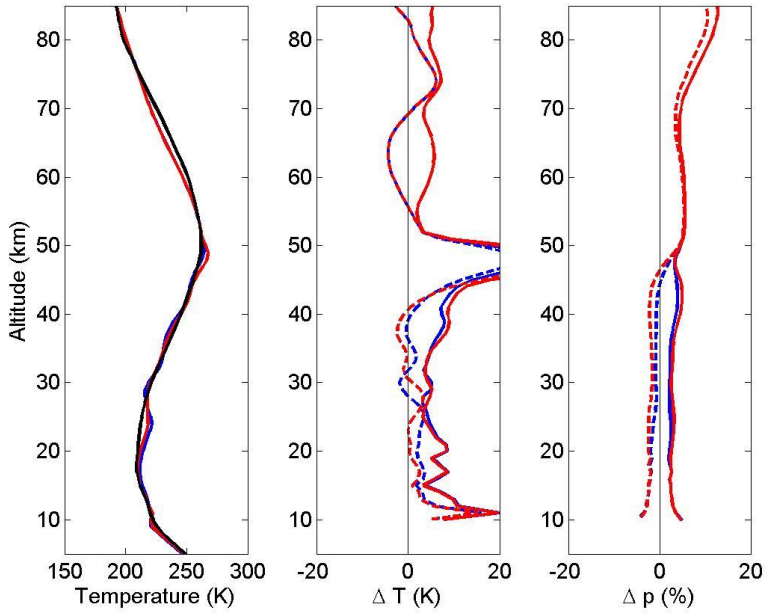

Figure 4.11: Arctic Summer Occultations; Mean temperature profiles from MAESTRO (blue: HITRAN 2004/ red: HITRAN 2012), and ACE-FTS (black); Mean (dashed) and RMS (Solid) differences between MAESTRO (blue: HITRAN 2004/ red: HITRAN 2012) and ACE-FTS.

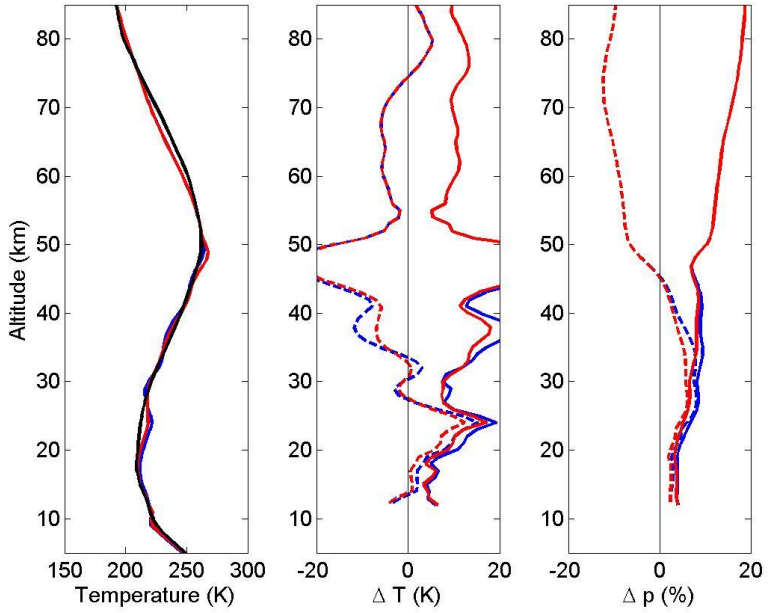

Figure 4.12: Arctic Winter Occultations; Same as Figure 4.11.

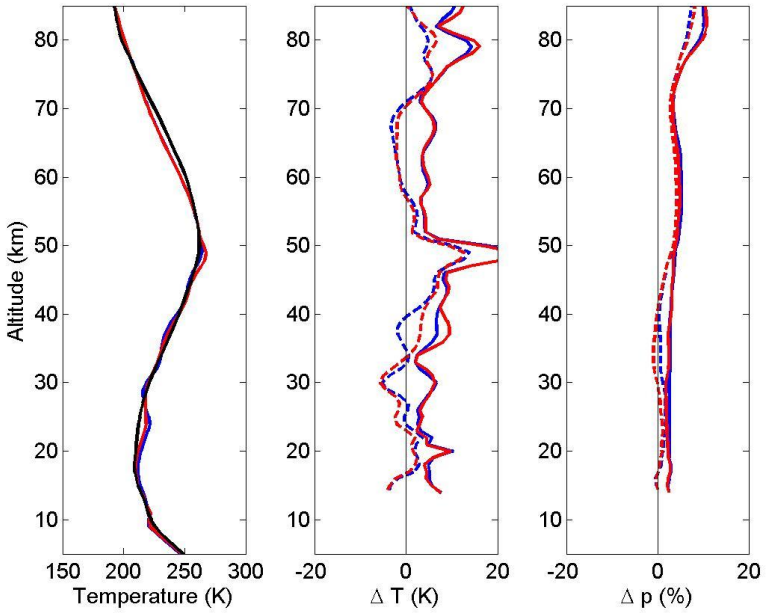

Figure 4.13: Tropic Occultations; Same as Figure 4.11.

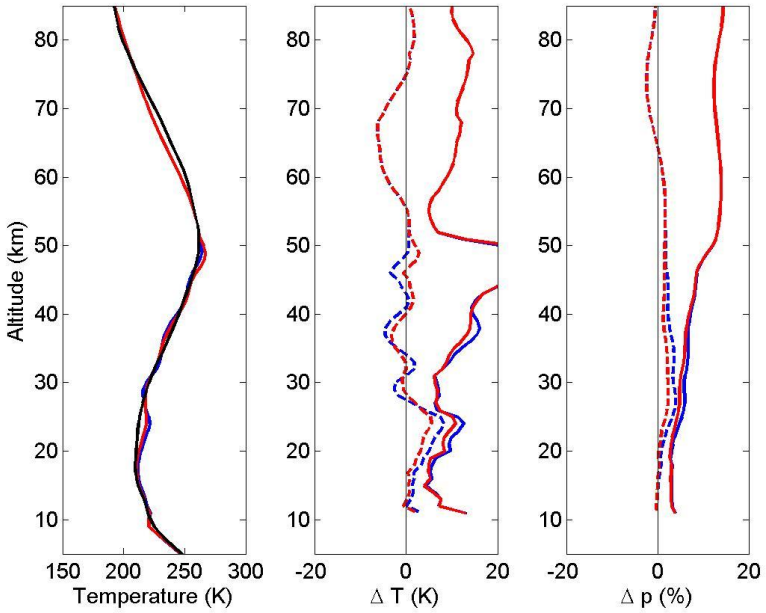

Figure 4.14: All profiles: Same as Figure 4.11.

4.7. Summary and conclusions

In this chapter the MAESTRO preliminary pressure-Temperature retrievals are reprocessed using the improved spectroscopic parameters from HITRAN 2012 database and compared with the ACE-FTS profiles and the processed results with HITRAN 2004. The retrieval algorithm and the forward model employed for the MAESTRO retrieval of p-T profiles are presented and discussed. The retrievals are based on the measurements of O_2 absorption in the *A*- and *B*-bands. A global fit and a fast and accurate radiative transfer model are used to calculate the O_2 number density in the atmosphere. Then the hydrostatic balance and the ideal gas law are employed to derive temperature and pressure from the density profile. The MAESTRO input data are discussed as well as the derived pointing information from the FTS p-T retrievals.

Three subsets of the occultations from the Arctic winter and summer as well as the tropics were selected for comparison with coincident ACE-FTS profiles. Sample retrieved profiles were shown to discuss the impact of HITRAN 2012 parameters on the MAESTRO p-T retrievals as compared with ACE-FTS and profiles retrieved using HITRAN 2004. A combined *A*- and *B*- band retrieval is used to derive the MAESTRO p-T profiles above 30 km. *A*-band is not used for the retrieval below 30 km due to unknown sources of errors which make the retrievals poor compared to ACE-FTS. Uncertainties in the instrument line shape, pointing knowledge and remaining O_2 spectroscopic issues could be among them. The MAESTRO p-T profiles agree with the FTS profiles reasonably well. The RMS differences between measured MEASTRO and FTS pressures are usually within 2–10% and for temperatures within 5-10 K. However, large biases at certain altitudes strongly influence the RMS differences. The O_2 retrievals suffer from a forward model underestimation of the

signal near 30 km and a larger overestimation of the signal close to 20-25 km. As the density profile adjusts itself accordingly, the MAESTRO retrievals are usually poor near 20-30 km. This error may be caused by FTS pointing information, MAESTRO characterization or O_2 spectroscopic parameters. Using HITRAN 2012 usually reduces these irregularities and improves the biases in pressures and temperatures up to 2% and 2 K respectively indicating the role of the O_2 parameters. This is promising as the O_2 band spectroscopic parameters are still being improved as these bands are being increasingly considered for future satellite missions. In terms of the RMS differences, the new spectroscopic parameters (HITRAN 2012) usually improve the differences by 1% and 1 K for pressures and temperatures below 50 km.

Currently, the pointing information derived from the FTS p-T retrievals are used by the MAESTRO retrievals. Ideally, the MAESTRO retrievals must be completely independent of those of FTS. The p-T profiles retrieved from O_2 bands could be used to derive pointing information for MAESTRO which then could be employed to improve the MAESTRO trace gas profiles.

Future work could include the use of the reprocessed pressure profiles to recalculate the MAESTRO tangent heights which might improve the MAESTRO ozone and other constituent profiles. Rewriting the software in C language would improve the speed of retrieval which helps to produce new product for more than 14 years of MAESTRO measurements.

5. Quantifying the Impact of Wildfires on Tropospheric Ozone Concentrations

In this study, a Differential Back Trajectory (DBT) method was developed, employing HYSPLIT back-trajectories and MODIS fire data to calculate the average difference between ozone concentrations associated with fire-affected and fire-unaffected parcels at 18 ozone sounding sites located across Northern America. The DBT method was applied to more than 1000 ozonesonde profiles collected from these sites during campaigns and regular measurements from June to August 2006, 2008, 2010 and 2011. Layers of high ozone associated with low humidity were first removed from ozonesonde profiles to minimize the effects of stratospheric intrusions in the calculations. The analyses show that none of the stations located at Arctic or far northern latitudes were significantly affected by fires. The ozone enhancement for stations nearer large fires such as Trinidad Head, Bratt's Lake was up to 4.2±0.8% of the TTOC (Total Tropospheric Ozone Column). Fire ozone accounted for up to 8.3±1.3% of TTOC at downwind sites such as Yarmouth, Sable Island,

Narragansett, and Walsingham. The results are consistent with other studies that have reported an increase in O_3 production with the age of the smoke plume.

A manuscript on this study is in-progress to be submitted to Journal of "*Atmospheric Chemistry and Physics"*.

5.1. Introduction

Tropospheric Ozone (O_3) is an important regulated air pollutant. Exposure to elevated concentrations of O_3 has been linked to respiratory illness such as irritated lungs, aggravated bronchitis, and asthma [*Lippmann*, 1991; *McConnell et al.*, 2002]. Ozone in the troposphere is formed by the interaction of nitrogen oxides (NOx = NO + NO_2) and non-methane hydrocarbons (NMHCs) in the presence of sun-light. Wildfires generate large amounts of O_3 precursors (NOx and NMHCs) and a number of studies suggest that fires can contribute to exceedances of the O_3 air quality threshold concentrations via production and long-range transport of O_3 and its photochemical precursors [*Jaffe et al.*, 2004; *Palmer et al.*, 2013; *Parrington et al.*, 2013]. In addition, the frequency and intensity of forest fires is likely to increase over Canada and the US as a result of climate change. *Gillett et al.* [2004] and *Westerling et al.* [2006] have shown that an increase of the area burned for Canadian and US forests is related to an increase in temperature and reduction of moisture in the area of interest. They both concluded that climate change is the key factor in explaining changes in fire frequency and intensity over recent decades. Various global warming scenarios have been examined to evaluate the possibility of an increasing in fire occurrences in the future. *Wotton et al.* [2010] estimate an increase of 30% in boreal forest fire occurrence by 2030 and

Spracklen et al. [2009] estimate an increase in the annual mean area burned of 54%, 78% and 175% by 2050 for the entire western USA, the Pacific Northwest, and the Rocky Mountain regions, respectively.

Ozone production from tropical biomass burning has been well established [*Andreae et al.*, 1994; *Andreae* and *Merlet*, 2001; *Backer* and *Muer*, 1991; *Jacob et al.*, 1996; *Thompson et al.*, 1996; *Thompson* and *Witte*, 2001; *Weller et al.*, 1996]. Both fuel consumption and the intensity of boreal fires are typically an order of magnitude larger than for savanna fires [*Stocks et al.*, 1998]. Higher intensity means higher transport of emissions into the troposphere and even into the stratosphere [*Fromm* and *Servranckx*, 2003] which may tend to increase transport distances. Data collected by aircraft, ground-based instruments and satellites during dozens of field investigations that have taken place in the last two decades over the Arctic and sub-Arctic have been used in various approaches to study the ozone production from boreal fires. A review of past observations finds that 2/3 of all chemical studies of fire plumes have reported ozone enhancement [*Jaffe* and *Wigder*, 2012].

Different approaches and datasets used to address the ozone source issue appear to give conflicting results. For instance, the data collected by the DC-8 aircraft from summertime (ARCTAS-B) flights in central and eastern Arctic Canada (designated as $> 50^{o}$ N latitude) were used by *Olson et al.* [2012] to constrain a photochemical box model. They found 1-2 ppbv/day net ozone photochemical formation in the boundary-layer (BL) and upper troposphere (UT), with significant uncertainty due to uncertainties in measured NO and HOx. *Alvarado et al.* [2010] also used aircraft data obtained during the ARCTAS-B campaign to determine the enhancement ratio of reactive nitrogen (NOy) species from fresh plumes to examine the impact of these emissions on tropospheric ozone in the Arctic. The

GEOS-Chem model showed very modest ozone formation, mainly due to rapid conversion of NOx, produced from fresh Arctic biomass burning, to PAN and inorganic nitrates. In contrast, biomass burning from central Canada was found as a modest but significant source of ozone by *Parrington et al.* [2012]. They also used FLAMBE emissions for 2010 in GEOS-Chem but the difference, as suggested by *Parrington et al.* [2013], seems to be that while fresh plumes (< 2 days old) show little increase in ozone, in aged (> 4 days) plumes PAN decomposition will release its constituent NO_2 and peroxy radicals which can then photolyze or react with NO to produce ozone. This is consistent with the review of observations of ozone production in boreal biomass burning outflow by *Jaffe* and *Wigder* [2012]. *Busilacchio et al.* [2016] used the aircraft data collected during the BORTAS–B (2011) campaign to analyze ozone and total peroxy nitrate (ΣPNs, $\Sigma ROONO_2$) production in fire affected and background air masses. Using different approaches, (1) direct calculation and (2) a 0-D photochemical model, the ozone and ΣPN formation in plumes impacted by fire emissions were compared with that in background air. They found that, on average, ΣPN production is more strongly enhanced than O_3 production: 5-12 times versus 2-7 times. They observed enhancement of the concentration and production of ΣPNs, which can act as a source and enhance ozone production downwind of the plume.

In this study ozonesonde profiles collected in June, July and August of 2006, 2008, 2010 and 2011 from 18 sites across Northern America were used to determine ozone enhancement empirically. The novel method developed here is objective and can be applied to all ozonesonde data collected from regular and campaign sites as long as the fire data are available. This method is applicable to evaluating the contribution of biomass burning to the ozone budget as it uses a network of observing sites at fixed locations.

5.2. Data and methods

5.2.1. Ozonesonde data

Balloon-borne ozonesonde is a lightweight instrument that is connected and launched with a conventional meteorological radiosonde. As the package flown by a large weather balloon ascends trough the atmosphere, the ozone concentration and standard meteorological parameters such as temperature, pressure, and humidity are telemetered to a ground receiver through the radiosonde transmitter. The balloon ascent rate is about 4-5 m s^{-1} to the typical burst altitude of 30-35 k. This gives the sonde a vertical resolution of about 100-150 m for a typical ozone sensor response time (e^{-1}) of about 20-30 s [*Smit* and *Kley*, 1998]. Ozonesondes utilize electrochemical detection methods through the reaction of potassium iodide by ozone in an aqueous solution:

$$2KI + O_3 + H_2O = 2KOH + I_2 + O_2 \quad \textbf{(5.1)}$$

followed by

$$I_2 + 2e^- = 2I^- \quad \textbf{(5.2)}$$

Therefore, two electrons are produced for each molecule of ozone [Komhyr, 1969]. The Electrochemical Concentration Cell (ECC) sondes (Figure 5.1) developed by Komhyr [1969] are the most widely used ozonesondes. ECC ozonsondes have a precision of 3-5% and a total (random and systematic) uncertainty of 10% below about 28 km [Deshler et al., 2008; Kerr et al., 1994; Smit et al., 2007]. The ozonesondes provide a long record of information about ground ozone and ozone profiles in the troposphere and part of the stratosphere at a particular location. Height limitations of the balloons and lack of reliability of the ozonesondes at low

pressure and temperature are among the limitations of ozonesonde measurements [*Smit et al.*, 2007; *Tarasick et al.*, 2016].

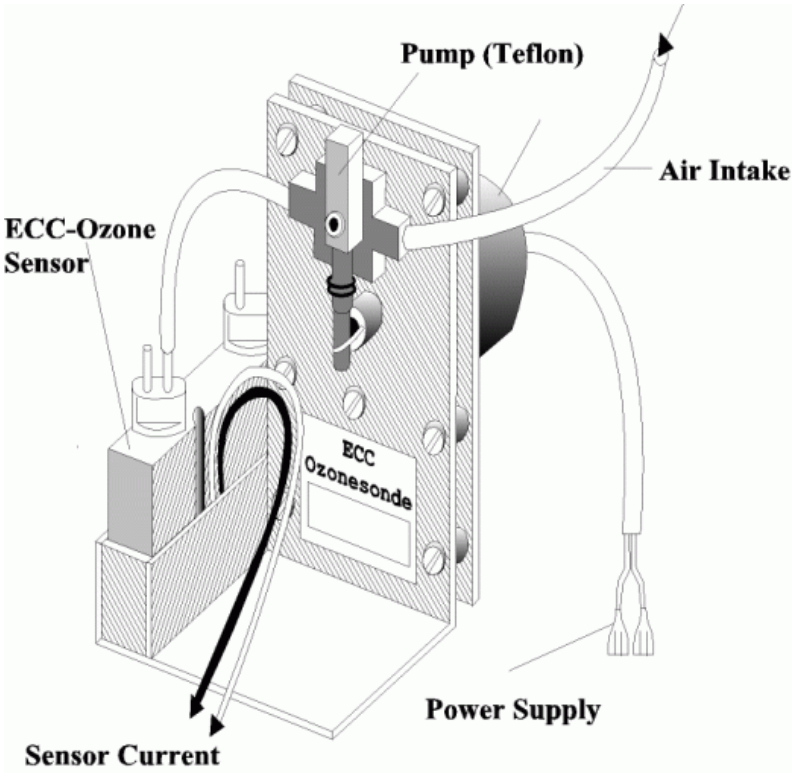

Figure 5.1: Schematic of an electrochemical concentration cell (ECC) ozonesonde (from http://www.fz-juelich.de/iek/iek-8/EN/Expertise/Infrastructure/WCCOS/WCCOS_node.html)

Figure 5.2 shows the locations of ozonesonde launch sites across Canada and the US that participated in the IONS and BORTAS campaigns [*Palmer et al.*, 2013; *Parrington et al.*, 2012; *Tarasick et al.*, 2010; *Thompson et al.*, 2007]. Table 5.1 and Table 5.2 describes these stations, including their geolocation (latitude, longitude and elevation) and the total number of profiles available for this study.

Table 5.1: Information on the sites contributing data during the IONS-06, ARCTAS and BORTAS campaigns.

Site Name	ID	Lat	Lon	Alt
Alert	18	82	-62	47
Eureka	315	79.99	-85.94	10
Resolute	24	74.71	-94.97	46
Summit	491	72.57	-38.48	3238
Whitehorse	998	60.7	-135.07	704
Yellowknife	999	62.5	-114.48	210
Churchill	77	58.74	-94.07	30
Trinidad	445	40.8	-124.16	20
Kelowna	457	49.92	-119.4	456
Stonyplain	21	53.55	-114.11	766
Bratt's Lake	338	50.2	-104.7	1550
Walsingham	482	42.64	-80.57	182
Egbert	456	44.23	-79.78	251
CSA-Montreal	496	45.51	-73.39	35
Narragansett	487	41.4	-71.5	23
Yarmouth	458	43.87	-66.1	9
Goose Bay	76	53.32	-60.3	44
Sable Island	480	44.95	-59.92	4

Pressure and temperature data measured by the coupled radiosonde were used to calculate the altitude using the hydrostatic relation. The determination of the tropopause height is done using the World Meteorological Organization [1957] criterion which is the lowest height, at which the temperature lapse rate falls to 2 ^{o}C /km or less, provided that the average lapse rate for 2 km above this height is also not more than 2 ^{o}C /km. The ozone sensor response time (e^{-1}) is about 25 seconds, which given a typical balloon ascent rate of 4 ms^{-1} in the troposphere, implies a vertical resolution of about 100 meters.

All ozonesonde profiles have been processed to 100-m altitude resolution up to the tropopause height or 15 km, whichever occurs first. Ozone partial pressures are integrated and averaged for 100 m thick layers from sea level up to top of the profile. Dividing by the average pressure in each layer, the average ozone mixing ratio is obtained.

Table 5.2: Number of profiles, by month and year, measured at different sites.

	2006			2008			2010			2011			
Site Name	Jun	Jul	Aug	Jun	Jul	Aug	Jun	Jul	Aug	Jun	Jul	Aug	**Total**
Alert	4	3	5	4	4	5	4	2	2	3	3	4	43
Eureka	3	4	5	4	4	5	5	3	3	5	4	5	50
Resolute	3	1	0	3	5	3	4	2	3	2	2	1	29
Summit	5	4	2	15	26	4	3	2	4	5	4	5	79
Whitehorse	0	0	0	7	11	0	0	0	0	0	0	0	18
Yellowknife	0	0	0	4	11	0	0	0	0	0	0	0	15
Churchill	4	4	4	8	8	1	2	4	3	5	1	1	45
Trinidad	5	4	30	10	15	4	18	3	4	4	4	4	105
Kelowna	5	2	27	8	13	4	18	2	3	2	3	5	92
Stonyplain	4	1	4	8	14	3	5	4	3	5	4	5	60
Bratt's Lake	4	2	29	6	11	4	4	17	4	4	21	5	111
Walsingham	0	0	22	0	0	0	0	12	0	0	0	0	34
Egbert	3	4	15	1	12	3	4	20	5	5	17	4	93
CSA-Montreal	0	0	0	0	0	0	0	14	0	0	0	0	14
Narragansett	4	4	24	4	3	5	2	2	2	0	0	0	50
Yarmouth	3	3	11	8	14	1	5	20	8	5	20	7	105
Goose Bay	3	2	5	4	11	0	4	18	8	4	22	7	88
Sable Island	0	0	28	4	11	0	0	16	0	0	19	1	79
Total	50	38	211	98	173	42	78	141	52	49	124	54	1110

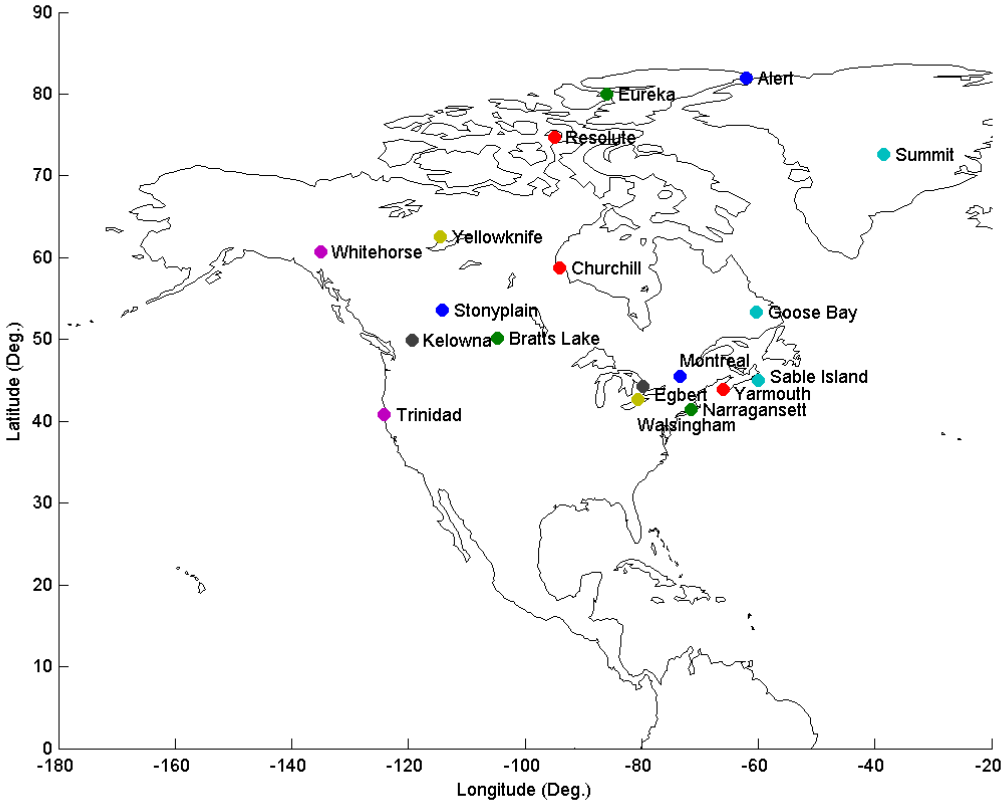

Figure 5.2: Location of stations assigned for IONS and BORTAS campaigns and used for this work.

5.2.2. Fire data

MODIS (MODerate Image Spectroradiometer) fire data (provided by NOAA/NESDIS) are used to determine the location of the fire hotspots. Figure 5.3 and Figure 5.4 show the location and intensity of fire hotspots between June and August of 2006, 2008, 2010, and 2011. The total area burned was above the long-term average (2.1 million Hectares) for 2006, 2010, and 2011 (Figure 5.5). Among these years, 2006 had the largest number of fires with more than 9800 fires (Figure 5.5), while for the others it was below the long-term average of 8000 fires (The Canadian Interagency Forest Fire Centre (CIFFC)).

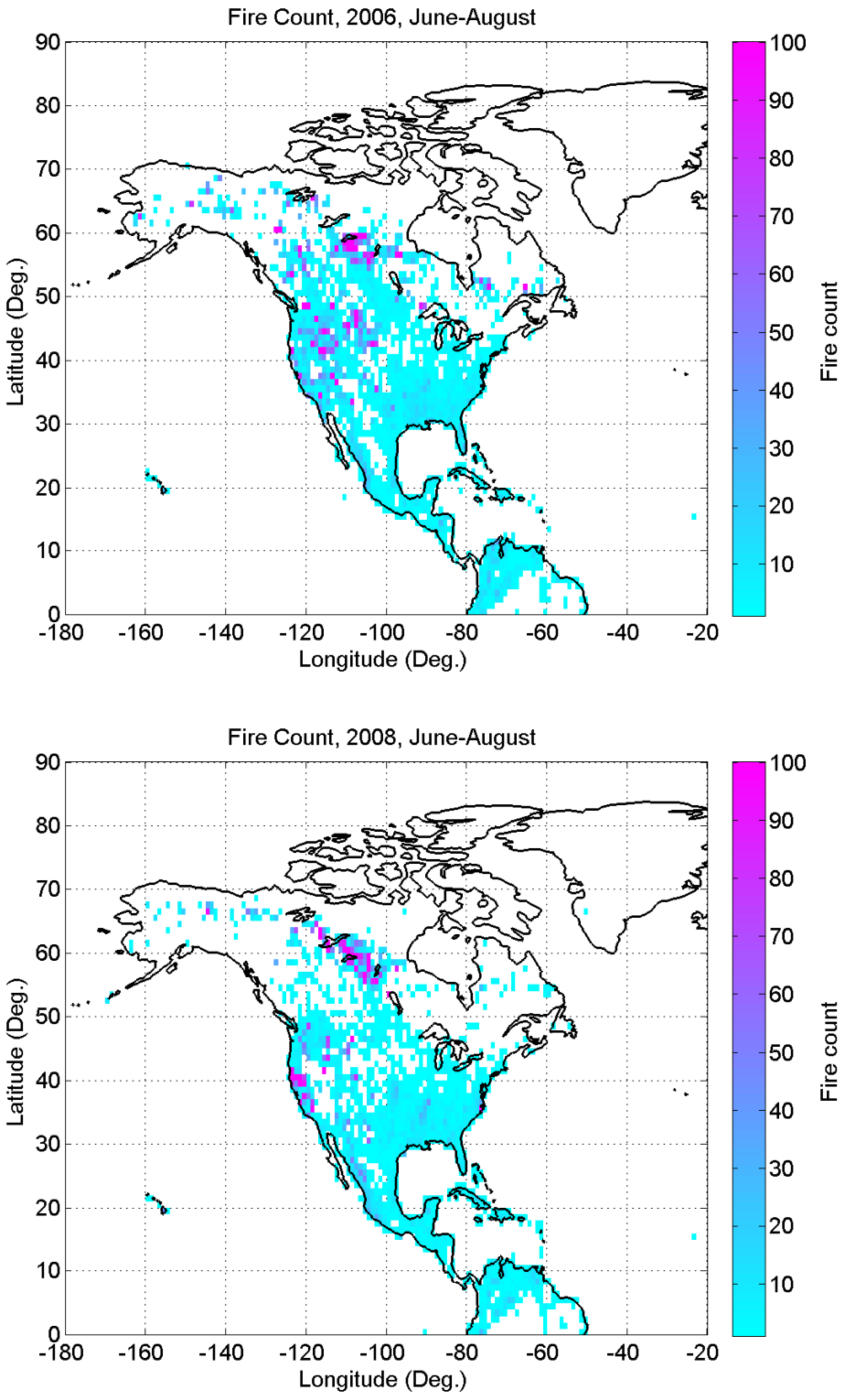

Figure 5.3: MODIS Fire Hot Spots during Jun.-Aug. 2006, 2008.

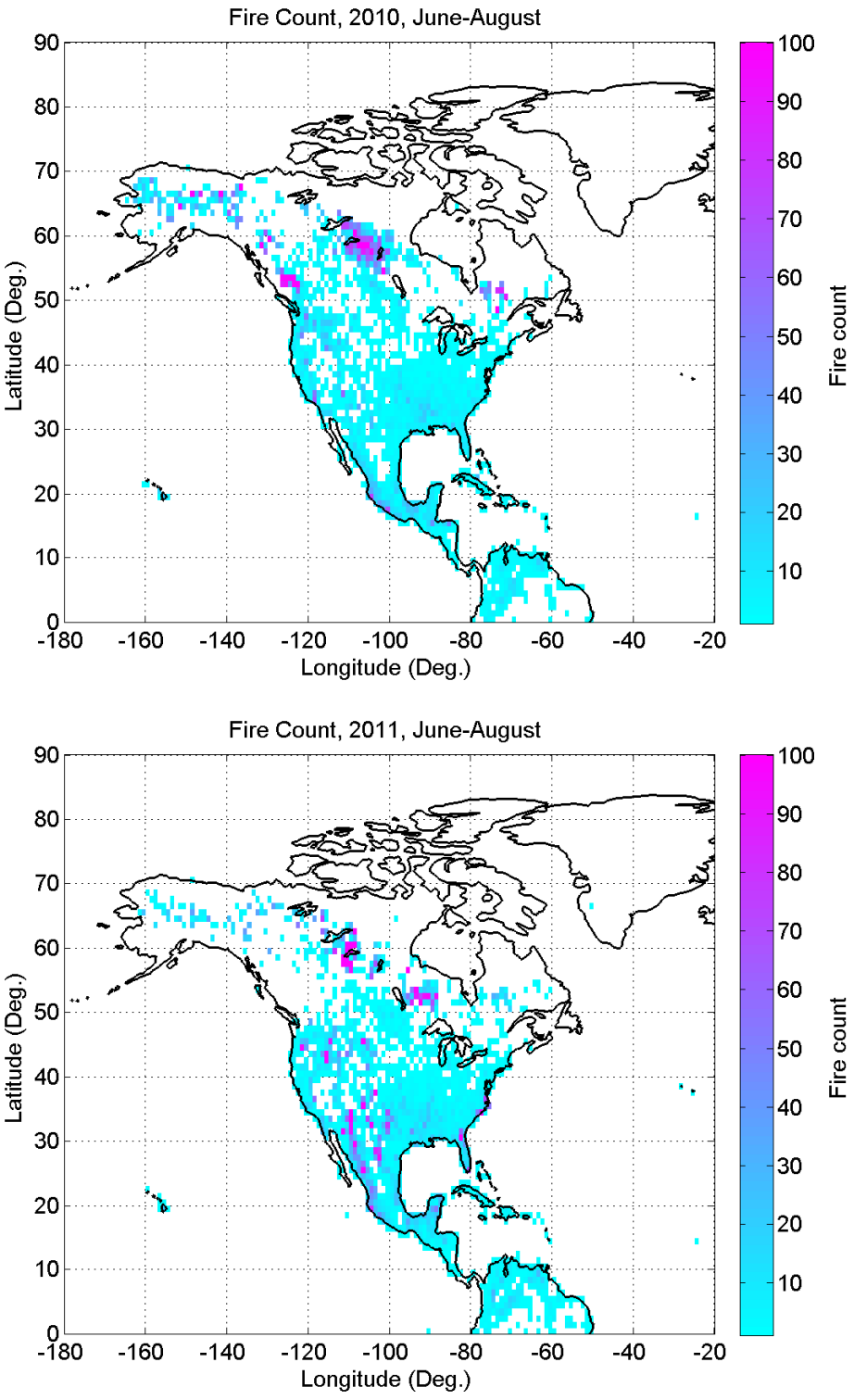

Figure 5.4: MODIS Fire Hot Spots during Jun.-Aug. 2010, 2011.

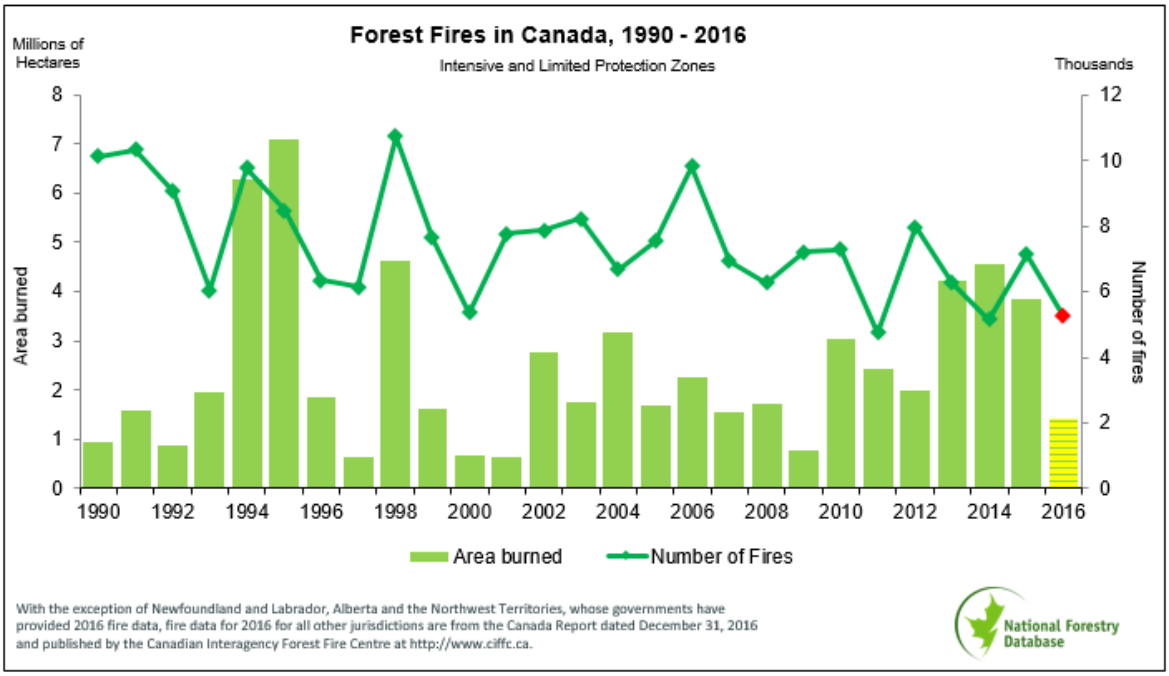

Figure 5.5: Area burned and number of fires in Canada between 1990 and 2016; Retrieved from Canada National Forestry Database (http://www.ciffc.ca).

5.2.3. Trajectory calculations

The HYSPLIT (Hybrid Single-Particle Lagrangian Integrated Trajectory) model [*Draxler* and *Hess*, 1998] developed by the NOAA Air Resources Laboratory (NOAA ARL), was used to calculate backward trajectories for each ozonesonde profile at 100 m height intervals from sea level. An air parcel is assumed to be released at the center of each 100 m altitude (50 m, 150 m, etc.) from the ozonesonde station (the releasing time, latitude, and longitude are taken from the ozonesonde launch). Minimum requirements for the HYSPLIT model to be run are the horizontal wind components (U, V), temperature (T), height (Z) or pressure (P) and the surface pressure (P_0). Meteorological models' output is used as input data for the HYSPLIT model to calculate the trajectories. The global NOAA-NCEP/NCAR (National Centers for Environmental Prediction/National Center for Atmospheric Research)

reanalysis data provide required parameters for HYSPLIT for 1948 through the present year. Data are updated annually for each additional year. The other dataset that can provide the global meteorological parameters for trajectories are ECMWF (European Centre for Medium-Range Weather Forecasts) data. The ECMWF datasets were not available free of charge for the years needed for this study also the data had to be reprocessed into the HYSPLIT compatible format. Thus, the global NOAA-NCEP/NCAR reanalysis dataset (NCEP Reanalysis data provided by the NOAA/OAR/ESRL PSD, Boulder, Colorado, USA, from their Web site at http://www.esrl.noaa.gov/psd/) was used as it was the only publicly available dataset for the summer of 2006, 2008, 2010, and 2011. These data provide 4-times-daily meteorological parameters at 17 pressure levels from 1000 to 10 hPa with 2.5×2.5^{o} horizontal resolution. This relatively coarse vertical resolution (corresponding to 2 km in the upper troposphere) implies that the trajectories are not entirely independent, a point that needs to be kept in mind when estimating statistical significance. Six days (144 hours) of backward trajectories were computed for the air parcel movement.

Several studies have attempted to estimate the accuracy of trajectories using different methods. *Stohl* [1998] reviewed a number of studies and found typical errors of 20% of the trajectory distance, or about 100-200 km day^{-1}. More recently, *Harris et al.* [2005] reported uncertainties of 30-40% of the horizontal trajectory distance, or 600-1000 km after 4 days, while *Engström* and *Magnusson* [2009], using an ensemble analysis method, estimated the uncertainty of trajectories to be within 350-400 km after 3 days and about 600 km after 4 days. These are consistent with the *Stohl* [1998] estimate.

Figure 5.6 displays the number of parcels for each individual site for 2006, 2008, 2010 and 2011 calculated from the reprocessed ozonesonde profiles from the surface up to

the tropopause or 15 km height. Only the regular ozonesonde stations have data for all four years. Some of the sites have contributed only in campaigns, and so do not have data for other years. There are a number of regular stations that also have participated in campaign measurements. These sites provide the most data and yield the most reliable and robust results.

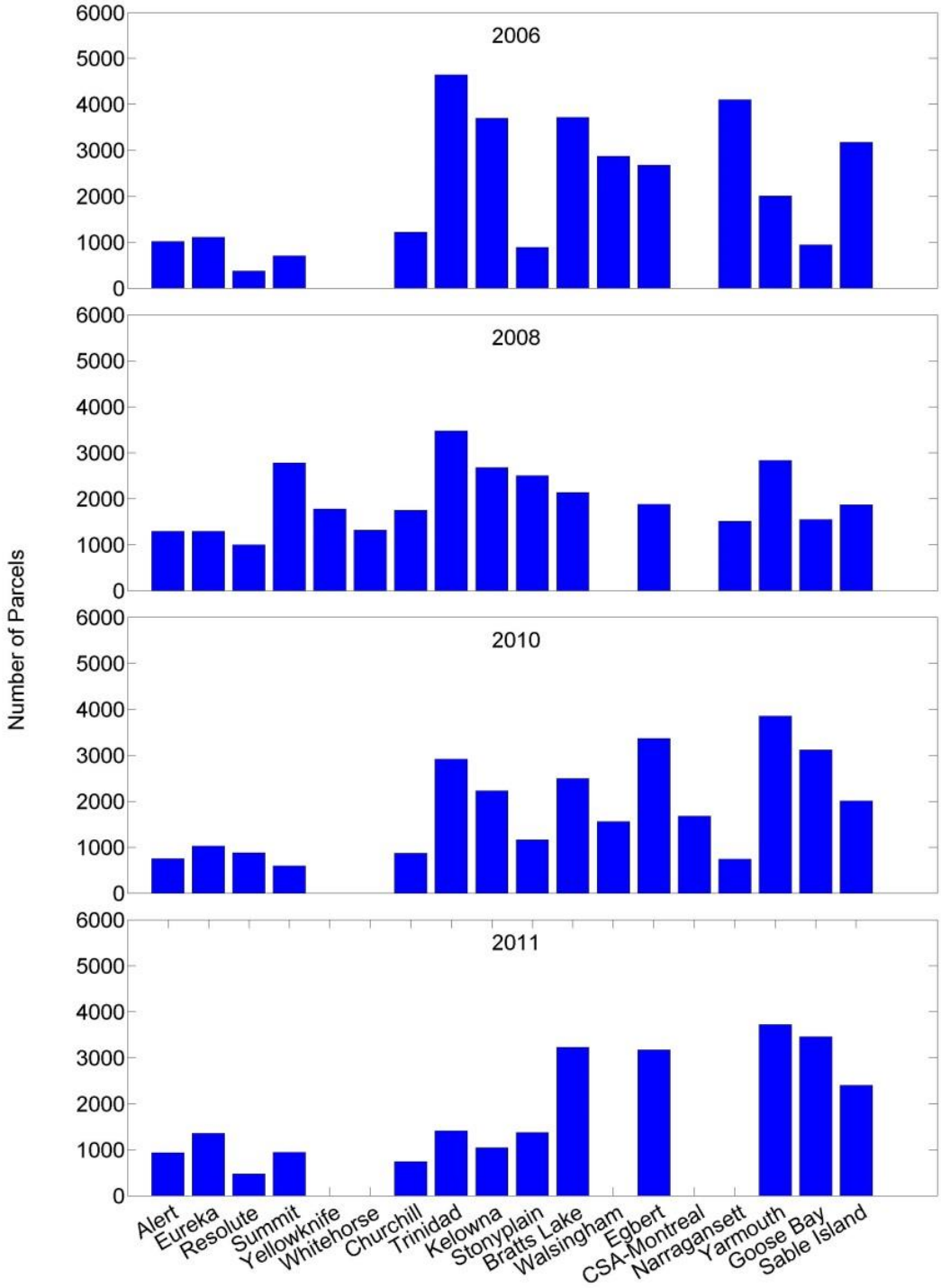

Figure 5.6: Number of parcels for each site during the year 2006, 2008, 2010, and 2011 calculated from reprocessed ozonesonde profiles from surface up to tropopause or 15 km.

5.2.4. Examples of elevated ozone layers

Figure 5.7 and Figure 5.8 illustrate elevated ozone layers detected in ozone profiles collected at a site near large fire activity (Stony Plain) and at a downwind site (Yarmouth). The MODIS fire hotspots for six days preceding the ozonesonde measurements show large fires in central Canada.

Six-day back-trajectories suggest that the layers of high ozone have crossed areas with of large fire activity before arriving at the sounding site locations. The humidity profiles are also depicted for these two examples. The layers with high ozone that trace back to the fires sometimes are associated with low humidity indicating the possibility of a stratospheric influence. Transport from the stratosphere is also a source of high ozone in the troposphere. In the next section a method is developed to remove the suspected stratospheric layers from the profiles.

5.2.5. Stratospheric ozone intrusion

The observations made by *Dobson* [1973] and others (e.g. [*Holton*, 1987; *Reid* and *Vaughan*, 1991]) from large datasets of soundings indicate that the ozone profile is relatively constant within the troposphere or stratosphere. Similar observations were made by *Newell et al.* [1999] from aircraft O_3 profiles. Stratospheric ozone-rich air intrusion or stratosphere-troposphere transport (STT) is one of the most common phenomena that perturb the tropospheric ozone profile. Observations show that tropospheric dry layers associated with high ozone are often STT events [*Haver* and *Muer*, 1996; *Thouret et al.*, 2000].

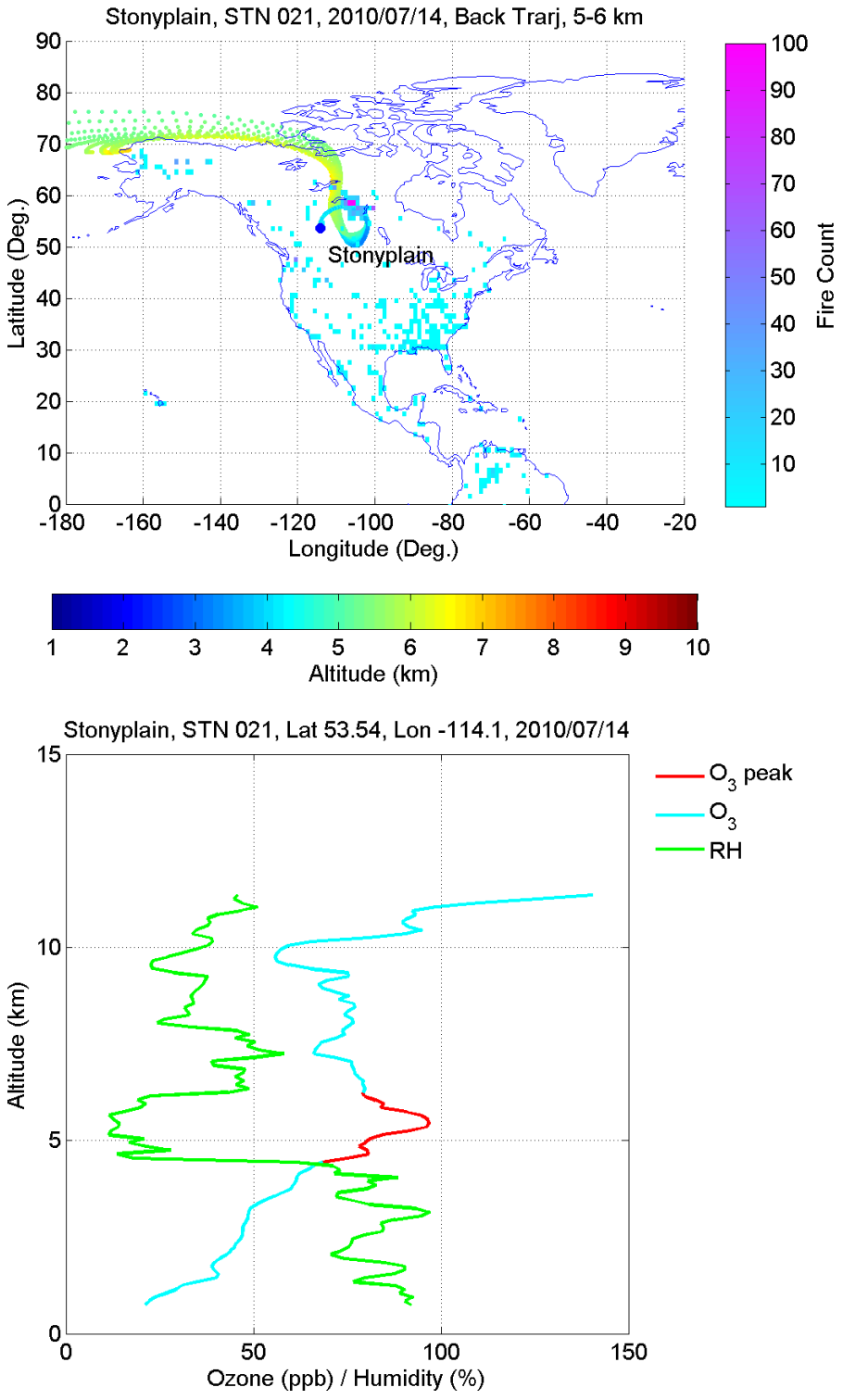

Figure 5.7: (bottom) Ozone and humidity profiles collected in Stony Plain. (top) back-trajectories indicate that the ozone anomalies could be produced by fires. It should be noted that the layers with high ozone are associated with low humidity.

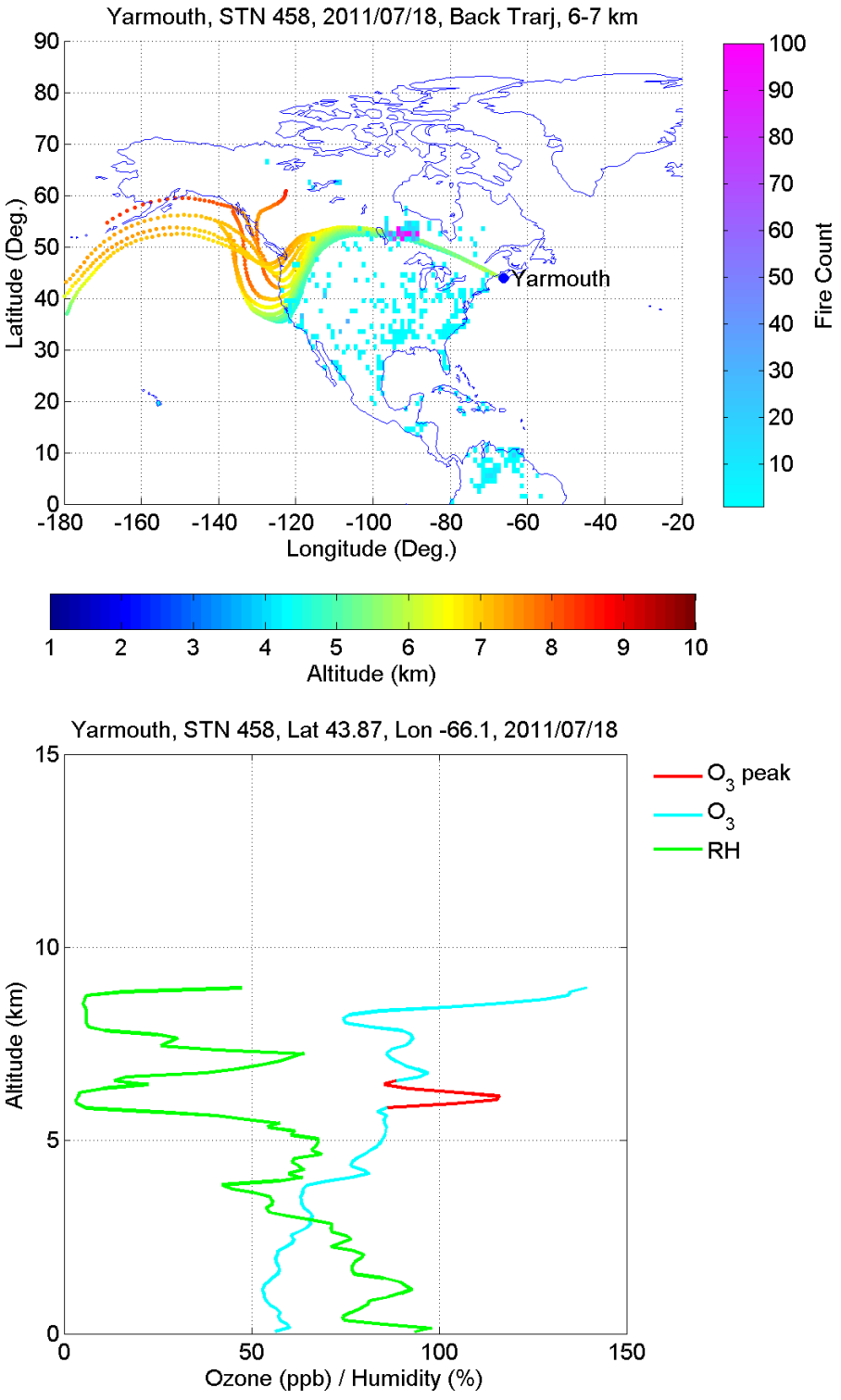

Figure 5.8: Same as Figure 5.7 for Yarmouth.

Colette et al. [2005] considered 21 principal factors to identify the free tropospheric segment of European summer ozone profiles affected by STT. They reduced the factors to 6 and no difference was detected. Eventually, the RH (Relative Humidity)-O_3 relationship turned out to be the most robust indicator of STT impact.

As noted, preliminary studies revealed that some elevated ozone layers that trace back to fires are associated with low humidity which is an indication of STT. Hence, to avoid the impact of STT ozone amounts on the calculations presented here, suspected stratospheric intrusions (STT) were removed from the ozone profiles. The identification of STT was based on the humidity (RH)-O_3 relationship. The suspected layers were determined through the following steps (all steps were applied to the entire ozone profiles):

1. To locate the ozone peak laminae a mean profile was obtained by box car smoothing the high resolution profile to remove variations of vertical half-width less than 2.5 km. Then, the difference between the high resolution profile and the mean profile, divided by the mean profile was calculated and defined as the normalized perturbation profile.
2. The same method was used to filter out the variations of vertical half-width less than 5 km from RH profile to find the relative humidity negative peaks.
3. The laminae with average amplitudes greater than 10% of the mean ozone mixing ratio were considered significant and removed from the profile if associated with negative RH laminae with average amplitudes greater than 20% of the mean relative humidity.

Figure 5.9 shows an ozone profile with a large anomaly between 5 and 6 km. Back trajectories suggest that this layer may have been affected by a stratospheric intrusion. The

tropopause height (shown in the middle panel) was derived from tropopause height data provided by the NOAA Physical Sciences Division (http://www.esrl.noaa.gov/psd) from the same NCEP/NCAR reanalysis database used as input to the HYSPLIT model. The WMO (1992) thermal lapse rate criterion was used by NOAA to compute the tropopause heights. In addition, tropopause heights at pressure levels smaller than 85 hPa and larger than 450 hPa are not allowed by the NOAA calculations. The bottom panel illustrates how the algorithm removes the suspected layer from the profile.

The percentage occurrence of stratospheric intrusions for each site during the selected years based on the method presented here is shown in Figure 5.10.

5.2.6. Differential Back Trajectory (DBT) method

The DBT method uses back-trajectories calculated at 100 m intervals from the surface to the tropopause, for each sounding, up to 144 hours long. A parcel is defined as "fire-affected" if the back-trajectory corresponding to a parcel passes through a 1×1 degree grid box containing one or more MODIS fire counts. The remaining parcels are classified as background or "fire-unaffected". For this study, only parcels that are affected by fires in North America and Mexico were considered as "fire-affected". Parcels affected by fires outside this zone (e.g. Asia, South America, etc.) were removed from the analysis.

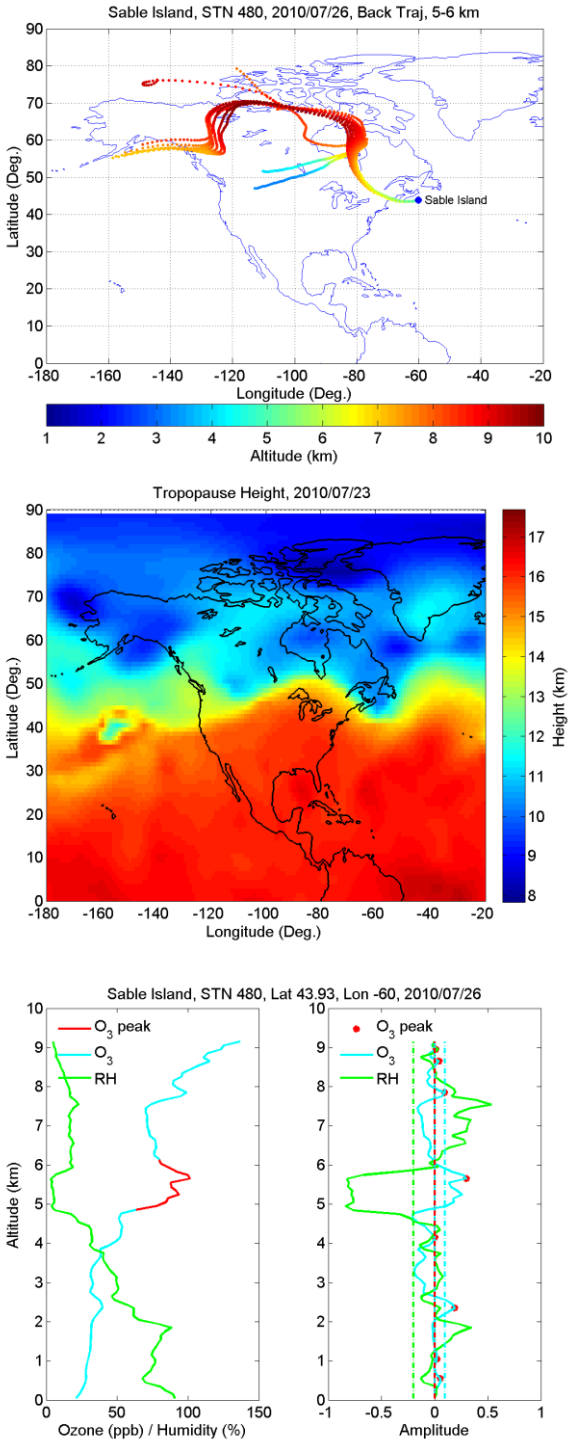

Figure 5.9: (top) Back-trajectories for the layers between 5 and 6 km indicate the possibility of stratospheric intrusions. (middle) Tropopause height retrieved from NCEP/NCAR reanalysis data. (bottom) Ozone and humidity profiles of July 26, 2011 at Sable Island. Ozone peaks are shown in red.

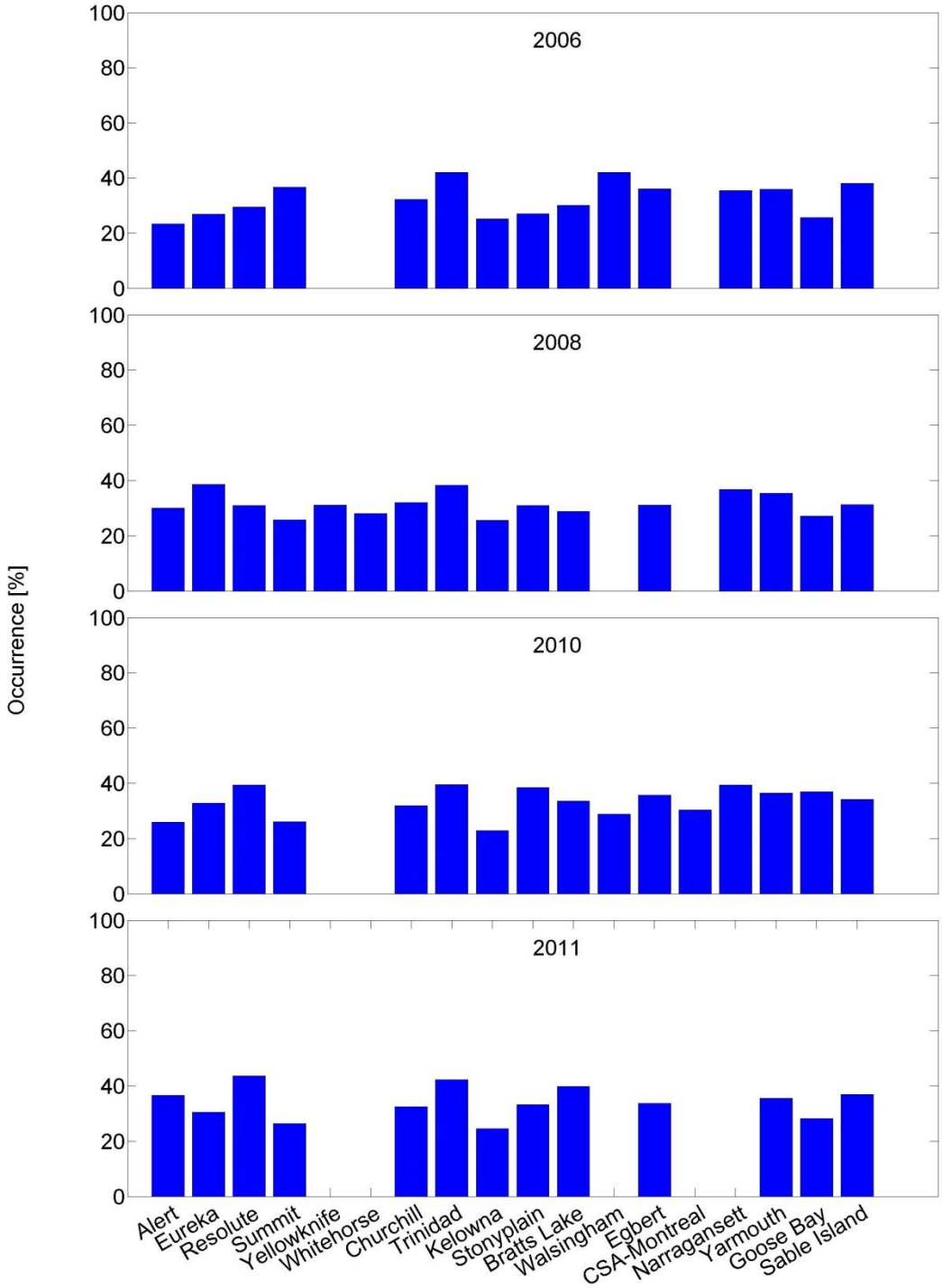

Figure 5.10: Number of suspected stratospheric layers expressed in percentage.

At each 100 m level, for each sonde site, the average difference in ozone concentrations associated with “fire-affected” parcels in each year and “fire-unaffected” parcels from all four years (2006, 2008, 2010, and 2011) is calculated. To calculate the average fire contribution to ozone, the computed average is multiplied by the ratio of the number of “fire-affected” parcels to the total number of parcels (sum of “fire-affected” and “fire-unaffected”) for that specific year. Suspected stratospheric intrusions, as described in section 5.2.5, are first removed from all profiles, to avoid skewing the averages.

The average total tropospheric ozone calculated from fire-unaffected parcels is depicted in Figure 5.11. The TTOC is lower for high latitude sites such as Alert, Eureka, and resolute compared to the middle latitude sites. The percentage of fire-affected occurrences for each individual site is given in Figure 5.12. Minimum occurrences can be observed in high-latitude and Arctic sites. However, it should be noted that only a limited number of profiles were available for those sites compared to that of the other sites (Table 5.2). In addition, as noted, fires in Asia and Europe were excluded. Generally, the eastern sites are more affected than those sites located in the middle and western areas. As an example the profiles of average “fire-affected” and “fire-unaffected” parcels for Yarmouth station for year 2010 are depicted in Figure 5.13.

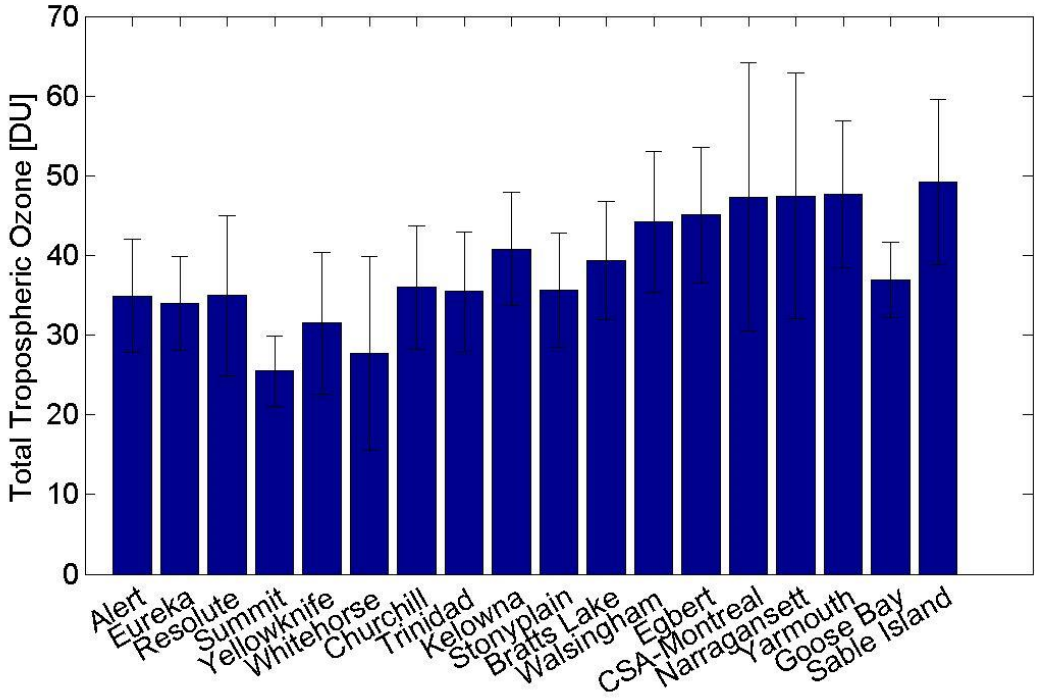

Figure 5.11: Total tropospheric ozone expressed in DU calculated from fire-unaffected parcels. The error bar equals 2 Standard Error (SE).

The DBT method offers a statistical estimate of the amount of additional ozone generated by fires. It neglects any contribution from fires more than 144 hours previous to the sounding. This is likely a small error, since back-trajectories from any of the sonde sites will generally cross the continent in less than 6 days. A more important source of error is the misassignment of air parcels due to trajectory errors: any systematic difference in ozone concentration between "fire-affected" and "fire-unaffected" air parcels will be diluted by such misassignment. Since trajectory errors over several days can be quite large [*Downey et al.*, 1990; *Engström* and *Magnusson*, 2009; *Harris et al.*, 2005; *Stohl*, 1998], this probably causes the DBT method to produce a serious underestimate of the amount of ozone generated by fires.

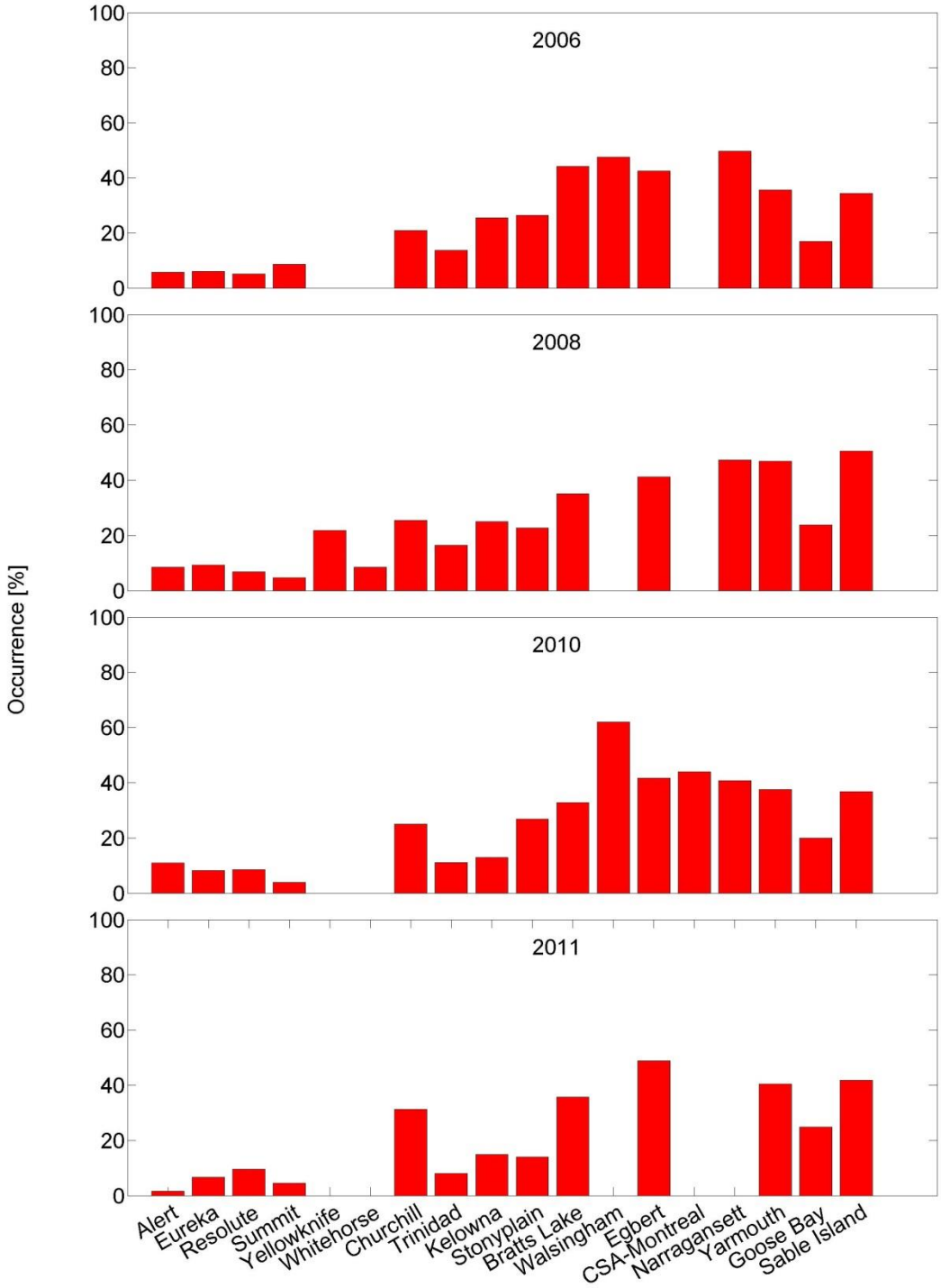

Figure 5.12: Number of fire-affected parcels given in percentage detected by the DBT method for selected sites in 2006, 2008, 2010, and 2011.

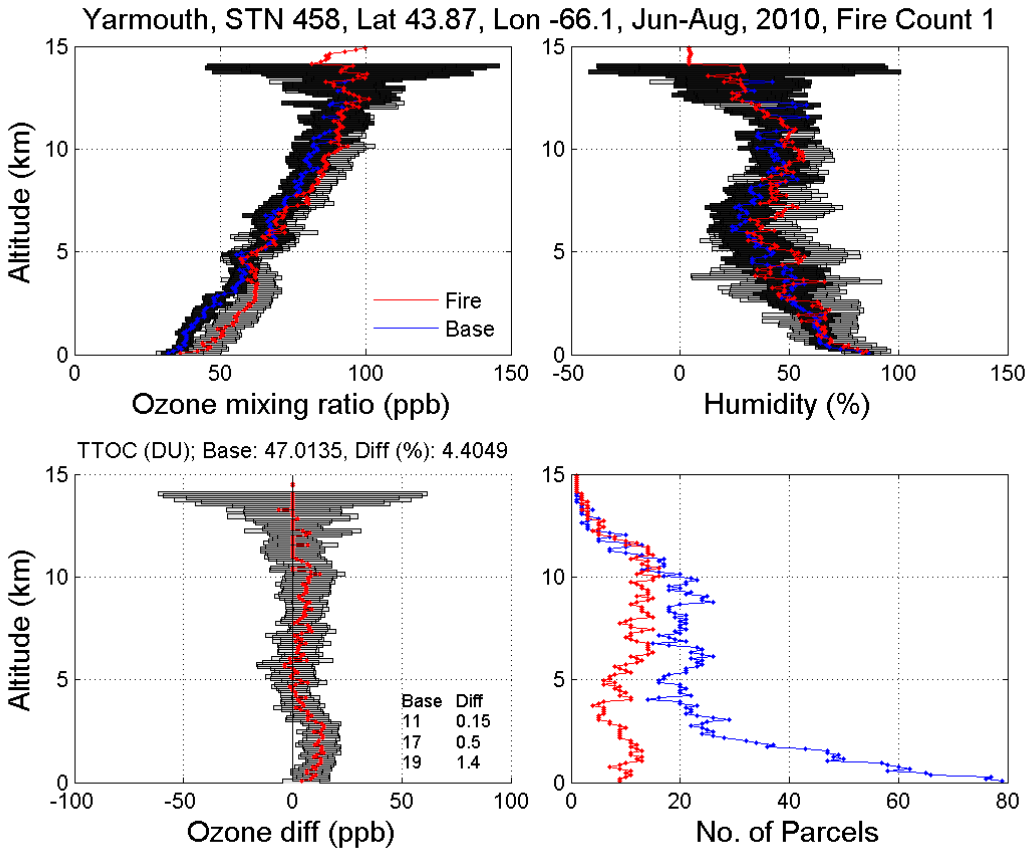

Figure 5.13: An example of results from the Differential back trajectory (DBT) method, for Yarmouth, NS. Top: average ozone and humidity for fire-affected (Red) and non-affected (Blue) parcels. The horizontal bars represent 2 SE. Bottom left: average difference between fire-affected and non-affected parcels. Bottom right: number of fire affected (red) parcels during summer 2010 and number of non-affected (blue) parcels over four years (2006, 2008, 2010, and 2011). Total column ozone calculated from non-affected parcels is also depicted along with the difference in DU.

5.3. Result and discussion

5.3.1. Ozone enhancements

The intensity and location of fires is quite variable. As shown in Figure 5.3, large fire activity in 2006 was concentrated in Central Canada, the Western U.S. and Southern U.S. The average enhancement in total tropospheric ozone column (TTOC) over four years (2006, 2008, 2010 and 2011) is shown for 18 sites in Figure 5.14. The analysis shows that none of the high latitude sites has been affected significantly. Overall, Narragansett and Yarmouth had the largest ozone enhancements. Kelowna and Stonyplain were not affected significantly although they were occasionally close to large fire activity.

Figure 5.15 shows the average ozone enhancement for each site during 2006, 2008, 2010, and 2011 summertime (June – August). The analysis shows that 8 sites out of 14 were significantly affected by fires in 2006. The fire contribution was significant in 0-5 km total column ozone over 8 sites in 2006 ranging between 0.4 ± 0.2 and 2.0 ± 1.2 DU (1.2 ± 0.6 and 4.5 ± 0.5 %) with a minimum in Stony Plain and a maximum at Bratt's Lake. In terms of TTOC, 4 sites were significantly affected. The fire ozone contribution in the TTOC at Trinidad Head and Bratt's Lake, that were close to large fires (Figure 5.3), was 4.1 ± 0.6% and 2.0 ± 1.2%, respectively. The ozone enhancement for Yarmouth, and Sable Island (downwind sites) was 4.7 ± 1.1%, 2.8 ± 1.0%, respectively.

Two large fire events occurred during summer of 2008 (Figure 5.3). One was caused by large fires in Saskatchewan in Central Canada and the other was in the Western and Midwestern U.S. The ozone profiles from 16 sites were used to calculate the average fire ozone amount in the TTOC during June to August, 2008. The DBT method shows that fire ozone significantly contributed to the TTOC of 6 sites during 2008.

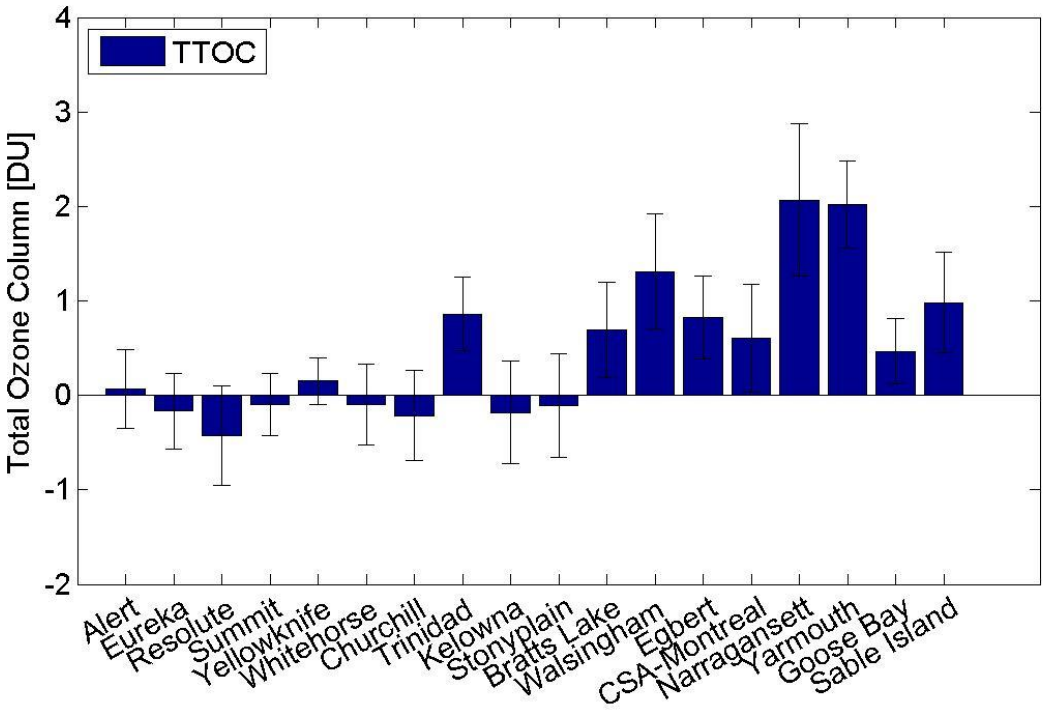

Figure 5.14: Average enhancement in total tropospheric ozone column at different sites over 2006, 2008, 2010, and 2011. Error bar equals 2 Standard Error (SE).

Trinidad Head was the closest to the U.S. fires in 2008 where fire ozone accounted for 1.5 ± 0.4 DU (4.2 ± 0.8 %) of TTOC at this station. Bratt's Lake was also nearby large fires in Canada. The ozone enhancement for Bratt's Lake was 0.8 ± 0.5 DU (2.2±1.3%). Narragansett, Yarmouth, Goose Bay, and Sable Island were also significantly affected by fires. Fire ozone contribution in the TTOC was computed, respectively, as 2.0 ± 0.8 DU (4.4 ± 1.8%), 2.0 ± 0.5 (4.3 ± 1.0%), 1.9 ± 0.4 (5.2 ± 1.0%), 4.0 ± 0.7 DU (8.3 ± 1.3%) for these sites. Large Canadian fires in 2008 took place near to five Canadian sites: Yellowknife, Churchill, Kelowna, and Stony Plain. Although, the analysis shows minimal enhancement to 0-5 km (above ground) ozone columns at these sites, the TTOC was not significantly enhanced.

The year of 2010 was an exceptional year in terms of the total area burned by Canadian boreal fires (Figure 5.5). The large fire events were recorded in North Central and Western Canada (Figure 5.4). The data collected at 14 regular sites plus Walsingham, Montreal and Narragansett were analyzed for 2010. Of the sites close to the fires Bratt's Lake was significantly affected with ozone enhancement of 1.8 ± 0.5 DU (4.5 ± 1.3%). Fire ozone accounted for 1.4 ± 0.4 (3.1 ± 0.9%), 0.6 ± 0.6 (1.3 ± 1.2%), 3.6±0.9 (8.0 ± 2.1%), 2.0 ± 0.5 (4.4 ± 1.0%), 0.6 ± 0.4 (1.7 ± 1.0%), 0.8 ± 0.4 (1.5±0.9%) DU of the TTOC at the downwind sites: Egbert, Montreal, Narragansett, Yarmouth, Goose bay, and Sable Island, respectively.

The number of fires in 2011 was about 4200 which is almost half of the long-term average of 8000 fires in Canada (Figure 5.5). The ozone profiles collected by 11 Canadian sites plus summit and Trinidad Head were used to calculate the influence of fires on the tropospheric ozone at downwind sites. Only two sites were significantly affected by fires. Egbert where 2.0 ±0.4 (4.4 ± 1.0%) ozone enhancement was detected and Yarmouth with 1.8 ± 0.4 (3.8 ± 0.8%) fire ozone contribution in the TTOC. Ozone in the 0-5 km layer was also enhanced at Churchill and Stonyplain sites. Surprisingly, the analysis shows that Sable Island was negatively affected by fires in 2011. Although apparent ozone destruction in boreal fire plumes has been reported previously [*Real et al.*, 2007; *Verma et al.*, 2009] this is likely an indication of the magnitude of possible error in this statistical method. Generally, the DBT method showed that downwind sites were more affected by fires than the sites nearer to the large fires indicating the transport of ozone and/or its precursors from fire locations to the downwind locations.

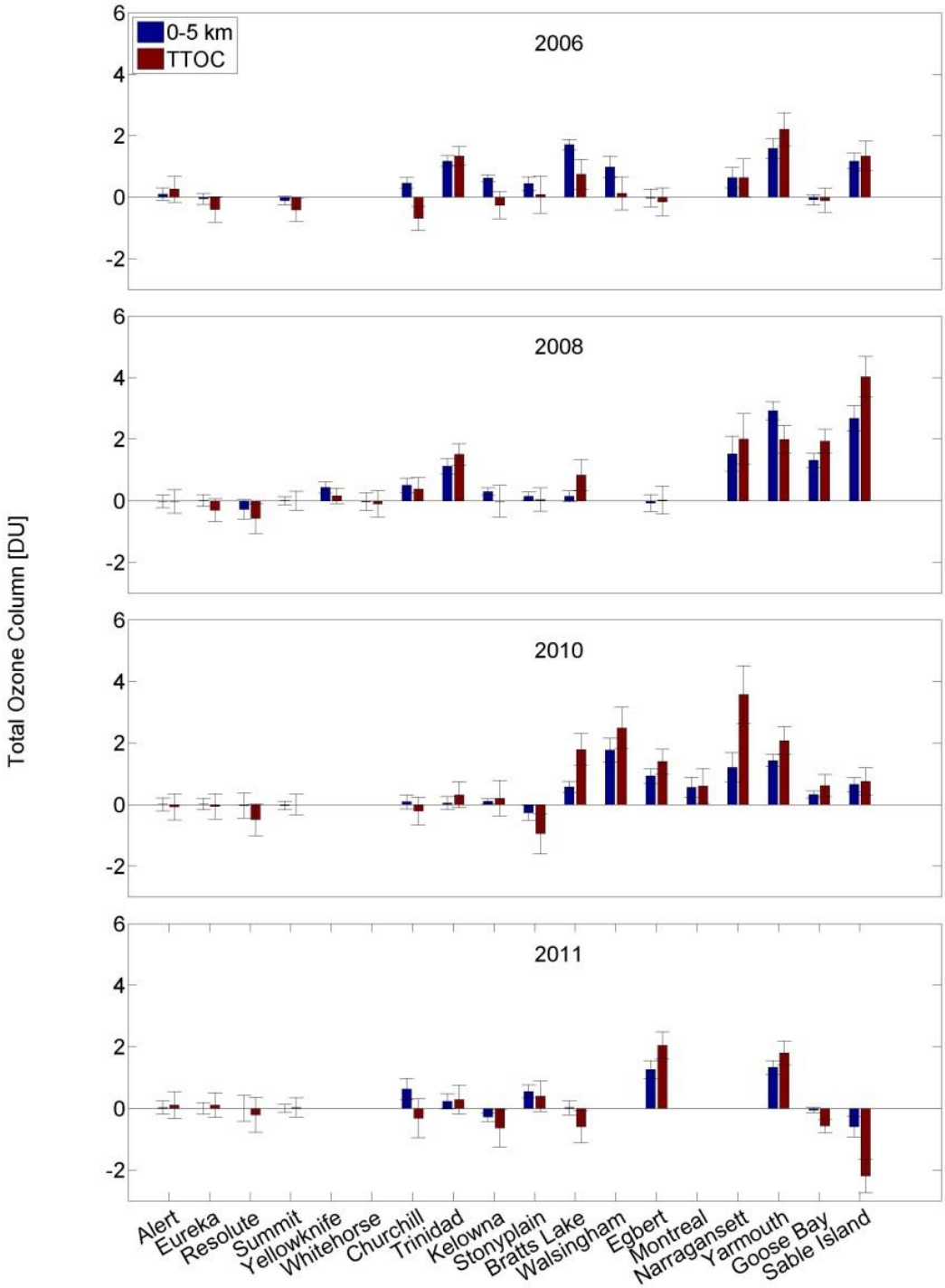

Figure 5.15: Average enhancement in the 0-5 km layer and total tropospheric ozone column (TTOC) at different stations during the 2006, 2008, 2010 and 2011 summer, expressed in DU.

5.3.2. Fire plume injection height

In this section the fire plume injection height is considered in calculation to show the robustness of the results. The fire plume height and the maximum altitude expected to be influenced are highly variable as they depends on fire size and power and also the atmospheric conditions [*Freitas et al.*, 2007; *Kahn et al.*, 2008; *Labonne*, 2007]. Different approaches have been used by several groups to develop algorithms and models to determine the appropriate heights for biomass burning emissions [*Freitas et al.*, 2007; *Kaiser et al.*, 2012; *Paugam et al.*, 2016; *Sofiev et al.*, 2012]. Studies show that fire plumes are likely able to reach 10 km altitude or even into the lower stratosphere depend on fire radiative power (FRP) and fire size [*Freitas et al.*, 2007]. There is no general formula recommended to estimate the fire plume height. For this study, it is assumed that the more concentrated fires provide higher injection heights. The concentration of fires is determined by counting the fire hotspots in each 1×1^{o} grid box over 24 hours. Table 5.3 shows the assumed smoke plume height for a given MODIS fire count. Hence, for this section, both altitude and fire count are considered to identify the fire-affected parcels.

Table 5.3: MODIS fire count and corresponding smoke plume height.

Fire Count	Expected Plume Height
1 – 10	0 – 2 km
11 – 50	2 – 5 km
51 – 90	5 – 7 km
91 – 120	7 – 9 km
120<	9 km<

For example, if the back-trajectory corresponding to a parcel passes through a 1×1 degree grid box containing 1-10 fire counts that parcel only is identified as fire-affected if its altitude

is 0-2 km; otherwise it is excluded from the analysis. As before, the remaining parcels are classified as background or fire-unaffected.

After applying assumed fire plume injection heights into the DBT method the contribution of fire ozone to TTOC is calculated. Figure 5.16 shows the number of fire affected parcels considering fire plume injection heights in percentage for each site during 2006, 2008, 2010 and 2011.

The average ozone enhancements in TTOC over four years are displayed in Figure 5.17. Although the assumption of an injection height reduces the number of fire-affected parcels by about 2/3, the calculated contributions of fire ozone to TTOC are much less reduced, and still positive and significant for most of the sites.

On average, the lowest significant enhancement in TTOC accounted for Sable Island with 0.5 DU (1%) and the largest occurred over Yarmouth with 1.2 DU (2.6%) followed by Narragansett and Montreal with 1.0 DU. The analysis shows that Trinidad head, Walsingham, Egbert, Montreal, Narragansett, Yarmouth, and Sable Island were significantly affected by fires. The enhancements over the sites nearer the large fire activities such as Bratt's Lake, Stony Plain, and Kelowna are positive but insignificant. Like the results presented in previous section, this analysis also showed none of the Arctic sites was affected significantly. Figure 5.18 shows the ozone enhancements in TTOC and 0-5 km over each site in 2006, 2008, 2010, and 2011. Consideration of smoke plume height influenced Sable Island the most by reducing the fire ozone contribution in 2008 from about 8% (4.0 DU) to 3% (1.4 DU), and reducing to non-significant the negative fire contribution in 2011. This assumption also lowered the ozone enhancements between 0.2 and 2.6 DU over other sites.

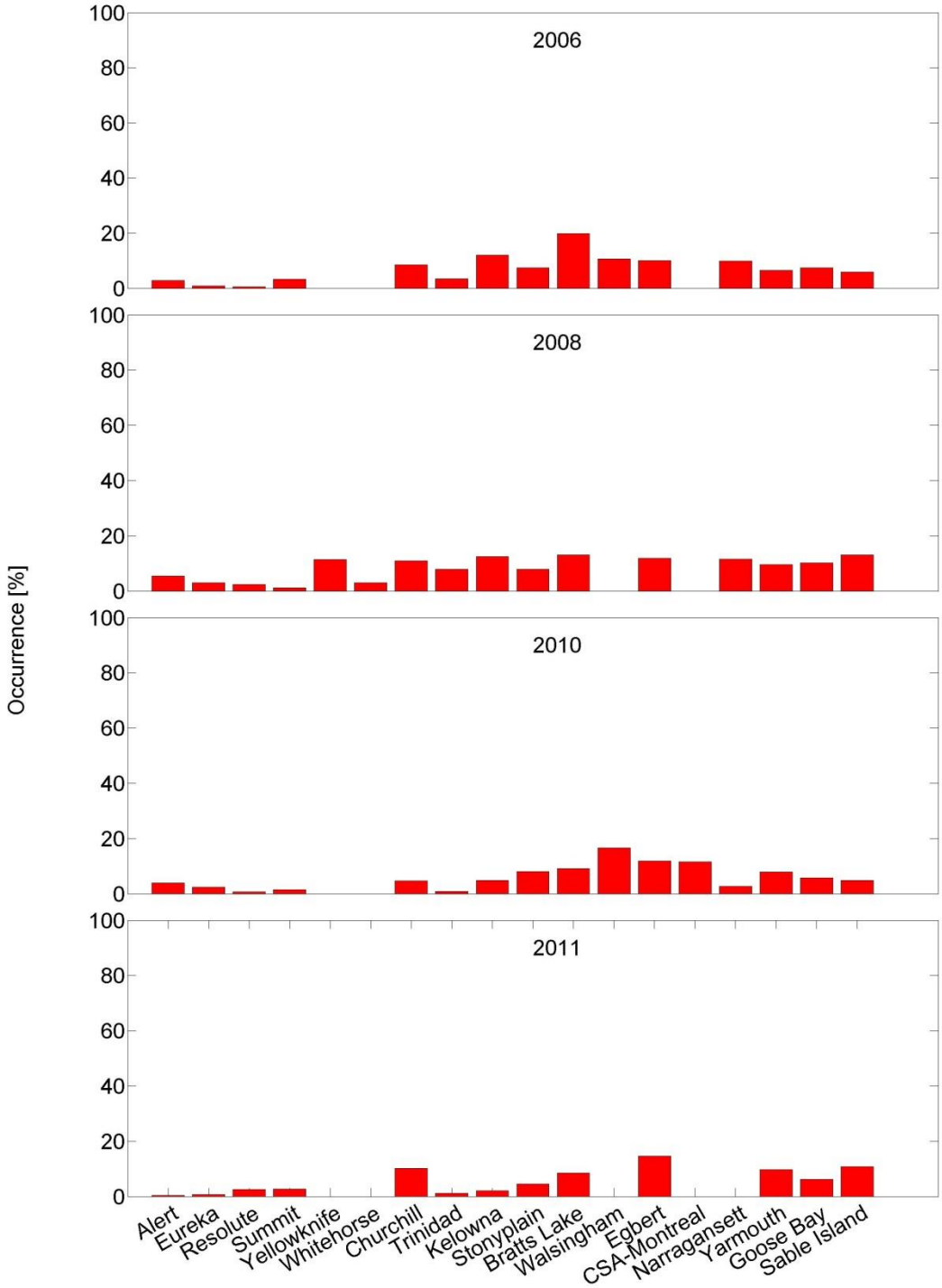

Figure 5.16: Number of fire-affected parcels given in percentage detected by DBT method in 2006, 2008, 2010, and 2011.

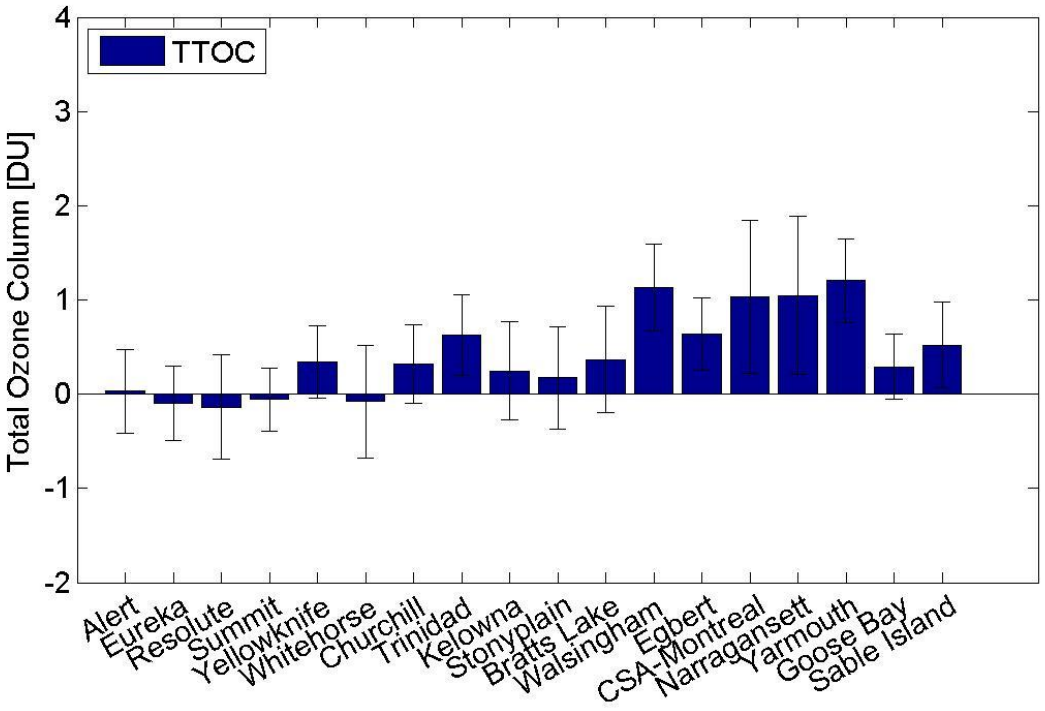

Figure 5.17: Average enhancement in total tropospheric ozone column at different sites over 2006, 2008, 2010, and 2011. Error bar equals 2 SE.

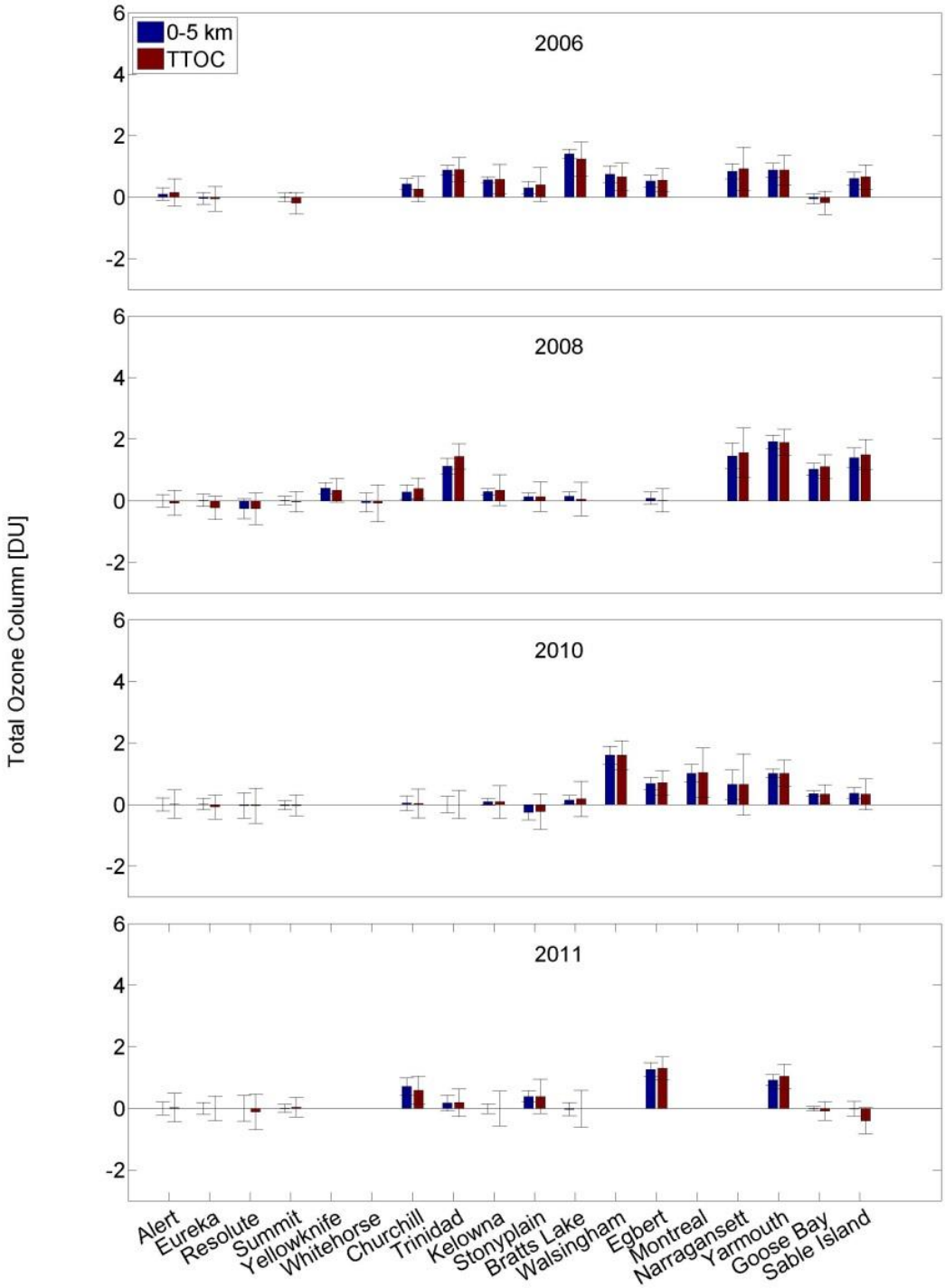

Figure 5.18: Same as Figure 5.15 but taking into account the fire plume injection heights.

5.3.3. Uncertainty due to regional bias in the origin of parcels

The origin of the parcels could be a source of error in this method. For instance, if many of the fire-affected parcels come from areas with higher background ozone levels (e.g. the southern US), while more fire-unaffected parcels originate from areas with low levels of background ozone, the results could show a significant difference that is not necessarily related to fire activity. Figure 5.19 shows the average total tropospheric column ozone for summer time 2000 to 2009 retrieved from the TOST (Trajectory-mapped Ozonesonde dataset for the Stratosphere and Troposphere) dataset [*Liu et al.*, 2013]. Regional averages (Figure 5.20) are also shown in lower left of the figure. As can be seen, there are higher ozone levels over the southern US and Mexico compared to other areas of North America. This is a potential source of error; if a large number of fire-affected parcels originate in these areas while the background parcels come from other clean areas such as northern latitudes a misleading positive signal may be seen at some sites.

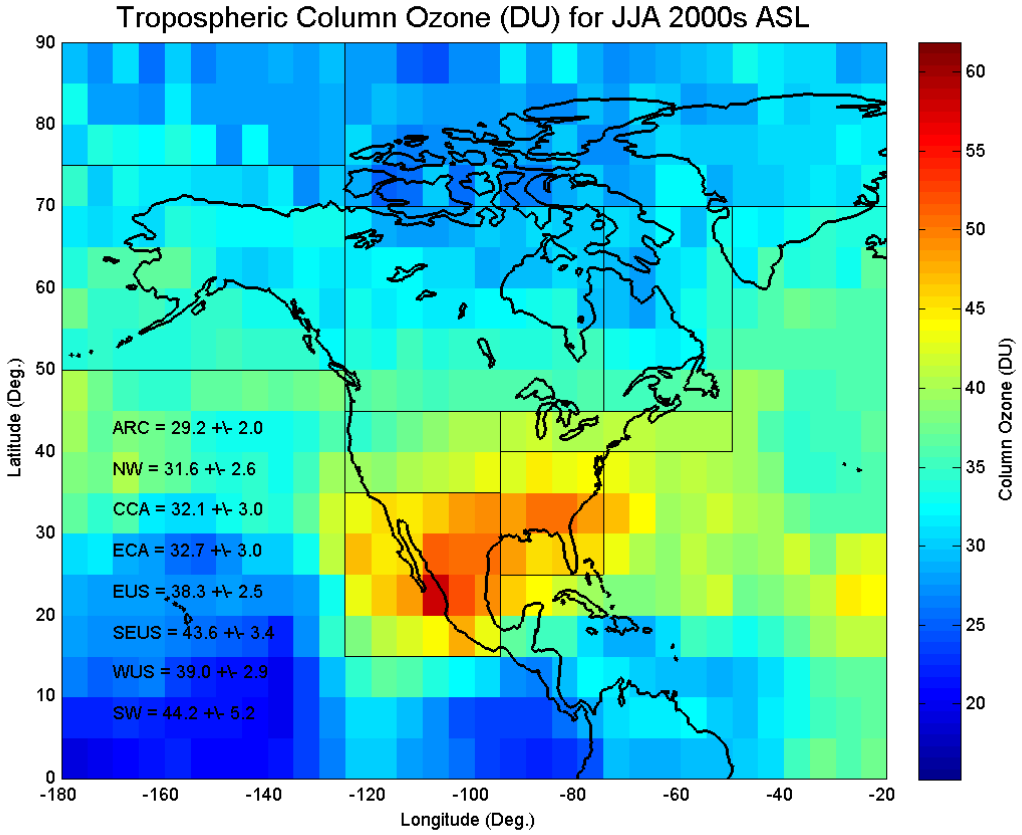

Figure 5.19: The average total tropospheric column ozone in DU for summertime 2000 to 2009 retrieved from the TOST dataset (more details in the text). ARC: Arctic; NW: Northwest America; CCA: Central Canada; ECA: East Canada; EUS: East US; SEUS: South east US; WUS: West US; SW: Southwest America;

The contribution of different regions in fire-affected and fire-unaffected parcels

To investigate the contribution of different areas in fire ozone enhancements six geographical regions were defined to tag the parcels based on their origins: Arctic (ARC); Northwest America (NW); Central Canada (CCA); East Canada (ECA); East US (EUS); South east US (SEUS); West US (WUS); Southwest America (SW) (Figure 5.20). The regions were selected based on similarities in ozone climatology and also the record of forest fires.

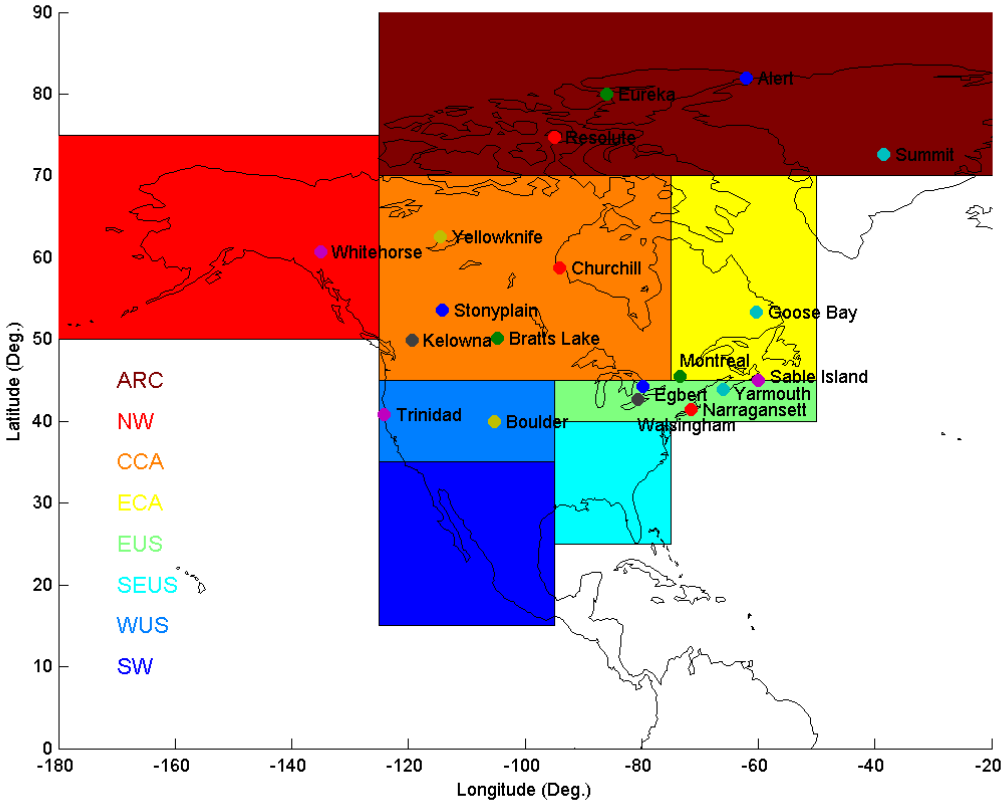

Figure 5.20: The location of stations assigned for ARC-IONS and BORTAS campaigns and defined areas to tag the parcels in different colors.

Figure 5.21 shows the origin of fire-affected parcels and also the baseline for Yarmouth in 2011. The top of the panel illustrates the number of the fire-affected parcels for each year. The number of unaffected parcels is also shown in the last column of the top panel. The rest of the six pie chart rows show the percentage contribution of each region in total number of parcels for six 24-hour periods prior to the ozonesonde lunch time (From 24 hours at the top to 144 hours at the bottom before the lunch time). In the first 24 hours, as is expected, the majority of the parcels are in the region of the site location (EUS) and nearby area (ECA).

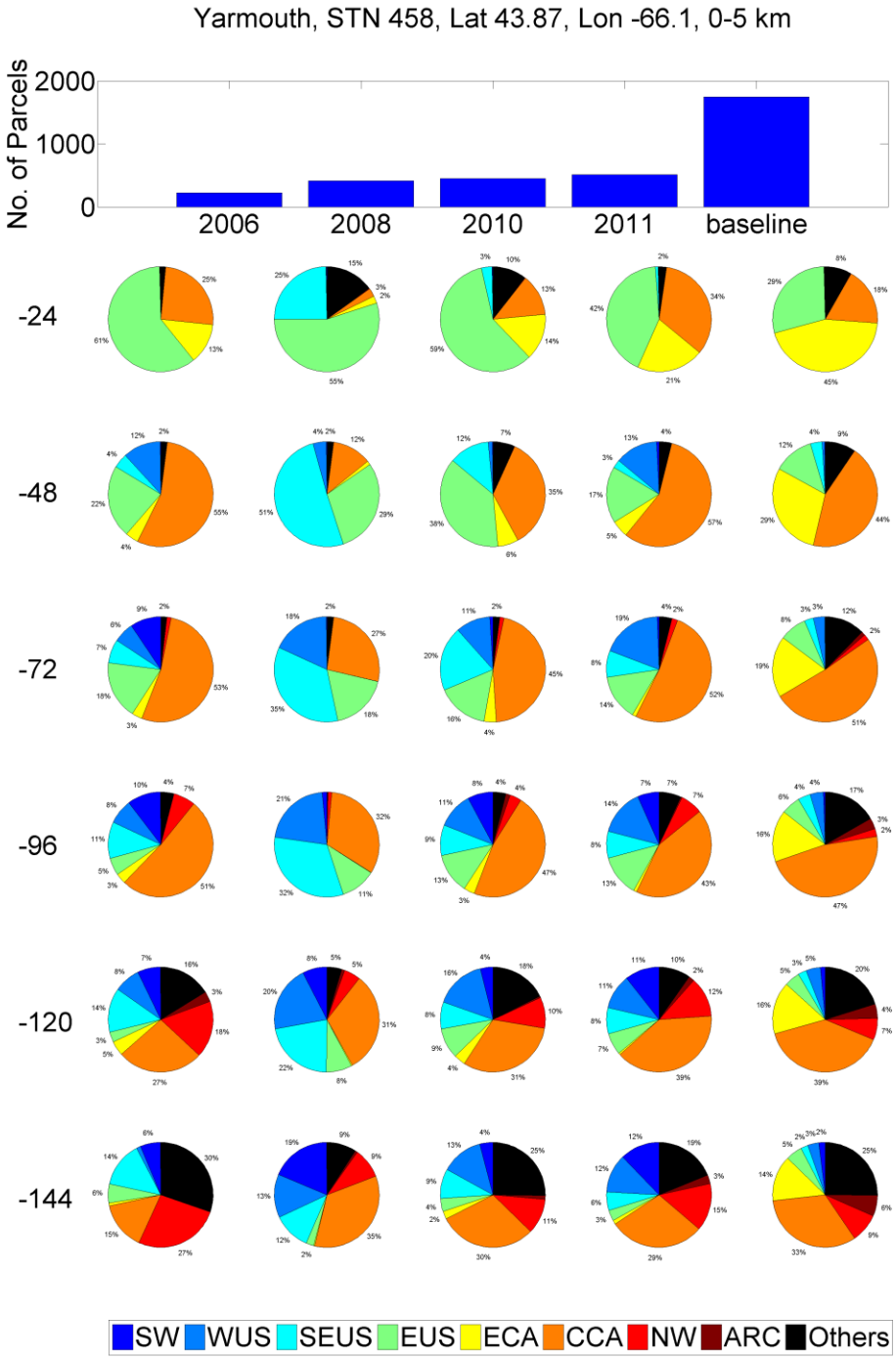

Figure 5.21: The number of fire-affected and unaffected parcels (Top) at Yarmouth for 2006, 2008, 2010 and 2011 from surface to 5km; Percent contribution of each tagged region to the number of fire-affected and unaffected parcels from age -24 to -144 (Bottom).

From the second time interval, the contribution of the Central Canada pixels (denoted by an orange color) starts to show and increase for the both fire-affected and unaffected parcels. Evidently, nearly half of the fire-affected and unaffected parcels originated from Central and Eastern Canada 96 hours (4 days) before the measurements.

As a test, only the parcels originating from Central Canada were considered to calculate the ozone enhancements at downwind sites. Figure 5.22 shows the contribution of each region in the number of fire-affected and unaffected parcels after setting the criteria. It can be seen that only parcels that have been in the CCA region (orange color) 72 hours before the launch time are used for calculations. Although this criterion excludes about half of the parcels, the results still show significant positive signals for downwind sites and also for the sites closer to the large fire activities. Figure 5.23 depicts the ozone enhancements in TTOC and 0 - 5 km at different sites in 2006, 2008, 2010, and 2011, considering only air parcels from the CCA region.

In another test, the trajectories that pass 40^{o}N latitude were removed from the calculations to prevent the influence of the low-level, high ozone amount from the Southern US and Mexico areas. This condition also reduced the number of parcels but it minimally affected the outcomes.

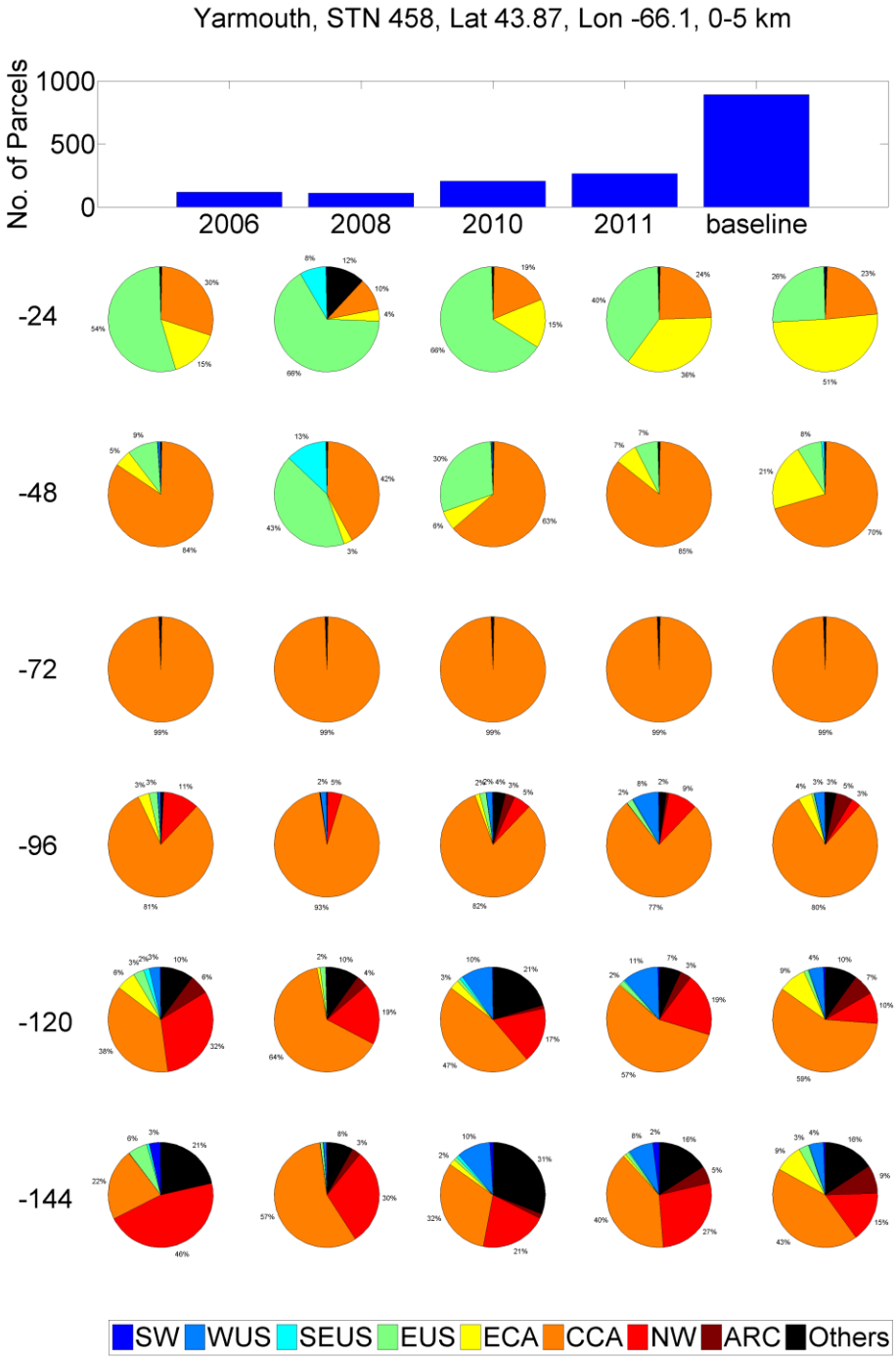

Figure 5.22: Same as Figure 5.21 after setting a criterion to consider only parcels that have been in CCA region (denoted by the orange color) 72 hours before launch time.

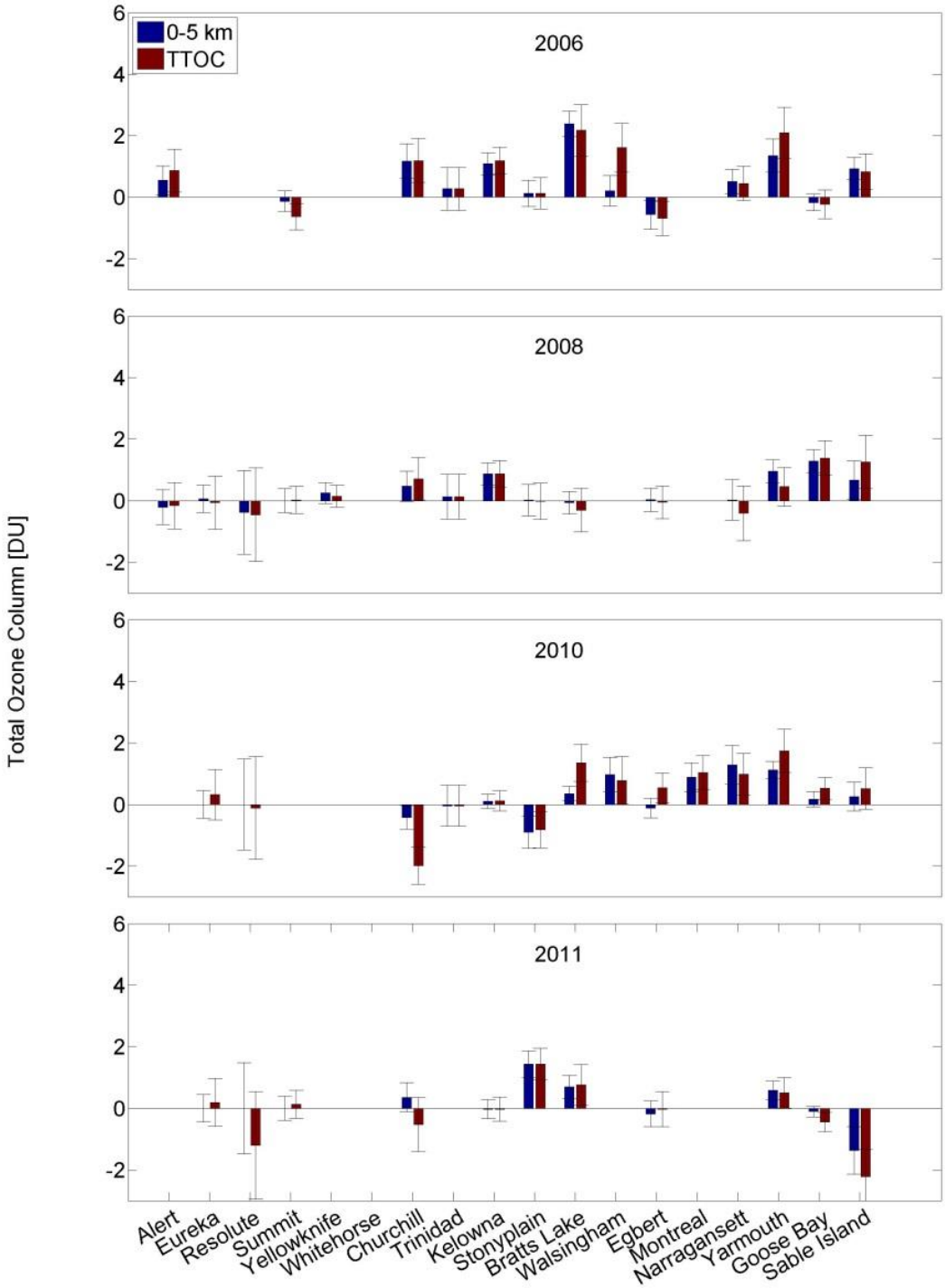

Figure 5.23: Average enhancement in 0 - 5 km and total tropospheric ozone column (TTOC), considering only air parcels from the CCA region, at different stations during the 2006, 2008 summers, expressed in DU.

Cluster analysis

In this section potential regional biases in the origins of fire-affected and unaffected air-parcels are addressed by employing a cluster analysis of the back-trajectories. HYSPLIT clustering tool is used to identify the most significant paths followed by the air parcels arriving over each site. HYSPLIT clustering computation is based on the minimum total spatial variance. The cluster spatial variance is the sum of the squared distances between the endpoints of the cluster's component trajectories and the mean of the trajectories in that cluster. The cluster spatial variance is calculated for every combination of trajectory pairs. Then the sum of all cluster spatial variances (TSV) is calculated and the pair with the lowest increase in total spatial variance is combined as a cluster [*Draxler et al.,* 2016]. Preliminary analysis using the back-trajectories ending at different altitude levels showed that the back-trajectories ending at 5 km can be a representative of the entire profile. In addition, it was revealed that usually maximum six main paths can be found for the parcels arriving at each site. Therefore, the back-trajectories ending at the 5 - km altitude level were grouped using the HYSPLIT clustering tool to identify the six most significant paths followed by the air parcels arriving over each site. Since at least 16 trajectories are needed for HYSPLIT trajectory tool to be run, the stations with less than 16 profiles (Whitehorse and CSA-Montreal) were excluded from this analysis.

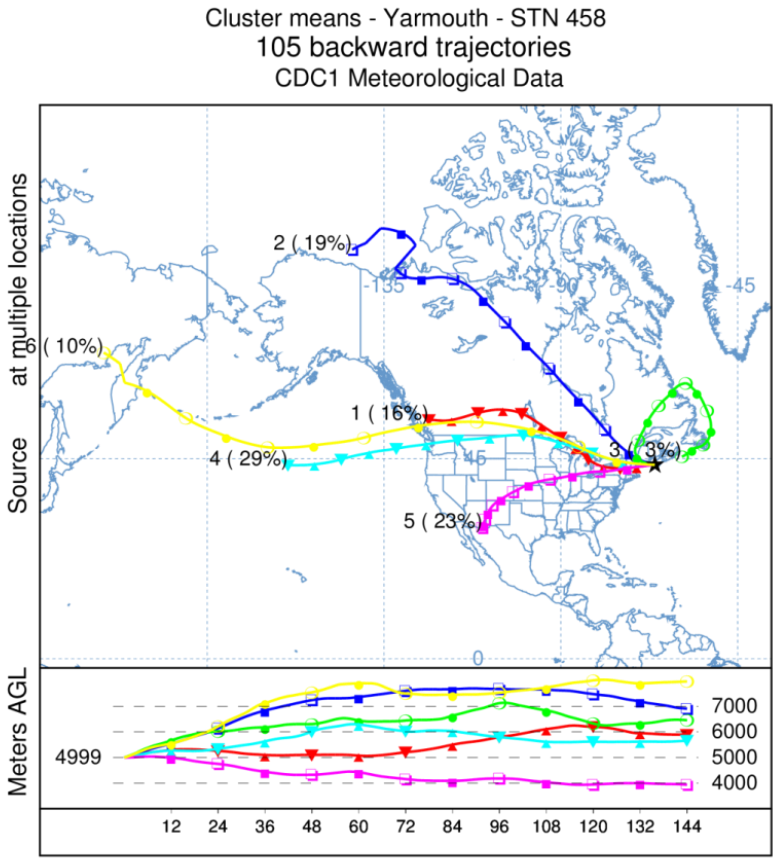

Figure 5.24: Cluster means calculated using profiles measured during the summers of 2006, 2008, 2010 and 2011. Back-trajectories calculated for parcels ending at 5 km at Yarmouth.

Figure 5.24 illustrates six different cluster means calculated for parcels ending at 5 km at Yarmouth and Figure 5.25 shows examples of the individual trajectories grouped in each cluster for two different sites. For each site one group of the trajectories originating from central Canada and one group originating from the Southern US are depicted.

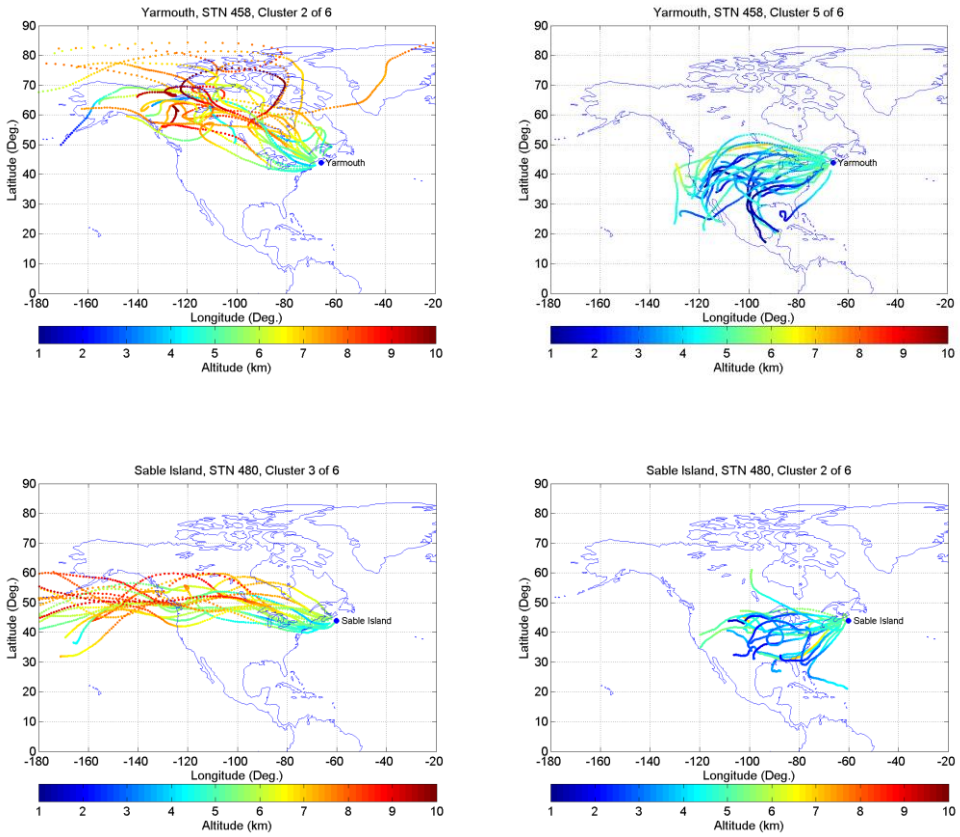

Figure 5.25: Back-trajectories for two different paths classified using HYSPLIT clustering analysis for Yarmouth and Sable Island. The Yarmouth cluster means can be seen in Figure 5.24.

To minimize the impact of the parcels originating from the Southern areas on calculations the profiles corresponding to the paths that come from the Southern US and Mexico are excluded from the calculations. The number of profiles grouped in each cluster is compiled in Table 5.4 for each individual site. A zero for the number of profiles shows that the respective cluster is excluded from the analysis. The total number of profiles remaining for each site, after removing excluded profiles, is also shown in percentage in Table 5.4. Less than 30% of profiles are removed from the calculations for most of the sites. The largest percentage of removed profiles corresponds to Egbert and Sable Island with 57% and 47% respectively.

Table 5.4: The number of profiles grouped in each cluster mean. The total number of profiles remaining for each site after removing the excluded profiles is also shown as a percentage.

Site Name	ID	Cluster 1	Cluster 2	Cluster 3	Cluster 4	Cluster 5	Cluster 6	Total	
Alert	18	7	13	9	3	8	3	43	(100%)
Eureka	315	10	18	5	7	6	4	50	(100%)
Resolute	24	5	4	6	1	8	5	29	(100%)
Summit	491	8	20	8	15	7	3	61	(100%)
Yellowknife	999	3	3	1	3	5	3	18	(100%)
Churchill	77	11	14	5	0	8	1	83	(87%)
Trinidad	445	35	14	0	0	23	7	51	(75%)
Kelowna	457	22	0	27	13	11	10	79	(90%)
Stonyplain	21	14	0	18	9	6	4	39	(85%)
Bratt's Lake	338	24	27	5	21	0	2	79	(71%)
Walsingham	482	0	3	4	6	0	0	13	(54%)
Egbert	456	10	17	0	0	0	12	30	(43%)
Narragansett	487	0	6	0	12	10	2	81	(56%)
Yarmouth	458	17	20	3	30	0	11	85	(77%)
Goose Bay	76	10	14	22	30	0	9	42	(98%)
Sable Island	480	0	0	19	4	12	7	30	(53%)

Figure 5.26 illustrates the ozone enhancements for different sites in 2006, 2008, 2010 and 2011 after removing the profiles originating from the Southern regions. While the fire ozone contribution to the TTOC is reduced for most of the sites it is still positive and significant for downwind sites. Narragansett was influenced more than other sites by the parcels coming from the southern areas. Ozone enhancements were reduced at Narragansett from 3.6 DU (8.0%) to 0.5 DU (1.0%) in 2010. Also, fire ozone decreased from 1.7 DU to 0.7 DU at Bratt’s Lake in 2010. Ozone enhancements slightly increased at Egbert and Walsingham in 2010. However, it should be noted that about 50% of the profiles were removed from the calculations for these two sites. Other downwind sites such as Yarmouth and Goose Bay were minimally affected.

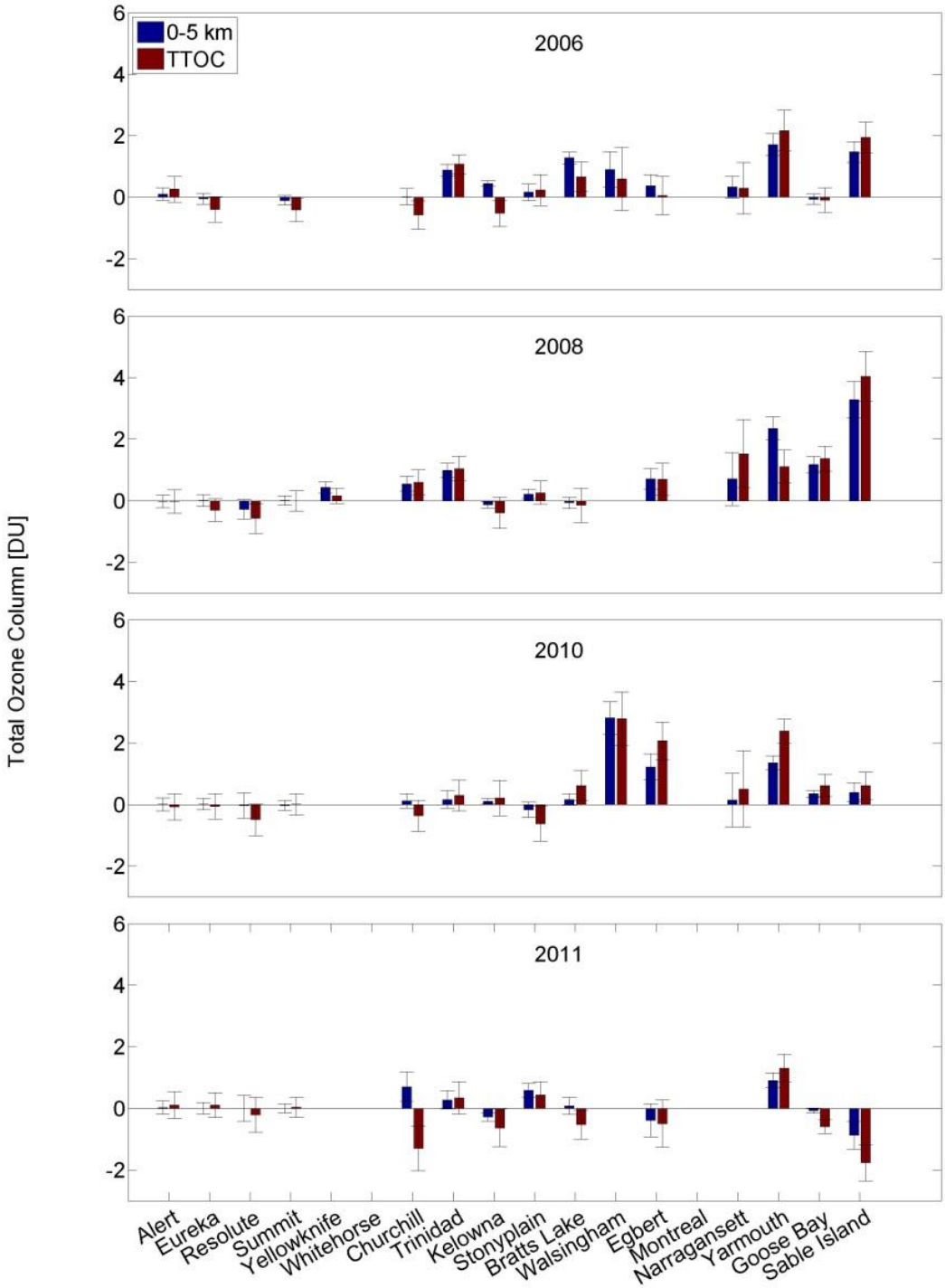

Figure 5.26: Same as Figure 5.15 after removing the profiles originating from the southern US and Mexico.

5.4. Summary and conclusions

Using more than 1000 ozone profiles collected at regular Canadian ozonesonde sites and through a number of campaigns in June to August 2006, 2008, 2010 and 2011, this study presents the fire-generated ozone budget in total tropospheric ozone column using the DBT (Differential Back Trajectory) method. This new method is suitable for evaluating the contribution of fire ozone to the tropospheric ozone budget as it uses a network of observing sites at fixed locations. The DBT method was applied to the data from 18 ozone sounding sites located across Canada and the U.S. The analyses show that none of the stations located at Arctic or Northern latitudes was significantly affected by North American fires. The ozone enhancement for stations near the large fires such as Trinidad, Bratt's Lake, Kelowna and Stony Plain was up to 4.8% of the TTOC. Fire ozone accounted for up 8.3% of TTOC at downwind sites such as Sable Island, Yarmouth, Narragansett and Walsingham. On average, over four years, the maximum fire ozone contribution accounted for about 2.0 DU at Narragansett and Yarmouth and the minimum significant ozone enhancement at downwind sites of 0.4 DU occurred at Goose Bay. However, we note that the DBT method likely produces an underestimate of ozone production by fires. Our analysis shows that sites nearer to the large fires were less influenced by the fires. Our results are consistent with the analyses that reported an increase in O_3 production with the age of the plume (e.g. [*Baylon et al.*, 2015; *Busilacchio et al.*, 2016; *Jaffe* and *Wigder*, 2012; *Parrington et al.*, 2013; *Real et al.*, 2007; *Teakles et al.*, 2016; *Val Martin et al.*, 2006; *Wigder et al.*, 2013]). Several different approaches were used to show that geographic differences in background ozone of the parcels do not greatly affect the results of the analysis presented in this study. These approaches including eliminating trajectories that cross certain latitudes (e.g. 40^o N or 50^o N) or

considering only parcels that cross Central Canada were used to address this issue and all confirmed the robustness of our the results. However, the criteria chosen for some of these approaches significantly reduced the number of trajectories making them less suitable to be used by the statistical DBT method.

The DBT method could be extended to the entire Canadian fire and ozone profile record using more than 50 years of ozonesonde and fire data collected from various sites across Canada to better quantify the impact of wildfires on tropospheric ozone, including a half-century of changes with time.

6. Conclusions

The overall theme of this research thesis is atmospheric ozone. It embraces three topics that are outstanding issues in ozone research: Error analysis of Brewer and Dobson ozone spectrophotometers, Improvements to the ACE-MAESTRO satellite measurements, and Estimating boreal fire-generated ozone over North America using ozonesonde measurements. These are addressed by:

1. Developing a physical model of the Dobson instrument and two types of Brewer spectrophotometer. The data collected by a Brewer MKIII and three Dobson instruments collocated at South Pole station also are compared to characterize the effect of stray light on the instrument measurements.
2. Implementing the HITRAN 2012 database into the MAESTRO retrieval software. Using the new spectroscopic parameters (from HITRAN 2012), 82 p-T retrievals were reprocessed and compared with the coincident ACE-FTS profiles and the earlier results with HITRAN 2004.

3. Developing a trajectory-based statistical method suitable for evaluating the contribution of fire ozone to the tropospheric ozone budget. This was developed and applied to more than 1000 ozonesonde profiles collected at 18 sites across North America during the summer of 2006, 2008, 2010, and 2011.

6.1. Summary of achievements

6.1.1. Brewer and Dobson error analysis

Physical models of the Dobson instrument and two types of Brewer spectrophotometer were developed using their parameterized slit functions and a forward model to help better understand the effects of stray light on ozone measurements. While the target accuracy for ground-based ozone measurements is 1%, the models show that the error caused by stray light for a typical single Brewer at large ozone slant paths can be up to 5%, and up to 25% for a Dobson using the AD pair. At 2000 DU OSP the discrepancy for a double Brewer is up to 0.8%, while for a Dobson using the CD-pair with a very low level of stray light (10^{-5}), it can be 1.8%. This effect usually restricts measurements at high latitudes, like polar stations, especially in the late winter and early spring when the ozone slant column is particularly large.

Stray light also can affect the calculation of ozone absorption coefficients. The analysis shows that using a measured slit function (instead of an idealized trapezoidal one) and taking into account the solar spectrum, leads to a 0.7% difference in calculated coefficients for a typical single Brewer. Using the parameterized slit functions from the measured slit functions of Dobson #83 the effect of stray light on the calculation of Dobson

ozone absorption coefficients was also examined. The analyses show the effect of a 10^{-5} level of stray light is negligible on absorption coefficient calculations, while for an instrument with 10^{-4} level of stray light the uncertainties could be up 4.0% and 6.9% for AD and CD coefficients respectively. Typical Dobson instruments likely have stray light levels between these two extremes.

For decades the Dobson community has faced unresolved discrepancies between the values deduced from AD and CD pairs when quasi-simultaneous measurements are made. The analysis presented in this study indicates that these differences are related to the level of stray light inside each individual Dobson instrument. Higher levels of stray light lead to larger differences between the values deduced from AD and CD wavelengths.

In this research also the influence of assuming a fixed ozone layer height on air mass calculations and its error contribution to the ozone retrieval were also examined. To calculate the ozone air mass both Brewer and Dobson retrievals assume a height for the ozone layer. The Brewer network uses a fixed height of 22 km for all sites while a variable ozone layer height changing with latitude is employed by the Dobson community. Because of the curvature of the Earth, the assumption of a 22 km height for the ozone layer causes a 2.2% difference in measured total column ozone, at an air mass of 5.4, from that calculated by assuming a 17 km height for the ozone layer, as in the Dobson analysis for the South Pole site.

Dobson total ozone measurements at South Pole show some dependence on OSP (Ozone Slant Path) when compare to quasi-simultaneous measurements of a double Mark III Brewer spectrophotometer. While the total ozone values deduced from Dobson AD pairs are generally 1% higher than those measured by the Brewer for OSPs lower than 800 DU, for

OSPs larger than 800 DU the Dobson AD measurements are lower than the Brewer values by up to 4% at 1400 DU OSP. The Dobson CD pair observations also show dependence on OSP. The CD values are, on average, 4% higher than those that quasi-simultaneously collected by the Brewer for almost entire air mass range of measurements. However, as is the case for the AD pair, the CD pair values also decrease at larger OSPs. It should be noted that Dobson measurements are not reported for air mass factors above 2.5 (AD pair) and 3.5 (CD pair) due to stray light.

6.1.2. Improvement to the MAESTRO measurements

The impact of new spectroscopic parameters contained in HITRAN 2012 on the MAESTRO p-T retrievals was examined. The MAESTRO preliminary pressure-temperature retrievals are reprocessed using the improved spectroscopic parameters from HITRAN 2012 database and compared with the ACE-FTS profiles and the processed results with HITRAN 2004. Three subsets of the occultations from Arctic winter and summer as well as the tropics are compared with coincident ACE-FTS profiles. The MAESTRO p-T profiles agree with the FTS profiles reasonably well. As had been shown before by *Nowlan* [2006] the RMS differences between measured MAESTRO and FTS pressures are usually within 2–10%, and temperatures within 5-10 K. However, large biases at certain altitudes strongly influence the RMS differences. These irregularities are related to a forward model underestimation of the signal near 30 km and a larger overestimation of the signal close to 20-25 km. As the density profile adjusts itself accordingly, the over- and underestimation of the signal results in poor MAESTRO retrievals near 20-30 km. The analysis presented here shows these irregularities are related to uncertainty in the O_2 spectroscopic parameters used in the retrieval. When the improved parameters contained in HITRAN 2012 are used as input for the forward model the

biases in pressure and temperatures are reduced by up to 2% and 2 K respectively. This is promising, since the O_2 bands spectroscopic parameters are still being improved as these bands are being increasingly considered for future satellite missions. In terms of RMS differences, 1% improvement in pressure and 1 K in temperature differences are expected below 50 km from the use of new spectroscopic parameters (HITRAN 2012).

6.1.3. Quantifying the impact of wildfires on tropospheric ozone concentrations

A unique method is developed to estimate the fire-generated ozone budget in tropospheric ozone. The Differential Back Trajectory (DBT) method is an objective method for evaluating the contribution of fire ozone to the tropospheric ozone budget as it uses a network of observing sites at fixed locations. The DBT method was applied to more than 1000 ozonesonde profiles collected at 18 ozone sounding sites located across Canada and U.S., through regular measurements and a number of summer campaigns in 2006, 2008, 2010 and 2011. The result do not show significant fire ozone enhancement at Arctic or northern latitude sites from North American fires. At stations near large fires such as Trinidad Head, Bratt's Lake, Kelowna and Stony Plain the ozone enhancement was up to 4.2±0.8% of the total tropospheric ozone column (TTOC). At downwind sites such as Sable Island, Yarmouth, Narragansett, and Walsingham fire ozone accounted for up 8.3±1.3% of the TTOC. The average over four years shows a maximum fire ozone contribution of 2 DU at Narragansett and Yarmouth and a minimum ozone enhancement at downwind sites of 0.4 DU at Goose Bay. The results of the analyses presented in this research are consistent with those of other studies that generally report an increase in O_3 production with the age of plume (e.g. [*Baylon*

et al., 2015; *Busilacchio et al.*, 2016; *Jaffe et al.*, 2013; *Jaffe* and *Wigder*, 2012; *Parrington et al.*, 2013; *Real et al.*, 2007; *Val Martin et al.*, 2006]). Several different approaches were used to show that geographic differences in background ozone of the parcels minimally affect the results of the analysis presented here.

6.2. Future work

Brewer and Dobson spectrophotometers

The goal of this research was to develop physical models of the Brewer and Dobson instruments to examine the effect of stray light on total ozone measurements. However, these models can be used to characterize the effects of other variables such as aerosol and Rayleigh scattering on total ozone measurements. In addition, the synthetic data generated using these models can be used to test methods that might be developed to correct the effects of the stray light.

In addition, the Brewer models can be used to estimate the relative uncertainties in total ozone measurements of specific Brewer instruments knowing their slit functions. As a result, it would be possible to estimate the maximum OSP at which a particular Brewer can make measurements with less than 1% uncertainty.

Next step could include re-analysis of the data collected at high-latitude sites. The re-analyzed data could be used for satellite data validation and also ozone trend analysis.

MAESTRO retrieval

Currently the MAESTRO retrievals rely on the pointing information derived from the FTS p-T retrievals. Any error in the pointing information will result in poor MAESTRO retrievals. Ideally the MAESTRO retrievals must be completely independent of those from the FTS. The p-T profile retrieved from O_2 number density could be used to derive the pointing information for MAESTRO. Future work could use the reprocessed pressure profiles to derive better pointing information for MAESTRO, which would improve MAESTRO ozone and other constituent profiles.

The retrieval algorithm developed for MAESTRO could also be used operationally to retrieve other constituents along with the p-T profile from each occultation. In addition, rewriting the software in the C language would improve the speed of retrievals for more than 14 years of MAESTRO measurements.

MAESTRO's high-vertical-resolution temperature profiles could be used as an independent data product for stratospheric temperature trend analysis. Moreover, the MAESTRO profile could be compared with the measurement of several different instruments including HALOE, SAGE III, and GPS missions.

Differential Back Trajectory method

The DBT method could be extended to the entire Canadian fire and ozone profile records. Using more than 50 years of ozonesonde and fire data collected from various sites across Canada this method could be used to better quantify the impact of wildfires on tropospheric ozone, including a half-century of changes with time.

Bibliography

Akimoto, H., (2003), Global Air Quality and Pollution, *Science*, *302*, 1716–1720.

Allraat, M. A. F., H. Kelder, and L. C. Heijboer, (1993), On The Relation Between Ozone and Potential Vorticity, *Geophys. Res. Lett.*, *20*(9), 811–814.

Alvarado, M. J., J. A. Logan, J. Mao, E. Apel, D. Riemer, D. Blake, R. C. Cohen, K. E. Min, A. E. Perring, E. C. Browne, P. J. Wooldridge, G. S. Diskin, G. W. Sachse, H. Fuelberg, W. R. Sessions, D. L. Harrigan, G. Huey, J. Liao, A. Case-Hanks, J. L. Jimenez, M. J. Cubison, S. A. Vay, A. J. Weinheimer, D. J. Knapp, D. D. Montzka, F. M. Flocke, I. B. Pollack, P. O. Wennberg, A. Kurten, J. Crounse, J. M. St. Clair, A. Wisthaler, T. Mikoviny, R. M. Yantosca, C. C. Carouge, and P. Le Sager, (2010), Nitrogen oxides and PAN in plumes from boreal fires during ARCTAS-B and their impact on ozone: An integrated analysis of aircraft and satellite observations, *Atmos. Chem. Phys.*, *10*(20), 9739–9760, doi:10.5194/acp-10-9739-2010.

Andreae, M. O., B. E. Anderson, D. R. Blake, J. D. Bradshaw, J. E. Collins, G. L. Gregory, G. W. Sachse, and M. C. Shipham, (1994), Influence of plumes from biomass burning on atmospheric chemistry over the equatorial and tropical South Atlantic during CITE 3, *J. Geophys. Res.*, *99*(D6), 12793–12808.

Andreae, M. O., and P. Merlet, (2001), Emission of trace gases and aerosols from biomass

burning, *Glob. Biodeochemical Cycles*, *15*(4), 955–966.

Andrews, D. G., J. R. Holton, and C. B. Leovy, (1987), Middle atmosphere dynamics, Academic press.

Anenberg, S. C., L. W. Horowitz, D. Q. Tong, and J. J. West, (2010), An Estimate of the Global Burden of Anthropogenic Ozone and Fine Particulate Matter on Premature Human Mortality Using Atmospheric Modeling, *Environ. Health Perspect.*, *118*(9), 1189–1195, doi:10.1289/ehp.0901220.

ASTM, E.-00a, (2014), Standard Solar Constant and Zero Air Mass Solar Spectral Irradiance Tables, *ASTM International*, West Conshohocken, PA.

Avnery, S., D. L. Mauzerall, J. Liu, and L. W. Horowitz, (2011), Global crop yield reductions due to surface ozone exposure : 1 . Year 2000 crop production losses and economic damage, *Atmos. Environ.*, *45*(13), 2284–2296, doi:10.1016/j.atmosenv.2010.11.045.

Backer, H., and D. Muer, (1991), Intercomparison of total ozone data measured with Dobson and Brewer ozone spectrophotometers at Uccle (Belgium) from January 1984 to March 1991, including zenith sky observations, *J. Geophys. Res.*, *96*(D11), 20711–20719, doi:199110.1029/91JD02159.

Bais, A. F., C. S. Zerefos, and C. T. McElroy, (1996), Solar UVB measurements with the double- and single-monochromator Brewer ozone spectrophotometers, *Geophys. Res. Lett.*, *23*(8), 833–836, doi:10.1029/96GL00842.

Barnes, J., and K. Mauersberger, (1987), Temperature Dependence of the Ozone Absorption Cross Section at the 253.7-nm Mercury Line, *J. Geophys. Res.*, *92*(D12), 14861–14864.

Basher, R. E., (1982a), Ozone Absorption Coefficients' Role in Dobson Instrument Ozone Measurement Accuracy, *Geophys. Res. Lett.*, *9*(11), 1235–1238.

Basher, R. E., (1982b), Review of the Dobson Spectrophotometer and its Accuracy, *WMO Global Ozone Research and Monitoring Project, Report No. 13*, World Meteorological Organization, Geneva, Switzerland.

Bass, A. M., and R. J. Paur, (1985), The Ultraviolet Cross-Sections of Ozone: I. The Measurements, in *Atmospheric Ozone*, pp. 606–610, Springer, Netherlands, doi:10.1007/978-94-009-5313-0_120.

Bates, D. R., (1984), Rayleigh-scattering by air, *Planet. Space Sci.*, *32*(6), 785–790, doi:10.1016/0032-0633(84)90102-8.

Bates, D. R., and M. Nicolet, (1950), Atmospheric Hydrogen, *Publ. Astron. Soc. Pacific*, *62*(366), 106–110.

Bates, D. V, (2005), Ambient Ozone and Mortality, *J. Epidemiol.*, *16*, 427–429, doi:10.1097/01.ede.0000165793.71278.ec.

Baylon, P., D. A. Jaffe, N. L. Wigder, H. Gao, and J. Hee, (2015), Ozone enhancement in western US wild fire plumes at the Mt. Bachelor Observatory : The role of NOx, *Atmos. Environ.*, *109*(x), 297–304, doi:10.1016/j.atmosenv.2014.09.013.

Bell, M. L., R. Goldberg, C. Hogrefe, P. L. Kinney, K. Knowlton, B. Lynn, J. Rosenthal, C. Rosenzweig, and J. A. Patz, (2007), Climate change, ambient ozone, and health in 50 US cities, *Clim. Change*, *82*, 61–76, doi:10.1007/s10584-006-9166-7.

Bell, M. L., A. Mcdermott, S. L. Zeger, and J. M. Samet, (2004), Ozone and Short-term Mortality in 95 US Urban Communities, *J. Am. Med. Assoc.*, *292*(19), 2372–2378.

Bernhard, G., R. D. Evans, G. J. Labow, and S. J. Oltmans, (2005), Bias in Dobson total ozone measurements at high latitudes due to approximations in calculations of ozone absorption coefficients and air mass, *J. Geophys. Res.*, *110*, D10305, doi:10.1029/2004JD005559.

Bhartia, P. K., D. Silberstein, B. Monosmith, and A. J. Fleig, (1985), Standard profiles of ozone from ground to 60 km obtained by combining satellite and ground based measurements, in *Atmospheric Ozone*, pp. 243–247, Springer, Netherlands.

Bloss, W. J., J. D. Lee, G. P. Johnson, R. Sommariva, D. E. Heard, J. M. C. Plane, G. Mcfiggans, H. Coe, M. Flynn, P. Williams, A. R. Rickard, and Z. L. Fleming, (2005), Impact of halogen monoxide chemistry upon boundary layer OH and HO2

concentrations at a coastal site, *Geophys. Res. Lett.*, *32*(L06814), 1–4, doi:10.1029/2004GL022084.

Bodhaine, B. A., N. B. Wood, E. G. Dutton, and J. R. Slusser, (1999), On Rayleigh Optical Depth Calculations, *J. Atmos. Sci. Ocean. Technol.*, *16*, 1854–1861, doi:10.1175/1520-0426(1999)016<1854:ORODC>2.0.CO;2.

Bogumil, K., J. Orphal, T. Homann, S. Voigt, P. Spietz, O. C. Fleischmann, A. Vogel, M. Hartmann, H. Kromminga, H. Bovensmann, and others, (2003), Measurements of molecular absorption spectra with the SCIAMACHY pre-flight model: instrument characterization and reference data for atmospheric remote-sensing in the 230-2380 nm region, *J. Photochem. Photobiol. A Chem.*, *157*(2), 167–184.

Bojkov, R. D., and V. E. Fioletov, (1996), Total Ozone Variations in the Tropical Belt : An Application for Quality of Ground Based Measurements, *Meteorol. Atmos. Phys.*, *58*, 223–240.

Boone, C. D., R. Nassar, K. A. Walker, Y. Rochon, S. D. McLeod, C. P. Rinsland, and P. F. Bernath, (2005), Retrievals for the atmospheric chemistry experiment Fourier-transform spectrometer., *Appl. Opt.*, *44*, 7218–7231, doi:10.1364/AO.44.007218.

Boone, C. D., K. A. Walker, and P. F. Bernath, (2013), Version 3 Retrievals for the Atmospheric Chemistry Experiment Fourier Transform Spectrometer (ACE-FTS), in *The Atmospheric Chemistry Experiment ACE at 10: A Solar Occultation Anthology*, pp. 103–127, A. Deepak Publishing, Hampton, Virg.

Bowman, K., (1989), Global Patterns of the Quasi-biennial Oscillation in Total Ozone, *J. Atmos. Sci.*, *46*(21), 3328–3343.

Brasseur, G., and M. H. Hitchman, (1988), Stratospheric response to trace gas perturbations: Changes in ozone and temperature distributions, *Science*, *240*(4852), 634–638.

Brewer, A. W., (1949), Evidence for a world circulation provided by the measurements of Helium and Water vapour distribution in the stratosphere, *Q. J. R. Meteorol. Soc.*, *75*(326), 351–363.

Brewer, A. W., (1973), A replacement for the Dobson spectrophotometer?, *Pure Appl. Geophys.*, *106–108*(1), 919–927, doi:10.1007/BF00881042.

Brewer MKIII Spectrophotometer Operators Manual, (2005), KIPP & ZONEN, Delftechpark, the Netherlands.

Brewer MKIV Spectrophotometer Operator's Manual, (1999), SCI-TEC Instruments Inc., Saskatoon, Sask. , Canada.

Brion, J., A. Chakir, D. Daumont, J. Malicet, and C. Parisse, (1993), High-resolution laboratory absorption cross section of O3. Temperature effect, *Chem. Phys. Lett.*, *213*(5–6), 610–612, doi:10.1016/0009-2614(93)89169-I.

Bruhl, C., J. Lelieveld, P. J. Crutzen, and H. Tost, (2012), The role of carbonyl sulphide as a source of stratospheric sulphate aerosol and its impact on climate, *Atmos. Chem. Phys.*, *12*, 1239–1253, doi:10.5194/acp-12-1239-2012.

Busilacchio, M., P. Di Carlo, E. Aruffo, F. Biancofiore, C. D. Salisburgo, F. Giammaria, S. Bauguitte, J. Lee, S. Moller, J. Hopkins, S. Punjabi, S. Andrews, A. C. Lewis, M. Parrington, P. I. Palmer, E. Hyer, and G. M. Wolfe, (2016), Production of peroxy nitrates in boreal biomass burning plumes over Canada during the BORTAS campaign, *Atmos. Chem. Phys.*, *16*(5), 3485–3497, doi:10.5194/acp-16-3485-2016.

Butchart, N., and A. A. Scaife, (2001), Removal of chlorouorocarbons by increased mass exchange between the stratosphere and troposphere in a changing climate, *Nature*, *410*, 799–803.

Butchart, N., A. A. Scaife, M. Bourqui, J. De Grandpre, S. H. E. Hare, J. Kettleborough, U. Langematz, E. Manzini, F. Sassi, K. Shibata, D. Shindell, and M. Sigmond, (2006), Simulations of anthropogenic change in the strength of the Brewer – Dobson circulation, *Clim. Dyn.*, *27*(7–8), 727–741, doi:10.1007/s00382-006-0162-4.

Chameides, W., and J. C. C. Walker, (1973), A Photochemical Theory Tropospheric Ozone, *J. Geophys. Res.*, *78*(36), 8751–8760.

Chance, K., and R. L. Kurucz, (2010), An improved high-resolution solar reference spectrum

for earth's atmosphere measurements in the ultraviolet, visible, and near infrared, *J. Quant. Spectrosc. Radiat. Transf.*, *111*(9), 1289–1295, doi:10.1016/j.jqsrt.2010.01.036.

Chandra, S., and R. D. Mcpeters, (1994), The solar cycle variation of ozone in the stratosphere inferred from Nimbus 7 and NOAA 11 satellites, *J. Geophys. Res.*, *99*(D10), 20665–20671.

Chandra, S., and S. Stolarski, (1991), RECENT TRENDS IN STRATOSPHERIC TOTAL OZONE : IMPLICATiONS OF DYNAMICAL AND EL CHICHON PERTURBATIONS, *Geophys. Res. Lett.*, *18*(12), 2277–2280.

Chapman, S., (1930), XXXV. On ozone and atomic oxygen in the upper atmosphere, *London, Edinburgh, Dublin Philos. Mag. J. Sci.*, *10*(64), 369–383.

Charney, J. G., and P. G. Drazin, (1961), Propagation of Planetary-Scale Disturbances from the Lower into the Upper Atmosphere, *J. Geophys. Res.*, *66*(1), 83–109.

Chatfield, R., and H. Harrison, (1976), Ozone in the remote troposphere: mixing versus photochemistry, *J. Geophys. Res.*, *81*(3), 421–423.

Chossière, G. P., R. Malina, A. Ashok, B. Ford, R. A. Silva, J. J. West, Y. Zhang, S. C. Anenberg, D. T. Shindell, W. J. Collins, S. Dalsoren, G. Faluvegi, G. Folberth, L. W. Horowitz, T. Nagashima, V. Naik, S. Rumbold, and R. Skeie, (2013), Global premature mortality due to anthropogenic outdoor air pollution and the contribution of past climate change, *Environ. Res. Lett.*, *8*(34005), 1–11, doi:10.1088/1748-9326/8/3/034005.

Colette, A., G. Ancellet, and F. Borchi, (2005), Impact of vertical transport processes on the tropospheric ozone layering above Europe. Part I: Study of air mass origin using multivariate analysis, clustering and trajectories, *Atmos. Environ.*, *39*(29), 5409–5422, doi:10.1016/j.atmosenv.2005.06.014.

Cooper, O. R., (2010), Increasing springtime ozone mixing ratios in the free troposphere over western North America, *Nature*, *463*, 344–348, doi:10.1038/nature08708.

Cooper, O. R., D. D. Parrish, J. Ziemke, N. V. Balashov, M. Cupeiro, I. E. Galbally, S. Gilge, L. Horowitz, N. R. Jensen, J.-F. Lamarque, V. Naik, S. J. Oltmans, J. Schwab, D. T.

Shindell, A. M. Thompson, V. Thouret, Y. Wang, and R. M. Zbinden, (2014), Global distribution and trends of tropospheric ozone: An observation-based review, *Elem. Sci. Anthr.*, *2*(29), 1–29, doi:10.12952/journal.elementa.000029.

Crisp, D., C. E. Miller, and P. L. DeCola, (2008), NASA Orbiting Carbon Observatory: measuring the column averaged carbon dioxide mole fraction from space, *J. Appl. Remote Sens.*, *2*, 23508, doi:10.1117/1.2898457.

Crutzen, P. J., (1970), Influence of Nitrogen Oxides on the Atmospheric Ozone Content, *Q. J. R. Meteorol. Soc.*, *96*, 320–325.

Crutzen, P. J., (1971), Ozone Production Rates in an Oxygen-Hydrogen-Nitrogen Oxide Atmosphere P., *J. Geophys. Res.*, *76*, 7311–7327.

Crutzen, P. J., (1974), Estimates of Possible Future Ozone Reductions from Continued Use of Fluoro-Chloro-Methanes (CF2Cl2, CFCL3), *Geophys. Res. Lett.*, *1*(5), 205–208.

Crutzen, P. J., L. E. Heidt, J. P. Krasnec, W. H. Pollock, and W. Seiler, (1979), Biomass burning as a source of atmospheric gases CO, H2, N2O, NO, CH3Cl and COS, *Nature*, *282*(5736), 253–256.

Daniel, J. S., S. Solomon, H. L. Miller, a O. Langford, R. W. Portmann, and C. S. Eubank, (2003), Retrieving cloud information from passive measurements of solar radiation absorbed by molecular oxygen and O2-O2, *J. Geophys. Res.*, *108*(D16), 1–12, doi:10.1029/2002JD002994.

Danielsen, E., (1968), Startospheric-Tropospheric Exchange Based on Radioactivity, Ozone and Potential Vorticity, *J. Atmos. Sci.*, *25*, 502–518.

Darrall, N. M., (1989), The effect of air pollutants on physiological processes in plants, *Plant. Cell Environ.*, *12*(1), 1–30.

Daumont, D., J. Brion, J. Charbonnier, and J. Malicet, (1992), Ozone UV spectroscopy I: Absorption cross-sections at room temperature, *J. Atmos. Chem.*, *15*(2), 145–155, doi:10.1007/BF00053756.

Deshler, T., J. L. Mercer, H. G. J. Smit, R. Stubi, G. Levrat, B. J. Johnson, S. J. Oltmans, R. Kivi, A. M. Thompson, J. Witte, J. Davies, F. J. Schmidlin, G. Brothers, and T. Sasaki, (2008), Atmospheric comparison of electrochemical cell ozonesondes from different manufacturers, and with different cathode solution strengths: The Balloon Experiment on Standards for Ozonesondes, *J. Geophys. Res.*, *113*(4), 1–17, doi:10.1029/2007JD008975.

Diallo, M., B. Legras, and A. Ch, (2012), Age of stratospheric air in the ERA-Interim, *Atmos. Chem. Phys.*, *12*, 12133–12154, doi:10.5194/acp-12-12133-2012.

Dobson, G. M. B., (1929), Measurements of the Amount of Ozone in the Earth's Atmosphere and Its Relation to Other Geophysical Conditions. Part III, in *Proceedings of Royal Society of London. Series A, Containing Papers of a Mathematical and Physical Character*, Vol. 122, pp. 456–486, Royal Society.

Dobson, G. M. B., (1931), A Photoelectric spectrophotometer for measuring the amount of atmospheric ozone, in *Proceedings of the Physical Society*, Vol. 43, pp. 324–339, doi:10.1088/0959-5309/43/3/308.

Dobson, G. M. B., (1956), Origin and Distribution of the Polyatomic Molecules in the Atmosphere, in *Proceedings of the Royal Society of London . Series A, Mathematical and Physical*, Vol. 236, pp. 187–193, Royal Society.

Dobson, G. M. B., (1973), The laminated structure of the ozone in the atmosphere, *Q. J. R. Meteorol. Soc.*, *99510*(99), 599–607, doi:10.1002/qj.49709942202.

Downey, A., J. D. Jasper, J. J. Gras, and S. Whittlestone, (1990), Lower tropospheric transport over the Southern Ocean, *J. Atmos. Chem.*, *11*(1–2), 43–68, doi:10.1007/BF00053667.

Draxler, R. R., and G. D. Hess, (1998), An Overview of the HYSPLIT_4 Modelling System for Trajectories, Dispersion, and Deposition., *Aust. Meteorol. Mag.*, *47*, 295–308.

Draxler, R. R., B. Stunder, G. Rolph, A. Stein, and A. Taylor, (2016), HYSPLIT4 User 's Guide, *NOAA Air Resour. Lab.*

Engström, a, and L. Magnusson, (2009), Estimating trajectory uncertainties due to flow dependent errors in the atmospheric analysis, *Atmos. Chem. Phys. Discuss.*, *9*(4), 15747–15767, doi:10.5194/acp-9-8857-2009.

EPA, U. S., (2009), Assessment of the impacts of global change on regional US air quality: a synthesis of climate change impacts on ground-level ozone, *USEP Agency. Washington, DC*.

Evans, R., and W. Komhyr, (2008), Operations Handbook - Ozone Observations with a Dobson Spectrophotometer, *WMO/GAW Report No. 183*, World Meteorological Organization, Geneva, Switzerland.

Evans, R., G. McConville, S. Oltmans, I. Petropavlovskikh, and D. Quincy, (2009), Measurement of internal stray light within Dobson ozone spectrophotometers, *Int. J. Remote Sens.*, *30*(15), 4247–4258, doi:10.1080/01431160902825057.

Eyring, V., I. Cionni, G. E. Bodeker, D. E. Kinnison, J. F. Scinocca, and D. W. Waugh, (2010), Multi-model assessment of stratospheric ozone return dates and ozone recovery in CCMVal-2 models, *Atmos. Chem. Phys.*, *10*, 9451–9472, doi:10.5194/acp-10-9451-2010.

Fabian, P., and P. G. Pruchniewicz, (1977), Meridional Distribution of Ozone in the Troposphere and Its Seasonal Variations, *J. Geophys. Res.*, *82*(15), 2063–2073.

Farman, J. C., B. G. Gardiner, and J. D. Shanklin, (1985), Large losses of total ozone in Antarctica reveal seasonal ClOx/NOx interaction, *Nature*, *315*(6016), 207–210.

Fioletov, V. E., (2008), Ozone climatology , trends , and substances that control, *Atmos. Ocean*, *46*(1), 39–67, doi:10.3137/ao.460103.

Fioletov, V. E., J. B. Kerr, C. T. McElroy, D. I. Wardle, V. Savastiouk, and T. S. Grajnar, (2005), The Brewer reference triad, *Geophys. Res. Lett.*, *32*, L20805, doi:10.1029/2005GL024244.

Fioletov, V. E., J. B. Kerr, D. I. Wardle, and E. Wu, (2000), Correction of stray light for the Brewer single monochromator, in *Proceedings of Quadrennial Ozone Symposium*, Vol.

21, pp. 369–370, Sapporo, Japan.

Forster, P. M., V. Ramaswamy, P. Artaxo, T. Berntsen, R. Betts, D. W. Fahey, J. Haywood, J. Lean, D. C. Lowe, G. Myhre, J. Nganga, R. Prinn, G. Raga, M. Schulz, and R. Van Dorland, (2007), Changes in Atmospheric Constituents and in Radiative Forcing, in *Climate Change 2007: The Physical Science Basis. Contribution of Working Group I to the Fourth Assessment Report of the Intergovernmental Panel on Climate Change*, pp. 129–234, Cambridge University Press, Cambridge, United Kingdom and New York, NY, USA.

Fragkos, K., A. F. Bais, D. Balis, C. Meleti, and M. E. Koukouli, (2015), The Effect of Three Different Absorption Cross-Sections and their Temperature Dependence on Total Ozone Measured by a Mid-Latitude Brewer Spectrophotometer, *Atmos. Ocean*, *53*(1), 19–28, doi:10.1080/07055900.2013.847816.

Frankenberg, C., A. Butz, and G. C. Toon, (2011), Disentangling chlorophyll fluorescence from atmospheric scattering effects in O2 A-band spectra of reflected sun-light, *Geophys. Res. Lett.*, *38*(3), 1–5, doi:10.1029/2010GL045896.

Freitas, S. R., K. M. Longo, R. Chatfield, D. Latham, M. A. F. S. Dias, M. O. Andreae, E. Prins, and F. E. G. Unesp, (2007), Including the sub-grid scale plume rise of vegetation fires in low resolution atmospheric transport models, *Atmos. Chem. Phys.*, *7*, 3385–3398.

Fromm, M. D., and R. Servranckx, (2003), Transport of forest fire smoke above the tropopause by supercell convection, *Geophys. Res. Lett.*, *30*(10), 1–4, doi:10.1029/2002GL016820.

Furukawa, P. M., P. L. Haagenson, and M. J. Scharberg, (1967), A Composite, High-Resolution Solar Spectrum from 2080 to 3600 A, *NCAR TN-26*, National Center for Atmospheric Research, Boulder, Colo.

Garcia-Comas, M., B. Funke, A. Gardini, T. Von Clarmann, and G. Stiller, (2014), MIPAS temperature from the stratosphere to the lower thermosphere : Comparison of vM21

with ACE-FTS , MLS , OSIRIS , SABER , SOFIE and lidar measurements, *Atmos. Meas. Tech.*, *7*, 3633–3651, doi:10.5194/amt-7-3633-2014.

Gille, J., J. Barnett, P. Arter, M. Barker, P. Bernath, C. Boone, C. Cavanaugh, J. Chow, M. Coffey, J. Craft, C. Craig, M. Dials, V. Dean, T. Eden, D. P. Edwards, G. Francis, C. Halvorson, L. Harvey, C. Hepplewhite, R. Khosravi, D. Kinnison, C. Krinsky, A. Lambert, H. Lee, L. Lyjak, J. Loh, W. Mankin, S. Massie, J. Mcinerney, J. Moorhouse, B. Nardi, D. Packman, C. Randall, J. Reburn, W. Rudolf, M. Schwartz, J. Serafin, K. Stone, B. Torpy, K. Walker, A. Waterfall, R. Watkins, J. Whitney, D. Woodard, and G. Young, (2008), High Resolution Dynamics Limb Sounder : Experiment overview , recovery , and validation of initial temperature data, *J. Geophys. Res.*, *113*(D16S43), 1–23, doi:10.1029/2007JD008824.

Gillett, N. P., and D. W. J. Thompson, (2003), Simulation of Recent Southern Hemisphere Climate Change, *Science*, *302*, 273–276.

Gillett, N. P., A. J. Weaver, F. W. Zwiers, and M. D. Flannigan, (2004), Detecting the effect of climate change on Canadian forest fires, *Geophys. Res. Lett.*, *31*(18), doi:10.1029/2004GL020876.

Goody, R., R. West, L. Chen, and D. Crisp, (1989), The correlated-k method for radiation calculations in nonhomogeneous atmospheres, *J. Quant. Spectrosc. Radiat. Transf.*, *42*(6), 539–550, doi:10.1016/0022-4073(89)90044-7.

Gordon, I. E., L. S. Rothman, and G. C. Toon, (2011), Revision of spectral parameters for the B- and -bands of oxygen and their validation against atmospheric spectra, *J. Quant. Spectrosc. Radiat. Transf.*, *112*(14), 2310–2322, doi:10.1016/j.jqsrt.2011.05.007.

Granier, C., B. Bessagnet, T. Bond, A. D. Angiola, H. D. Van Der Gon, G. J. Frost, A. Heil, J. W. Kaiser, S. Kinne, Z. Klimont, S. Kloster, and J. Lamarque, (2011), Evolution of anthropogenic and biomass burning emissions of air pollutants at global and regional scales during the 1980 – 2010 period, *Clim. Chang.*, *109*, 163–190, doi:10.1007/s10584-011-0154-1.

Haagen-Smit, A. J., C. E. Bradley, and M. M. Fox, (1952), Formation of ozone in Los Angeles smog, in *Proceedings of the Second National Air Pollution Symposium*, pp. 54–56.

Hansen, G., and S. Trond, (2005), Multilinear regression analysis of the 65-year Tromsø total ozone series, *J. Geophys. Res.*, *110*(D10103), 1–11, doi:10.1029/2004JD005387.

Hansen, J. E., and L. D. Travis, (1974), Light scattering in planetary atmospheres, *Space Sci. Rev.*, *16*(4), 527–610.

Hansen, P. C., (1992), Analysis of discrete ill-posed problems by means of the L-curve, *SIAM Rev.*, *34*(4), 561–580.

Harris, J. M., R. R. Draxler, and S. J. Oltmans, (2005), Trajectory model sensitivity to differences in input data and vertical transport method, *J. Geophys. Res. D Atmos.*, *110*(14), 1–8, doi:10.1029/2004JD005750.

Hartley, W. N., (1881), On the Absorption Spectrum of Ozone, *J. Chem. Soc.*, 57–60.

Hartmann, D. J., A. M. G. Klein Tank, M. Rusticucci, L. V Alexander, S. Brönnimann, Y. A.-R. Charabi, F. J. Dentener, E. J. Dlugokencky, D. R. Easterling, A. Kaplan, B. J. Soden, P. W. Thorne, M. Wild, and P. Zhai, (2013), Observations: Atmosphere and Surface, in *Climate Change 2013: The Physical Science Basis. Contribution of Working Group I to the Fifth Assessment Report of the Intergovernmental Panel on Climate Change*, pp. 159–254, doi:10.1017/CBO9781107415324.008.

Hauglustaine, D. A., G. P. Brasseur, S. Walters, P. J. Rasch, J. Mfiller, L. K. Ernrnons, and M. A. Carroll, (1998), MOZART, a global chemical transport model for ozone and related chemical tracers 2. Model results and evaluation, *J. Geophys. Res.*, *103*(D21), 28291–28335.

Haver, P. Van, and D. De Muer, (1996), Climatology of tropopause folds at midlatitudes, *Geophys. Res. Lett.*, *23*(9), 1033–1036.

Havey, D. K., D. A. Long, M. Okumura, C. E. Miller, and J. T. Hodges, (2009), Ultra-sensitive optical measurements of high-J transitions in the O2 A-band, *Chem. Phys.*

Lett., *483*(1–3), 49–54, doi:10.1016/j.cplett.2009.10.067.

Hegglin, M. I., and T. G. Shepherd, (2009), Large climate-induced changes in ultraviolet index and stratosphere-to-troposphere ozone flux, *Nat. Geosci.*, *2*(10), 687–691.

Holton, J. R., (1987), The production of temporal variability in trace constituent concentrations, in *Transport processes in the middle atmosphere*, pp. 313–326, Springer.

Holton, J. R., P. H. Haynes, M. E. Mcintyre, A. R. Douglass, and B. Rood, (1995), Stratosphere-Troposphere Exchange, *Rev. Geophys.*, *33*(4), 403–439.

Hood, L. L., and S. Zhou, (1999), Stratospheric effects of 27-day solar ultraviolet variations : The column ozone response and comparisons of solar cycles 21 and 22, *J. Geophys. Res.*, *104*(D21), 473–479.

Huang, M., K. W. Bowman, G. R. Carmichael, R. Bradley Pierce, H. M. Worden, M. Luo, O. R. Cooper, I. B. Pollack, T. B. Ryerson, and S. S. Brown, (2013), Impact of Southern California anthropogenic emissions on ozone pollution in the mountain states: Model analysis and observational evidence from space, *J. Geophys. Res. Atmos.*, *118*(22), 12784–12803, doi:10.1002/2013JD020205.

IPCC, (2013), Climate Change 2013 – Contribution of Working Group 1 to the Fifth Assessment Report of the Intergovernmental Panel on Climate Change; The Physical Science Basis, Cambridge University Press, Cambridge, United Kingdom and New York, NY, USA.

Jacob, D. J., (2000), Heterogeneous chemistry and tropospheric ozone, *Atmos. Environ.*, *34*, 2131–2159.

Jacob, D. J., J. H. Crawford, H. Maring, A. D. Clarke, J. E. Dibb, L. K. Emmons, R. A. Ferrare, C. A. Hostetler, P. B. Russell, H. B. Singh, A. M. Thompson, G. E. Shaw, E. McCauley, J. R. Pederson, and J. A. Fisher, (2010), The arctic research of the composition of the troposphere from aircraft and satellites (ARCTAS) mission: Design, execution, and first results, *Atmos. Chem. Phys.*, *10*(11), 5191–5212, doi:10.5194/acp-10-5191-2010.

Jacob, D. J., B. G. Heikes, S. Fan, J. A. Logan, D. L. Mauzerall, H. B. Singh, G. L. Gregory, R. W. Talbot, D. R. Blake, J. Et, and A. L. Photochemistry, (1996), Origin of ozone and NOx in the tropical troposphere : A photochemical analysis of aircraft observations over the South Atlantic basin, *J. Geophys. Res. Atmos.*, *101*(D19), 24235–24250.

Jaffe, D. A., I. Bertschi, L. Jaeglé, P. Novelli, J. S. Reid, H. Tanimoto, R. Vingarzan, and D. L. Westphal, (2004), Long-range transport of Siberian biomass burning emissions and impact on surface ozone in western North America, *Geophys. Res. Lett.*, *31*(16), 6–9, doi:10.1029/2004GL020093.

Jaffe, D. A., N. Wigder, N. Downey, P. Gabriele, A. Boynard, and S. B. Reid, (2013), Impact of Wild fi res on Ozone Exceptional Events in the Western U.S., *Environ. Sci. Technol.*, *47*, 11065–11072.

Jaffe, D. A., and N. L. Wigder, (2012), Ozone production from wildfires: A critical review, *Atmos. Environ.*, *51*, 1–10, doi:10.1016/j.atmosenv.2011.11.063.

Jerrett, M., R. T. Burnett, and C. A. Pope III, (2009), Long-Term Ozone Exposure and Mortality, *N. Engl. J. Med.*, *360*(11), 1085–1095.

Junge, C. E., (1962), Global ozone budget and exchange between stratosphere and troposphere, *Tellus XIV*, *14*(4), 363–377, doi:10.3402/tellusa.v14i4.9563.

Kahn, R. A., Y. Chen, D. L. Nelson, F. Leung, Q. Li, D. J. Diner, and J. A. Logan, (2008), Wildfire smoke injection heights : Two perspectives from space, *Geophys. Res. Lett.*, *35*(L04809), 1–4, doi:10.1029/2007GL032165.

Kaiser, J. W., A. Heil, M. O. Andreae, A. Benedetti, N. Chubarova, L. Jones, J. Morcrette, and M. Razinger, (2012), Biomass burning emissions estimated with a global fire assimilation system based on observed fire radiative power, *Bio Geosci.*, *9*, 527–554, doi:10.5194/bg-9-527-2012.

Kangasjärvi, J., J. Talvinen, M. Utriainen, and R. Karjalainen, (1994), Plant defence systems induced by ozone, *Plant. Cell Environ.*, *17*(7), 783–794.

Kasischke, E. S., and M. R. Turetsky, (2006), Recent changes in the fire regime across the

North American boreal region — Spatial and temporal patterns of burning across Canada and Alaska, *Geophys. Res. Lett.*, *33*, doi:10.1029/2006GL025677.

Kerr, J. B., (2002), New methodology for deriving total ozone and other atmospheric variables from Brewer spectrophotometer direct sun spectra, *J. Geophys. Res.*, *107*(23), 1–17, doi:10.1029/2001JD001227.

Kerr, J. B., I. A. Asbridge, and W. F. J. Evans, (1988), Intercomparison of total ozone measured by the Brewer and Dobson spectrophotometers at Toronto, *J. Geophys. Res.*, *93*(D9), 11129–11140, doi:198810.1029/JD093iD09p11129.

Kerr, J. B., H. Fast, and C. McElroy, (1994), The 1991 WMO international ozonesonde intercomparison at Vanscoy, Canada, *Atmos. Ocean*, *32*(4), 685–716, doi:10.1080/07055900.1994.9649518.

Kerr, J. B., and C. T. McElroy, (2000), Aberration Correction in the Brewer Spectrophotometer, *Radiat. Prot. Dosimetry*, *91*, 133–138, doi:10.1093/oxfordjournals.rpd.a033182.

Kerr, J. B., C. T. McElroy, and R. A. Olafson, (1981), Measurements of ozone with the Brewer ozone spectrophotometer, in *Quadrennial Ozone Symposium*, pp. 74–79, National Center for Atmospheric Research, Boulder, Colo.

Komhyr, W. D., (1969), Electrochemical concentration cells for gas analysis, *Ann. Geophys*, *25*(1), 203–210.

Komhyr, W. D., (1980), Dobson Spectrophotometer Systematic Total Ozone Measurement Error, *Geophys. Res. Lett.*, *7*(2), 161–163.

Komhyr, W. D., R. D. Grass, and R. K. Leonard, (1989), Dobson Spectrophotometer 83: A Standard for Total Ozone Measurements, 1962-1987, *J. Geophys. Res.*, *94*(D90), 9847–9861, doi:http://dx.doi.org/10.1029/JD094iD07p09847.

Komhyr, W. D., C. L. Mateer, and R. D. Hudson, (1993), Effective Bass-Paur 1985 Ozone Absorption Coefficients for Use With Dobson Ozone Spectrophotometers, *J. Geophys. Res.*, *98*(D11), 20451–20456, doi:10.1029/93JD00602.

Kuhlmann, R. Von, M. G. Lawrence, P. J. Crutzen, and P. J. Rasch, (2003), A model for studies of tropospheric ozone and nonmethane hydrocarbons : Model description and ozone results, *J. Geophys. Res. Atmos.*, *108*(D9), doi:10.1029/2002JD002893.

Kuze, A., and K. V Chance, (1994), Analysis of cloud top height and coverage from satellites using the O2 A and B band, *J. Geophys. Res.*, *99*(2), 14481–14491.

Labonne, M., (2007), Injection height of biomass burning aerosols as seen from a spaceborne lidar, *Geophys. Res. Lett.*, *34*(L11806), 1–5, doi:10.1029/2007GL029311.

Lacis, A., and V. Oinas, (1991), A Description of the Correlated k Distribution Method for Modeling Nongray Gaseous Absorption, Thermal Emission, and Multiple Scattering in Vertically Inhomogeneous Atmospheres, *J. Geophys. Res.*, *96*(D5), 9027–9063, doi:10.1029/90JD01945.

Lantz, K., P. Disterhoft, E. Early, A. Thompson, J. Deluisi, J. Berndt, L. Harrison, P. Kiedron, J. Ehramjian, G. Bernhard, L. Cabasug, J. Robertson, W. Mou, T. Taylor, J. Slusser, D. Bigelow, B. Durham, G. Janson, D. Hayes, M. Beaubien, and A. Beaubien, (2002), The 1997 North American Interagency Intercomparison of Ultraviolet Spectroradiometers Including Narrowband Filter Radiometers, *J. Res. Natl. Institue Stand. Technol.*, *107*, 19–62.

Levy, R., Y. J. Chiu, and H. L. Cromroy, (1972), Effects of ozone on three species of Diptera, *Environ. Entomol.*, *1*(5), 608–611.

Lin, M., L. W. Horowitz, O. R. Cooper, D. Tarasick, S. Conley, L. T. Iraci, B. Johnson, T. Leblanc, I. Petropavlovskikh, and E. L. Yates, (2015), Revisiting the evidence of increasing springtime ozone mixing ratios in the free troposphere over western North America, *Geophys. Res. Lett.*, *42*, 1–10, doi:10.1002/2015GL065311.Received.

Lin, P., Q. Fu, S. Solomon, and J. M. Wallace, (2009), Temperature Trend Patterns in Southern Hemisphere High Latitudes : Novel Indicators of Stratospheric Change, *J. Clim.*, *22*(23), 6325–6341, doi:10.1175/2009JCLI2971.1.

Lin, X., M. Trainer, and S. C. Liu, (1988), On the Nonlinearity of the Tropospheric Ozone

Production, *J. Geophys. Res.*, *93*(D12), 15879–15888.

Liou, K.-N., (2002), An introduction to atmospheric radiation, Vol. 84, Academic press.

Lippmann, M., (1991), Health Effects of Tropospheric Ozone, *Environ. Sci. Technol.*, *25*(12), 1954–1962, doi:10.1021/es00180a002.

Liu, G., J. Liu, D. W. Tarasick, V. E. Fioletov, J. J. Jin, O. Moeini, X. Liu, C. E. Sioris, and M. Osman, (2013), A global tropospheric ozone climatology from trajectory-mapped ozone soundings, *Atmos. Chem. Phys.*, *13*(21), 10659–10675, doi:10.5194/acp-13-10659-2013.

Liu, J., D. W. Tarasick, V. E. Fioletov, C. McLinden, T. Zhao, S. Gong, C. Sioris, J. J. Jin, G. Liu, and O. Moeini, (2013), A global ozone climatology from ozone soundings via trajectory mapping: A stratospheric perspective, *Atmos. Chem. Phys.*, *13*(22), 11441–11464, doi:10.5194/acp-13-11441-2013.

Long, D. A., D. K. Havey, M. Okumura, C. E. Miller, and J. T. Hodges, (2010), O2 A-band line parameters to support atmospheric remote sensing, *J. Quant. Spectrosc. Radiat. Transf.*, *111*(14), 2021–2036, doi:10.1016/j.jqsrt.2010.05.011.

Long, D. A., D. K. Havey, S. S. Yu, M. Okumura, C. E. Miller, and J. T. Hodges, (2011), O2 A-band line parameters to support atmospheric remote sensing. Part II: The rare isotopologues, *J. Quant. Spectrosc. Radiat. Transf.*, *112*(16), 2527–2541, doi:10.1016/j.jqsrt.2011.07.002.

Lovelock, J. E., (1974), Atmospheric Halocarbons and Atratospheric Ozone, *Nature*, *252*.

Malicet, J., D. Daumont, J. Charbonnier, C. Parisse, A. Chakir, and J. Brion, (1995), Ozone UV spectroscopy. II. Absorption cross-sections and temperature dependence, *J. Atmos. Chem.*, *21*(3), 263–273, doi:10.1007/BF00696758.

Mamun, A., J. Kaminski, A. Lupu, K. Semeniuk, and J. C. McConnell, (2013), Evaluation of stratospheric temperature and water vapor from GEM using ACE-FTS and MLS measurements, in *The Atmospheric Chemistry Experiment ACE at 10: A Solar Occultation Anthology*, pp. 295–302, A. Deepak Publishing, Hampton, Virg.

Marshall, B. T., L. E. Deaver, R. E. Thompson, L. L. Gordley, M. J. McHugh, M. E. Hervig, and J. M. Russell III, (2011), Retrieval of temperature and pressure using broadband solar occultation: SOFIE approach and results, *Atmos. Meas. Tech.*, *4*(5), 893.

Mauzerall, D. L., and X. Wang, (2001), Protecting Agricultural Crops from the Effects of Tropospheric Ozone Exposure: Reconciling Science and Standard Setting in the United States, Europe, and Asia, *Annu. Rev. Energy Environ.*, *26*(1), 237–268.

McConnell, R., K. Berhane, F. Gilliland, S. J. London, T. Islam, W. J. Gauderman, E. Avol, H. G. Margolis, and J. M. Peters, (2002), Asthma in exercising children exposed to ozone: A cohort study, *Lancet*, *359*(9304), 386–391, doi:10.1016/S0140-6736(02)07597-9.

McElroy, C. T., C. R. Nowlan, J. R. Drummond, P. F. Bernath, D. V Barton, D. G. Dufour, C. Midwinter, R. B. Hall, A. Ogyu, A. Ullberg, D. I. Wardle, J. Kar, J. Zou, F. Nichitiu, C. D. Boone, K. a Walker, and N. Rowlands, (2007), The ACE-MAESTRO instrument on SCISAT: description, performance, and preliminary results., *Appl. Opt.*, *46*(20), 4341–4356, doi:10.1364/AO.46.004341.

McElroy, M. B., R. J. Salawitch, S. C. Wofsy, and J. A. Logan, (1986), Reductions of Antarctic ozone due to synergistic interactions of chlorine and bromine, *Nature*, *321*(6072), 759–762.

McIntyre, M. E., and T. N. Palmer, (1983), Breaking planetary waves in the stratosphere, *Nature*, *305*(5935), 593–600.

Mckendry, I., K. Strawbridge, M. L. Karumudi, N. O. Neill, A. M. Macdonald, R. Leaitch, D. Jaffe, and P. Cottle, (2011), Californian forest fire plumes over Southwestern British Columbia: lidar, sunphotometry, and mountaintop chemistry observations, *Atmos. Chem. Phys.*, *11*, 465–477, doi:10.5194/acp-11-465-2011.

McLandress, C., T. G. Shepherd, J. F. Scinocca, D. A. Plummer, M. Sigmond, A. Jonsson, and M. C. Reader, (2011), Separating the Dynamical Effects of Climate Change and Ozone Depletion . Part II : Southern Hemisphere Troposphere, *J. Clim.*, *24*, 1850–1868,

doi:10.1175/2010JCLI3958.1.

Mclinden, C. A., S. C. Olsen, B. Hannegan, O. Wild, and M. J. Prather, (2000), Stratospheric ozone in 3-D models: A simple chemistry and the cross-tropopause flux, *J. Geophys. Res.*, *105*(D11), 14653–14665.

Meyer, J., A. Bracher, A. Rozanov, A. C. Schlesier, H. Bovensmann, and J. P. Burrows, (2005), Solar occultation with SCIAMACHY: algorithm description and first validation, *Atmos. Chem. Phys.*, *5*, 1589–1604.

Molina, L. T., and M. J. Molina, (1987), Production of Cl202 from the Self-Reaction of the ClO Radical, *J. Phys. Chem.*, *91*(2), 433–436, doi:10.1021/j100286a035.

Monks, P. S., (2000), A review of the observations and origins of the spring ozone maximum, *Atmos. Environ.*, *34*, 3545–3561.

Monks, P. S., (2005), Gas-phase radical chemistry in the troposphere, *Chem. Soc. Rev.*, *34*, 376–395, doi:10.1039/b307982c.

Monks, P. S., A. T. Archibald, A. Colette, O. Cooper, M. Coyle, R. Derwent, D. Fowler, and C. Granier, (2015), Tropospheric ozone and its precursors from the urban to the global scale from air quality to short-lived climate forcer, *Atmos. Chem. Phys.*, 8889–8973, doi:10.5194/acp-15-8889-2015.

Monks, P. S., C. Granier, S. Fuzzi, A. Stohl, M. L. Williams, H. Akimoto, M. Amann, A. Baklanov, U. Baltensperger, … D. Simpson, (2009), Atmospheric composition change – global and regional air quality, *Atmos. Environ.*, *43*, 5268–5350, doi:10.1016/j.atmosenv.2009.08.021.

Montreal protocol on substances that deplete the ozone layer, (1987), US Government Printing Office, Washington, DC.

Myhre, G., D. Shindell, F.-M. Bréon, W. Collins, J. Fuglestvedt, J. Huang, D. Koch, J.-F. Lamarque, D. Lee, B. Mendoza, and others, (2013), Anthropogenic and natural radiative forcing, *Clim. Chang.*, *423*, 658–740.

Newell, R. E., V. Thouret, J. Y. N. Cho, P. Stoller, A. Marenco, and H. G. Smit, (1999), Ubiquity of quasi-horizontal layers in the troposphere, *Nature*, *398*(6725), 316–319, doi:10.1038/18642.

Newman, P. A., S. R. Kawa, and E. R. Nash, (2004), On the size of the Antarctic ozone hole, *Geophys. Res. Lett.*, *31*(L21104), 1–4, doi:10.1029/2004GL020596.

Nowlan, C. R., (2006), Atmospheric Temperature and Pressure Measurements from the ACE-MAESTRO Space Instrument, *PhD thesis*, University of Toronto.

Nowlan, C. R., J. R. Drummond, C. T. Mcelroy, and D. V Barton, (2013), Solar Occultation Measurements of Atmospheric Pressure and Temperature from the A - and B -bands of Molecular Oxygen, in *The Atmospheric Chemistry Experiment ACE at 10: A Solar Occultation Anthology*, pp. 261–270, A. Deepak Publishing, Hampton, Virg.

Nowlan, C. R., C. T. McElroy, and J. R. Drummond, (2007), Measurements of the O2 A- and B-bands for determining temperature and pressure profiles from ACE–MAESTRO: Forward model and retrieval algorithm, *J. Quant. Spectrosc. Radiat. Transf.*, *108*(3), 371–388, doi:10.1016/j.jqsrt.2007.06.006.

Olson, J. R., J. H. Crawford, W. Brune, J. Mao, X. Ren, A. Fried, B. Anderson, E. Apel, M. Beaver, D. Blake, G. Chen, J. Crounse, J. Dibb, G. Diskin, S. R. Hall, L. G. Huey, D. Knapp, D. Richter, D. Riemer, J. St. Clair, K. Ullmann, J. Walega, P. Weibring, A. Weinheimer, P. Wennberg, and A. Wisthaler, (2012), An analysis of fast photochemistry over high northern latitudes during spring and summer using in-situ observations from ARCTAS and TOPSE, *Atmos. Chem. Phys.*, *12*(15), 6799–6825, doi:10.5194/acp-12-6799-2012.

Olson, J. R., J. H. Crawford, D. D. Davis, G. Chen, M. A. Avery, J. D. W. Barrick, G. W. Sachse, S. A. Vay, S. T. Sandholm, D. Tan, I. C. Faloona, B. G. Heikes, R. E. Shetter, B. L. Lefer, H. B. Singh, R. W. Talbot, and D. R. Blake, (2001), Seasonal differences in the photochemistry of the South Pacific : A comparison of observations and model results from PEM-Tropics A and B, *J. Geophys. Res.*, *106*(D23), 32749–32766.

Oltmans, S. J., A. S. Lefohn, D. Shadwick, J. M. Harris, H. E. Scheel, I. Galbally, D. W. Tarasick, B. J. Johnson, E. Brunke, H. Claude, G. Zeng, S. Nichol, F. Schmidlin, J. Davies, E. Cuevas, A. Redondas, H. Naoe, T. Nakano, and T. Kawasato, (2013), Recent tropospheric ozone changes e A pattern dominated by slow or no growth, *Atmos. Environ.*, *67*, 331–351, doi:10.1016/j.atmosenv.2012.10.057.

Osman, M. K., D. W. Tarasick, J. Liu, O. Moeini, V. Thouret, and V. E. Fioletov, (2016), Carbon monoxide climatology derived from the trajectory mapping of global MOZAIC-IAGOS data, *Atmos. Chem. Phys.*, *16*, 10263–10282, doi:10.5194/acp-16-10263-2016.

Palmer, P. I., M. Parrington, J. D. Lee, A. C. Lewis, A. R. Rickard, P. F. Bernath, T. J. Duck, D. L. Waugh, D. W. Tarasick, … J. C. Young, (2013), Quantifying the impact of BOReal forest fires on Tropospheric oxidants over the Atlantic using Aircraft and Satellites (BORTAS) experiment: Design, execution and science overview, *Atmos. Chem. Phys.*, *13*(13), 6239–6261, doi:10.5194/acp-13-6239-2013.

Parrington, M., P. I. Palmer, D. K. Henze, D. W. Tarasick, E. J. Hyer, R. C. Owen, D. Helmig, C. Clerbaux, K. W. Bowman, M. N. Deeter, E. M. Barratt, P. F. Coheur, D. Hurtmans, Z. Jiang, M. George, and J. R. Worden, (2012), The influence of boreal biomass burning emissions on the distribution of tropospheric ozone over North America and the North Atlantic during 2010, *Atmos. Chem. Phys.*, *12*(4), 2077–2098, doi:10.5194/acp-12-2077-2012.

Parrington, M., P. I. Palmer, A. C. Lewis, J. D. Lee, A. R. Rickard, P. Di Carlo, J. W. Taylor, J. R. Hopkins, S. Punjabi, D. E. Oram, G. Forster, E. Aruffo, S. J. Moller, J. B. S. Bauguitte, J. D. Allan, H. Coe, and R. J. Leigh, (2013), Ozone photochemistry in boreal biomass burning plumes, *Atmos. Chem. Phys.*, *13*(15), 7321–7341, doi:10.5194/acp-13-7321-2013.

Parrish, D. D., K. S. Law, J. Staehelin, R. Derwent, O. R. Cooper, H. Tanimoto, A. Volz-Thomas, S. Gilge, H. E. Scheel, M. Steinbacher, and E. Chan, (2013), Lower tropospheric ozone at northern midlatitudes: Changing seasonal cycle, *Geophys. Res. Lett.*, *40*(8), 1631–1636, doi:10.1002/grl.50303.

Paugam, R., M. Wooster, S. Freitas, and M. V. Martin, (2016), A review of approaches to estimate wildfire plume injection height within large-scale atmospheric chemical transport models, *Atmos. Chem. Phys.*, *16*, 907–925, doi:10.5194/acp-16-907-2016.

Penndorf, R., (1957), Tables of the Refractive Index for Standard Air and the Rayleigh Scattering Coefficient for the Spectral Region between 0.2 and 20.0 μ and Their Application to Atmospheric Optics, *J. Opt. Soc. Am.*, *47*(2), 176–182.

Pfister, G. G., L. K. Emmons, P. G. Hess, R. Honrath, J. F. Lamarque, M. Val Martin, R. C. Owen, M. A. Avery, E. V. Browell, J. S. Holloway, P. Nedelec, R. Purvis, T. B. Ryerson, G. W. Sachse, and H. Schlager, (2006), Ozone production from the 2004 North American boreal fires, *J. Geophys. Res.*, *111*(24), 1–13, doi:10.1029/2006JD007695.

Pfister, G. G., C. Wiedinmyer, and L. K. Emmons, (2008), Impacts of the fall 2007 California wildfires on surface ozone: Integrating local observations with global model simulations, *Geophys. Res. Lett.*, *35*(19), L19814, doi:10.1029/2008GL034747.

Picone, J. M., A. E. Hedin, and D. P. Drob, (2002), NRLMSISE-00 empirical model of the atmosphere : Statistical comparisons and scientific issues, *J. Geophys. Res.*, *107*(A12), 1–16, doi:10.1029/2002JA009430.

Pitari, G., S. Palermi, G. Visconti, and R. G. Prinn, (1992), Ozone Response to a CO2 Doubling' Results From a Stratospheric Circulation Model With Heterogeneous Chemistry, *J. Geophys. Res.*, *97*(D5), 5953–5962.

Pitts, M. C., and L. W. Thomason, (2003), SAGE III temperature and pressure retrievals: initial results, in *Proceedings of SPIE*, pp. 62–70, doi:10.1117/12.463004.

Planck, M., (1901), On the Law of the Energy Distribution in the Normal Spectrum, *Ann. Phys.*, *4*(553), 1–11.

Plumb, R. A., (2002), Stratospheric Transport, *J. Meteorol. Soc. Japan*, *80*(4B), 793–809.

Polvani, L. M., D. Waugh, J. P. C. Gustavo, and S.-W. Son, (2011), Stratospheric Ozone Depletion : The Main Driver of Twentieth-Century Atmospheric Circulation Changes in the Southern Hemisphere, *J. Clim.*, *24*(2002), 795–812, doi:10.1175/2010JCLI3772.1.

Portmann, R. W., J. S. Daniel, and A. R. Ravishankara, (2012), Stratospheric ozone depletion due to nitrous oxide : influences of other gases, *Philos. Trans. R. Soc. B*, *367*, 1256–1264, doi:10.1098/rstb.2011.0377.

Quine, B. M., and J. R. Drummond, (2002), GENSPECT: A line-by-line code with selectable interpolation error tolerance, *J. Quant. Spectrosc. Radiat. Transf.*, *74*(2), 147–165, doi:10.1016/S0022-4073(01)00193-5.

Randel, W. J., and J. B. Cobb, (1994), Coherent variations of monthly mean and lower stratospheric temperature, *J. Geophys.*, *99*(D3), 5433–5447.

Randel, W. J., and A. M. Thompson, (2011), Interannual variability and trends in tropical ozone derived from SAGE II satellite data and SHADOZ ozonesondes, *J. Geophys. Res.*, *116*(D07303), 1–9, doi:10.1029/2010JD015195.

Randel, W. J., F. Wu, H. Vo, G. E. Nedoluha, and P. M. Forster, (2006), Decreases in stratospheric water vapor after 2001 : Links to changes in the tropical tropopause and the Brewer-Dobson circulation, *J. Geophys. Res.*, *111*(D12312), 1–11, doi:10.1029/2005JD006744.

Ravishankara, A. R., J. S. Daniel, and R. W. Portmann, (2009), Nitrous Oxide (N2O): The Dominant Ozone-Depleting Substance Emitted in the 21st Century, *Science*, *326*(5949), 123–125.

Rayleigh, J. W. S. B., (1871), On the scattering of light by small particles.

Real, E., K. S. Law, B. Weinzierl, M. Fiebig, A. Petzold, O. Wild, J. Methven, S. A. Arnold, A. Stohl, H. Huntrieser, A. E. Roiger, H. Schlager, D. Stewart, M. A. Avery, G. W. Sachse, E. V. Browell, R. A. Ferrare, and D. Blake, (2007), Processes influencing ozone levels in Alaskan forest fire plumes during long-range transport over the North Atlantic, *J. Geophys. Res. Atmos.*, *112*(10), 1–19, doi:10.1029/2006JD007576.

Redondas, A., R. Evans, R. Stuebi, U. Köhler, and M. Weber, (2014), Evaluation of the use of five laboratory-determined ozone absorption cross sections in Brewer and Dobson retrieval algorithms, *Atmos. Chem. Phys.*, *14*(3), 1635–1648, doi:10.5194/acp-14-1635-

2014.

Reed, R. J., (1950), The Role of Vertical Motions in Ozone-Weather Relationships, *J. Meterology*, *7*(4), 263–267.

Reid, S. J., and G. Vaughan, (1991), Lamination in ozone profiles in the lower stratosphere, *Q. J. R. Meteorol. Soc.*, *117*(500), 825–844, doi:10.1002/qj.49711750009.

Revell, L. E., G. E. Bodeker, P. E. Huck, B. E. Williamson, and E. Rozanov, (2012), and Physics The sensitivity of stratospheric ozone changes through the 21st century to N2O and CH4, *Atmos. Chem. Phys.*, *12*, 11309–11317, doi:10.5194/acp-12-11309-2012.

Revell, L. E., G. E. Bodeker, D. Smale, R. Lehmann, P. E. Huck, B. E. Williamson, E. Rozanov, and H. Struthers, (2012), The effectiveness of N2O in depleting stratospheric ozone, *Geophys. Res. Lett.*, *39*(L15806), 1–6, doi:10.1029/2012GL052143.

Robichaud, D. J., J. T. Hodges, P. Maslowski, L. Y. Yeung, M. Okumura, C. E. Miller, and L. R. Brown, (2008), High-accuracy transition frequencies for the O2 A-band, *J. Mol. Spectrosc.*, *251*(1–2), 27–37, doi:10.1016/j.jms.2007.12.008.

Rodgers, C. D., (2000), Inverse methods for atmospheric sounding: theory and practice, Vol. 2, World scientific.

Rothman, L. S., I. E. Gordon, Y. Babikov, A. Barbe, D. Chris Benner, P. F. Bernath, M. Birk, L. Bizzocchi, V. Boudon, L. R. Brown, A. Campargue, K. Chance, E. A. Cohen, L. H. Coudert, V. M. Devi, B. J. Drouin, A. Fayt, J. M. Flaud, R. R. Gamache, J. J. Harrison, J. M. Hartmann, C. Hill, J. T. Hodges, D. Jacquemart, A. Jolly, J. Lamouroux, R. J. Le Roy, G. Li, D. A. Long, O. M. Lyulin, C. J. Mackie, S. T. Massie, S. Mikhailenko, H. S. P. Muller, O. V. Naumenko, A. V. Nikitin, J. Orphal, V. Perevalov, A. Perrin, E. R. Polovtseva, C. Richard, M. A. H. Smith, E. Starikova, K. Sung, S. Tashkun, J. Tennyson, G. C. Toon, V. G. Tyuterev, and G. Wagner, (2013), The HITRAN2012 molecular spectroscopic database, *J. Quant. Spectrosc. Radiat. Transf.*, *130*, 4–50, doi:10.1016/j.jqsrt.2013.07.002.

Rothman, L. S., D. Jacquemart, A. Barbe, D. C. Benner, M. Birk, L. R. Brown, M. R.

Carleer, C. C. Jr, K. Chance, L. H. Coudert, V. Dana, V. M. Devi, J. Flaud, R. R. Gamache, A. Goldman, J. Hartmann, K. W. Jucks, A. G. Maki, J. Mandin, S. T. Massie, J. Orphal, A. Perrin, C. P. Rinsland, M. A. H. Smith, J. Tennyson, R. N. Tolchenov, R. A. Toth, J. Vander Auwera, P. Varanasi, and G. Wagner, (2005), The HITRAN 2004 molecular spectroscopic database, *J. Quant. Spectrosc. Radiat. Transf.*, *96*, 139–204, doi:10.1016/j.jqsrt.2004.10.008.

Rowland, F. S., and M. J. Molina, (1975), Chlorofluoromethans in the Environment, *Rev. Geophys. Sp. Phys.*, *13*(I).

Scarnato, B., J. Staehelin, T. Peter, J. Gröbner, and R. Stübi, (2009), Temperature and slant path effects in Dobson and Brewer total ozone measurements, *J. Geophys. Res.*, *114*, D24303, doi:10.1029/2009JD012349.

Scarnato, B., J. Staehelin, R. Stübi, and H. Schill, (2010), Long-term total ozone observations at Arosa (Switzerland) with Dobson and Brewer instruments (1988–2007), *J. Geophys. Res.*, *115*, D13306, doi:10.1029/2009JD011908.

Schoenbein, C. F., (1850), On Ozone., *R. Scociety London*, 1–2.

Schwartz, M. J., A. Lambert, G. L. Manney, W. G. Read, N. J. Livesey, L. Froidevaux, C. O. Ao, P. F. Bernath, C. D. Boone, R. E. Cofield, W. H. Daffer, B. J. Drouin, E. J. Fetzer, R. A. Fuller, R. F. Jarnot, J. H. Jiang, Y. B. Jiang, J. F. Li, M. G. Mlynczak, S. Pawson, J. M. Russell III, M. L. Santee, W. V Snyder, P. C. Stek, R. P. Thurstans, A. M. Tompkins, P. A. Wagner, K. A. Walker, J. W. Waters, and D. L. Wu, (2008), Validation of the Aura Microwave Limb Sounder temperature and geopotential height measurements, *J. Geophys.*, *113*(D15S11), 1–23, doi:10.1029/2007JD008783.

Serdyuchenko, A., V. Gorshelev, M. Weber, W. Chehade, and J. P. Burrows, (2014), High spectral resolution ozone absorption cross-sections – Part 2: Temperature dependence, *Atmos. Meas. Tech*, *7*, 625–636, doi:10.5194/amt-7-625-2014.

Sheese, P. E., K. Strong, E. J. Llewellyn, R. L. Gattinger, J. M. Russell III, C. D. Boone, M. E. Hervig, R. J. Sica, and J. Bandoro, (2012), Assessment of the quality of OSIRIS

mesospheric temperatures using satellite and ground-based measurements, *Atmos. Meas. Tech.*, *5*(12), 2993.

Shepherd, T. G., and A. I. Jonsson, (2008), On the attribution of stratospheric ozone and temperature changes to changes in ozone-depleting substances and well-mixed greenhouse gases, *Atmos. Chem. Phys.*, *8*, 1435–1444.

Shindell, D. T., J. C. I. Kuylenstierna, E. Vignati, R. Van Dingenen, M. Amann, Z. Klimont, S. C. Anenberg, N. Muller, G. Janssens-maenhout, F. Raes, J. Schwartz, G. Faluvegi, L. Pozzoli, K. Kupiainen, L. Höglund-isaksson, L. Emberson, D. Streets, V. Ramanathan, K. Hicks, N. T. K. Oanh, G. Milly, and M. Williams, (2012), Simultaneously Mitigating Near-Term Climate Change and Improving Human Health and Food Security, *Science*, *335*, 183–190.

Shine, K. P., M. S. Bourqui, P. M. Forster, S. H. E. Hare, and U. Langematz, (2003), A comparison of model-simulated trends in stratospheric temperatures, *Q. J. R. Meteorol. Soc.*, *129*, 1565–1588, doi:10.1256/qj.02.186.

Sica, R. J., M. R. M. Izawa, K. A. Walker, C. Boone, S. V Petelina, P. S. Argall, P. Bernath, and G. B. Burns, (2008), Validation of the Atmospheric Chemistry Experiment (ACE) version 2.2 temperature using ground-based and space-borne measurements, *Atmos. Chem. Phys.*, *8*, 35–62.

Singh, H. B., B. E. Anderson, W. H. Brune, C. Cai, R. C. Cohen, J. H. Crawford, M. J. Cubison, E. P. Czech, L. Emmons, H. E. Fuelberg, G. Huey, D. J. Jacob, J. L. Jimenez, A. Kaduwela, Y. Kondo, J. Mao, J. R. Olson, G. W. Sachse, S. A. Vay, A. Weinheimer, P. O. Wennberg, and A. Wisthaler, (2010), Pollution influences on atmospheric composition and chemistry at high northern latitudes: Boreal and California forest fire emissions, *Atmos. Environ.*, *44*(36), 4553–4564, doi:10.1016/j.atmosenv.2010.08.026.

Sioris, C. E., C. A. Mclinden, V. E. Fioletov, C. Adams, J. M. Zawodny, A. E. Bourassa, C. Z. Roth, D. A. Degenstein, and A. Studies, (2014), Trend and variability in ozone in the tropical lower stratosphere over 2 . 5 solar cycles observed by SAGE II and OSIRIS, *Atmos. Chem. Phys.*, *14*, 3479–3496, doi:10.5194/acp-14-3479-2014.

Smit, H. G. J., and D. Kley, (1998), JOSIE: The 1996 WMO International Intercomparison of Ozonesondes under Quasi Flight Conditions in the Environmental Simulation Chamber at Jülich, WMO Global Atmosphere Watch report series, No. 130 (Technical Document No. 926), World Meteorological Organization, Geneva, Switzerland.

Smit, H. G. J., W. Straeter, B. J. Johnson, S. J. Oltmans, J. Davies, D. W. Tarasick, B. Hoegger, R. Stubi, F. J. Schmidlin, T. Northam, A. M. Thompson, J. C. Witte, I. Boyd, and F. Posny, (2007), Assessment of the performance of ECC-ozonesondes under quasi-flight conditions in the environmental simulation chamber: Insights from the Juelich Ozone Sonde Intercomparison Experiment (JOSIE), *J. Geophys. Res.*, *112*(19), 1–18, doi:10.1029/2006JD007308.

Sofiev, M., T. Ermakova, and R. Vankevich, (2012), Evaluation of the smoke-injection height from wild-land fires using remote-sensing data, *Atmos. Chem. Phys., 12*, 1995–2006, doi:10.5194/acp-12-1995-2012.

Solomon, A., (2006), Impact of latent heat release on polar climate, *Geophys. Res. Lett.*, *33*(L07716), 2–5, doi:10.1029/2005GL025607.

Solomon, S., (1999), Stratospheric ozone depletion: A review of concepts and history, *Rev. Geophys.*, *37*(3), 275–316, doi:10.1029/1999RG900008.

Solomon, S., S. Borrmann, R. R. Garcia, R. Portmann, L. Thomason, L. R. Poole, D. Winker, and M. P. Mccormick, (1997), Heterogeneous chlorine chemistry in the tropopause region, *J. Geophys. Res.*, *102*(D17), 21411–21429.

Solomon, S., R. R. Garcia, F. S. Rowland, and D. J. Wuebbles, (1986), On the depletion of Antarctic ozone, *Nature*, *321*(6072), 755–758.

Solomon, S., R. Garcia, and A. R. Ravishankara, (1994), On the role of iodine in ozone depletion, *J. Geophys. Res.*, *99*(D10), 20491–20499.

Spracklen, D. V., L. J. Mickley, J. A. Logan, R. C. Hudman, R. Yevich, M. D. Flannigan, and A. L. Westerling, (2009), Impacts of climate change from 2000 to 2050 on wildfire activity and carbonaceous aerosol concentrations in the western United States, *J.*

Geophys. Res. Atmos., *114*(20), 1–17, doi:10.1029/2008JDO10966.

Staehelin, J., A. Renaud, J. Bader, R. McPeters, P. Viatte, B. Hoegger, V. Bugnion, M. Giroud, and H. Schill, (1998), Total ozone series at Arosa (Switzerland): Homogenization and data comparison, *J. Geophys. Res.*, *103*(D5), 5827, doi:10.1029/97JD02402.

Staehelin, J., J. Thudium, R. Buehler, A. Volz-Thomas, and W. Graber, (1994), Trends in Surface Ozone Concentrations at Arosa (Switzerland), *Atmos. Environ.*, *28*(1), 75–87.

Steinbrecht, W., and H. Claude, (1998), Correlations between tropopause height and total ozone : Implications for long-term changes, *J. Geophys. Res.*, *103*(D15), 183–192.

Stevens, M. H., L. E. Deaver, M. E. Hervig, J. M. Russell III, D. E. Siskind, P. E. Sheese, E. J. Llewellyn, R. L. Gattinger, J. Höffner, and B. T. Marshall, (2012), Validation of upper mesospheric and lower thermospheric temperatures measured by the Solar Occultation for Ice Experiment, *J. Geophys.*, *117*(D16304), 1–13, doi:10.1029/2012JD017689.

Stevenson, D. S., F. J. Dentener, M. G. Schultz, K. Ellingsen, T. P. C. Van Noije, O. Wild, G. Zeng, M. Amann, C. S. Atherton, N. Bell, D. J. Bergmann, and I. Bey, (2006), Multimodel ensemble simulations of present-day and near-future tropospheric ozone, *J. Geophys. Res.*, *111*(D08301), 1–23, doi:10.1029/2005JD006338.

Stevenson, D. S., P. J. Young, V. Naik, J. Lamarque, D. T. Shindell, A. Voulgarakis, and R. B. Skeie, (2013), Tropospheric ozone changes , radiative forcing and attribution to emissions in the Atmospheric Chemistry and Climate Model Intercomparison Project (ACCMIP), *Atmos. Chem. Phys.*, *13*, 3063–3085, doi:10.5194/acp-13-3063-2013.

Stiller, G. P., M. Kiefer, E. Eckert, T. Von Clarmann, S. Kellmann, and M. Garc, (2012), Validation of MIPAS IMK / IAA temperature , water vapor , and ozone profiles with MOHAVE-2009 campaign measurements, *Atmos. Meas. Tech.*, *5*, 289–320, doi:10.5194/amt-5-289-2012.

Stocks, B. J., M. A. Fosberg, T. J. Lynham, L. Mearns, B. M. Wotton, Q. Yang, J. Z. Jin, K. Lawrence, G. R. Hartley, J. A. Mason, and D. W. McKenney, (1998), Climate change

and forest fire potential in Russian and Canadian boreal forests, *Clim. Change*, *38*(1), 1–13, doi:10.1023/A:1005306001055.

Stohl, A., (1998), Computation, accuracy and applications of trajectories-A review and bibliography, *Atmos. Environ.*, *32*(6), 947–966, doi:10.1016/S1474-8177(02)80024-9.

Stolarski, R. S., S. M. Frith, and G. Space, (2006), Search for evidence of trend slow-down in the long-term TOMS / SBUV total ozone data record : the importance of instrument drift uncertainty, *Atmos. Chem. Phys.*, *6*, 4057–4065.

Stolarski, S., and J. Cicerone, (1974), Stratospheric Chlorine: a Possible Sink for Ozone, *Can. J. Chem.*, 1–6.

Sudo, K., M. Takahashi, and H. Akimoto, (2003), Future changes in stratosphere-troposphere exchange and their impacts on future tropospheric ozone simulations, *Geophys. Res. Lett.*, *30*(24), 2–5, doi:10.1029/2003GL018526.

Sugita, T., T. Yokota, H. Nakajima, H. Kobayashi, N. Saitoh, H. Kawasaki, M. Usami, H. Saeki, M. Horikawa, and Y. Sasano, (2004), A comparative study of stratospheric temperatures between ILAS-II and other data, in *Proceedings of SPIE*, Vol. 5652, pp. 279–289, doi:10.1117/12.570872.

Sugita, T., T. Yokota, T. Nakajima, H. Nakajima, K. Waragai, M. Suzuki, A. Matsuzaki, Y. Itou, H. Saeki, and Y. Sasano, (2001), Temperature and pressure retrievals from O2 A-band absorption measurements made by ILAS: Retrieval algorithm and error analyses, in *Proceedings of SPIE*, Vol. 4150, pp. 94–105, doi:10.1117/12.416949.

Tang, X., S. R. Wilson, K. R. Solomon, M. Shao, and S. Madronich, (2011), Changes in air quality and tropospheric composition due to depletion of stratospheric ozone and interactions with climate, *Photochem. Photobiol. Sci.*, *10*, 280–291, doi:10.1039/C0PP90040K.

Tarasick, D. W., J. Davies, H. G. J. Smit, and S. J. Oltmans, (2016), A re-evaluated Canadian ozonesonde record : measurements of the vertical distribution of ozone over Canada from 1966 to 2013, *Atmos. Meas. Tech.*, *9*, 195–214, doi:10.5194/amt-9-195-2016.

Tarasick, D. W., J. J. Jin, V. E. Fioletov, G. Liu, A. M. Thompson, S. J. Oltmans, J. Liu, C. E. Sioris, X. Liu, O. R. Cooper, T. Dann, and V. Thouret, (2010), High-resolution tropospheric ozone fields for INTEX and ARCTAS from IONS ozonesondes, *J. Geophys. Res. Atmos.*, *115*(20), 1–12, doi:10.1029/2009JD012918.

Teakles, A., R. So, B. Ainslie, R. Nissen, C. Schiller, R. Vingarzan, A. M. Macdonald, D. A. Jaffe, A. K. Bertram, K. B. Strawbridge, R. Leaitch, S. Hanna, D. Toom, J. Baik, and L. Huang, (2016), Impacts of the July 2012 Siberian Fire Plume on Air Quality in the Pacific Northwest, *Atmos. Chem. Phys. Discuss.*, doi:10.5194/acp-2016-302.

Thompson, A. M., K. E. Pickering, D. P. Mcnamara, M. R. Schoeberl, R. D. Hudson, J. H. Kim, E. V Browell, V. W. J. H. Kirchhoff, and D. Nganga, (1996), Where did tropospheric ozone over southern Africa and the tropical Atlantic come from in October 1992? Insights from TOMS, GTE TRACE A, and SAFARI 1992, *J. Geophys. Res.*, *101*(D19), 24251–24278.

Thompson, A. M., J. B. Stone, J. C. Witte, S. K. Miller, S. J. Oltmans, T. L. Kucsera, K. L. Ross, K. E. Pickering, J. T. Merrill, G. Forbes, D. W. Tarasick, E. Joseph, F. J. Schmidlin, W. W. McMillan, J. Warner, E. J. Hintsa, and J. E. Johnson, (2007), Intercontinental Chemical Transport Experiment Ozonesonde Network Study (IONS) 2004: 2. Tropospheric ozone budgets and variability over northeastern North America, *J. Geophys. Res.*, *112*(D12), D12S13, doi:10.1029/2006JD007670.

Thompson, A. M., and J. C. Witte, (2001), Tropical Tropospheric Ozone and Biomass Burning, *Science*, *291*, 2128–2133.

Thompson, D. W. J., D. J. Seidel, W. J. Randel, C. Zou, A. H. Butler, C. Mears, A. Osso, C. Long, and R. Lin, (2012), The mystery of recent stratospheric temperature trends, *Nature*, *491*(7426), 692–697, doi:10.1038/nature11579.

Thouret, V., J. Y. N. Cho, R. E. Newell, and G. J. Smit, (2000), General characteristics of tropospheric' trace constituent layers observed in the MOZAIC program, *J. Geophys. Res.*, *105*(D13), 17379–17392.

Tikhonov, A. N., (1966), On the stability of the functional optimization problem, *USSR Comput. Math. Math. Phys.*, *6*(4), 28–33.

Tran, H., C. Boulet, and J. M. Hartmann, (2006), Line mixing and collision-induced absorption by oxygen in the A band: Laboratory measurements, model, and tools for atmospheric spectra computations, *J. Geophys. Res.*, *111*(15), 1–14, doi:10.1029/2005JD006869.

Tung, K.-K., M. K. W. Ko, J. M. Rodriguez, and N. D. Sze, (1986), Are Antarctic ozone variations a manifestation of dynamics or chemistry?, *Nature*, *322*(6082), 811–814.

Turner, D. S., (1995), Absorption coefficient estimation using a two-dimensional interpolation procedure, *J. Quant. Spectrosc. Radiat. Transf.*, *53*(6), 633–637, doi:10.1016/0022-4073(95)00024-F.

US Standard Atmosphere, (1976), US Government Printing Office, Washington, DC, 1976.

Val Martin, M., R. E. Honrath, R. C. Owen, G. Pfister, P. Fialho, and F. Barata, (2006), Significant enhancements of nitrogen oxides , black carbon , and ozone in the North Atlantic lower free troposphere resulting from North American boreal wildfires, *J. Geophys.*, *111*(D23S60), 1–17, doi:10.1029/2006JD007530.

Van Roozendael, M., P. Peeters, H. K. Roscoe, H. De Backer, A. E. Jones, L. Bartlett, G. Vaughan, F. Goutail, J. P. Pommereau, E. Kyro, C. Wahlstrom, G. Braathen, and P. C. Simon, (1998), Validation of ground-based visible measurements of total ozone by comparison with Dobson and Brewer spectrophotometers, *J. Atmos. Chem.*, *29*(1), 55–83, doi:10.1023/A:1005815902581.

Vanicek, K., (2006), Differences between ground Dobson, Brewer and satellite TOMS-8, GOME-WFDOAS total ozone observations at Hradec Kralove, Czech, *Atmos. Chem. Phys.*, *6*, 5163–5171, doi:10.5194/acpd-6-5839-2006.

Vanicek, K., M. Stanek, and M. Dubrovskỳ, (2003), Evaluation of Dobson and Brewer total ozone observations from Hradec Králové Czech Republic, 1961-2002, *Publ. Czech Hydrometeorol. Institute, Prague, ISBN*, *80*, 86690–10.

Vanier, J., and D. I. Wardle, (1969), The effects of spectral resolution on total ozone measurements, *Q. J. R. Meteorol. Soc.*, *95*(404), 395–399, doi:10.1002/qj.49709540411.

Verma, S., J. Worden, B. Pierre, D. B. A. Jones, J. Al-Saadi, F. Boersma, K. Bowman, A. Eldering, B. Fisher, L. Jourdain, S. Kulawik, and H. Worden, (2009), Ozone production in boreal fire smoke plumes using observations from the Tropospheric Emission Spectrometer and the Ozone Monitoring Instrument, *J. Geophys. Res.*, *114*(2), doi:10.1029/2008JD010108.

Voulgarakis, A., V. Naik, D. T. Shindell, P. J. Young, M. J. Ptather, and O. Wild, (2013), Analysis of present day and future OH and methane lifetime in the ACCMIP simulations, *Atmos. Chem. Phys.*, *13*, 2563–2587, doi:10.5194/acp-13-2563-2013.

Wallace, J. M., and P. V Hobbs, (2006), Atmospheric science: an introductory survey, Vol. 92, Academic press.

Wang, P., P. Stammes, R. van der A, G. Pinardi, and M. van Roozendael, (2008), FRESCO+: an improved O2 A-band cloud retrieval algorithm for tropospheric trace gas retrievals, *Atmos. Chem. Phys. Discuss.*, *8*(3), 6565–6576, doi:10.5194/acpd-8-9697-2008.

Wang, Y., J. Jacob, and A. Logan, (1998), Global simulation of tropospheric O3-NOx-hydrocarbon chemistry 3 . Origin of tropospheric ozone and effects of nonmethane hydrocarbons, *J. Geophys. Res.*, *103*(D9), 10757–10767.

Waugh, D. W., L. Oman, S. R. Kawa, R. S. Stolarski, S. Pawson, A. R. Douglass, P. A. Newman, and J. E. Nielsen, (2009), Impacts of climate change on stratospheric ozone recovery, *Geophys. Res. Lett.*, *36*(L03805), 1–6, doi:10.1029/2008GL036223.

Weatherhead, E. C., and S. B. Andersen, (2006), The search for signs of recovery of the ozone layer., *Nature*, *441*(7089), 39–45, doi:10.1038/nature04746.

Weiss, A. K., and J. Staehelin, (2001), Chemical and dynamical contributions to ozone profile trends of the Payerne (Switzerland) balloon soundings, *J. Geophys. Res.*, *106*(D19), 22685–22694.

Weller, R., R. Lilischkis, O. Schrems, R. Neuber, and S. Wessel, (1996), Vertical ozone

distribution in the marine atmosphere over the central Atlantic Ocean (56S - 50N), *J. Geophys. Res.*, *101*(D1), 1387–1399.

Westerling, A. L., H. G. Hidalgo, D. R. Cayan, and T. W. Swetnam, (2006), Warming and earlier spring increase western U.S. forest wildfire activity, *Science*, *313*(5789), 940–3, doi:10.1126/science.1128834.

Wigder, N. L., D. A. Jaffe, and F. A. Saketa, (2013), Ozone and particulate matter enhancements from regional wildfires observed at Mount Bachelor during 2004-2011, *Atmos. Environ.*, *75*, 24–31, doi:10.1016/j.atmosenv.2013.04.026.

Wild, O., and P. I. Palmer, (2008), How sensitive is tropospheric oxidation to anthropogenic emissions ?, *Geophys. Res. Lett.*, *35*(L22802), 1–5, doi:10.1029/2008GL035718.

WMO, (1957), A three-dimensional science: Second session of the commission for aerology, *WMO Bull*, *4*(2), 134–138.

WMO, (2002), Scientific Assessment of Ozone Depletion, 2002, World Meteorological Organization.

WMO, (2006), Scientific Assessment of Ozone Depletion, 2006, World Meteorological Organization.

WMO, (2010), Scientific Assessment of Ozone Depletion, 2010, World Meteorological Organization.

WMO, (2014), Scientific Assessment of Ozone Depletion, 2014, World Meteorological Organization.

Wofsy, C., M. B. Mcelroy, and Y. L. Yung, (1975), The Chemistry of Atmospheric Bromine, *Geophys. Res. Lett.*, *2*(6), 215–218.

Wotton, B. M., C. A. Nock, and M. D. Flannigan, (2010), Forest fire occurrence and climate change in Canada, *Int. J. Wildl. Fire*, *19*, 253–271.

Yang, E., D. M. Cunnold, M. J. Newchurch, and R. J. Salawitch, (2005), Change in ozone trends at southern high latitudes, *Geophys. Res. Lett.*, *32*(L12812), 1–5,

doi:10.1029/2004GL022296.

Yang, Y., A. Marshak, J. Mao, A. Lyapustin, and J. Herman, (2013), A method of retrieving cloud top height and cloud geometrical thickness with oxygen A and B bands for the Deep Space Climate Observatory (DSCOVR) mission: Radiative transfer simulations, *J. Quant. Spectrosc. Radiat. Transf.*, *122*, 141–149, doi:10.1016/j.jqsrt.2012.09.017.

Young, P. J., A. T. Archibald, K. W. Bowman, J. Lamarque, V. Naik, D. S. Stevenson, and S. Tilmes, (2013), Pre-industrial to end 21st century projections of tropospheric ozone from the Atmospheric Chemistry and Climate Model Intercomparison Project (ACCMIP), *Atmos. Chem. Phys.*, *13*, 2063–2090, doi:10.5194/acp-13-2063-2013.

Zerefos, C., A. F. Bais, and I. Ziomas, (1992), On the Relative Importance of Quasi-Biennial Oscillation and El Nino/Southern Oscillation in the Revised Dobson Total Ozone Records, *J. Geophys. Res.*, *97*(D9), 10135–10144.

Zhang, Y., O. R. Cooper, A. Gaudel, A. M. Thompson, P. Nédélec, S. Ogino, and J. J. West, (2016), Tropospheric ozone change from 1980 to 2010 dominated by equatorward redistribution of emissions, *Nat. Geosci.*, *9*, 875–879, doi:10.1038/NGEO2827.

Ziemke, J. R., S. Chandra, B. N. Duncan, L. Froidevaux, P. K. Bhartia, P. F. Levelt, and J. W. Waters, (2006), Tropospheric ozone determined from Aura OMI and MLS : Evaluation of measurements and comparison with the Global Modeling Initiative ' s Chemical Transport Model, *J. Geophys. Res.*, *111*(D19303), 1–18, doi:10.1029/2006JD007089.

Appendix

A. List of Publications

Moeini O., C. T. McElroy, D. W. Tarasick, C. R. Nowlan, J. R. Drummond, (2017), Impact of HITRAN 2012 database on MAESTRO pressure-Temperature profiles, *J. Quant. Spectrosc. Radiat. Transf.*, In progress.

Moeini O., D. W. Tarasick, C. T. McElroy, J. Liu, M. K. Osman, A. M. Thompson, (2017), Estimating Boreal Fire-generated Ozone over Canada using Ozonesonde Profiles and a Differential Back Trajectory Technique, *Atmos. Chem. Phys.*, In progress.

Moeini O., Z. Vaziri, C. T. McElroy, D. W. Tarasick, R. D. Evans, I. Petropavlovskikh, K. H. Feng, (2017), Effect of Instrumental Stray Light on Brewer and Dobson Total Ozone Measurements, *Atmos. Meas. Tech.*, In progress.

Osman M. K., D. W. Tarasick, J. Liu, **O. Moeini**, V. Thouret, V. E. Fioletov, M. Parrington, P. Nédélec, (2016), Carbon Monoxide Climatology derived from the Trajectory Mapping of Global MOZAIC-IAGOS Data, *Atmos. Chem. Phys.*, 16, 10263-10282, doi:10.5194/acp-16-10263-2016.

Sioris C. E., J. Zou, D.A. Plummer, C. D. Boone, C. T. McElroy, P. E. Sheese, **O. Moeini**, and P. F. Bernath, (2016), Upper tropospheric water vapour variability at high latitudes – Part 1: Influence of the annular modes, *Atmos. Chem. Phys.*, 16, 3265-3278, doi:10.5194/acp-16-3265-2016.

Liu J., D. W. Tarasick, V. E. Fioletov, C. McLinden, T. Zhao, S. Gong, C. Sioris, J. J. Jin, G. Liu, and **O. Moeini**, (2013), A Global Ozone Climatology from Ozone Soundings via Trajectory Mapping: A Stratospheric Perspective, *Atmos. Chem. Phys.*, 13, 11441-11464.

Liu G., J. Liu, D. W. Tarasick, V. E. Fioletov, J. J. Jin, **O. Moeini**, X. Liu, C. E. Sioris, and M. K. Osman, (2013), A global tropospheric ozone climatology from trajectory-mapped ozone soundings, *Atmos. Chem. Phys.*, 13, 10659-10675.